

UC Santa Barbara

UC Santa Barbara Electronic Theses and Dissertations

Title

Magnetic Resonance and SQUID Magnetometry Studies of Lithium Transition Metal Oxide Cathodes

Permalink

<https://escholarship.org/uc/item/28k5999v>

Author

Nguyen, Howie

Publication Date

2024

Peer reviewed|Thesis/dissertation

UNIVERSITY OF CALIFORNIA

Santa Barbara

Magnetic Resonance and SQUID Magnetometry Studies of Lithium Transition Metal Oxide

Cathodes

A dissertation submitted in partial satisfaction of the
requirements for the degree Doctor of Philosophy
in Materials

by

Howie Nguyen

Committee in charge:

Professor Raphaële Clément, Chair

Professor Ram Seshadri

Professor Anton Van der Ven

Professor Songi Han, Northwestern University

March 2024

The dissertation of Howie Nguyen is approved.

Ram Seshadri

Anton Van der Ven

Songi Han

Raphaële Clément, Committee Chair

January 2024

Magnetic Resonance and SQUID Magnetometry Studies of Lithium Transition Metal Oxide

Cathodes

Copyright © 2024

by

Howie Nguyen

Curriculum Vitae
Howie Nguyen

EDUCATION

- Ph.D. Materials, University of California Santa Barbara January 2024
Advisor: Professor Raphaële J. Clément
- B.S. in Chemistry *magna cum laude*, Georgetown University May 2017
Senior thesis advisor: Professor Sarah L. Stoll

PUBLICATIONS

1. **H. Nguyen**, E.N. Bassegy, E.E. Foley, R. Giovine, and R.J. Clément, “Operando electron spin probes for battery applications”, *manuscript in preparation (working title)*.
2. **H. Nguyen**, P. Vassilaras, R. Silverstein, P. Kurzhals, K. Seidel, and R.J. Clément, “Dopant performance improvement mechanisms in Mg and Al doped LiNiO₂”, *manuscript in preparation (working title)*.
3. **H. Nguyen**, U. Berner, J. Chamorro, L. Cheng, R.J. Clément, R. Seshadri, and D.A. Kitchaev, “Rapid characterization of Pt-Co fuel cell catalyst degradation using magnetometry”, *manuscript in preparation (working title)*.
4. **H. Nguyen**, P. Kurzhals, M. Bianchini, K. Seidel, and R.J. Clément, “New insights into degradation modes in the LiNiO₂ cathode from NMR Spectroscopy”, *manuscript in preparation (working title)*.
5. J. Zhou, M.L.H. Chandrappa, S. Tan, S. Wang, C. Wu, **H. Nguyen**, C. Wang, H. Liu, S. Yu, Q.R.S. Miller, G. Hyun, J. Holoubek, J. Hong, C. Soulen, Z. Liang, C. Wang, R.J. Clément, Y. Yao, E. Hu, S.P. Ong, and P. Liu, “Healable Electrically Conducting Sulfur Iodide for Solid-State Li-S batteries”, *accepted*.
6. **H. Nguyen**, R. Silverstein, A. Zaveri, W. Cui, P. Kurzhals, S. Siculo, M. Bianchini, K. Seidel, and R.J. Clément, “Twin boundaries contribute to the first cycle irreversibility of LiNiO₂”, *Adv. Funct. Mater.*, **2023**, 2306168. doi:[10.1002/adfm.202306168](https://doi.org/10.1002/adfm.202306168).
7. S.D. Jones, **H. Nguyen**, P.M. Richardson, Y.Q. Chen, K.E. Wyckoff, C.J. Hawker, R.J. Clément, G.H. Fredrickson, and R.A. Segalman, “Design of Polymeric Zwitterionic Solid Electrolytes with Superionic Lithium Transport”, *ACS Cent. Sci.*, **2022**, 8,2, 169-175. doi:[10.1021/acscentsci.1c01260](https://doi.org/10.1021/acscentsci.1c01260).
8. **H. Nguyen**, and R.J. Clément, “Rechargeable batteries from the perspective of the electron spin”, *ACS Energy Lett.*, **2020**, 5, 12, 3848-3859. doi:[10.1021/acseenergylett.0c02074](https://doi.org/10.1021/acseenergylett.0c02074).

ABSTRACT

Magnetic Resonance and SQUID Magnetometry Studies of Lithium Transition Metal Oxide

Cathodes

by

Howie Nguyen

High energy density batteries are essential for compact and lightweight power storage, enabling longer lasting and more efficient portable electronic devices, electric vehicles, and grid storage solutions. Advancements in battery technology to enhance energy storage capacity and extend range are crucial for the complete transition to renewable energy. Currently, the capacity of state-of-the-art batteries is limited by the cathode and improvements in their design are contingent on better understanding of their working mechanisms. This dissertation investigates the layered lithium transition metal oxide class of cathodes, with a focus on Co-free compositions ($\text{LiNi}_{0.5}\text{Mn}_{0.5}\text{O}_2$ and LiNiO_2), and explores the relationship between cathode composition, structure, and performance.

We first develop advanced characterization techniques that probe the electron spins in cathodes to investigate reaction mechanisms occurring during battery operation. *Operando* cells for magnetometry and electron paramagnetic resonance (EPR) were designed and tested. These electron spin probes provide complementary insights, which aid in interpretation of ambiguous data. We demonstrate the tandem use of these cells on $\text{LiNi}_{0.5}\text{Mn}_{0.5}\text{O}_2$ and show that the magnetism and redox reactions in the charge cycle are largely influenced by the Ni/Li

antisite defects in the material. Similarly, in LiNiO_2 the defects in the as-synthesized material are found to have a significant contribution to its irreversible capacity. Twin boundaries and Ni over-stoichiometry (y in $\text{Li}_{1-y}\text{Ni}_{1+y}\text{O}_2$) are quantified through X-ray diffraction, magnetometry, and solid-state nuclear magnetic resonance (NMR) assisted with first-principles calculation of ssNMR parameters. These planar and point defects prevent lithium reinsertion at low voltages in the initial cycle due to impeded lithium diffusion. Finally, the electrochemical aging mechanism in LiNiO_2 is investigated. Structural changes in LiNiO_2 induced by extended high voltage cycling are correlated with diminishing capacity retention. The capacity decay is attributed to Li inventory loss and interlayer Ni-migration. The methodology and defect-property relationships established here will aid in future design of improved batteries.

TABLE OF CONTENTS

Chapter 1. Introduction	1
1.1. The Role of Batteries in the Renewable Energy Transition	1
1.2. Layered Lithium Transition Metal Oxides	3
1.4. Dissertation outline and goals	9
1.6. Rechargeable Batteries from the Perspective of the Electron Spin	11
1.6.1 Introduction.....	11
1.6.2 EPR studies of transition metal based battery electrodes.	21
1.6.3 EPR studies of Li microstructures formed during electrochemical cycling.....	26
1.6.4 EPR studies of beyond Li-ion batteries.	27
1.6.5 Magnetometry studies of battery electrodes and devices.	28
1.6.6 Conclusion	34
Chapter 2. Methods	35
2.1. Electrochemical Testing.....	35
2.2. X-Ray Diffraction	37
2.3. Magnetometry	39
2.4 Magnetic Resonance Spectroscopy.....	42
Chapter 3. <i>Operando</i> Electron Spin Probes for Battery Applications	47
3.1 Introduction.....	47
3.2 Methodology	49
3.3 <i>Operando</i> Cell Designs and Experiments	51

3.3.1 EPR Cell.....	52
3.3.2 Magnetometry Cell	54
3.4 Reaction mechanisms of $\text{LiNi}_{0.5}\text{Mn}_{0.5}\text{O}_2$	56
3.5 Conclusions.....	64
Chapter 4. Twin Boundaries Contribute to the First Cycle Irreversibility of LiNiO_2 .	66
4.1. Introduction.....	66
4.2. Experimental	72
4.3. Results and Discussion	78
4.3.1. Defects in as-synthesized LiNiO_2 samples.	78
4.3.2. Impact of twin boundaries on the first cycle irreversible capacity of LiNiO_2	91
4.4. Conclusions.....	100
4.5. Appendix for Twin Boundaries Contribute to the First Cycle Irreversibility of LiNiO_2	102
Chapter 5. New Insights into the Composition of Fatigued Phases Formed During Long-term Cycling of LiNiO_2	119
5.1. Introduction.....	119
5.2 Results and Discussion	121
5.3 Conclusions.....	130
5.4 Appendix for New Insights into the Composition of Fatigued Phases Formed During Long-term Cycling of LiNiO_2	131
Chapter 6. Conclusions and Future work.....	152
Bibliography	158

Chapter 1. Introduction

1.1. The Role of Batteries in the Renewable Energy Transition

Anthropogenic generation of greenhouse gases has resulted in a gamut of environmental issues, necessitating the transition to renewable energy to curb society's reliance on fossil fuels. While the share of electricity generated worldwide through renewable sources has been steadily increasing from ~20% in 1990 to ~28% in 2020, these improvements remain insufficient to meet the goals of the Paris Climate Accords and to limit the global rise in temperature to 1.5° C. Solar photovoltaics and wind power has seen the largest increase in electricity generation since 1990, but one barrier to overcome before the complete adoption of renewable energy is its intermittent nature. These resources are not consistent throughout the day and change constantly based on the time, weather, and geographic location. As such, it is pertinent that energy storage technologies can scale with the pace of renewable energy adoption to store electricity that is generated during peak hours to be used during off-peak periods. Batteries are a promising energy storage solution that has seen tremendous improvements in recent years and will play a key role in enabling the usage of intermittent sources of energy for home and transportation.

Within the battery space, lithium-ion batteries (LIB) are the most widely adopted due to their high energy density, long cycle life, and efficiency. A typical LIB cell is depicted in **Figure 1** and has several components that are essential to its operation. There are two electrodes, cathode and anode, which are deposited on current collector substrates (aluminum for the cathode and copper for the anode). The electrodes are separated by a porous polymer

membrane to prevent short circuiting of electrodes while allowing for the transport of ions. The entire cell is soaked in an electrolyte typically comprised of non-aqueous organic solvent blends and a lithium salt. The electrodes are composites with an active material(s), conductive carbon additive, and a polymer binder which binds the active material particles into a film. State of the art batteries utilize cathode active materials containing lithium transition metal oxides and anode active materials comprised of graphite.

During operation of LIBs, Li ions shuttle from the cathode to anode during the charge process, which is accompanied by the oxidation of the transition metal in the cathode to compensate for the loss positive charge of the Li ion. This reaction is driven by an external power source, which applies a potential to the cell. On discharge, the reverse process occurs and Li ions leave the graphite anode and intercalate back into the cathode. The transport of ions back into the cathode is accompanied by the transport of electrons through the external circuit, which is used to do work. The initial cycles, so-called formation cycles, induce the formation of a solid-electrolyte interphase (SEI) at the surface of the material, which passivates the surface from further reaction while still allowing for Li to diffuse in and out of the particles.

The energy density of the battery is determined by the potential at which these redox reactions occur, the number of Li-ions that can be shuttled between electrodes reversible, and the mass/volume of the cell. Beyond energy density, additional performance metrics that are important include rate capability, calendar/cycle life, cost, efficiency, and safety. These properties are inherently linked to the materials, both active and inactive, which batteries are comprised of.

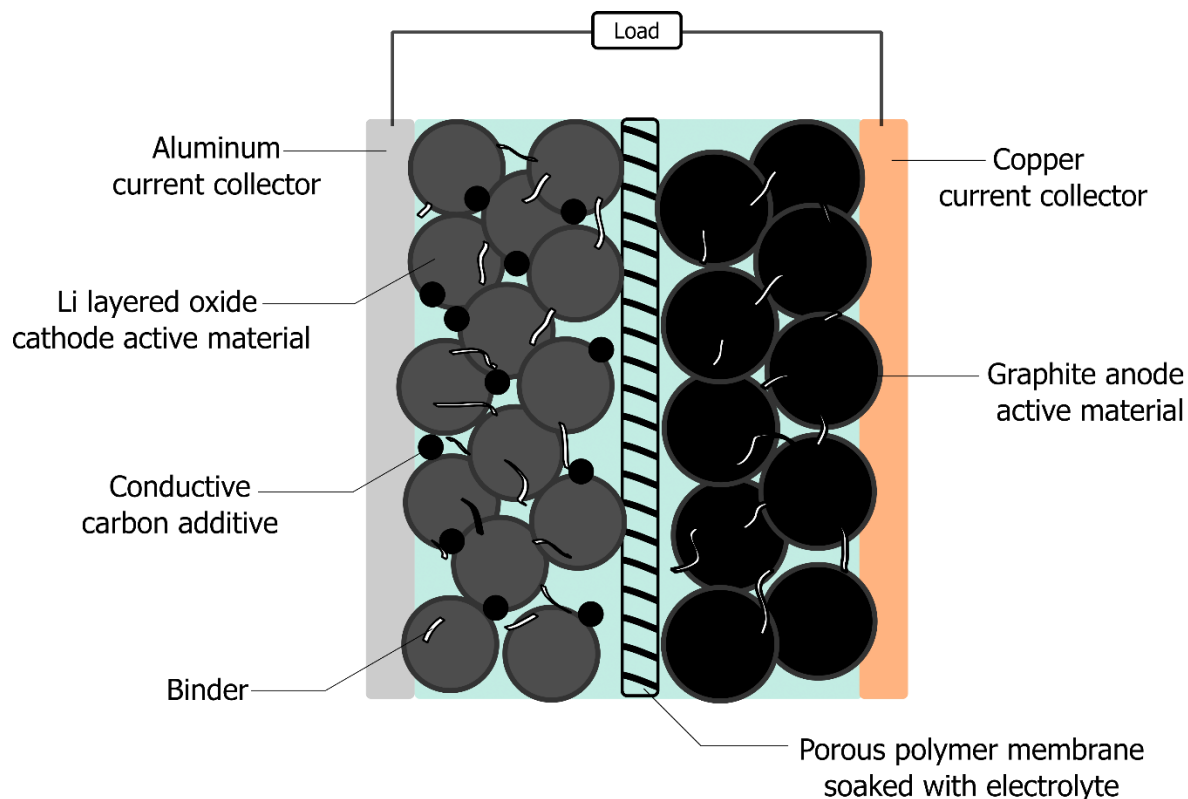


Figure 1 Schematic of a Li-ion battery cell with different components labeled.

1.2. Layered Lithium Transition Metal Oxides

The capacity in batteries is currently limited by the cathode, which remains an active field of research with the goal of improving current materials as well as discovering novel cathode materials. Layered lithium transition metal oxides remain the most widely adopted cathode material since the commercialization of the first Li-ion battery by Sony in 1991.¹ This class of structures has the general chemical formula of LiMO_2 and exhibit an $\alpha\text{-NaFeO}_2$ structure with $R\text{-}3m$ symmetry. The structure is comprised of alternating layers of transition metals (M) and Li ions, which are all held together by an oxygen anion sublattice (**Figure 2**) These layers are stacked along the c -lattice and Li ions have a 2D diffusion pathway along the a - b plane. The layered nature of these materials facilitates the reversible insertion and extraction of Li ions during charging and discharging cycles, allowing for efficient energy storage and release. The

cubic-close packing of oxygen allows for dense packing of M and Li ions in the octahedral sites of the structure, which improves the inherent energy density of the material.

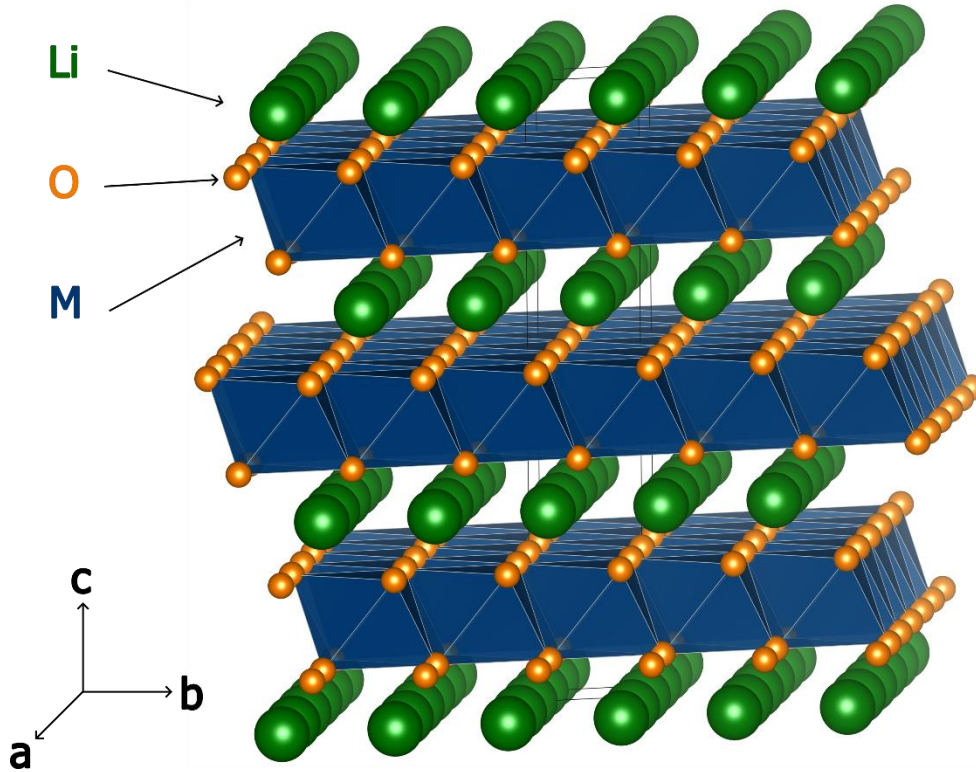


Figure 2 The layered rock salt lithium transition metal oxide structure (LiMO_2 , $R\text{-}3m$ symmetry) comprises alternating layers of transition metals (M) and lithium (Li), which are held together by an oxygen (O) anionic sublattice. Li diffusion through the Li slabs occur during the (dis)charge processes in Li-ion batteries.

The electrochemical performance of layered lithium transition metal oxide cathodes is governed by the interplay of various factors, including crystal structure, ion diffusion kinetics, and electronic conductivity. These properties can be tuned by the composition of the transition metal layer (M). The M layer can contain a single or blends of metals, which alters the performance of the cathode material. Common formulations are the NCM/NCA type cathodes, which contain nickel, cobalt, and manganese or aluminum.^{2,3} The desire for high energy density restricts the M layer to light elements such as $3d$ transition metals with each element contributing to a different property of the material. Manganese and aluminum in these systems

are in the 4+ and 3+ oxidation state, respectively, which makes them redox inactive in these systems. However, they improve the stability of the material.^{4,5} Cobalt is essential for improving rate capability of the material and is also redox active, utilizing the $\text{Co}^{3+/4+}$ redox couple.⁶ However, due to the cost of cobalt and the fact that it is a geographically limited resource with problematic mining practices, the current goal of the field is to eliminate the dependence on cobalt. Nickel is typically used because the potentials for the $\text{Ni}^{2+}/\text{Ni}^{3+}$ and $\text{Ni}^{3+/4+}$ redox couples are within the electrolyte electrochemical stability window.

When layered oxides are delithiated during charge, the lattice parameters evolve as a function of the state of charge (SOC) or remaining Li content in the system.⁷ Oxidation of the transition metals during charge leads to a decrease in the a, b -lattice parameters as the increased positive charge attracts its remaining electrons more strongly, which leads to a reduction in size of the transition metal. The c -lattice parameter evolves in a non-monotonic fashion with an initial increase and then decrease. The initial rise is due to increased repulsion between the oxygen anion as a loss of the Li ions, which screens the charge between oxygen in adjacent layers. However, at high states of charge, the c -lattice experiences a sharp decrease arises due to charge transfer between the oxygen and transition metal, which results in less oxygen-oxygen repulsion and leading to a collapse of the c -lattice.⁸ This is a common phenomenon of all layered cathodes at sufficiently high SOC and the SOC that this c -lattice collapse occurs at is dependent on the composition as well as defects present in the material.⁷

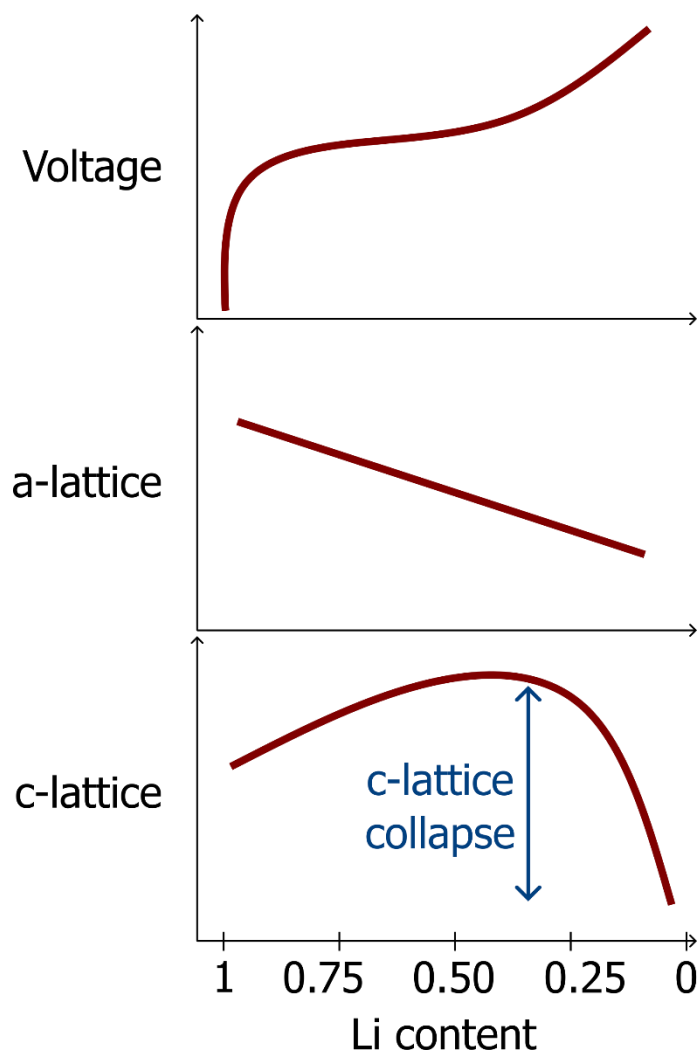


Figure 3 Relationship between state of charge and lattice parameters in layered oxides.

Advancements in the synthesis of layered lithium transition metal oxides has given researchers precise control over composition, structure, and morphology to optimize electrochemical performance of these materials. Typically, these oxides are synthesized through solid-state reactions, co-precipitation methods, or sol-gel techniques, each offering distinct advantages in tailoring material properties.⁹ Solid-state reactions involve the high temperature annealing of precursor compounds, promoting the formation of crystalline structures.¹⁰ Co-precipitation methods, on the other hand, allow for homogeneous mixing of metal cations and lithium salts and upon co-calcination, transform into the desired oxide

phase.¹¹ Sol-gel processes provide versatility in manipulating the precursor's chemistry and are conducive to achieving nanoscale control.¹² Subsequent thermal treatments and annealing steps are often employed to enhance crystallinity and optimize the electrochemical properties of the resulting layered lithium transition metal oxide.

Co-precipitation is the most industrially relevant route to cathode synthesis.¹³ In a typical synthesis, *M* sulfate salts are dissolved in solution to achieve a desired composition. When a mixture of *M* sulfate salts is used, the metals are mixed at the atomic level in the precipitate, which produces a homogenous mixing of metals in the final layered oxide product. The sulfate solution is added to a basic solution of lithium hydroxide, which results in the metal salts precipitating out of solution as a *M* hydroxide ($M(OH)_2$). The morphology of these precipitates is controlled by the reaction temperature, reaction time, pH, mixing speed, as well as surfactants and other additives in the solution.¹³⁻¹⁵ The *M* hydroxides are collected, dried, and mixed with Li precursors (typically LiOH or Li_2CO_3) and cocalcined to get the final layered oxide product, which inherits the morphology of the hydroxide precursor. This process produces spherical particles with uniform size and shape distribution, improved packing density, and reduced agglomeration.

The most common morphology of cathode particles consists of a large spherical secondary particle that is comprised of smaller single crystal primary particles.¹³ A schematic of this morphology is shown in **Figure 4**. Given the symmetry of the layered crystal structure, the orientation of grains at the surface of the particle and the interconnection of particles plays a key role in the performance of the material.¹⁶⁻¹⁸ Particles with exposed (104) facets allow for facile Li diffusion out of the particle. For particles with exposed (001) facets, the Li ions must diffuse through grain boundaries to a particle with an exposed (104) facet before the Li

ion can leave the particle. Additionally, given the anisotropic lattice changes during operation in layered oxides, repeated cycling leads to particle cracking at the grain boundary when the primary particles are randomly oriented.^{16,19} This particle cracking in turn leads to additional SEI formation at the newly exposed electrode surfaces, which depletes the Li inventory as well as lead to increased impedance.^{19,20} Furthermore, the cracking can lead to pulverization of the particle and subsequent loss of electrical contact and/or active material.

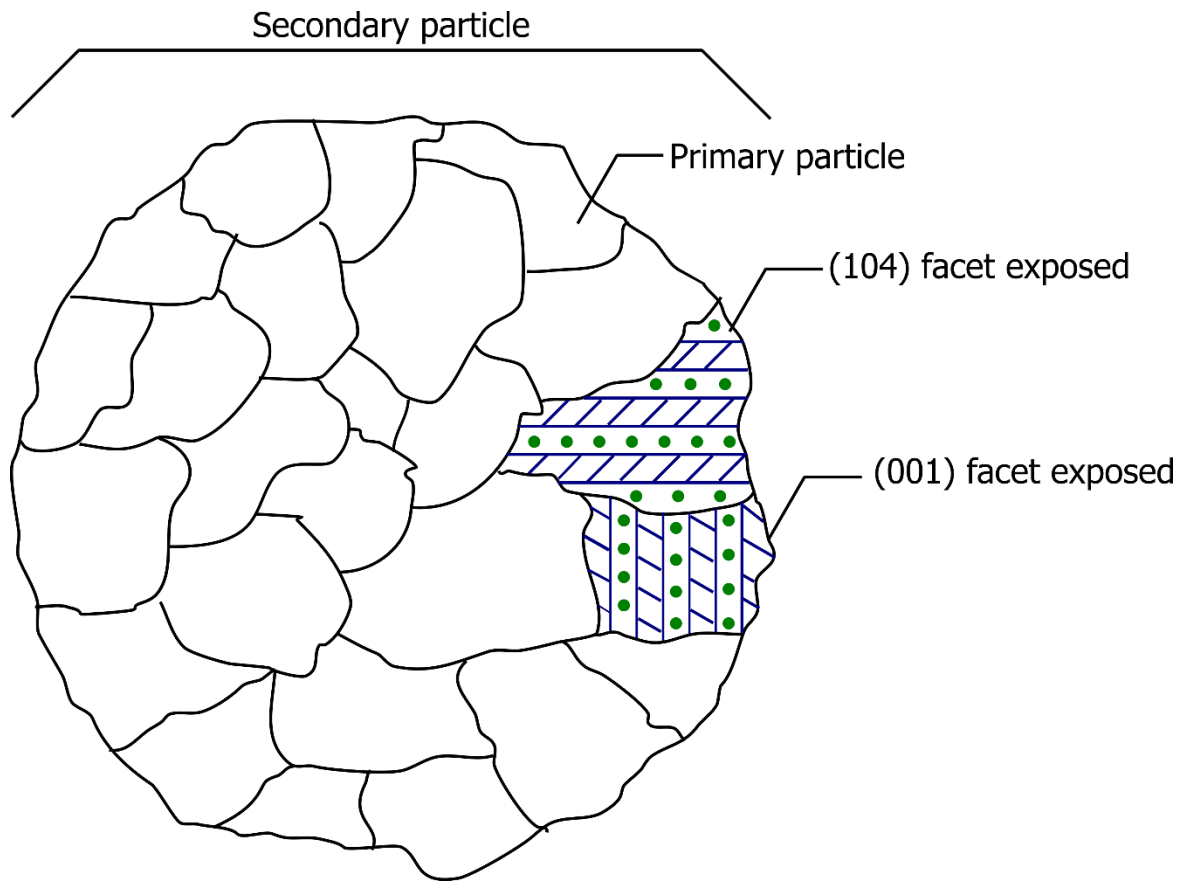


Figure 4 A schematic of the active material particle morphology when synthesized using a coprecipitation and calcination route. Large secondary particles are composed of smaller single crystal primary particles. The crystal structure orientation of two primary particles is shown with Li ions (green) and the transition metal layer (blue). The exposed facet of each primary particle governs the lithium diffusion properties of the particle with (104) exposed facets promoting facile (de)lithiation and sluggish diffusion for particles with (001) exposed facets, which must diffuse through grain boundaries to other particles.

1.4. Dissertation outline and goals

Despite being a relatively mature class of cathodes, layered lithium transition metal oxides are still an active area of research. Progress in the field is made possible with the recent advent of *operando* characterization techniques and improved synthetic control, as will be illustrated in this dissertation. The following section provides a focused review of recent studies that utilize electron paramagnetic resonance (EPR) and magnetometry to study rechargeable batteries. Rechargeable batteries generate current through the transfer of electrons between paramagnetic and/or metallic electrode materials. Electron spin probes, such as electron EPR and magnetometry, can therefore provide detailed insight into the underlying energy storage mechanisms. These techniques have been applied *ex situ*, and more recently *operando*, to both intercalation- and conversion-type batteries. After briefly reviewing the principles of EPR and magnetometry, this perspective provides a critical discussion of recent studies that leverage these tools to understand the local structure, defect chemistry and charge/discharge and failure mechanisms of rechargeable batteries. Challenges in data collection and interpretation are addressed and strategies to facilitate EPR spectral assignment and expand the scope of EPR and magnetometry studies of battery systems are suggested.

Chapter 2 will cover the working principles of the characterization techniques used in the experimental sections of this dissertation. Chapter 3 outlines the design and testing of two *operando* cells for EPR and magnetometry. *Operando* electron spin probes provide real-time insights into the electrochemical processes occurring in batteries. This work details the development and design criteria for *operando* magnetometry and EPR cells and demonstrates their tandem use to understand the electrochemical processes occurring during charge for $\text{LiNi}_{0.5}\text{Mn}_{0.5}\text{O}_2$ cathodes. High fidelity electrochemistry is achieved through application of

sufficient pressures through a clamping and spring mechanism for the magnetometry and EPR cells that match the performance of traditional Swagelok cells. Three redox processes are identified in $\text{LiNi}_{0.5}\text{Mn}_{0.5}\text{O}_2$ with a preferential oxidation of Ni^{2+} in the transition metal layer that are involved in 180° superexchange interactions with antisite defect Ni in the Li layer. Subsequent oxidation of the remaining Ni^{2+} in the transition metal layer occurs next and finally Ni^{3+} oxidation to diamagnetic Ni^{4+} . These processes are found to occur in sequential steps and the transition of each step is identified with the real-time insights provided by *operando* magnetometry and EPR. These unique tools can be applied to novel electrode materials to understand the processes occurring during operation. These insights will enable the development of better batteries.

Chapter 4 utilizes the cell developed in chapter 3 to investigate the first cycle irreversibility in LiNiO_2 cathodes. LiNiO_2 remains a target for layered oxide Li-ion cathode development as it can theoretically deliver the highest energy density of this materials class. In practice, LiNiO_2 suffers from poor capacity retention due to electrochemically induced structural changes. While the impact of Ni off-stoichiometry on the electrochemical performance has been extensively studied, that of planar defects present in the as-synthesized cathode is not well understood. Using advanced *ex situ* and *operando* structure probes, we identify and quantify point and planar defects present in as-synthesized $\text{Li}_{1-y}\text{Ni}_{1+y}\text{O}_2$ cathodes and monitor their evolution during the first cycle. Specifically, we identify a ^7Li solid-state nuclear magnetic resonance (ssNMR) signature characteristic of Li environments near twin boundaries; an assignment supported by first-principles calculations and STEM images of twin boundary defects. Our ^7Li ssNMR results suggest that the concentration of twin boundaries depends on the amount of Ni excess y . Moreover, *operando* magnetometry and *ex situ* synchrotron X-ray

diffraction and ssNMR demonstrate that these planar defects impede Li reinsertion into the bulk cathode at reasonable discharge rates and contribute to the first cycle irreversible capacity. These findings provide design rules for $\text{Li}_{1-y}\text{Ni}_{1+y}\text{O}_2$ cathodes, whereby minimal twin boundaries in the pristine material reduces kinetically limited Li reinsertion sites and improves capacity retention.

Finally, chapter 5 builds upon the work on chapter 4 by investigating the aging mechanisms in LiNiO_2 and characterizing structural defects that arise as the material degrades. Bulk degradation modes in the LiNiO_2 cathode are examined using ex situ X-ray diffraction, magnetometry, and ssNMR. While a small amount of Ni migration is observed within the layered structure, the bulk structure evolves into a mosaic of domains with different electrochemical activities and Li stoichiometries, a phenomenon exacerbated upon high voltage cycling. This leads to the formation of so-called “fatigued” phases, which have limited capacity and impeded lithium extraction. Our combined XRD and ssNMR analysis can for the first time differentiate between fatigued phases in LiNiO_2 and determine their Li content.

1.6. Rechargeable Batteries from the Perspective of the Electron Spin¹

1.6.1 Introduction.

The 2019 Nobel prize honored John B. Goodenough, M. Stanley Whittingham, and Akira Yoshino for their contributions to the development of lithium (Li)-ion batteries. Ever since their pioneering work resulting in the first commercially viable Li-ion battery based on a LiCoO_2 (LCO) cathode and a graphitic anode, extensive efforts have been invested in energy

¹ The content of section 1.6 are reproduced from a publication from the American Chemical Society: <https://doi.org/10.1021/acseenergylett.0c02074>

storage research. The discovery of LCO is owed, in part, to Whittingham's seminal work on Li intercalation hosts²¹ and Goodenough's substantial work on the magnetic and electronic behavior of transition metal oxides.²²⁻²⁵ High electronic conductivity and the high oxidation potential of the $\text{Co}^{3+}/\text{Co}^{4+}$ redox couple make LCO a rather good cathode material that is still in use today.¹ We, and many others, find inspiration in this example, which illustrates the interrelation between a material's magnetic and electronic properties and its performance as a battery electrode, and intimates the use of the electron spin as a probe of redox processes in electrochemical energy storage systems.²⁶ Two techniques are appropriate, EPR and magnetometry, which interrogate the local environments of unpaired electrons, i.e., of open-shell species in the system, and possible long-range magnetic couplings. A focus on local structure and local redox properties, as obtained from a combination of these techniques, especially in the presence of defects or compositional inhomogeneities, is indispensable in order to realize higher energy density and structurally stable electrodes. As such, EPR and magnetometry have and will continue to make significant contributions to our understanding of the function of electrode materials and inform the design of next-generation chemistries.

Recent years have witnessed a strong push towards *operando* analysis of battery materials, with the development of electrochemical setups (sample holders, probes, etc.) for real-time X-ray absorption spectroscopy (XAS), XRD, differential electrochemical mass spectrometry (DEMS), transmission electron microscopy (TEM), and ssNMR.^{27,28} Techniques based on *operando* monitoring of electron spins occupy a unique position in this gamut of techniques, yet are not as developed and widely used. In this perspective, we briefly review the technical background of *ex situ* and *operando* EPR and magnetometry and critically evaluate results from studies to date. We provide strategies for data disambiguation and

interpretation and argue that these two complementary techniques should be used in conjunction. Finally, future opportunities for the application of EPR and magnetometry to battery research are discussed.

Electron transfer processes during electrochemical (charge-discharge) cycling of a battery result in the formation (or are enabled by the presence) of unpaired electrons in the bulk of the electrodes. In insulating or semiconducting electrode compounds comprising redox-active transition metal species, these unpaired electrons are localized in d orbitals and generally result in Curie-Weiss paramagnetism under normal operating conditions. Bulk metal electrodes, on the other hand, contain itinerant electrons and display Pauli paramagnetism. In both cases, magnetometry and EPR can be used to monitor electron transfer mechanisms in real time and are therefore ideal for full device analysis.

Magnetometry is the measurement of the magnetization or magnetic susceptibility ($\chi = \frac{M}{H}$) of a sample as a function of applied magnetic field (H) or temperature (T). The evolution of the room temperature magnetization M of the electrode with charge-discharge provides insight into the sequence of redox processes and into the formation of metallic phases.

The temperature-dependent magnetic susceptibility (χ) of Curie-Weiss paramagnets can be fitted to the Curie–Weiss law above the critical temperature (the Néel temperature for antiferromagnets and the Curie temperature for ferromagnets):

$$\chi = \frac{C}{T - \theta_{\text{CW}}} \quad (1.1)$$

where C is the material-dependent Curie constant, T is the temperature, and θ_{CW} is the Curie temperature. θ_{CW} is a measure of the strength of magnetic exchange interactions (J) mediated by open-shell M centers with spin S , as described by the approximate mean field expression

$$\theta_{CW} = \frac{2 S(S + 1)zJ}{3 k_B} \quad (1.2)$$

where z is the number of interacting nearest-neighbor paramagnetic centers and k_B is Boltzmann's constant. A negative θ_{CW} signifies an overall antiferromagnetic system, while a positive θ_{CW} indicates a ferromagnetic material.

Magnetometry is a powerful tool for the study of conversion-type alkali-ion batteries, where alloying reactions between the alkali species and the electrode often result in the formation of ferro(i)magnetic nanoparticles. A characteristic hysteretic magnetization curve (M-H plot) for a ferromagnet is shown in **Fig. 1.1a**. **Fig. 1.1b** illustrates the hysteretic magnetization loop for three particle sizes. The corresponding plot of coercivity against nanoparticle size is shown in **Fig. 1.1c**.

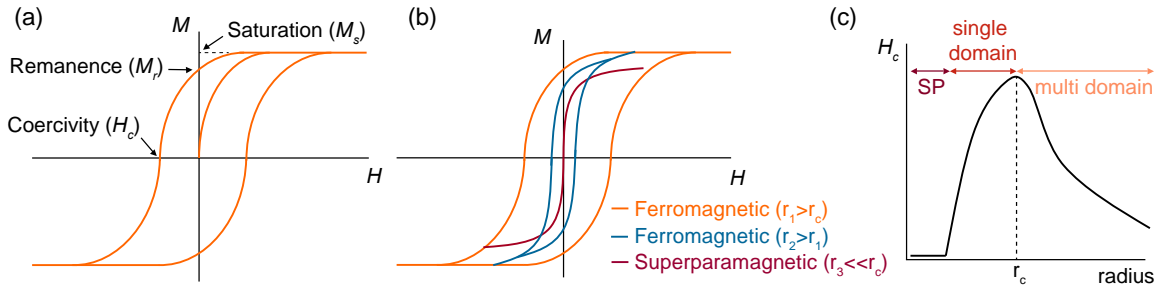


Figure 1.1. (a) Typical magnetization curve of a ferromagnet, featuring a saturation magnetization (M_s) at high applied H field and a magnetic hysteresis resulting in a remanent magnetization (M_r) as the field is switched off. A coercive field (H_c) is required to reduce the magnetization of the material to zero after being driven to saturation. Particle size effects on (b) the magnetic hysteresis loop and (c) the coercive field (H_c). For ferromagnetic materials, there exists a critical particle size r_c such that for particles with radius $r > r_c$, the hysteretic loop becomes narrower with increasing particle size, as shown with the orange and blue curves in (b). Conversely, for $r < r_c$, the hysteresis loop starts to narrow with decreasing particle size, until the superparamagnetic (SP) threshold is reached (r_3 , dark red curve), when the magnetic response curve takes a sigmoidal shape but loses the hysteresis.

Superparamagnetism occurs in ferro(i)magnetic nanoparticles consisting of a single magnetic domain ($\varnothing \approx 3 - 50$ nm). In this regime, the magnetization of each particle behaves as a single giant magnetic moment that randomly flips direction. The Néel relaxation time (τ_N) is the critical reorientational time. When the magnetization is measured over time intervals $\tau < \tau_N$, a blocked state occurs in which the measured magnetization is the instantaneous magnetization at the beginning of the measurement because there was no direction flip. In this state, the nanoparticles behave like normal paramagnets in an applied H field, but with a much higher susceptibility. When the measurement time $\tau \gg \tau_N$, a superparamagnetic state is observed whereby the net moment is zero due to the fluctuations in magnetization.

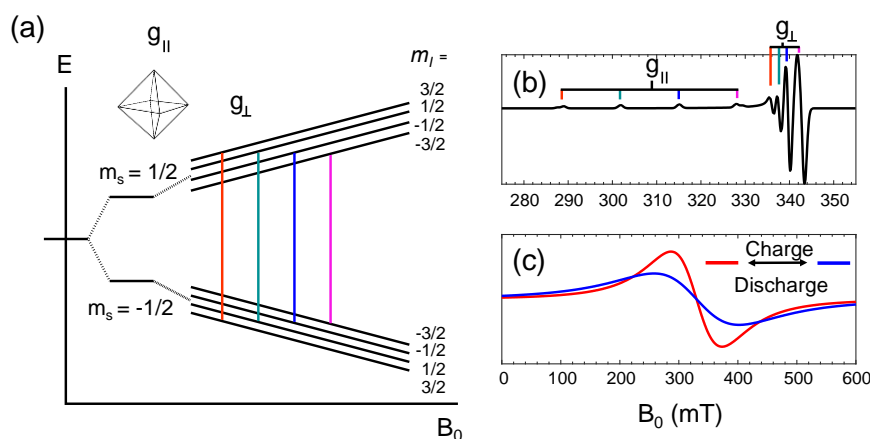


Figure 1.2. (a) Zeeman effect of an external magnetic field B_0 on the energy levels of a hypothetical two spin system ($S=1/2$; $I=3/2$) with axial symmetry, resulting in a parallel and perpendicular component of the \mathbf{g} -tensor, $g_{||}$ and g_{\perp} , respectively. (b) Simulated EPR spectrum of the isolated spin from (a) with hyperfine splitting. (c) Simulated EPR spectra of spin concentrated systems exhibiting different linewidths, *e.g.*, as observed for paramagnetic battery electrodes at different states of charge. Simulations were performed with EasySpin.²⁹

EPR uses low energy microwave (MW) radiation to probe the energy levels of unpaired electron spins that are split in an external magnetic field through the Zeeman effect (**Fig. 1.2a**). Interactions between neighboring electron spins, or between electron and nuclear spins (hyperfine interactions), provide insight into the local environment and oxidation states of open-shell species in the sample. Notably, EPR is a site-specific technique, whereby each

unique paramagnetic environment results in a distinct spectral signature. This resolution is advantageous over more standard characterization tools probing the long-range structure (e.g., XRD) or for which significant signal overlap complicates the deconvolution of contributions from redox-active species in various oxidation states (e.g., X-ray absorption near edge spectroscopy (XANES)). In EPR, the “fingerprint” of a specific unpaired electron spin environment takes the form of a **g**-tensor, which depends on the oxidation state, coordination geometry, and spin-orbit coupling properties of the paramagnetic species under consideration. Isotropic spin systems can be fully described using a single g-factor (a scalar value), while axial and rhombic systems require two (g_{\parallel} and g_{\perp}) and three (g_x , g_y , and g_z) components, respectively. **g**-tensor components are experimentally determined from the resonant field of the signal at a given MW frequency and/or from a fit of the signal lineshape. A simulated EPR spectrum corresponding to a spin $S=1/2$ open-shell species in an octahedral environment (local axial symmetry) and hyperfine coupled to a nuclear spin $I=3/2$ is shown in **Fig. 1.2b**. The EPR signal linewidth is affected by interactions with neighboring electron spins. In general, both through space dipole-dipole and through bond exchange interactions are present and have competing effects on the linewidth. Anisotropic dipole-dipole interactions, with an r^{-3} dependence, broaden the signal, while magnetic exchange (J) interactions lead to electron hopping between coupled sites and an average electron spin resonant frequency, effectively narrowing the EPR signal linewidth. Based on the phenomenological theory of Van Vleck³⁰ and Moriya³¹, Stoyanova *et al.*³² derived an expression for the peak-to-peak EPR signal linewidth, ΔH_{pp} :

$$\begin{aligned} \Delta H_{pp} & \hspace{15em} (1.3) \\ & = \text{const} * g^2 \beta^2 \frac{\{S(S + 1)\}^{3/2} z^{3/2}}{r^{-6} \theta_{CW}} \end{aligned}$$

where β is the Bohr magneton, z is the number of nearest-neighbor paramagnetic centers with spin S , and r is the distance between neighboring species. Compounds containing a high concentration of open-shell M species, such as many battery electrodes, often lead to the formation of a percolating network of magnetic exchange couplings (**Fig. 1.3a**) and are in the exchange dominated regime, where the EPR signal is averaged between the different sites and effectively narrowed (**Fig. 1.3b**). Strong exchange interactions, such as those found in Ni^{2+} – Mn^{4+} systems, are expected to lead to significant narrowing of EPR resonances. Table 1 shows the relative magnetic exchange strengths for some transition metal combinations found in Li-ion batteries. The resulting exchange-narrowed EPR signal lineshapes are Lorentzian in the center and fall off rapidly on either side of the central frequency.³³ Due to dipole-dipole broadening effects, hyperfine splittings resulting from electron-nuclear spin interactions are scarcely resolved in EPR spectra, as shown in the simulation in **Fig. 1.2c**, and only an average g -factor can be obtained from a fit of the broad lineshape. Lastly, the signal intensity is proportional to the number density of the corresponding local environment in the sample, and can be used (semi-)quantitatively. Variation of these three parameters (g -tensor, linewidth, and signal intensity) with temperature and battery state of charge (SOC) provide a comprehensive picture of the processes occurring in rechargeable batteries.

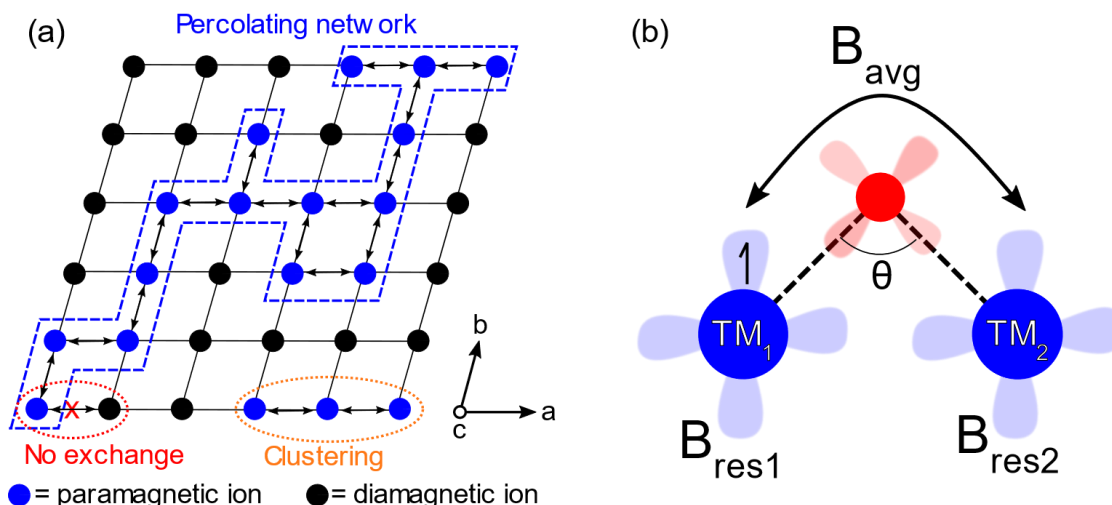


Figure 1.3. (a) Cation lattice of a paramagnetic battery electrode material. The formation of an extended network of magnetic exchange couplings between paramagnetic transition metal species in a matrix of diamagnetic cations leads to EPR signal narrowing. Yet, significant clustering of open-shell transition metals results in an increase in the threshold concentration for percolation. (b) Unpaired electrons at two different transition metal sites result in distinct resonant fields, B_{res1} and B_{res2} . In paramagnetic battery electrodes, a distribution of resonant fields leads to signal overlap and additional spectral broadening. However, in the presence of magnetic exchange interactions, unpaired electrons hop between neighboring transition metal sites and an average resonant field, B_{avg} , is obtained thereby narrowing the resonant signal. The degree of narrowing is dependent on the strength of the magnetic exchange interactions, i.e., on the transition metal identity, orbital filling and degree of orbital overlap (interaction angle). Most magnetic exchange interactions in transition metal oxides are superexchange couplings mediated by oxygen atoms.

Table 1.1. Magnitude of common magnetic superexchange interactions in lithium transition metal oxides.

Angle of interaction	Transition metal identities	Relative Strength	Reference
180°	$Ni^{2+} - Ni^{2+}$	very strong	34,35
180°	$Ni^{2+} - Mn^{4+}$	strong	34,35
180°	$Ni^{2+} - Co^{4+}$	strong	34
180°	$Ni^{2+} - Ni^{3+}$	moderate	34,35
180°	$Ni^{2+} - Co^{3+}$	very weak	34
180°	$Ni^{2+} - Ni^{3+}$	moderate	35
90°	$Ni^{2+} - Mn^{4+}$	strong	35
90°	$Ni^{2+} - Ni^{2+}$	weak	35
90°	$Mn^{4+} - Mn^{4+}$	moderate	35

An important consideration for the investigation of battery devices with EPR is the existence of skin effects, which limit the penetration of MW radiation into metallic solids to a surface layer with a depth δ on the order of 100s of nanometers to micrometers at commonly used X-band frequencies (~ 9.5 GHz). The diffusion of conducting electrons in and out of the skin of the metal has a decisive effect on the shape and intensity of the observed resonance.^{36,37} A Dysonian lineshape (a phase-shifted Lorentzian) is observed for metallic solids of thickness $D \gg \delta$, while a Lorentzian with no phase shift is observed for metallic structures with a thickness $D \approx \delta$. Hence, the EPR lineshape can provide clues as to the size of metallic structures formed during electrochemical cycling.

Magnetometry and EPR experiments can be performed *ex situ*, where the battery is disassembled after electrochemical cycling and electrode samples are extracted for analysis, or *operando*, where battery components are characterized as the cell is charged and discharged. *Ex situ* experiments are not time-constrained and can be carried out over a wide range of temperatures, magnetic fields and MW frequencies. *Ex situ* experiments conducted outside of the typical operating temperature range of battery devices can probe the magnetic ordering behavior of the electrode material via EPR and magnetometry. Additionally, measurements at cryogenic temperatures result in enhanced EPR signal resolution and sensitivity, as well as longer signal lifetimes, while high field high frequency EPR experiments can resolve small g anisotropies and detect spin transitions with large energy splittings. Low temperature high frequency measurements are particularly useful to investigate non-Kramers integer spin M centers, such as Ni^{2+} ($S=1$), exhibiting strong zero field splitting (ZFS) interactions that lift the degeneracy of the spin states in the absence of an external magnetic field. ZFS results in high energy EPR transitions that cannot be excited at X-band frequencies, as well as fast signal

decay. High frequency measurements are restricted to *ex situ* studies as they generally require the material of interest to be loaded into a thin sample tube — tube diameters for Q-band (34 GHz) and W-band (94 GHz) experiments are 1.6 mm and 0.9 mm, respectively—. Unlike *ex situ* experiments, which entail the collection of many electrode samples at different states of charge to capture the behavior of a system, *operando* experiments can follow the evolution of a single electrode sample over the entire operational range of the electrochemical cell. *Operando* experiments also prevent sample damage that might occur on removal from the cell and are better suited for detecting transient species and monitoring reaction kinetics. Yet, despite the advantage of time-resolved data, the resolution of *operando* measurements is limited by the presence of other necessary battery components, such as current collectors, which introduce sharp and intense signals that overlap with the generally broad and low intensity signals from paramagnetic electrodes. Moreover, MW absorption by electronically conducting elements and high dielectric (aqueous and organic) electrolytes reduces the quality (Q) factor of the EPR resonator cavity, which indicates how efficiently it stores MW energy, and the overall sensitivity of the measurement.

The limited number of real-time EPR and magnetometry studies of secondary batteries to date is in part due to the challenges of *operando* cell development. EPR and magnetometry measurements involve the application of a strong magnetic field to the sample, requiring non-standard battery designs to minimize interactions with the electrical circuit, as well as shielding effects. For example, metal casings used in research-standard coin cells or Swagelok-type batteries must be replaced, while all the time ensuring that sufficient pressure is applied to the battery stack to maintain good electronic contact between individual components.

1.6.2 EPR studies of transition metal based battery electrodes.

Paramagnetically-dilute electrodes are advantageous for EPR studies as they enable the analysis of hyperfine splittings and the determination of **g**-tensor components, providing detailed information on the local structure. This has motivated several studies on diamagnetic LCO cathodes (containing low spin octahedral Co^{3+}) doped with paramagnetic *M* species.³⁸⁻⁴⁴ In such systems, large **g**-tensor anisotropies ($\Delta g = g_{\perp} - g_{\parallel}$) indicate distortions of the paramagnetic MO_6 octahedra. For instance, Mladenov *et al.*³⁸ elegantly deduced the distribution of diamagnetic Mg^{2+} dopants in LCO from the **g**-anisotropy of inherent Ni^{3+} impurities. For systems containing more than one paramagnetic spin environment or species, differentiating between individual **g**-tensors is complicated by signal overlap at X-band frequencies. This limitation can be overcome with high field EPR, where larger Zeeman splittings increase signal resolution, as demonstrated by Stoyanova *et al.*⁴⁴ on a Ni/Mn co-doped LCO cathode. The authors identified Ni^{3+} and Mn^{4+} EPR signatures by matching their lineshapes to Ni^{3+} -doped LCO and Mn^{4+} -doped LCO, as shown in **Fig. 1.4a**, and used ZFS parameters extracted from fits of the EPR data to obtain trigonal distortion angles for MnO_6 octahedra. Generally, resolution enhancements obtained on paramagnetically-dilute electrodes do not persist upon electrochemical cycling, as redox reactions taking place on charge-discharge result in a change in the magnetic character of *M* species and in the formation of spin-concentrated systems.

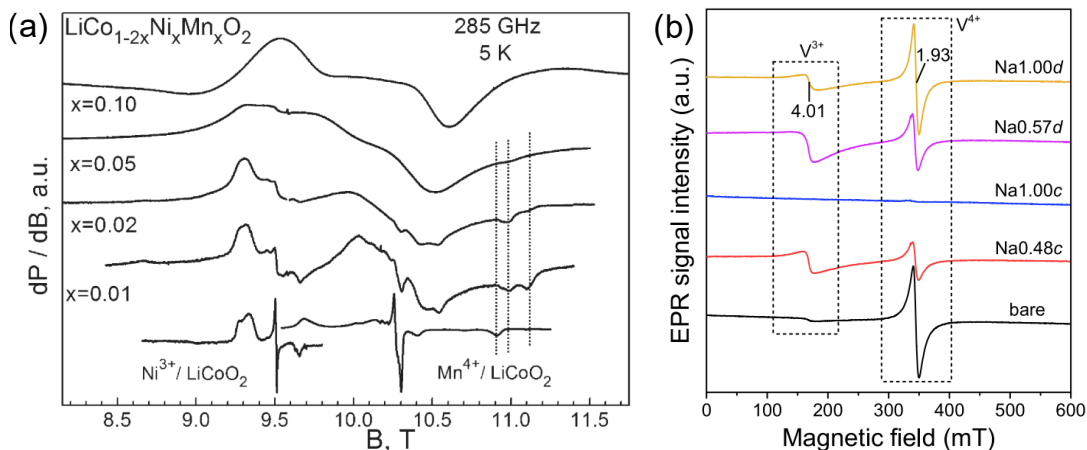


Figure 1.4. (a) High frequency (285 GHz) EPR spectra collected on a series of $\text{LiCo}_{1-2x}\text{Ni}_x\text{Mn}_x\text{O}_2$ cathodes. As the paramagnetic ion concentration decreases (decrease in x), the fine structure of EPR signals is further resolved. At $x=0.01$, distinct Ni^{3+} and Mn^{4+} spectral signatures are identified by comparing with spectra obtained on Ni^{3+} doped LiCoO_2 and Mn^{4+} doped LiCoO_2 . **Fig. 1.4a** reproduced with permission from reference 25. (b) Ex situ EPR spectra obtained on cycled $\text{Na}_{3-x}\text{V}_2^{3+/4+}(\text{PO}_4)_2\text{O}_{1.6}\text{F}_{0.4}$ cathode samples. The label above each spectrum indicates the state of charge, where 1.00c signifies 100% charged, and 1.00d signifies 100% discharged. V oxidation states were assigned based on the average g -factor of the two EPR signals. The evolution of V^{3+} and V^{4+} species was monitored through changes in the intensity of the two resonances, which provided evidence for the participation of V^{3+} in charge compensation processes. **Fig. 1.4b** reproduced with permission from reference 26.

In paramagnetically concentrated systems, EPR enables the detection of M clusters through dipole-dipole and magnetic exchange interactions. Departure from a statistical distribution of paramagnetic species can be identified using eq. (3) and has been attributed to cation ordering in a variety of electrode systems, including layered and spinel transition metal oxides.^{32,40,42,45,46} Further evidence for the formation of M clusters can be obtained from the onset of exchange narrowing of the EPR signal. In systems featuring M clustering, the onset of exchange narrowing occurs at a higher M concentration than that expected based on a homogeneous distribution of paramagnetic species, as shown in **Fig. 1.3**. For example, it has been shown that exchange narrowing begins at $x \geq 0.62$ for $\text{LiNi}_x\text{Co}_{1-x}\text{O}_2$, despite the $x = 0.5$ percolation threshold for layered M oxide systems featuring a 2D triangular lattice, which highlights the tendency for Ni and Co species to cluster and prevent the formation of a continuous network of magnetically coupled Ni^{3+} ions.⁴²

EPR measurements as a function of charge can provide key insights into redox and structural processes in electrode materials. For instance, gradual changes in the average g -factor are indicative of smooth changes in oxidation states, as occurs in solid solution reactions.⁴⁶ Alternatively, two-phase reactions can lead to the evolution of new EPR signals, such as in the V_2O_5 system studied by Gourier *et al.*⁴⁷ Upon discharge past the reversible limit, the authors detected the formation of an electrochemically-inactive phase with EPR, which provided an explanation for capacity loss in V_2O_5 cathodes. Another example is provided by Chao *et al.*⁴⁸, who studied mixed-valent $Na_3V_2^{3+/4+}(PO_4)_2O_{1.6}F_{0.4}$ cathodes at different states of charge using parallel-mode EPR, which enables the detection of integer spins such as V^{3+} (d^2 , $S=1$), and found evidence for the oxidation of V^{3+} species previously thought to be redox-inactive in this system, as shown in **Fig. 1.4b**. More recently, researchers have claimed to detect oxidized oxygen species at high voltages in alkali rich cathodes, whose anomalous capacity is often attributed to anionic redox.^{49,50}

Significant progress in *operando* EPR data processing and analysis has been made by Niemöller *et al.*⁵¹ The introduction of a ruby reference into the *operando* EPR-electrochemical cell enabled them to correct for signal phase changes due to the cell's evolving impedance during electrochemical cycling, and a methodology was devised to monitor battery processes through a combined analysis of the evolution of the signal intensity and linewidth as a function of charge. Within this scheme, changes in M oxidation states are monitored through the degree of exchange narrowing, which not only depends on the concentration of paramagnetic centers, as previously seen, but also on the nature and strength of magnetic couplings (J) between neighboring M species.

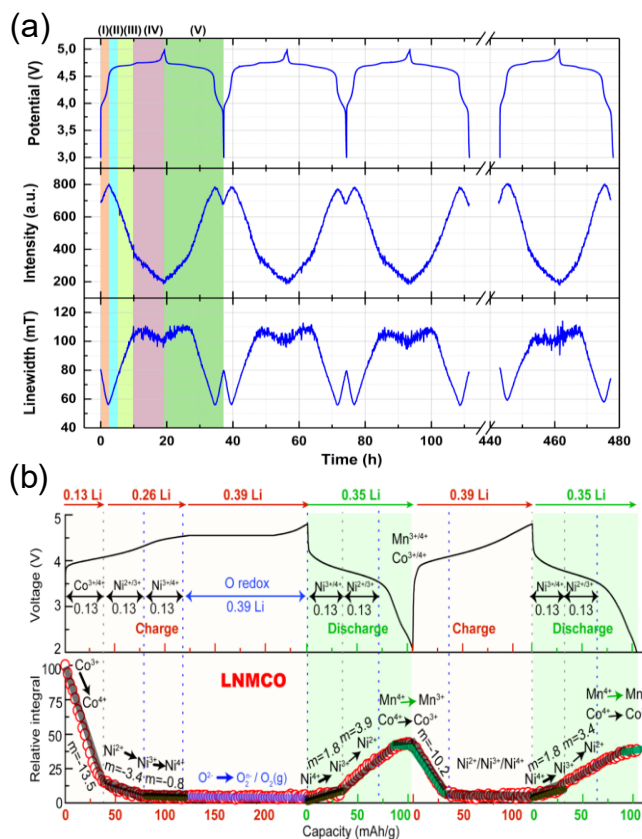


Figure 1.5. (a) *Operando* X-band EPR dataset collected on the $\text{LiNi}_{0.5}\text{Mn}_{1.5}\text{O}_{4-\delta}$ cathode, including the electrochemical profile (cell voltage vs. time, top panel) and corresponding changes to the cathode's EPR signal intensity (middle panel) and linewidth (bottom panel). Sequential redox events (I-V) are identified on the basis of the observed cell potential and of voltage regions corresponding to different rates of change (slope) of the EPR signal intensity and linewidth, as follows. Charge processes: (I) oxidation of residual Mn^{3+} in as-prepared O-deficient $\text{LiNi}_{0.5}\text{Mn}_{1.5}\text{O}_{4-\delta}$; (II) partial oxidation of Ni^{2+} to Ni^{3+} for those Ni species adjacent to the Mn^{3+} species in (I); (III) oxidation of the remaining Ni^{2+} species to Ni^{3+} ; (IV) oxidation of Ni^{3+} species formed in (III) to Ni^{4+} . Discharge processes: (V) reduction events occur in the reverse order as compared to the charge processes listed above. **Fig. 1.5a** reproduced with permission from reference 32. Copyright 2018 American Institute of Physics. (b) *Operando* X-band EPR dataset collected on the $\text{Li}_{1.2}\text{Ni}_{0.13}\text{Mn}_{0.54}\text{Co}_{0.13}\text{O}_2$ cathode: electrochemical profile (top panel) and corresponding changes to the cathode's integrated EPR signal intensity (bottom panel). The large decrease in the EPR signal integral at the beginning of charge is assigned to the oxidation of Co^{3+} to Co^{4+} , followed by the oxidation of Ni^{2+} to Ni^{3+} and eventually Ni^{4+} . Although significant capacity is observed over the 4.5 V plateau in the electrochemical profile, no EPR signal is observed over this potential range, which the authors attribute to O redox processes. **Fig. 1.5b** reproduced from reference 33.

In transition metal oxides, these couplings are dominated by M -O- M superexchange interactions, which in turn depend on the electronic configuration of the coupled M species, M - M distances and M -O- M bond angles and can, in simple cases, be predicted by the empirical Goodenough-Kanamori rules (**Fig. 1.3b**).^{22,24,52,53} Using this methodology, Niemöller *et al.*

identified sequential redox processes on charge-discharge of the spinel $\text{LiNi}_{0.5}\text{Mn}_{1.5}\text{O}_{4-\delta}$ cathode⁵¹ on the basis of potential regions corresponding to different rates of change (slope) of the EPR signal intensity and linewidth, as shown in **Fig. 1.5a**. Notably, EPR's unique sensitivity to local redox processes allowed the resolution of two distinct Ni^{2+} oxidation processes, whereby Ni species closest to Mn^{3+} defects (and likely O^{2-} vacancies) in the as-prepared $\text{LiNi}_{0.5}\text{Mn}_{1.5}\text{O}_{4-\delta}$ cathode are oxidized first. These local processes are not discernable with electrochemical methods nor with XANES, yet provide crucial information on the impact of defects on the electrochemical properties of battery electrode materials.⁵¹

EPR data interpretation remains a complex task and, in the absence of corroborating evidence, incomplete or erroneous conclusions can be made. We note, for instance, the tendency of EPR studies on *M* oxide cathodes to attribute charge compensation processes to oxygen species based on ambiguous observations and without further support from techniques that provide complementary insight into redox events (e.g., XANES, resonant inelastic X-ray scattering). An *operando* EPR study of the LCO cathode interpreted the absence of EPR signal during cycling between 3.0 and 4.2 V vs. Li^+/Li as evidence for purely O-based charge compensation processes and for the electrochemical inactivity of Co^{3+} species⁵⁴, even though prior work^{55,56} has provided unequivocal evidence for $\text{Co}^{3+/4+}$ redox in this prototypical cathode material. Since Co^{4+} species have been observed at X-band frequencies and at room temperature in related materials⁵⁷, the absence of a detectable EPR signal as LCO is electrochemically cycled could result from the metal-insulator transition reported upon delithation⁵⁸, as such processes are known to cause EPR signal decay.⁵⁹ A recent *operando* EPR study of the $\text{Li}_{1.2}\text{Ni}_{0.13}\text{Mn}_{0.54}\text{Co}_{0.13}\text{O}_2$ cathode rationalized the absence of EPR signal over the plateau at approximately 4.5 V vs. Li^+/Li in the electrochemical profile (see **Fig. 1.5b**) to

the oxidation of O^{2-} species in the bulk.⁶⁰ While consistent with previous reports attributing the characteristic high voltage plateau of Li-excess layered $Li_{1+x}M_{1-x}O_2$ cathodes to O redox, this analysis is problematic in various ways. First, several experimental parameters, as well as the spin properties of the electrode material, are expected to evolve over the course of the *operando* measurement, and these have a direct impact on the integrated EPR signal intensity. Specifically, changes in the EPR signal lifetime, in the magnetic susceptibility of the cathode and in the Q factor of the resonator⁶¹. Second, no consensus has been reached on the exact charge compensation and structural processes at play in $Li_{1+x}M_{1-x}O_2$ cathodes, and mechanisms that do not involve O-based redox have been proposed.⁶² Hence, if using the integrated EPR signal intensity as the sole metric for identifying redox processes, it is particularly important to eliminate confounding factors. For example, the evolution of the Q factor of the resonator can be accounted for by using a ruby reference⁵¹, while changes in the magnetic properties and EPR signal lifetime of the cathode can be monitored by conducting *ex situ* magnetometry and low temperature EPR experiments. Moreover, the absence of EPR signal over the 4.5 V plateau is surprising given that both EPR-active Co^{4+} and Mn^{4+} have been reported at high voltage⁶³, and warrants further studies investigating the origin of signal disappearance. More generally, the absence of an EPR signal at X-band frequencies and at room temperature is an ambiguous result and should be treated with caution, since high energy electron spin transitions in, *e.g.*, paramagnetic species subject to ZFS cannot be excited and fast EPR signal decay can be an issue.

1.6.3 EPR studies of Li microstructures formed during electrochemical cycling.

EPR experiments are uniquely positioned to monitor the evolution of metallic Li microstructures in Li-ion batteries. At X-band frequencies, skin effects limit the penetration of

MWs to about one micron into bulk Li metal³¹, such that a Lorentzian signal with zero phase shift is observed for Li structures with a sub-micron radius, while a Dysonian lineshape is obtained for thicker Li structures and smoothly plated Li, as shown in **Fig. 1.6a**. EPR methods have therefore been used to quantify (**Fig. 1.6b**)^{60,64} and image mossy and dendritic Li (**Fig. 1.6c**).^{65,66} Researchers have also taken advantage of conducting electron-nuclear spin interactions to identify Li microstructures using related electron-nuclear double resonance (ENDOR) methods⁶⁷ and, more recently, to hyperpolarize nuclei through DNP in the solid electrolyte interphase (SEI) forming at the surface of Li metal anodes⁶⁸. Although Na is also EPR active³⁶, to the best of our knowledge, no EPR studies of Na metal anodes have been published to date.

1.6.4 EPR studies of beyond Li-ion batteries.

EPR has been used to investigate Li-S and Li-O₂ batteries, where the energy storage mechanism results in the formation of radical species. Compared to paramagnetic *M* species, S- and O-based radicals have longer relaxation times, resulting in higher sensitivity.⁶⁹ Additionally, these radicals are generally present in liquid phases, leading to motionally-narrowed signals and high resolution EPR spectra. Several *operando* or *ex situ* EPR studies of Li-S cells have monitored the concentration of long-lived S₃⁻ radicals in Li-S cells, to gain insight into the polysulfide dissolution mechanisms resulting in rapid performance degradation.⁷⁰⁻⁷² Oxygen radicals that form in Li-O₂ batteries are, on the other hand, highly reactive, and EPR studies have employed spin traps, which are reagents added to the electrolyte solution that form stable EPR active adducts with radical oxygen species, to elucidate the mechanism of O-based reactions.^{73,74}

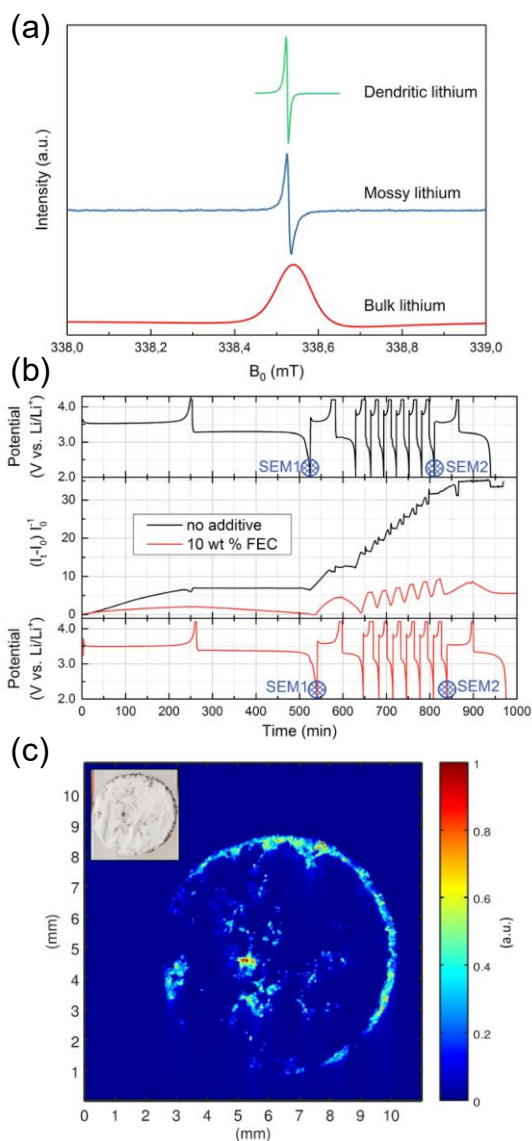


Figure 1.6. (a) Li metal microstructures that are much thicker than the skin depth $\delta = 1.1 \mu\text{m}$ at X-band frequencies lead to an EPR signal with a characteristic Dysonian lineshape (red spectrum). Microstructures that are on the same scale as δ (e.g. dendritic and mossy Li) lead to Lorentzian EPR signals with no phase shift (blue and green spectra). **Fig. 1.6a** reproduced from reference 47. (b) *Operando* quantification of dendritic Li with EPR. The top and bottom panels show two voltage profiles for a LiFePO₄/Li cell cycled with (red, bottom) and without (black, top) a fluoroethylene carbonate (FEC) additive in the electrolyte. The middle panel shows the normalized Li signal for both cells, which demonstrates the suppression of Li dendrites in FEC-containing cells. **Fig. 1.6b** reproduced from Wandt *et al.*⁶⁴ with permission from the Royal Society of Chemistry. (c) The Lorentzian Li signal for sub-micron Li structures is used to spatially map lithium dendrites in a Celgard separator extracted after electrochemical cycling. Dendrites are found to be agglomerated around the edges of the separator. **Fig. 1.6c** reproduced from Niemöller *et al.*⁶⁶ under the [Creative Commons CC BY](https://creativecommons.org/licenses/by/4.0/) license.

1.6.5 Magnetometry studies of battery electrodes and devices.

For electrode materials exhibiting Curie-Weiss behavior, the bulk magnetic susceptibility χ and Weiss constant θ_{CW} can provide insights into the local structure and the presence of defects^{26,75}. An analysis of *M-O-M* magnetic exchange interactions is particularly useful to monitor structural rearrangements in layered transition metal oxide cathodes.^{35,75,76} For instance, Li⁺/Ni²⁺ antisite disorder in Li_xNi_{0.5}Mn_{0.5}O₂, whereby Li⁺ and Ni²⁺ ions exchange

positions in the layers, results in 180° interlayer $M\text{-O-Ni}^{2+}$ couplings that are stronger than 90° intralayer $M\text{-O-M}$ interactions (**Fig. 1.7a**), and the large decrease in the low temperature bulk magnetic susceptibility across a series of cathode samples collected at the beginning of charge (**Fig. 1.7b**) has been attributed to preferential oxidation of M ions involved in 180° interlayer exchange couplings.³⁵

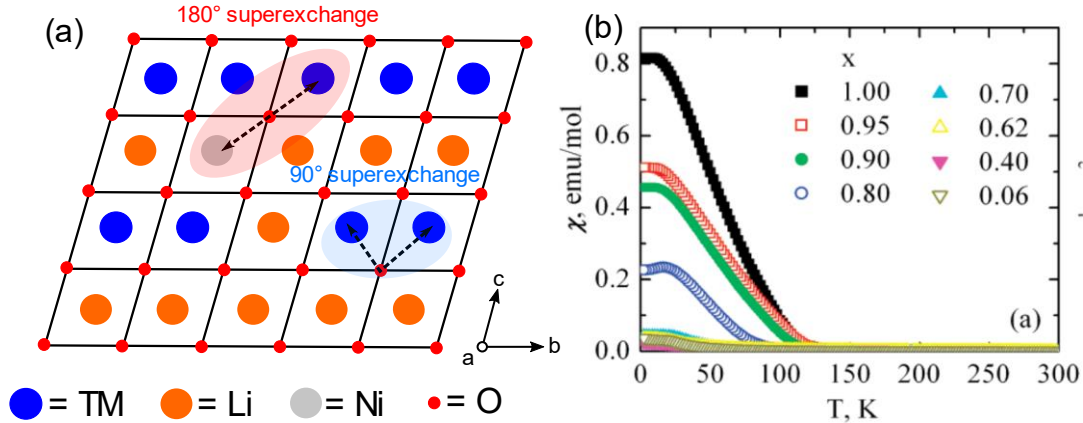


Figure 1.7. a) $\text{Li}^+/\text{Ni}^{2+}$ antisite disorder in layered oxides leads to strong 180° interlayer $M\text{-O-Ni}^{2+}$ superexchange interactions (red) compared to the weaker 90° intralayer $M\text{-O-M}$ superexchange interactions (blue). (b) Ex situ temperature-dependent bulk magnetic susceptibility measurements for $\text{Li}_x\text{Ni}_{0.5}\text{Mn}_{0.5}\text{O}_2$ samples. A rapid loss of magnetization is observed in the range $1.0 \geq x \geq 0.7$, which suggests that M species involved in the 180° interlayer couplings are oxidized first on charge. **Fig. 1.7b** reproduced from reference 16.

Beyond *ex situ* studies, very few *operando* magnetometry studies have been published to date. Unlike any other characterization technique, magnetometry can provide detailed insight into the nucleation and growth of ferromagnetic nanoparticles. Hence, it is perhaps unsurprising that the very first *operando* magnetometry study of a battery device was carried out on the conversion electrode FeSb_2 by Gershinsky *et al.*⁷⁷ The two-step conversion process on lithium insertion results in the formation of ferromagnetic Fe nanoparticles: (1) $\text{FeSb}_2 + 4 \text{Li} \leftrightarrow \text{Li}_4\text{FeSb}_2$ followed by (2) $\text{Li}_4\text{FeSb}_2 + 2 \text{Li} \leftrightarrow 2 \text{Li}_3\text{Sb} + \text{Fe}$. The stepwise increase in the room temperature cell magnetization measured with each new lithiation process (**Fig. 1.8a**) was attributed to the steady growth of Fe nanoparticles with increasing cycle number⁷⁷ and a switch from superparamagnetic to ferromagnetic behavior as the individual particles reached

a size greater than the critical radius (r_c , see **Fig. 1.1**). Notably, these results demonstrated that irreversible coarsening of metallic nanoparticles in conversion electrodes occurs even when the electrochemical profile remains relatively unchanged from one charge-discharge cycle to the next (**Fig. 1.8a**). *Ex situ* magnetic hysteresis measurements indicated that the conversion of FeSb₂ into separate Fe and Sb phases was already complete after the first lithiation and that Fe was no longer involved in the conversion process after the initial charge, leading the authors to propose a new reaction mechanism: $2 \text{Li}_3\text{Sb} + \text{Fe} \leftrightarrow 2 \text{Sb} + \text{Fe} + 6\text{Li}$.⁷⁷ Overall, this study proves that magnetometry can provide quantitative information on electrochemical processes when these involve the formation of a ferromagnetic phase, crystalline or amorphous, during cycling. More recent *operando* magnetometry studies of conversion electrodes have investigated the Fe₃O₄ Li-ion system⁷⁸ and the electrochemical sodiation of FeSb₂.⁷⁹ Regarding intercalation electrodes, Würschum and coworkers have explored redox processes in layered oxides^{80,81} and NASICON-type⁸² cathodes by comparing changes in the magnetic susceptibility on charge-discharge to theoretically predicted changes based on various *M* redox scenarios.

One particularly powerful application of magnetometry, which highlights the sensitivity and versatility of the technique, is high-throughput contactless battery diagnostics. Hu *et al.*⁸³ developed a susceptometry setup to spatially resolve weak induced magnetic fields in commercial Li-ion pouch cells. In a series of experiments on cells prepared and cycled under various conditions, the authors showed that the magnetic susceptibility, used as a proxy for state of charge, was inhomogeneously distributed across mechanically-deformed cells or when these were discharged beyond their rated voltage range (**Fig. 1.8b**).⁸³ This diagnostic technique is in principle scalable and could be adapted to screen larger commercial-type cell designs,

such as those used in the electric car industry, in their target form factors. Importantly, this method could provide detailed spatial information about the battery state, and possible internal defects and damage, without compromising the cell.⁸³

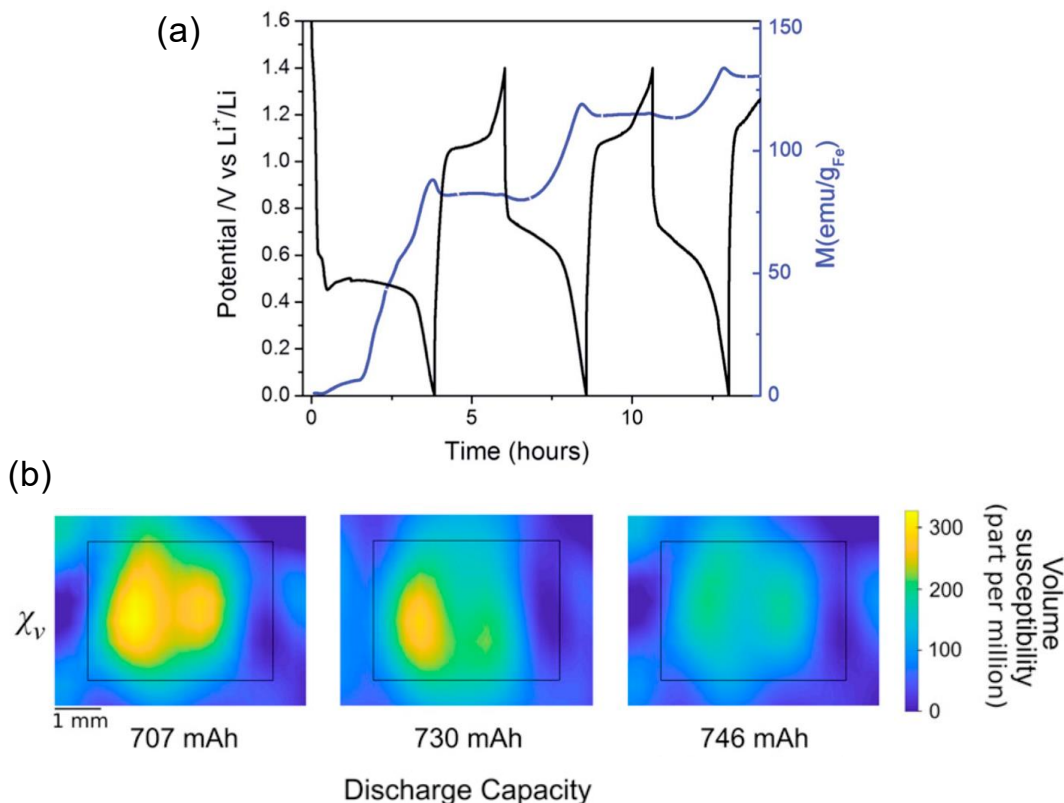


Figure 1.8. (a) Operando magnetometry data collected on the FeSb₂ conversion anode over several charge (lithiation)-discharge(delithiation) cycles. The electrochemical profile of the electrode is shown in black and the magnetic moment at 300 K in blue. The stepwise increase in magnetization with successive lithiation steps was attributed to coarsening of Fe nanoparticles formed in the initial charge process. **Fig. 8a** reproduced from reference 58 with permission from the Royal Society of Chemistry. (b) Magnetic susceptibility maps of a Li-ion pouch cell at different depths of discharge (discharge capacity shown below the plots). The pouch cell position is indicated by the black rectangular box with battery leads to the left of the box. The spatial distribution of the magnetic susceptibility decreases non uniformly from left to right, indicating heterogeneous reaction rates across the cell when the latter is discharged beyond its rated voltage range. **Fig. 8b** reproduced from reference 64.

While powerful tools for the study of battery processes, EPR and magnetometry results by themselves can be ambiguous. Their interpretation ought to be supported by corroborating evidence and by a robust theoretical framework, to prevent contradictory statements as to the nature of the electrochemical processes at play, as have been made for even prototypical electrode compounds such as LCO.^{54–56,80}

As mentioned earlier, many factors can affect the EPR signal intensity and line broadening, and an analysis based on such parameters needs to consider all factors that can affect the EPR response of the system. Importantly, the magnetization M (or χ) of a phase is directly related to its EPR signal intensity, while the strength and nature of the magnetic interactions (J) are related to the EPR signal linewidth. Hence, we argue that EPR and magnetometry should be used in combination, whereby a semi-quantitative analysis of the evolution of the EPR signal intensity and linewidth is compared against variations in the cell magnetization during cycling. Additionally, density functional theory (DFT) calculations of magnetic moments and exchange couplings on model compositions representative of charged/discharged states of the electrode material of interest can provide insight into the evolution of its EPR signal, M and χ with electrochemical cycling. This approach would allow, for example, to confirm the assignment of redox processes occurring at potentials where the EPR signal intensity/broadening and the magnetic susceptibility do not change significantly despite significant charge storage capacity being recorded, as observed in many Li-excess layered oxide cathodes.^{54,60} *Ex situ* EPR experiments at high fields and high frequencies can excite spin transitions with large energy splitting and greatly enhance spectral resolution. Consequently, *operando* and *ex situ* EPR measurements are best employed in combination, *ex situ* spectra providing high resolution “snapshots” of time-resolved *operando* data and

facilitating *operando* data interpretation. Furthermore, *ex situ* power saturation experiments, whereby the integrated EPR signal intensity is monitored as the MW power is gradually increased, are useful to distinguish between EPR resonances with similar g values. For instance, while oxygen radical signals have a g -factor close to the free electron g -value ($g_e = 2.00$),⁶⁵ polarization-type EPR signals (the oxygen radical) and conduction electron signals can easily be differentiated on the basis of their MW power relationship.⁸⁴ Finally, *ex situ* EPR measurements at cryogenic temperatures enable the observation of short-lived or fast relaxing species, but one then needs to consider possible structural, charge-ordering or magnetic ordering transitions at low temperatures that might affect the EPR data.

The unparalleled sensitivity of EPR and magnetometry to changes in chemistry and electronic structure calls for a thorough characterization of electrode materials using a range of techniques, to avoid data misinterpretation. Specifically, the presence of defects or compositional inhomogeneities in the starting electrode material can greatly affect EPR and magnetometry results. For instance, special care should be taken to identify magnetic impurity phases that could obscure EPR and magnetometry data interpretation, *e.g.*, through *ex situ* variable-temperature magnetometry measurements. Neutron diffraction can be used to quantify antisite disorder in Ni^{2+} -containing layered oxides and provide clues as to the origin of the strong antiferromagnetic interactions observed upon $\text{Li}^+/\text{Ni}^{2+}$ exchange between layers.³⁵ The oxidation states of M species can be obtained through XANES measurements to correctly identify paramagnetic centers that contribute to the EPR signal, to the bulk magnetization and susceptibility at a given state of charge. While average oxidation states are generally deduced from XANES data, EPR can determine the relative distribution of oxidation states and provide

clues as to the proximity of magnetically coupled M species, as demonstrated by Niemöller *et al.*⁵¹

1.6.6 Conclusion

EPR and magnetometry offer a rare perspective on structural and redox processes from the standpoint of electron spins and magnetic interactions between redox-active species, holding promise for breakthroughs in our understanding of electrochemical energy storage devices. Significant advances have recently been made in *operando* EPR and magnetometry cell development and data processing, opening new avenues for real-time investigation of local redox processes, phase transformations and structural rearrangements during charge-discharge. Data interpretation remains a complex task, which we believe could be greatly simplified through the concurrent use of *operando* EPR and magnetometry, as well as complementary scattering and X-ray absorption techniques to thoroughly characterize defects and compositional inhomogeneities that could affect EPR and magnetometry results. While EPR and magnetometry remain broadly unexplored by the battery community, they are uniquely positioned to provide atomic-level insight into the function of next-generation all-solid-state, Li-S and Li-O₂, as well as conversion battery chemistries.

Chapter 2. Methods

A brief overview of the techniques used in this dissertation is outlined in this section. Detailed discussion of the techniques is provided in the chapters when they become relevant.

2.1. Electrochemical Testing

Electrochemical tests are carried out with a potentiostat, which is an electronic instrument used to control and measure the voltage or current of an electrochemical cell. Voltage refers to the electric potential difference between two electrodes in a cell and is expressed in volts (V) vs a reference potential. It is a measure of the force that drives electric current. The potential difference is the energy required to move a unit charge from one point to another within an electric field. In the context of batteries, voltage describes the state of the electrodes and evolves as electrochemical reactions take place.

In a standard galvanostatic experiment, a constant current is flowed through the cell and the voltage across the cell is allowed to vary. The voltage profile has characteristic shapes based on the type of reactions occurring. In a solid-solution reaction, a sloped voltage profile is observed due to the continually changing composition of the electrode. In a two-phase reaction, plateaus in the voltage profile are observed at the potentials which the conversion between phases occur.

The current measured in the cell can come from different sources such as electrode redox reactions, but also from parasitic reactions from the electrode and electrolyte. The lower and upper voltage cutoff potentials are set based on the expected working potentials of the electrodes as well as the electrochemical stability window of the cell components. When the

voltage exceeds the lower or upper cutoffs, the current from parasitic contributions is expected to be exacerbated.

The rate used in a galvanostatic experiment is typically expressed with the C-rate notation, which denotes the rate at which a battery is (dis)charged relative to its capacity. A C-rate of 1 C means that the battery is completely charged or discharged in one hour. Experiments are typically done at low C-rates to study the fundamental reaction mechanisms occurring in a battery. Faster C-rates result in large overpotentials which lead to less accessible capacity with a set upper voltage cutoff. The rate capability of electrodes is tested using different C-rates and comparing the capacity attained at each C-rates. Electrodes with similar capacities at fast and slow rates suggest that they have good rate capability. For kinetically hindered reactions, a slow C-rate can enable additional capacity that is not attained at fast cycling speeds. Another way to access kinetically hindered reactions is through application of voltage holds at the voltage limits for extended periods of time. The hold allows the entire electrode to equilibrate at the applied voltage.

Comparison of the voltage profiles on charge and discharge provide additional insights into the electrochemical properties of a cathode system (**Figure 2.1**). The voltage hysteresis between the charge and discharge processes hints at the structural stability or changes occurring during cycling. Large differences between the charge and discharge voltage profiles indicate inefficient cycling as energy is lost to overpotentials or an evolving crystal structure which leads to changes in the equilibrium voltage potentials. The irreversible capacity in a cell can be determined in the difference in capacity between the charge and discharge cycle. This irreversible capacity can come from different contributions such as parasitic reactions or bulk structural changes.

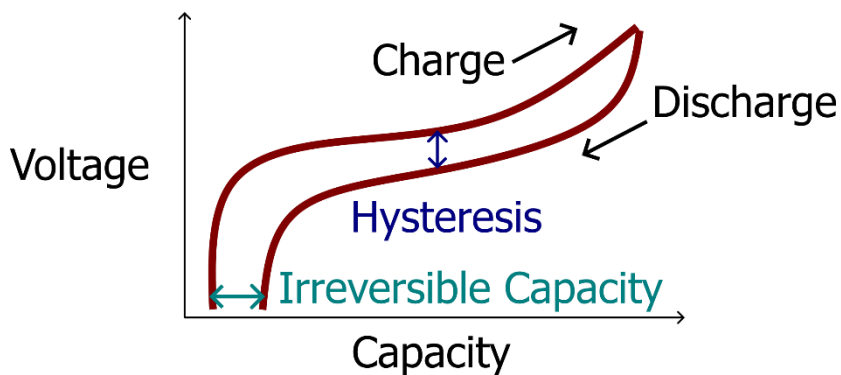


Figure 2.1 Voltage profile of a hypothetical battery. The energy inefficiency for a cycle can be determined by the difference in potential and capacity between the charge and discharge cycles.

Additional insights into the reactions occurring during cycling can be derived from differential capacity analysis. In this technique, the derivative of the voltage profile (dQ/dV) is plotted against voltage. This allows for the identification of potentials at which reactions occur in the cell. Notably, sharp peaks are evident at the potentials at which two phase reactions occur. The evolution of features in the differential capacity plots with electrochemical aging inform on the degradation mechanisms that are occurring in battery electrodes. In this dissertation, the insights from electrochemistry are then paired with structural characterizations to draw structure-property relationships in different electrode materials.

2.2. X-Ray Diffraction

X-ray diffraction is used to identify bulk crystalline phases in as-synthesized and cycled electrodes. X-ray diffraction relies on the interaction of X-rays with the periodic arrangement of atoms in a crystal lattice. The X-rays undergo diffraction due to the periodicity of the crystal structure. Constructive interference of scattered X-rays can be detected, and a diffraction pattern is produced which provides information on the spatial arrangement of atoms, their distances, and the symmetry of the crystal lattice. The condition for constructive interference in X-ray diffraction is described by Bragg's law:

$$2d_{hkl} \sin(\theta) = n\lambda \quad (2.1)$$

where d_{hkl} is the distance between hkl planes, θ is the angle of incidence, n is an integer, and λ is the wavelength of the incident X-ray beam. This work utilizes powder X-ray diffraction, in which the diffraction pattern is the superposition of diffraction from the randomly oriented crystals in the sample.

In powder diffraction patterns, the location of peaks, their intensities, peak shape, and number of peaks can be used to derive structural information of the phases in the sample. The intensity of the peaks is dependent on the X-ray scattering factor of the atoms in the crystal lattice as well as their arrangement and is encompassed in the so-called structure factor. The peak positions are dependent on the lattice parameters of the crystal structure. The peak shape is complicated by a number of factors including instrumental broadening, crystallite size and strain broadening, as well as defects such as stacking faults. All of this information can be used in full pattern fitting to gain structural insights into the sample. We use a combination of Le Bail and Rietveld refinements to identify structural insights. This work makes use of synchrotron quality X-ray diffraction data, which enables high quality and high-resolution data due to the brilliant source of X-rays.

Due to the air-sensitive nature of samples studied in this dissertation, samples are typically loaded into glass capillaries and sealed. Measurements are then done through with Debye-Scherrer geometry. This transmission geometry is advantageous over reflection geometry (Bragg-Brentano) as the latter has angle dependent absorption effects, which make pattern refinement difficult.

X-ray diffraction is an average technique that can only probe long range structure in crystalline materials. This information is supplemented by other characterization techniques

that can provide electronic structure and local environment information. Complementary information is especially needed for samples containing light atoms such as Li, which do not scatter as effectively as heavier elements.

2.3. Magnetometry

Magnetometry is used to investigate the magnetic properties of materials by measuring how the material responds to an external magnetic field. The interaction between the material and the magnetic field can be described by the magnetic susceptibility (χ), which relates the magnetization (M) of the material to an external magnetic field (H), by the equation:

$$M = \chi H \quad (2.2)$$

Materials can be grouped into five magnetic classes based on their magnetic behavior: diamagnetic, paramagnetic, ferromagnetic, ferrimagnetic, and antiferromagnetic. Diamagnetic materials are composed of atoms with no magnetic moment such as those with all paired electron spins. When placed in a magnetic field, H , diamagnets produce a negative magnetization and lead to a negative magnetic susceptibility. Additionally, the magnetic susceptibility of diamagnets have no dependence on temperature unlike the other classes of magnetic materials. Similarly, to diamagnetic materials, paramagnetic materials have no long range magnetic ordering. However, paramagnets do have unpaired electrons, which produce a positive magnetization when placed in a magnetic field. The magnetic susceptibility for paramagnets have a temperature dependence that follows Curie-Weiss law (Equation 1.1). The Curie-constant is proportional to the number of unpaired spins and can be used to calculate an effect magnetic moment (μ_{eff}) in units of Bohr Magneton (μ_B) by:

$$\mu_{\text{eff}} = \sqrt{8C} \mu_B \quad (2.3)$$

μ_{eff} can then be compared to a theoretical spin-only value ($\mu_{\text{spin-only}}$) in units of μ_B by:

$$\mu_{spin-only} = 2\sqrt{S(S+1)} \quad (2.4)$$

Where S is the spin quantum number determined by the number of unpaired spins. The spin-only value is a simplified model that ignores spin-orbit coupling. This assumption, however, is usually accurate for $3d$ transition metals, which are typically used in battery cathodes. Comparison of the measured μ_{eff} and $\mu_{spin-only}$ values can determine the type of magnetic species present in a material. The Curie-Weiss temperature is related to the strength of magnetic correlations in a material. Negative or positive values for θ_{cw} imply ferromagnetic or antiferromagnetic interactions and the magnitude of θ_{cw} is related to the strength of these interactions. C and θ_{cw} are important parameters for understanding the structure of materials through their magnetic properties. These parameters can be obtained through linear fits in a high temperature regime of inverse magnetic susceptibility vs temperature curves. Some samples may have an additional temperature independent contribution to magnetic susceptibility (χ_0) such as Pauli-paramagnetism. In this case, a fit in the high temperature regime is performed with the following equation:

$$\chi = \frac{C}{T - \theta_{cw}} + \chi_0 \quad (2.5)$$

Upon cooling paramagnetic materials, a magnetic transition can occur at lower temperatures that is characteristic of ferro/ferrimagnetism or antiferromagnetism. Variable temperature magnetic susceptibility measurements are typically performed by cooling at zero field and under field cooled conditions. Divergence between zero field and field cooled curves can indicate the presence of ordered magnetic states. Ferromagnetism and ferrimagnetism are related groups as both have a net parallel magnetic moment that aligns with the applied field. Ferrimagnetic materials have an additional magnetic sublattice that is antiparallel although with a smaller magnetic moment, which leads to incomplete cancellation of the main magnetic

lattice and thus a net parallel magnetic moment. Antiferromagnetism leads to antiparallel moments that cancel each other out completely. These magnetic classes display characteristic χ vs. temperature curves that can be seen in **Figure 2.2**. The transition temperature for ferro/ferrimagnets and antiferromagnets are denoted as the Curie temperature (T_c) and Neel temperature (T_N). Magnetic interactions can be predicted in oxides following the Kanamori-Goodenough rules. The magnetic behavior of cathodes are expected to change as they undergo charge-discharge processes. The evolution of their magnetic properties can be correlated to structural changes to better understand the reaction mechanisms governing their usage.

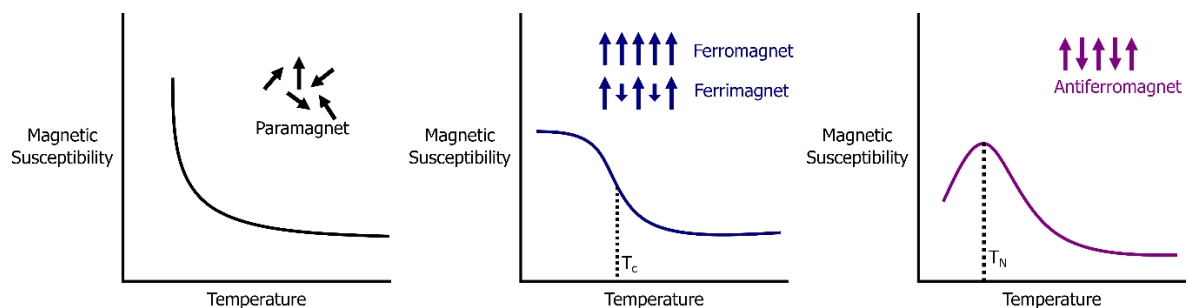


Figure 2.2 Typical magnetic susceptibility vs temperature curves for paramagnets, ferro/ferrimagnets, and antiferromagnets.

Magnetometry experiments utilize superconducting quantum interference device (SQUID) magnetometers to measure extremely weak fields and result in high sensitivity measurements. In an experiment, the sample is passed through detection coils and the magnetic fields from the sample induce a current in the detection coils, which is proportional to the magnetization of the sample.

2.4 Magnetic Resonance Spectroscopy

The magnetic moment of nuclear spins, in ssNMR or unpaired electron spins, in EPR can be aligned parallel or antiparallel to an applied field. The energy difference (ΔE) between these two states is described by the Zeeman effect:

$$\Delta E = g\mu_B B_0 \text{ (EPR)} \quad (2.6)$$

$$\Delta E = -\hbar\gamma B_0 \text{ (ssNMR)} \quad (2.7)$$

where g , or g -factor, is the proportionality factor between energy difference and applied field (B_0), \hbar is the reduced Planck's constant and γ is the gyromagnetic ratio for the nuclear spin. The lower energy spin state can be excited through absorption of radiation with the resonance condition:

$$h\nu = \Delta E \quad (2.8)$$

where h is Planck's constant and ν is the radiation frequency. Typical radiation frequencies for EPR and ssNMR are in the microwave and radio frequency range, respectively.

The resonant frequency of these techniques is altered by the local environment the spin (both nuclear and electron) and provide chemical information on the local structure. In EPR, deviation from g -factor of an electron in vacuum (2.0023) arises from spin-orbit coupling. In principal, the octahedral environments of transition metals in layered oxides should result in two g -factors labeled g_{\parallel} and g_{\perp} due to its axial symmetry. However, severe broadening typically leads to an averaged signal and a single g -factor. In ssNMR, the resonant frequency is related to a chemical shift (δ). The resonant frequency of the sample (ν_{sample}) is referenced against a standard ($\nu_{\text{reference}}$) to give the chemical shift in parts per million (ppm):

$$\delta = \frac{\nu_{\text{sample}} - \nu_{\text{reference}}}{\nu_{\text{reference}}} \quad (2.9)$$

In paramagnetic ssNMR, the largest contribution to the chemical shift is the Fermi contact interaction and can result in shifts of 100s to 1000s of ppm. In this interaction, unpaired electron density from paramagnetic species can delocalize onto the *s* orbital of the nuclei of interest. The magnitude and sign of the Fermi contact shift is dependent on the spin transfer pathways, which can transfer parallel or antiparallel electron spin density.

The intensity of the signal in magnetic resonance techniques is proportional to the number of spins and can be used to quantify different environments in the sample. Paramagnetic samples exhibit fast relaxation times because of coupling with dipolar fields. This makes it particularly important to correct for intensity losses due to relaxation effects in ssNMR. In EPR, quantification is reliant on being in a linear regime where the intensity is directly proportional to the microwave power used. This is typically not an issue for paramagnetically concentrated systems, where saturation is hard to reach due to the fast relaxation times. EPR signal intensity can be correlated to the static magnetic susceptibility since both have a dependence on the number of unpaired spins in the sample.

In traditional ssNMR and EPR, hyperfine and J coupling between magnetic moments leads to additional energy level splitting that manifest as additional peaks in the spectrum. However, due to large dipolar fields generated paramagnetically concentrated materials, such as battery electrodes, severe broadening of the signals occurs, which wash out hyperfine structure. These dipolar fields scale with the external magnetic field and dipolar broadening can be minimized by utilizing low B_0 fields. Additionally, magic angle spinning (MAS) conditions can be used in ssNMR to improve resolution by averaging out dipolar interactions.

EPR experiments on paramagnetically concentrated samples are done in continuous-wave (CW) mode due to fast relaxation times that lead to signal decay in pulsed techniques. In

CW mode, the sample is placed into a microwave resonator, which increases the sensitivity of the experiment by concentrating the microwave power at the location of the sample. The sample is continually radiated throughout the experiment, and the external field is varied. When the external field creates an energy level splitting that matches the radiation frequency, radiation is absorbed and detected.

2.5 First Principles Calculation of ssNMR parameters

The Fermi contact shift in ssNMR can be predicted using first-principles calculations. Here, prior knowledge about the system is required to generate a supercell and the chemical shift of local environments in this structure can be predicted. The Fermi contact shift contribution is proportional to the unpaired electron spin density at the nucleus (A), which can be computed from first principles. This unpaired electron spin density is then scaled by the magnetic properties of the material to give the Fermi shift contribution. Paramagnetic species within the first two coordination shell can delocalize electron density to the nucleus. Fermi shift contributions are additive and can be used to predict distinct local environments.⁸⁷⁻⁸⁹

The overall Fermi contact shift (δ_{FC}) can be written as:

$$\delta_{FC} = \sum_i P_i \quad (2.10)$$

where P_i is the contribution from an individual M -O- A transfer pathway. Contributions from each P_i can be determined by the ‘spin flipping’ technique developed by Middlemiss et al.⁸⁷ In this method, the electron density at the nucleus is determined for a ferromagnetically-aligned cell ($p(r=0)_1$). Then the spin on a M of interest is flipped and the electron density at the nucleus is determined again ($p(r=0)_2$). The contribution from that M of interest is then determined by:

$$\begin{aligned}
 p(r = 0)_1 - p(r = 0)_2 & \quad (2.11) \\
 & = 2 \times \delta(P_i)
 \end{aligned}$$

where $\delta(P_i)$ is the Fermi shift contribution from the M of interest. This process can be repeated for the remaining M in the supercell to get contributions from all M . The contribution from each M will be dependent on the identify of M , bond lengths, and bond angles since these factors determine the orbital overlap between M and A .⁸⁷⁻⁸⁹

In the ideal layered lithium transition metal oxide structure, all Li ions have twelve M neighbors within the first two coordination shells which will contribute to its chemical shift. The local environment for a Li in the Li layer is shown in **Figure 2.3**. In a Jahn-Teller distorted system like LiNiO_2 with Ni^{3+} , the bonds are distributed into both short and long bonds.⁹⁰⁻⁹² This difference in bond lengths will lead to different orbital overlap and hence different Fermi shift contribution.⁹³ The total chemical shift for this environment can be altered through defects such as Li/Ni antisite defects, which can lead to an additional Fermi shift contribution from a Ni in the Li layer.

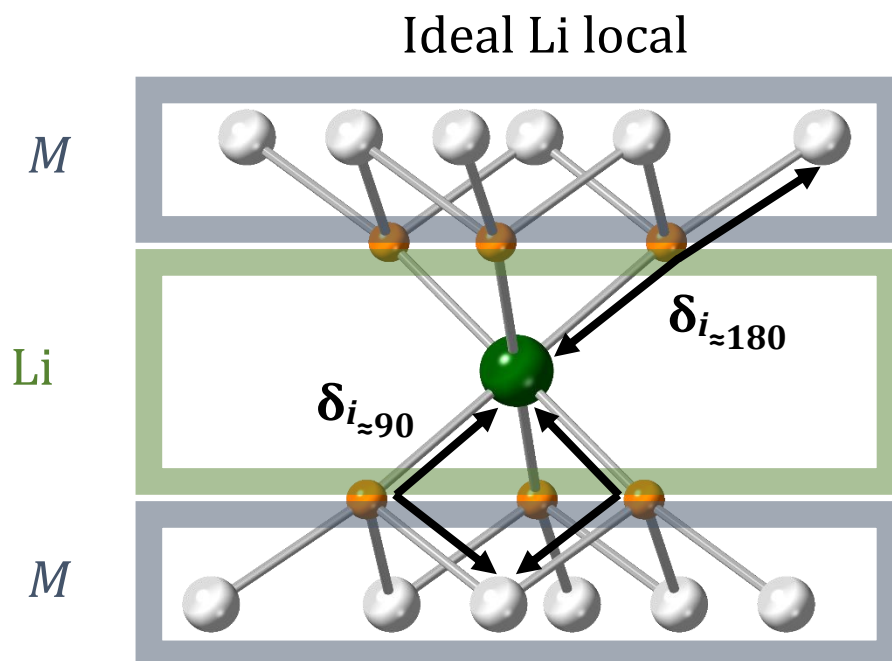


Figure 2.3. Li local environment in the layered structure. There are twelve M neighbors that can delocalize electron density onto the Li through 180° and 90° interactions. In this environment, there is a total of six 180° and six 90° interactions.

Chapter 3. *Operando* Electron Spin Probes for Battery Applications²

Abstract. *Operando* electron spin probes provide real-time insights into the electrochemical processes occurring in batteries. This work details the development and design criteria for *operando* magnetometry and EPR cells and demonstrates their tandem use to understand the electrochemical processes occurring during charge for $\text{LiNi}_{0.5}\text{Mn}_{0.5}\text{O}_2$ cathodes. High fidelity electrochemistry is achieved through application of sufficient pressures through a clamping and spring mechanism for the magnetometry and EPR cells that match the performance of traditional Swagelok cells. Three redox processes are identified in $\text{LiNi}_{0.5}\text{Mn}_{0.5}\text{O}_2$ with a preferential oxidation of Ni^{2+} in the transition metal layer that are involved in 180° superexchange interactions with antisite defect Ni in the Li layer. Subsequent oxidation of the remaining Ni^{2+} in the transition metal layer occurs next and finally Ni^{3+} oxidation to diamagnetic Ni^{4+} . These processes are found to occur in sequential steps and the transition of each step is identified with the real-time insights provided by *operando* magnetometry and EPR. These unique tools can be applied to novel electrode materials to understand the processes occurring during operation. These insights will enable the development of better batteries.

² The contents of chapter 3 is currently being prepared for publication.

3.1 Introduction

Operando characterization is a pivotal methodology, which offers real-time insights into the dynamic behavior of batteries during cycling. Traditional post-mortem (*ex situ*) analyses have limitations in capturing the transient phenomena and dynamic evolution of materials during charge and discharge and reliable/reproducible results are highly dependent on careful sample harvesting and preparation procedures since the sample can degrade before it is analyzed.⁹⁴ *Operando* techniques, on the other hand, offer a dynamic perspective, allowing researchers to scrutinize the intricacies of electrode reactions, structural changes, and ion transport in real-time. These techniques enable monitoring and analysis of electrochemical processes within batteries while they are actively functioning by integrating advanced analytical techniques such as spectroscopy^{64,95,96}, microscopy⁹⁷⁻¹⁰⁰, and diffraction¹⁰¹⁻¹⁰⁴ with electrochemical measurements. *Operando* cells have been realized for many different analytical techniques to probe the gas reactions¹⁰⁵⁻¹⁰⁷, interfaces¹⁰⁸⁻¹¹⁰, and bulk structural changes in battery electrodes^{101,104,111}. Among these techniques, EPR^{51,60,64} and magnetometry^{80,112,113} are non-invasive probes that enable the direct detection of redox reactions as they are sensitive to the evolving electronic structure of electrodes during battery operation as mentioned in Chapter 1. EPR and magnetometry provide complementary insights and shortcomings of each techniques are circumvented when they are used in tandem. Since EPR probes local structure, it can differentiate between the multiple phases present in a battery assembly (e.g. electrodes, electrolyte, etc.). This distinction is lost in a bulk measurement such as magnetometry. However, as a magnetic resonance technique, EPR is reliant on favorable relaxation times and suitable excitation energies, which can be prohibitively large for species with zero-field splitting, to observe the species of interest. Magnetometry is agnostic to these

dependencies and signal detection is possible for all samples. The measured intensity in EPR is proportional to static magnetic susceptibility and provides a direct link between data sets generated by both techniques. As both techniques probe electron spins, they can be used simultaneously to aid in data analysis by establishing constraints for interpretation.

3.2 Methodology

Material Synthesis: $\text{LiNi}_{0.5}\text{Mn}_{0.5}\text{O}_2$ was synthesized through a carbonate coprecipitation and cocalcination route that was modified from a prior report.¹¹⁴ Manganese (II) sulfate monohydrate (Sigma) and Nickel (II) sulfate hexahydrate (Sigma) were dissolved in a 1:1 molar ratio in deionized water to prepare a solution with a total transition metal concentration of 0.5 M. A separate equivolume solution of 1 M sodium bicarbonate (Sigma) was prepared. The sodium bicarbonate solution was heated to 50°C in an oil bath. While stirring the sodium bicarbonate solution, the entire transition metal solution was added dropwise with a burette. After addition of the transition metal solution, the mixed solution was allowed to stir at 50°C for 24 hours. The solution was then removed and the precipitate was collected and washed with a centrifuge. The precipitate was washed three times with deionized water and then dried in an oven at 110°C. The dried precipitate was mixed with stoichiometric amounts of lithium carbonate (Sigma) with a mortar and pestle for 10 minutes. The powder was pressed into a pellet and heated to 900°C for 6 hours (5°C/min ramp rate). After 6 hours, the pellet was taken out of the furnace and quenched between copper plates and the pellet was immediately transferred into the glovebox.

Electrochemistry: Free-standing LNMO: carbon black (Super C65; MTI Corporation): polytetrafluoroethylene (PTFE; Sigma Aldrich) films were fabricated in a mass ratio of 80:10:10. The electrode was cycled in Li half cells with 1 M LiPF₆ in ethylene carbonate,

dimethylcarbonate, and diethylcarbonate (EC/DMC/DEC = 1/1/1 v/v/v) electrolyte, and Whatman GF/D glass microfiber separators. Cells were cycled from 3.0 V to an upper voltage cutoff of 4.4 V vs. Li/Li⁺ at a rate of C/20 (1 C = 280 mA g⁻¹). The loading density for the electrodes were ≈11-15 mg cm⁻². All cells were cycled on an Arbin BT2000 or Bio-logic VMP-3e potentiostat.

X-ray Diffraction: LNMO was loaded into glass capillaries and measured at Beamline 11-BM at the Advanced Photon Source (APS) using the mail-in program. All patterns were collected in Debye–Scherrer geometry from 0.5° to 50° 2θ at room temperature with data points collected every 0.001° 2θ and a scan speed of 0.01°/s. Refinements were done using the TOPAS software suite.¹¹⁵ Refinement of synchrotron XRD data was performed by an initial Le Bailie Fit, where a 10 term Chebyshev polynomial, axial divergence, zero error, sample absorption, lattice parameters, crystallite size and microstrain were sequentially refined. Two R-3m phases were needed to fit the pattern. A subsequent refinement was performed with all variables simultaneously allowed to vary. These values are then fixed in a subsequent Rietveld refinement to refine for the Li/Ni antisite concentration (y). Thermal parameters (B_{eq}) were then refined. Three thermal parameters were used for O, atoms in the 3a site, and atoms in the 3b site and each were refined sequentially. A final step was done where all variables were allowed to vary simultaneously until convergence.

ssNMR: ⁷Li ssNMR measurements were carried out on a wide bore Bruker BioSpin spectrometer with a DMX 500 MHz console and a home built 1.3 single X-broadband magic angle spinning (MAS) probe. All spectra were acquired at B₀ = 2.35 T (100 MHz for ¹H) with 60 kHz MAS using dry nitrogen and the probe was tuned to ⁷Li (38.9 MHz). Samples were packed into 1.3 mm zirconia rotors inside an Ar glovebox and closed with Vespel caps. ⁷Li

chemical shifts were referenced to 0 ppm with 1M aqueous LiCl solutions. All acquisitions were done with a rotor synchronized spin-echo sequence with a 90° pulse of $0.45 \mu\text{s}$. A recycle delay of 50 ms was sufficient for paramagnetic signals to be fully relaxed. ssNMR data was processed using Bruker TopSpin 3.6.5 and spectral fits were done with DMfit.¹¹⁶

Magnetometry: LNMO was loaded into sealed quartz tubes (1 mm ID and 3 mm OD). SiO₂ powder (Advalue Tech) was used to center the cathode samples inside the quartz tubes. Measurements were done on a Quantum Design MPMS3 SQUID magnetometer. Zero field and field cooled M(T) measurements were carried out from 2 to 350 K with $H = 0.1 \text{ T}$.

3.3 Operando Cell Designs and Experiments

One challenge of *operando* studies is the realization of electrochemical performance that is on par with traditional coin or Swagelok cells. High fidelity electrochemistry is a requirement for drawing conclusions based on *operando* data as the observed reactions are highly influenced by the voltages the materials experience and can be complicated by overpotentials or spurious reactions from the cell. Excessive overpotentials are prevented through application of sufficient stack pressure and hermetic seals, which provide good electrical contact between components and prevents electrolyte evaporation that can lead to sluggish ionic diffusion. Spurious reactions are prevented through judicious cell material selection. Traditional cells typically employ metallic parts (casings, spacers, springs, current collectors) with favorable mechanical strength, chemical stability, and electrical conductivity.¹¹⁷ As EPR and magnetometry operate with strong magnetic fields, these metallic parts need to be minimized in order to limit interactions with the field and replaced with diamagnetic materials. In the following section, we describe design rules specific to each

operando cell and demonstrate their usage. Cell designs are shown in **Figure 3.1** and CAD files with detailed dimensions for both designs are provided in the supplementary information.

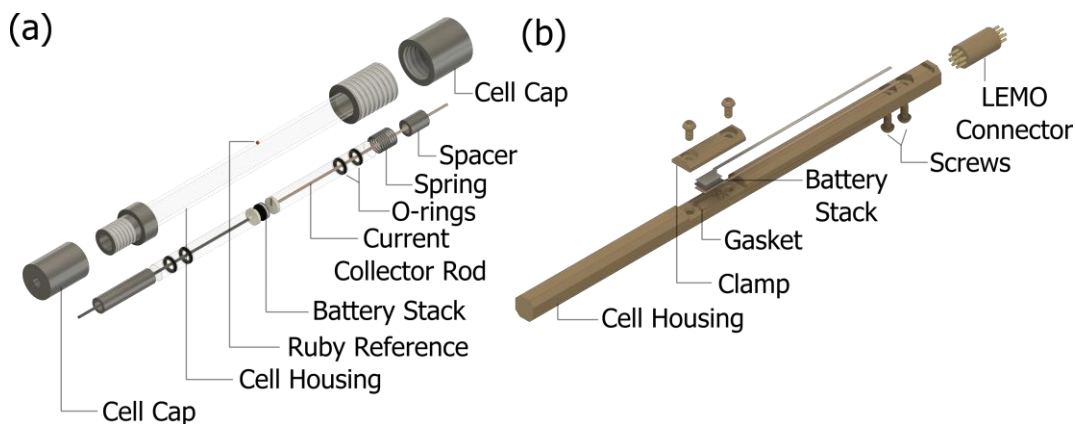


Figure 3.1. Schematic of *operando* cell designs for (a) EPR and (b) magnetometry. Details of dimensions and component materials are included in the supplementary information.

3.3.1 EPR Cell

Figure 3.1a shows a schematic diagram of the designed *operando* EPR cell. The cell is designed to be used with a continuous wave X-band EPR spectrometer (Bruker EMXplus) that is paired with a high sensitivity resonator (Bruker ER 4119HS-LC) operating in a perpendicular excitation mode. Within this resonator, the signal intensity is at a maximum at the center of the cavity and tapers off until the signal disappears far away from the resonator.¹¹⁸ This spatial dependence allows for the use of mechanically rigid steel parts and o-rings, which interact with the magnetic field and have impurity signals, respectively, by positioning these problematic components away from the center of the cell. The cell is modeled after the Swagelok cell geometry and utilizes a quartz tube (Advalue technology, 7 mm OD, 5 mm ID) body that is fixed between two metal end caps with machined threads. Quartz rods were machined to create grooves at the for o-rings (Viton, 5 mm OD, 3 mm ID) and to allow current collector wires through, which are fixed in the rod and sealed with epoxy (Henkel Loctite EA

E120-HP). In the assembled cell, the electrode stack is placed in the center between the two current collector rods and pressure is applied to the stack by compression of a spring between the end cap and current collector rod. Accidental shorts due to the leads and stainless-steel caps are prevented using an insulator heat shrink tubing. The top stainless-steel cap has a wider width than the opening of the resonator to allow the rod to rest on the resonator. A small single crystal ruby is fixed to on the quartz housing and is used as a reference to correct for phase and intensity changes due to the evolving electrode properties, which changes the conditions for critically coupling the EPR resonator.⁵¹

While the chosen cell geometry leads to exceptional electrochemistry, it exacerbates issues with non-resonant absorption of microwaves. As the radius of the cell increases, the cell interaction with the electric fields in the resonator increases and lowers the quality factor of the resonator. This absorption scales with the dielectric constant of each material. However, a sufficient thickness is required for the quartz components as thin pieces are fragile and prone to breaking. Additionally, reducing the thickness of the cell leads to a loss of signal intensity as smaller electrodes are then used to accommodate the smaller dimensions. Previous *operando* EPR designs have utilized a vertical stack orientation to overcome the microwave absorption issues.^{51,60} However, a wire loop or mesh of current collectors is needed to prevent magnetic shielding and can lead to inhomogeneous electrochemical reactions. We opted to maintain the horizontal stack orientation and circumvent the absorption issues through electrolyte selection. In *operando* battery cells, the electrolyte is the component with the largest dielectric constant. Typical alkali-ion batteries use electrolytes with an alkali hexafluorophosphate salt dissolved in a mixture of carbonate solvents. High dielectric cyclic carbonates, such as ethylene carbonate (EC), are added to enable the dissolution of the alkali hexafluorophosphate salt and

the dielectric constant of this blend can be minimized by reducing the EC component.¹¹⁹ We find an electrolyte mixture with 30% by volume of EC leads to sufficient quality factors for data acquisition.

Prior to performing the experiment, an ideal cell position is identified where the signals from the ruby reference and the sample of interest are well resolved. The ruby signal positions have a dependence on the crystal orientation relative to the magnetic field. As such, the cell can be rotated to minimize the overlap between the ruby reference signal and the sample of interest. The *operando* experiment is performed through time delayed acquisitions over the course of the cell cycling. The temporal resolution between measurements is dependent on the field sweep range and the number of scans needed to achieve sufficient signal to noise. Investigations of paramagnetically concentrated cathodes typically require the entire field sweep range and we have found 3 scans leads to adequate signal-to-noise, which results in a temporal resolution of ~5 minutes. Spectral fits for each data point was performed using the EasySpin toolbox on Matlab.²⁹ The fits were performed with an initial background subtraction and parameters refined for were g-factor, intensity, linewidth, and phase. Fits were performed on both the ruby and cathode signals with a Lorentzian lineshape. The intensity of the cathode signal was corrected by the intensity of the ruby signal with a correction factor set by the intensity of the ruby signal normalized by its initial intensity.⁵¹

3.3.2 Magnetometry Cell

Figure 3.1b shows a schematic diagram of the *operando* magnetometry cell. The cell is designed to be paired with a Quantum Design MPMS3 SQUID magnetometer and is used with a modified Quantum Design electrical transport option (ETO) sample rod. The cell features a hexagonal rod geometry to facilitate machining the various features. A cavity for the

battery stack is machined 66 mm from the bottom of the rod. The battery stack is oriented parallel to the length of the rod, which positions it parallel to the magnetic field in the MPMS3. This orientation prevents magnetic shielding effects from the current collectors over an orientation perpendicular to the magnetic field. Around the top of the cavity are grooves for a Viton gasket, which is custom cut with a laser cutter (Trotec Speedy 100). A cap piece is machined with a protrusion that extends into the cavity. The cap is clamped to the cell through two screws, which applies pressure to the battery stack and compresses the gasket. Two channels for leads are routed along the side of the cell. Custom cut current collectors are fixed in the cell and the channels are filled with epoxy. Electrical contact between the current collector and a modified LEMO connector (Quantum Design part # 4055-004) with soldered copper wires is established by a nut and washer. The LEMO connector is typically used to connect the ETO sample holder to the sample rod. The LEMO connector can then be connected to the ETO sample rod, which brings the leads outside of the MPMS3 sample chamber and can be connected to a potentiostat.

The ideal cell material is quartz due to its low background signal, chemical stability, and mechanical rigidity. However, due to quartz's fragility and difficulty machining, the design features (e.g. clamping mechanism and threading for screws) of the *operando* magnetometry cell would make it prone to breaking. A plastic cell material is chosen instead for this cell. While, fluoroelastomers, such as polytetrafluoroethylene (PTFE) and perfluoroalkoxy alkane (PFA), are desirable for their chemical inertness, we opted to make the cell from polyether ether ketone (PEEK) due to its rigidity, which is essential for the clamping mechanism of the cell. The applied pressure makes this cell advantageous over previously reported cells where no stack pressure was applied.^{80,113}

Prior to the experiment, a background scan is performed on all cell components except for the material of interest. The background of the fully assembled cell is corrected through the procedure outlined in MPMS3 application note 1500-023. The *operando* experiment is performed through a time delayed DC scan acquisition. In DC scan mode, the cell is lowered through SQUID detection coils and a change in the magnetic flux as the cell passes through the coils is measured. The magnitude of this change in flux is proportional to an output voltage that is detected in the instrument. A subsequent up scan is performed, and the sample rod is raised through the detection coils. The up and down scan voltage profiles should overlap with negligible hysteresis. Acquisition parameters in a time delayed DC scan mode include scan length, scan time, and delays between scans. The entire scan length of 60 mm is utilized to get reliable background subtractions. While the delay time between scans can be adjusted to acquire enough data points, the DC scan time must be set to the longest time of 15 seconds to get a reliable scan. Faster scan times will lead to hysteresis in the up and down scans, which leads to uncertainty in the voltage readings of the experiment. This leads to an inherent temporal resolution of 30 seconds per measurement and should be accounted for when choosing the desired cycling rate.

3.4 Reaction mechanisms of $\text{LiNi}_{0.5}\text{Mn}_{0.5}\text{O}_2$

The tandem use of *operando* EPR and magnetometry is demonstrated on $\text{LiNi}_{0.5}\text{Mn}_{0.5}\text{O}_2$ (LNMO) to understand the processes occurring during electrochemical cycling. LNMO was synthesized using a carbonate coprecipitation and calcination route. The synthesis from a prior study was modified to synthesize LNMO.¹¹⁴ Oxidation states for transition metal species in LNMO are be 2+ for Ni (S=1) and 4+ for Mn (S=3/2) based on previously reported XAS

results.¹²⁰ In addition to the electronic structure, the defects present in cathodes also highly influence its magnetic properties.^{121–123} One common defect in the layered structure is the Ni/Li antisite defect, which results in 180° superexchange pathways between Ni in the Li layer (Ni_{Li}) and transition metals in the M layer (M_M). In the defect free structure, only 90° superexchange interactions exist between M_M within the same layer. 180° superexchange interactions are strong interactions, which manifest in the layered structure to alleviate the magnetic frustration between antiferromagnetically coupled transition metals in a triangular lattice.^{34,35} We characterized antisite defects in the as-synthesized material with sXRD, ssNMR, and SQUID magnetometry. Rietveld refinements of sXRD data were used to determine the phase purity and to quantify Li/Ni antisite defects (y in $[\text{Li}_{1-y}\text{Ni}_y]_{3a}[\text{Li}_y\text{Ni}_{0.5-y}\text{Mn}_{0.5}]_{3b}\text{O}_2$) in LNMO (**Figure 3.2a**). Structural parameters are provided in **Table 3.1**. Two layered phases with $R\text{-}3m$ symmetry were identified in the sXRD data with differences in their antisite defect concentrations. The majority phase (72.5 wt%) has a larger antisite defect concentration of 0.1218(6) as compared to the minor phase's (27.5 wt%) concentration of 0.0748(9). This results in a total of ~0.11 mol of Li in the transition metal layer. Li in the transition metal layer (Li_M) and Li in the Li layer (Li_{Li}) have distinct ^7Li ssNMR chemical shifts and quantification of these sites can be used to support the model used for Rietveld refinements.¹²⁴ ^7Li ssNMR spectra acquired on LNMO and spectral decompositions are shown in **Figure 3.2b**. Two groups of resonances are observed in the range of 1000–1500 ppm and below 800 ppm corresponding to Li_M and Li_{Li} environments, respectively. Quantification of these sites lead to a total defect concentration of 0.14(5) of Li_M and is within error of the value determined by sXRD. SQUID magnetometry was also performed on LNMO to characterize the magnetic transitions that result from the antisite defects. Field cooled and zero field cooled magnetic

susceptibility curves are shown in **Figure 3.2c**. Two magnetic transitions are observed at 11 K and 120 K, which is consistent with the biphasic population identified in sXRD. The higher temperature transition is presumably associated with the majority phase A with a larger antisite defect concentration due to the correlation between antisite defects and magnetic ordering temperature.¹²⁵ The characterization of the antisite defects present in LNMO assists in the interpretation of *operando* data discussed in the following section. These three independent techniques corroborate the conclusion that there exists two phases in the sample with around 0.11 mol antisite defect concentration.

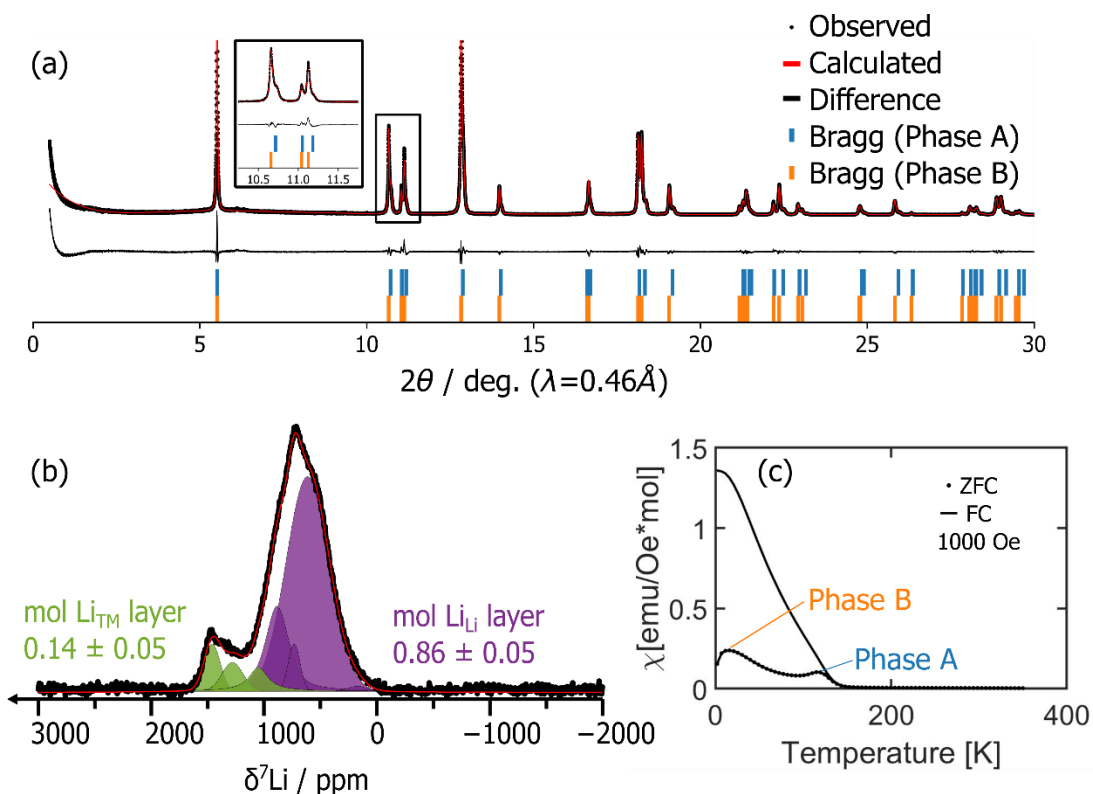


Figure 3.2. As-synthesized LNMO characterization. (a) synchrotron XRD data was acquired on LNMO and Rietveld refinements were performed to identify major crystalline phases. A secondary layered ($R\bar{3}m$) phase was present as identified by high-angle shoulders shown in the inset. (b) ^7Li ssNMR spectrum acquired on as-synthesized LNMO with quantification for Li_M and Li_{Li} environments. (c) Magnetic susceptibility measurements performed show the presence of two transition temperatures identified in the ZFC curve and supports the presence of two phases with different Li/Ni antisite concentrations.

Table 3.1. Refined Structural Parameters from sXRD on LNMO with a refinement Rwp value of 10.48

	Space Group	a (Å)	c (Å)	O_z	y in $[\text{Li}_{1-y}\text{Ni}_y]_{3a}[\text{Ni}_{0.5-y}\text{Mn}_{0.5}]_{3b}\text{O}_2$	Weight %
Phase A	R-3m	2.8802(7)	14.299(5)	0.2590(2)	0.0748(9)	72.5
Phase B	R-3m	2.8963(2)	14.309(1)	0.2577(1)	0.1218(6)	27.5

Operando magnetometry and EPR were conducted on LNMO during the first charge process up to 4.4 V at a rate of C/20. A comparison between the voltage profiles collected with the EPR and magnetometry cells is included in **Figure 3.3** and show comparable electrochemistry, which makes correlations between the two datasets possible. We first discuss the results from *operando* magnetometry. In the initial charge process for LNMO, a monotonic decrease in magnetization is observed up to 4.4 V as x in Li_xNiO_2 decreases (**Figure 3.4a**). This is consistent with the subsequent oxidation of Ni^{2+} ($S=1$) to Ni^{3+} ($S=1/2$) and then to Ni^{4+} ($S=0$). We note that prior work has shown that Mn^{4+} does not oxidize at these potentials in LNMO.^{120,126,127} Three regions (labeled (I), (II), and (III)) can be identified with different rates of demagnetization and are correlated with changes in the differential voltage (**Figure 3.4b**). Region (I) occurs at $x = 0.88$ and the mols of Li extracted at the end of this region is equivalent to the Ni/Li antisite defect content as determined by sXRD and ssNMR. This region also has the largest decrease in magnetization and is consistent with the oxidation of a Ni in a strong $180^\circ \text{Ni}_M\text{-O-Ni}_{\text{Li}}$ superexchange interaction. Prior *ex situ* measurements have also shown that Ni_M in these interactions are the first to be oxidized during the charge process.³⁵ At the end of region (I), LNMO has 0.11 mol Ni^{3+} and 0.28 mol Ni^{2+} in the M layer and 0.11 mol Ni^{2+} in the Li layer. In the following charge process denoted by region (II), an additional 0.3 mol of Li are extracted and is equivalent to the remaining Ni^{2+} content in the M layer. A near constant decrease in magnetization is observed in region (II) and is a result of the oxidation of the

remaining Ni^{2+}_M to Ni^{3+}_M . Finally, in the last region until the upper voltage limit, 0.18 mols of Ni are oxidized from Ni^{3+} to Ni^{4+} . Susceptibility changes are expected to be proportional to the change in $S(S+1)$. Oxidation from Ni^{2+} ($S=1$) to Ni^{3+} ($S=1/2$) leads to a change in $S(S+1)$ of 1.25 while oxidation from Ni^{3+} to Ni^{4+} ($S=0$) leads to a change of 0.75. This is consistent with the larger magnitude of dM/dT in region (II) over region (III).

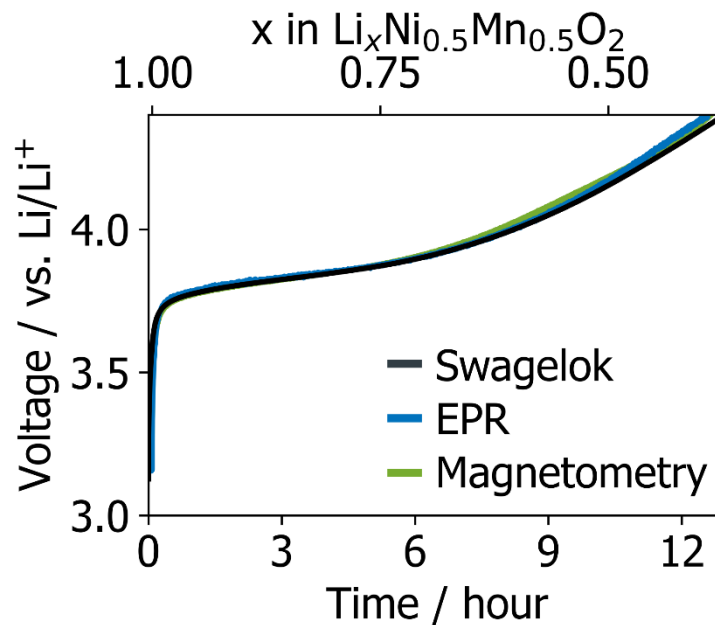


Figure 3.3. Electrochemistry comparison for LNMO cycled against Li half-cells using Swagelok, *operando* EPR, and *operando* magnetometry cells. All cells were cycled at a rate of C/20 up to 4.4 V.

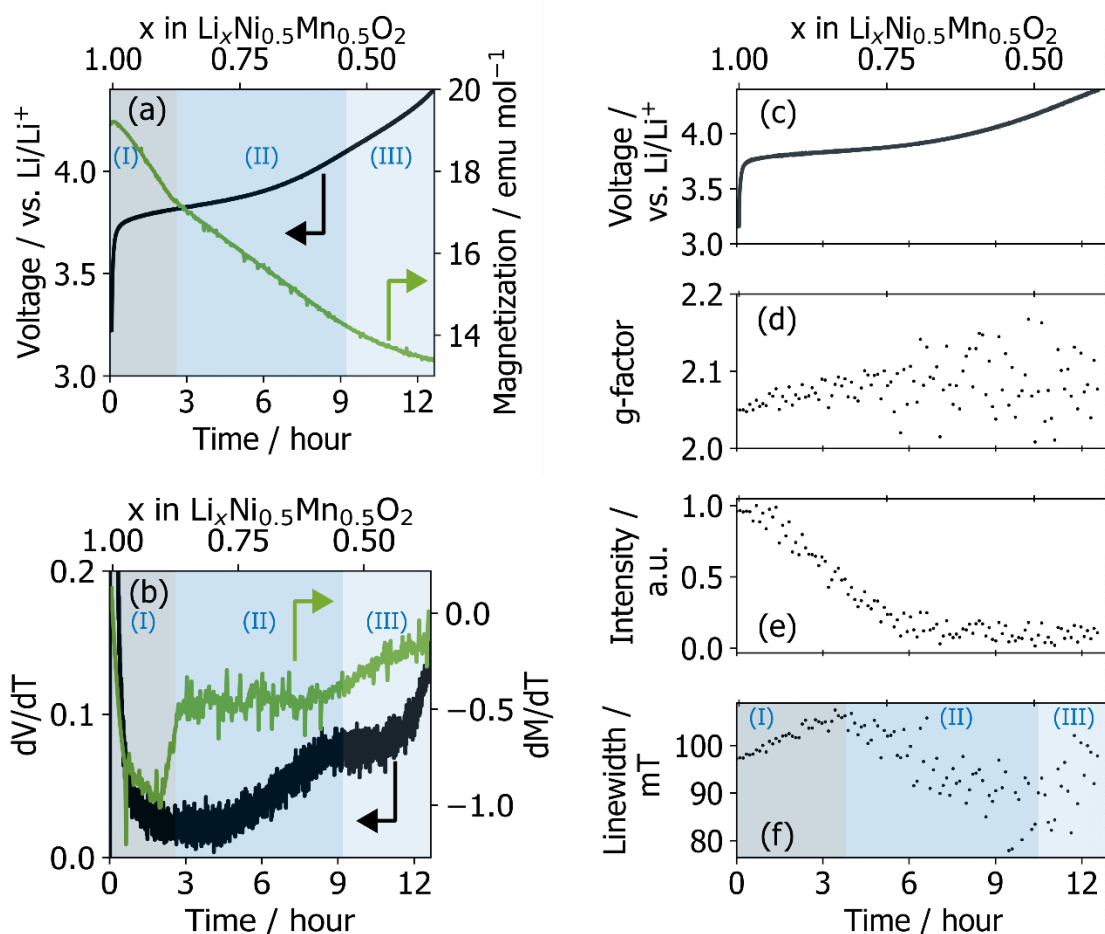


Figure 3.4. (a,b) *Operando* magnetometry and (c-f) EPR datasets collected during the first charge process of LNMO up to 4.4 V. (a) Correlation between magnetization and potential during the first charge process for LNMO. (b) Differential voltage, dV/dT (V hour^{-1}), and differential magnetization, dM/dT ($\text{emu mol}^{-1}\text{hour}^{-1}$) plots processed from (a) show three distinct regions labelled (I), (II), and (III). (c) Voltage profile for the *operando* EPR data set and correlation with the refined spectral parameters: (d) g-factor, (e) intensity, and (f) linewidth.

The initial and final EPR spectra at open circuit voltage and 4.4 V, respectively, are shown in **Figure 3.5a,b**. Three overlapping signals can be resolved with origins from the ruby reference, Li/carbon additives, and the cathode. The Li/carbon additives have a signal at approximately 350 mT (**Figure 3.5b**), which display a Dysonian lineshape due to skin depth effects.¹²⁸ The evolution of the Li EPR signal line shape with cycling has been used to differentiate between Li microstructures that form.⁶⁴ We focus on the cathode signal that spans

from approximately 100 mT to 590 mT and use the ruby signals at 200 mT, 250 mT, and 520 mT to normalize intensity between spectra. Spectral fits on the cathode signal are performed to extract g-factor, intensity, and linewidth.

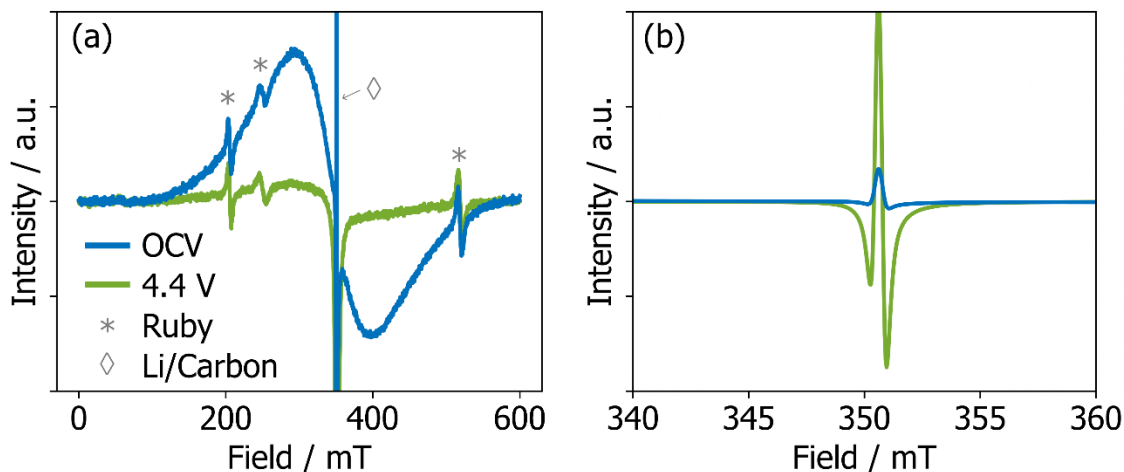


Figure 3.5. Selected spectral slices from operando EPR. (a) X-band spectra at open circuit voltage and at the end of charge (4.4 V). Signals from the ruby (*) and Li/carbon (◇) overlap the broad signal from the cathode. (b) zoomed in view of the Li/carbon signal

The voltage profile and spectral fit parameters for *operando* EPR are plotted in **Figures 3.4c-f**. The starting g-factor of 2.05 for LNMO is consistent with previously reported values for Mn^{4+} in lithium transition metal oxides.^{41,129} The g-factor shows an initial increase to approximately 2.1 before large fluctuations are observed (**Figure 3.4d**). A larger deviation from the g-factor of a free electron implies larger spin-orbit coupling interactions as LNMO is charged. The integrated intensity of the EPR signal decreases linearly until approximately $x = 0.7$ at which point the intensity remains around 11% of the initial intensity for the remainder of the charge process (**Figure 3.4e**). The loss of intensity is consistent with the decreasing magnetization observed in *operando* magnetometry. The number of unpaired electron spins in the system are decreasing during the charge process due to oxidation of Ni.

Three regions with similar positions to those observed in *operando* magnetometry are also evident in the EPR linewidth evolution of LNMO upon charge (**Figure 3.4f**). Here linewidth changes are interpreted due to changes in exchange-narrowing and dipolar interactions.^{51,130} An initial signal broadening occurs in region (I) and is consistent with the loss of 180° Ni_M-O-Ni_{Li} interactions. As previously mentioned, 180° superexchange interactions are strongest magnetic interactions in layered compounds and will have a more significant contribution to the linewidth than dipolar interactions. A loss of these superexchange interactions would expectedly lead to a decrease in exchange-narrowing and hence signal broadening. In the subsequent region (II), signal narrowing is observed and is likely due to decreasing dipolar interactions as LNMO becomes more diamagnetic from oxidation Ni²⁺ to Ni³⁺ and eventually Ni⁴⁺. The dipolar fields generated by each species in LNMO will be weaker and thus lead to less dipolar broadening. Finally, in region (III), the signal linewidth broadens again until the end of the charge process. Superexchange interactions are not possible between diamagnetic species such as Ni⁴⁺, which grows in concentration at region (III). As such, the extent of exchange narrowing decreases during this charge process and results in linewidth broadening.

In this section, we demonstrate the tandem use of *operando* magnetometry and EPR on LiNi_{0.5}Mn_{0.5}O₂. The magnetic and electrochemical properties of LNMO are largely influenced by the Ni/Li antisite defects present in the as-synthesized materials. The changes in magnetization and EPR signals both corroborate the initial oxidation of Ni that are 180° from Ni_{Li} defects, which results in a fast demagnetization rate and loss of exchange-narrowing interactions. The remaining Ni²⁺ in the transition metal layer are then oxidized to Ni³⁺, which leads to weakened dipolar fields and a gradual demagnetization rate. Finally, Ni³⁺ is oxidized to Ni⁴⁺, which leads to a lower rate of demagnetization as expected from the differences in

S(S+1) of Ni^{2+/3} and Ni^{3+/4+} and in EPR signal broadening from the absence of exchange-narrowing with Ni⁴⁺. This mechanism is corroborated by two independent measurements and highlights the capabilities of dual *operando* EPR and magnetometry in data interpretation.

3.5 Conclusions

In this work, *operando* cells are developed to study battery systems with EPR and magnetometry. Both techniques provide complementary information and can be used in conjunction to aid with data interpretation. Low background cells were developed with high fidelity electrochemistry by applying homogenous pressure and contact between cell components. The Magnetometry cell utilizes a clamping mechanism, which requires mechanically robust and diamagnetic materials such as PEEK to apply sufficient pressure. The EPR cell was modeled after a Swagelok cell, which uses springs to apply uniaxial pressure to the battery stack. The geometry of the EPR cell results in problematic non-resonate microwave absorption through interactions between the electrolyte and electric field. This issue is overcome for traditional Li-ion cells that rely on carbonate based liquid electrolytes by reducing the ethylene carbonate content in the mixture. The EPR cell could be used for ceramic based solid-state batteries, which overcome the absorption issue due to the rigid structure that prevents microwave dielectric loss from molecular motion. We demonstrate the tandem use of *operando* EPR and magnetometry on LiNi_{0.5}Mn_{0.5}O₂ (LNMO). Ni/Li antisite defects (y in [Li_{1-y}Ni_y]_{3a}[Li_yNi_{0.5-y}Mn_{0.5}]_{3b}O₂) were quantified in the as-synthesized material to be approximately 0.11. The antisite defect is found to influence the first charge process in LNMO and Ni ions that are 180° from the defect Ni in the Li layer are the first to be oxidized. This finding is corroborated by both the higher rate of demagnetization and EPR linewidth broadening. Successive oxidation of the remaining Ni²⁺ to Ni³⁺ and then partial oxidation of all Ni³⁺ to Ni⁴⁺

is consistent with the magnetization changes and linewidth evolution. These *operando* tools allow us to identify the redox processes occurring during cycling as well as pinpoint the exact voltage at which each process occurs and enable detailed insights into the reaction mechanisms of battery electrodes. While only room temperature galvanostatic cycling experiments were utilized in this work, we expect other electrochemical techniques such as galvanostatic intermittent titration techniques, cyclic voltammetry, or variable rate cycling to be applicable and can provide kinetic information into the processes occurring. Variable temperature experiments can also provide more insights into the magnetic properties of electrodes such as Curie-Weiss temperatures. However, the applicable temperature range is limited due to the constraints of *operando* cycling and will be system dependent.

Chapter 4. Twin Boundaries

Contribute to the First Cycle

Irreversibility of LiNiO_2^3

Abstract. LiNiO_2 remains a target for layered oxide Li-ion cathode development as it can theoretically deliver the highest energy density of this materials class. In practice, LiNiO_2 suffers from poor capacity retention due to electrochemically induced structural changes. While the impact of Ni off-stoichiometry on the electrochemical performance has been extensively studied, that of planar defects present in the as-synthesized cathode is not well understood. Using advanced *ex situ* and *operando* structure probes, we identify and quantify point and planar defects present in as-synthesized $\text{Li}_{1-y}\text{Ni}_{1+y}\text{O}_2$ cathodes and monitor their evolution during the first cycle. Specifically, we identify a ^7Li ssNMR signature characteristic of Li environments near twin boundaries; an assignment supported by first-principles calculations and STEM images of twin boundary defects. Our ssNMR results suggest that the concentration of twin boundaries depends on the amount of Ni excess y . Moreover, *operando* magnetometry and *ex situ* synchrotron X-ray diffraction and ssNMR demonstrate that these planar defects impede Li reinsertion into the bulk cathode at reasonable discharge rates and contribute to the first cycle irreversible capacity. These findings provide design rules for Li_1 .

³ The contents of chapter 4 and its corresponding appendix section is in collaboration with BASF SE and Prof. Matteo Bianchini at the University of Bayreuth and is reproduced from a publication from Wiley-VCH GmbH: <https://doi.org/10.1002/adfm.202306168>

$y\text{Ni}_{1+y}\text{O}_2$ cathodes, whereby minimal twin boundaries in the pristine material reduces kinetically limited Li reinsertion sites and improves capacity retention.

4.1. Introduction

As the specific capacities of long commercialized layered lithium transition metal oxide cathodes (LiMO_2), such as LiCoO_2 (LCO) and $\text{LiNi}_{1/3}\text{Co}_{1/3}\text{Mn}_{1/3}\text{O}_2$, approach their theoretical limit, new cathode materials must be developed to meet the ever-increasing demand for high energy density batteries for portable electronics and electric vehicles. Compositional tuning of layered oxide cathodes offers a promising avenue for short-term gains in energy density, while also providing opportunities to reduce the reliance on cobalt due to its problematic supply chain, scarcity, and toxicity.¹³¹ Ni-rich $\text{LiNi}_{1-x-y}\text{Co}_x\text{Mn}_y\text{O}_2$ (or NCM) and $\text{LiNi}_{1-x-y}\text{Co}_x\text{Al}_y\text{O}_2$ (or NCA) compositions (with $0 \leq x + y \leq 0.2$) containing stabilizing but electrochemically inactive elements (e.g. Mn^{4+} and Al^{3+}) constitute the current state-of-the-art.¹³² The LiNiO_2 (LNO) end member has the highest Ni content of the NCM and NCA compositions, and while it exhibits the largest initial energy density, it suffers from poor cyclability due to structural transformations during charge and discharge^{19,133–139}, high reactivity^{139–141}, and thermal instability^{139,142} in the charged state. Understanding degradation pathways in LNO is an important step towards further increases in Ni content in NCM- and NCA-type compounds.

Over the past few years, several studies have shed light on various bulk and surface structural degradation processes in LNO. Regarding bulk degradation processes, defects in the pristine cathode material have been found to play a key role in the structural evolution^{143,144} and overall performance^{145–147}. In fact, stoichiometric LNO is challenging to synthesize due to the propensity for Ni excess, resulting in $\text{Li}_{1-y}\text{Ni}_{1+y}\text{O}_2$ compounds (typically, $0 < y \leq 0.2$), and Li/Ni antisite mixing as Ni^{3+} is partially reduced to Ni^{2+} .^{139,148} Advances in synthetic control

have led to the now routine synthesis of near-stoichiometric LNO compounds, with off-stoichiometries in the range of 1-1.5% (i.e., $y = 0.015$). The excess Ni^{2+} ions occupy Li sites (Ni_{Li}), with an equal number of Ni^{3+} in the transition metal (M) layers (Ni_M) reduced to Ni^{2+} for charge balance, resulting in a distribution of cations amongst the Li ($3b$) and M ($3a$) sites of the trigonal $R\text{-}3m$ structure: $[\text{Li}_{1-y}\text{Ni}^{2+}_y]_{3b}[\text{Ni}^{3+}_{1-y}\text{Ni}^{2+}_y]_{3a}\text{O}_2$.¹²² The presence of Ni_{Li} defects, even in minute quantities, impacts the electrochemical performance of the material by hindering lithium diffusion within the interlayer space and altering the voltage profile.¹⁴⁵ For example, LNO undergoes several consecutive first order phase transitions on charge ($\text{H1} \rightarrow \text{M} \rightarrow \text{H2} \rightarrow \text{H3}$; noting that all of those phases are O3-type according to the nomenclature system developed by Delmas *et al.*¹⁴⁹), and with increasing Ni_{Li} contents the H2 to H3 phase transition shifts to higher potentials and the Li^+ extraction process at these high potentials becomes more solid solution-like.¹²² Some studies have also suggested that Ni_{Li} defects prevent a complete phase transformation from O3 to O1 during high voltage cycling of LNO, unlike isostructural LCO and NMC cathodes¹⁵⁰⁻¹⁵³. The absence of an O1 phase transition in LNO has been attributed to the pillaring effect of Ni defects initially present in the Li layers, as well as Ni migration into the interslab space in the delithiated state.¹⁵⁴ Instead, O3-O1 stacking faults accumulate in the bulk LNO structure and lead to a loss of Li inventory upon extended cycling.^{134,155,156} Links have been established between the evolution of bulk redox and structural processes with cycling and surface / interfacial degradation. For example, a combined XRD/XAS investigation has evidenced a gradual decay in Ni redox activity concomitant with the loss of the H3 phase at high states of charge.¹³³ The reduced capacity has been attributed to impedance build-up stemming from surface reconstruction and electrode-electrolyte interfacial reactivity at high voltage.^{19,141} Interestingly, some studies have proposed

that Ni_{Li} defects stabilize the particle surface by preventing Ni migration and oxygen release through an anchoring effect driven by the strong interlayer Ni-O-Ni magnetic interactions.^{136,157} Finally, Riewald *et al.* have recently showed that, at small values of y in $\text{Li}_{1-y}\text{Ni}_{1+y}\text{O}_2$ ($0.016 \leq y \leq 0.037$), the primary particle size of LNO plays a key role in both the first cycle irreversible capacity and longer-term cycling stability, in part due to rapid secondary particle fracture during cycling.¹⁵⁸ The authors showed that, while a smaller primary particle size results in greater impedance build-up during high voltage cycling (due to a greater electrode-electrolyte interfacial area), it also reduces the kinetic hindrance associated with Li reinsertion into LNO particles at the end of discharge, both during the first cycle and upon extended cycling, with the latter effect dominating the overall performance of the examined $\text{Li}_{1-y}\text{Ni}_{1+y}\text{O}_2$ /graphite full cells.

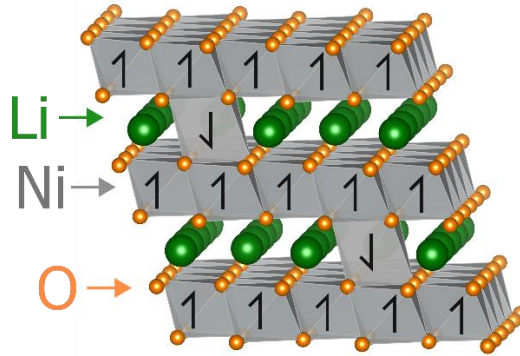


Figure 4.1. Schematic of the layered LNO structure with a Ni_{Li} defect. Alternating layers of Ni (grey) and Li (green) are held together by an O (orange) sublattice. Ni_{Li} induce ferromagnetic alignment between $\text{Ni}_M\text{-Ni}_M$ to form ferrimagnetic clusters.

Building upon those previous studies, the present work investigates the nature of bulk structural defects in near-stoichiometric, as-synthesized LNO cathodes, their evolution during Li extraction/reinsertion, and their contribution to the first cycle irreversible capacity. Structural and redox processes are investigated using combination of *ex situ* high-resolution sXRD, magnetometry, and ^7Li ssNMR, complemented with first principles simulations of

defect energetics and of paramagnetic ssNMR parameters, as well as state-of-the-art *operando* magnetometry. sXRD is used to examine the long-range structure of pristine and cycled LNO samples. The magnetic behavior of $\text{Li}_{1-y}\text{Ni}_{1+y}\text{O}_2$ compounds depends on the local crystal and electronic structure, and as such constitutes a sensitive probe of defects and off-stoichiometry.^{122,125,159} As shown in **Figure 4.1**, Ni_{Li} defects result in strong 180° antiferromagnetic (AFM) $\text{Ni}^{2+}_{\text{Li}}\text{-O-Ni}^{2+/3+}_{\text{M}}$ superexchange interactions between the layers that are not present in the defect-free material. These 180° interlayer interactions are much stronger than the 90° ferromagnetic (FM) $\text{Ni}_{\text{M}}\text{-O-Ni}_{\text{M}}$ superexchange interactions between Ni ions in the transition metal layers. These 180° and 90° Ni-O-Ni superexchange interactions together result in all Ni_{M} magnetic moments within a single layer pointing in the same direction (ferromagnetic alignment), with Ni_{Li} magnetic moments pointing in the opposite direction, leading to net ferrimagnetism (see **Figure 4.1**).¹²⁵ Here, insights into the 3D connectivity of Ni^{2+} and Ni^{3+} ions in LNO obtained from magnetometry are complemented with information about the material's local structure gained from ^7Li ssNMR. The presence of paramagnetic Ni ions results in large ^7Li chemical (Fermi contact) shifts that provide detailed and quantitative information on the distribution of Li local environments in the material, including the oxidation state and spatial arrangement of the neighboring Ni ions. However, through-space dipolar interactions between unpaired Ni *d* electron spins and ^7Li nuclear spins lead to severe broadening of ^7Li ssNMR spectra that scales with the magnetic field strength. Consequently, ^7Li ssNMR spectra reported here were acquired on a custom, ultralow field (100 MHz or 2.35 T) spectrometer equipped with an ultrafast magic angle spinning (MAS) probe (sample spinning at 60 kHz), resulting in the highest resolution ^7Li ssNMR data ever reported on a Li-Ni-O compound.

Importantly, this work sheds light on the impact of twin boundary defects present in as-synthesized LNO cathodes on the Li reintercalation behavior at the end of discharge, most clearly manifested by the first cycle irreversible capacity, and provides new materials design rules for the development of high energy density, Ni-rich layered oxide cathodes. Twin boundaries in LNO can be detected and quantified using ssNMR, as they result in new Li environments and a distinct 450 ppm resonance in the ^7Li ssNMR spectra. The ssNMR spectral assignment is supported by first principles calculations of paramagnetic ssNMR parameters, and further evidence for the presence of twins is obtained from scanning transmission electron microscopy (STEM). These planar defects are present alongside Ni_{Li} defects quantified via sXRD. *Operando* magnetometry and *ex situ* ^7Li ssNMR clearly indicate kinetic limitations associated with Li reinsertion near twin boundaries, contributing to the first cycle irreversibility alongside Ni_{Li} defects and surface/interfacial factors not studied here (e.g., primary particle size¹⁵⁸). Specifically, *operando* magnetometry allows us to quantify the bulk structural contribution to the first cycle irreversibility, as it uniquely isolates bulk redox processes that result in a change in the magnetization of the cathode from electrochemical side reactions that do not contribute magnetically. The fraction of irreversible Li cycled during the initial charge-discharge process is found to be approximately equal to the fraction of Li near twin boundaries in the pristine compound with near stoichiometric composition ($y = 0.015$). Consistent with this result, *ex situ* ssNMR spectra obtained on cycled cathode samples indicate that the 450 ppm ^7Li ssNMR signal associated to twin boundaries is not recovered on discharge, unless a low potential hold is applied. Those findings suggest that twin boundaries in LNO hinder Li reinsertion on discharge and contribute to the significant first-cycle irreversibility observed in this materials class.

4.2. Experimental

Material synthesis. $\text{Li}_{1-y}\text{Ni}_{1+y}\text{O}_2$ active materials were synthesized using a solid-state synthesis route from coprecipitated $\text{Ni}(\text{OH})_2$ precursors (Hunan Zoomwe Zhengyuan Advanced Material Trade Co., Ltd). $\text{LiOH}\cdot\text{H}_2\text{O}$ (Albemarle Corporation) was ground prior to the synthesis and mixed with $\text{Ni}(\text{OH})_2$ in a laboratory blender (Kinematica AG). Li:Ni mol ratio of 0.98, 1.01, and 1.04 were used to synthesize LNO3, LNO2.5, and LNO2, respectively. The mixture was placed in a ceramic crucible and fired in a laboratory box-type furnace (inn High Therm GmbH) under a flowing pure O_2 environment. The mixture was first heated to 400°C and fixed at that temperature for four hours and then the temperature was ramped up to 700°C and held there for six hours. A ramp rate of 3°C was used for both heating steps. Non-LNO phases ($\text{Li}_{0.25}\text{Ni}_{1.75}\text{O}_2$ and $\text{Li}_{0.05}\text{Ni}_{0.95}\text{O}$) were synthesized using a solid-state synthesis. Stoichiometric amounts of NiO (Sigma Aldrich) and Li_2CO_3 (Sigma Aldrich) were ground in a mortar with a pestle for 5 minutes and pressed into a pellet. An additional 10 mol% of Li was needed to synthesize $\text{Li}_{0.25}\text{Ni}_{1.75}\text{O}_2$. The pressed pellet was placed in an alumina crucible and heated to 800°C at a rate of 5°C min^{-1} and soaked at 800°C for 24 hours in air. The sample was slow cooled in the furnace at a rate of 1°C min^{-1} .

Electrochemistry. Free standing electrodes were fabricated from the cathode active material, carbon black (Super C65; MTI Corporation), and polytetrafluoroethylene (PTFE; Sigma Aldrich) in a 94:3:3 ratio. Electrodes of 40 - 60 μm thickness (approx. 11 – 15 mg cm^{-2}) were punched from the electrode film and assembled into Swagelok cells with Whatman GF/D glass microfiber separators, 1 M LiPF_6 in ethylene carbonate, dimethylcarbonate, and diethylcarbonate (EC/DMC/DEC = 1/1/1 v/v/v) electrolyte and a Li metal anode. All cells were cycled on an Arbin BT2000 or Bio-logic VMP-3e potentiostat at a rate of 20 mA/g (or

C/10) unless stated otherwise. *Ex situ* samples were prepared by cycling to the target conditions and cells were disassembled inside an Ar filled glovebox. Cycled cathodes were washed with DMC and dried under vacuum for 30 minutes.

X-ray diffraction. Samples were packed and sealed in glass capillaries to minimize exposure to air. High-resolution sXRD patterns were collected on Beamline 11-BM at the Advanced Photon Source (APS) at Argonne National Laboratory using an average wavelength of 0.46 Å. All patterns were collected in Debye–Scherrer geometry from 0.5° to 50° 2 θ at room temperature with data points collected every 0.001° 2 θ and a scan speed of 0.01°/s. Rietveld Refinements were done with TOPAS software suite.¹¹⁵ Pseudo-Voigt peak shapes were used with parameters set by the 11-bm instrument resolution file. In a typical refinement, an initial LeBail fit was first carried out to refine the background with a Chebyshev polynomial (10 terms), axial divergence, crystallite size, microstrain, zero shift, absorption, and lattice parameters. These values were fixed in a following Rietveld refinement to obtain oxygen z-coordinate and Ni_{Li} occupancies. Debye-Waller factors were initially set to published values from Li_{0.98}Ni_{1.02}O₂ (ICSD collection code 14676), which was then refined after oxygen z-coordinate and Ni_{Li} occupancies. All parameters were refined simultaneously in a last step. In Rietveld refinements of cycled LNO2 cathodes, the total Ni content was constrained to be equal to the as-synthesized value (1.015) and Li occupancies were set based on the capacity of the cycled cell. Stephens peak shapes were used to model anisotropic broadening effects in samples obtained from cycled cells.¹⁶⁰

Solid-state nuclear magnetic resonance. Solid state ⁷Li ssNMR measurements were done on a wide bore Bruker BioSpin spectrometer with a DMX 500 MHz console and a home built 1.3 single X-broadband magic angle spinning (MAS) probe. All spectra were acquired at $B_0 =$

2.35 T (100 MHz for ^1H) with 60 kHz MAS using dry nitrogen and the probe was tuned to ^7Li (38.9 MHz). Samples were packed into 1.3 mm zirconia rotors inside an Ar glovebox and closed with Vespel caps. ^7Li chemical shifts were referenced to 0 ppm with 1 M aqueous LiCl solutions. All acquisitions were done with a rotor synchronized spin-echo sequence with a 90° pulse of 0.45 μs . A recycle delay of 50 ms was sufficient for paramagnetic signals to be fully relaxed and a delay of 10 s was needed to fully relax diamagnetic signals. ssNMR data was processed using Bruker TopSpin 3.6.5 and spectral fits were done with DMfit.¹¹⁶ ssNMR quantifications were T2 corrected.

Computational methods. Structures for the ideal (LiNiO_2), off stoichiometric ($\text{Li}_{0.98}\text{Ni}_{1.02}\text{O}_2$), stoichiometric (LiNiO_2) twin boundary model, and stoichiometric (LiNiO_2) antiphase boundary model, based on the zig-zag Jahn-Teller distorted $P2_1/c$ unit cell of LNO⁹¹, were optimized (atomic positions and cell parameters) using the Vienna *ab initio* Simulation package (VASP)^{161–163}. For this, projector augmented wave (PAW) pseudopotentials were used, as well as the strongly constrained and appropriately normed (SCAN) meta-generalized gradient approximation supplemented with the long-range van der Waals interaction from rVV10, the revised Vydrov–van Voorhis nonlocal correlation functional, which has been proven to perform very well on layered materials¹⁶⁴. All structures were fully relaxed with a cutoff energy of 600 eV and a k-point spacing of 0.25 \AA^{-1} until the forces were lower than 0.01 $\text{eV}\text{\AA}^{-1}$. The optimized cell parameters can be found in **Table S4.3**. LiNiO_2 structural models containing twin and antiphase boundary defects were constructed starting from the rhombohedral $R-3m$ conventional cell and were optimized in a similar way as the regular bulk structures. During relaxation of those defective models, Ni ions spontaneously underwent the expected Jahn-Teller distortion. Spin-unrestricted hybrid density functional theory (DFT) /

Hartree Fock (HF) calculations of paramagnetic ssNMR parameters utilized the CRYSTAL17 all-electron linear combination of atomic orbital code.^{165,166} Two spin-polarized exchange-correlation functionals based upon the B3LYP form,¹⁶⁷⁻¹⁷⁰ and with Fock exchange weights of $F_0 = 20\%$ (B3LYP or H20) and 35% (H35), were chosen for their good performance regarding the prediction of the electronic structure and band gaps of transition metal compounds (B3LYP or H20),^{171,172} and for their accurate description of the magnetic properties of related compounds (H35)¹⁷³⁻¹⁷⁵. All-electron atom-centered basis sets comprising fixed contractions of Gaussian primitive functions were employed throughout. A flexible and extended TSDP-derived $(9s2p)/[5s2p]$ set for Li, an Ahlrichs DZP-derived¹⁷⁶ $(13s9p5d)/[7s5p3d]$ set for Ni, and a modified IGLO-III and $(10s6p2d)/[6s5p2d]$ set for O. Sufficient convergence in total energies and spin densities was obtained by application of integral series truncation thresholds of 10^{-7} , 10^{-7} , 10^{-7} , 10^{-7} , and 10^{-14} for Coulomb overlap and penetration, exchange overlap, and g- and n-series exchange penetration, respectively as defined in the CRYSTAL17 documentation.¹⁶⁶ The final total energies and spin and charge distributions were obtained in the absence of any spin and eigenvalue constraints. ssNMR parameters were obtained on ferromagnetically aligned cells, and on cells where one Ni spin was flipped using a method described by Middlemiss et al.⁸⁷ Anisotropic Monkhorst-Pack reciprocal space meshes¹⁷⁷, with shrinking factors of 2 3 4 for the ideal, 5 3 3 for the off-stoichiometric, 8 4 2 for the twin boundary, and 8 14 1 for the antiphase boundary structural models, were used throughout.

Magnetometry. Samples were loaded into sealed quartz tubes (1 mm ID and 3 mm OD). SiO₂ powder (Advalue Tech) was used to center the cathode samples inside the quartz tubes. Measurements were done on a Quantum Design MPMS3 SQUID magnetometer. Zero field and field cooled M(T) measurements were carried out from 2 K to 350 K with $H = 0.1$ T.

Transmission electron microscopy. As-synthesized LNO₂ was deposited on carbon tape and prepared for TEM measurements with a FEI Helios Dualbeam Nanolab 600 FIB/SEM. Two adjacent particles were coated with a Pt protective layer, cross-sectioned, and attached to a Cu TEM grid. The sectioned particles were milled down to a thickness of ~100 nm using 30 kV Ga-ion down to a thickness of ~1000 nm, followed by 16 kV, 8 kV, and 5 kV down to 100 nm. Further low kV thinning at 2 kV was used for the final milling. Low-magnification and atomic resolution HAADF imaging were collected using the ThermoFisher Spectra 200, a probe aberration corrected (S-CORR) S/TEM equipped with a cold field emission gun (X-CFEG), and an accelerating voltage of 200 kV. For atomic resolution images, a series of 20 frames (each frame is collected for 125 ns) was collected and post-processed into a single image using a drift-corrected frame integration (DCFI) function. Strain maps were generated using a geometric phase analysis (GPA) filter from DIGITAL MICROGRAPH software by GATAN (<https://www.hremresearch.com/gpa/>), and CrysTBox (<https://www.fzu.cz/en/crystbox>). GPA represents a digital signal processing technique that leverages fast Fourier transform algorithms to quantitatively assess displacements and strain fields within crystalline lattices, operating at nanoscale resolutions. This method was initially developed by Hytch et al.^{178–180}

Operando magnetometry. A custom-built cell was made of polyether ether ketone (PEEK), which interfaces to an MPMS3 ETO sample rod. Cu and Al foils were used as current collectors for the anode and cathode, respectively. The cathode was cut to be ~3x4 mm² and cycled against Li metal with Whatman GF/A glass fiber separators and 1 M LiPF₆ in (EC/DMC/DEC = 1/1/1 v/v/v) electrolyte. The *operando* experiment was carried out at a rate of 15 mA/g with a Bio-logic SP200 potentiostat. The magnetic moment was recorded every

minute at a field of 0.5 T and at 300 K in DC scan mode. Background subtraction of the cell with current collectors, anode, separator, gasket, and electrolyte was done following the procedure in MPMS3 application note 1500-023.

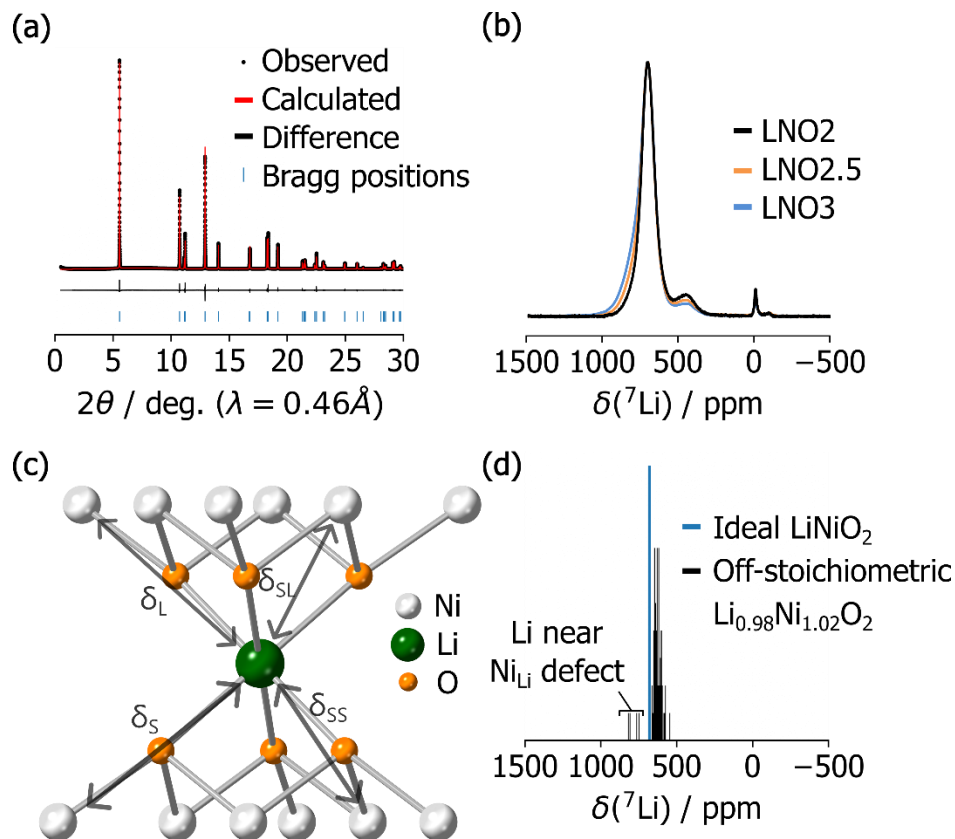


Figure 4.2. (a) Synchrotron XRD pattern of as-synthesized LNO2. Rietveld refinement indicates an $R\text{-}3m$ phase with a Ni_{Li} defect concentration of approximately 2% and no additional crystalline impurities. (b) ${}^7\text{Li}$ ssNMR spectra collected on as-synthesized LNO2, LNO2.5, and LNO3 samples at $B_0 = 2.35$ T and 60 kHz magic angle spinning (MAS) using a spin echo pulse sequence. Spectra are normalized to the most intense signal. (c) Local coordination of Li (green) in the ideal LNO structure, including Ni species (grey) within the first and second coordination shells. Jahn-Teller distortion of Ni^{3+} ions leads to short and long Ni-O bonds, and four unique Li-O-Ni interaction pathways denoted δ_S , δ_L , δ_{SS} , and δ_{SL} . (d) Histogram of the distribution of the ${}^7\text{Li}$ chemical shifts computed from first principles using the CRYSTAL17 code for the ideal LiNiO_2 (blue) structure and for an off-stoichiometric $\text{Li}_{0.98}\text{Ni}_{1.02}\text{O}_2$ (black) structure. For simplicity, the chemical shift values plotted here are those obtained using the HYB20 (20% HF exchange) functional.

4.3. Results and Discussion

4.3.1. Defects in as-synthesized LiNiO₂ samples.

Three LNO compositions were synthesized using a standard co-calcination route outlined in a previous report,¹²² where the degree of off-stoichiometry (y in Li_{1-y}Ni_{1+y}O₂) was controlled by the number of Li equivalents per mol of Ni. Synchrotron X-ray diffraction (sXRD) and lab XRD patterns obtained for the various compositions can be fit using a single $R-3m$ phase with composition Li_{0.9854(6)}Ni_{1.0146(6)}O₂ (LNO2, approximately 2% Ni excess), Li_{0.9754(6)}Ni_{1.0245(6)}O₂ (LNO2.5, approximately 2.5% Ni excess), and Li_{0.9695(6)}Ni_{1.0305(6)}O₂ (LNO3, approximately 3% Ni excess), respectively. A representative sXRD pattern obtained on LNO2 and its Rietveld refinement are shown in **Figure 4.2a**, while additional patterns and refinements obtained on LNO2.5 and LNO3 are shown in **Figure S4.1a** and **Figure S4.1b**, respectively, of the Supporting Information. All Rietveld refinement parameters are listed in **Table S4.1**. The average primary particle size increases from LNO3 to LNO2 (**Figure S4.2**), as expected from the higher Li content used in the synthesis of LNO2 and its ability to act as a flux and induce particle growth.

The trends in Ni-excess determined from the Rietveld refinements are in good agreement with the trend in Curie-Weiss (θ_{CW}) constants of the samples, with the bulk magnetic susceptibility curves obtained on all samples shown in **Figure S4.3**. As has been shown previously, the degree of off-stoichiometry and concentration of Ni_{Li} defects have a significant impact on the θ_{CW} of Li_{1-y}Ni_{1+y}O₂ compounds, which measures the strength of the magnetic exchange interactions in the material.^{122,125,181,182} Here, θ_{CW} equals 36(1) K, 46(1) K, and 55(1) K for LNO2, LNO2.5, and LNO3, and increases with increasing Ni_{Li} defect concentration in the crystal structure. The experimental effective magnetic moments, μ_{eff} , of

LNO2, LNO2.5, and LNO3 are 1.83(1), 1.75(1), and 1.71(1) μ_B , respectively. The spin-only magnetic moments for these samples were calculated using $\mu_{theo} = g\sqrt{S(S+1)}$, where the g-factor was extracted from a fit of their electron paramagnetic resonance (EPR) spectra and was approximately 2.1 for all three samples (**Figure S4.4**), in good agreement with previously reported values.^{40,183} While the observed μ_{eff} for LNO2 is close to its theoretical value of 1.85 μ_B , the measured μ_{eff} for LNO2.5 and LNO3 differ significantly from their theoretical value of 1.87 and 1.89 μ_B . These deviations may arise from the fact that the g-factor derived from low frequency, X-band EPR data corresponds to the Ni^{3+} centers in the material (Ni^{2+} is a non-Kramers ion with a large zero-field splitting that requires much higher excitation frequencies) and may deviate substantially from the average Ni g-factor for the more off-stoichiometric LNO2.5 and LNO3 compositions. Notably, the observed trend of decreasing experimental μ_{eff} with increasing Ni excess is in line with previous reports.¹²²

The local structure of LNO was investigated using 7Li ssNMR, complemented with first principles calculations of paramagnetic ssNMR parameters. The 7Li spin echo spectra acquired on three pristine LNO cathodes at $B_0 = 2.35$ T and 60 kHz magic angle spinning (MAS), shown in **Figure 4.2b**, display three main resonances at approximately 0 ppm, 450 ppm, and 700 ppm, and a minor signal at -90 ppm, consistent with previous reports.^{142,184–186} The sharp 0 ppm signal corresponds to Li in diamagnetic impurity phases (e.g., Li_2CO_3 , Li_2O , and/or $LiOH$ – the 7Li shifts of these three phases are too close to be distinguished here), while the highly shifted signals at -90 , 450, and 700 ppm result from Li in paramagnetic environments, presumably in the LNO phase. Indeed, for compounds containing open-shell transition metal ions, such a LNO, the observed 7Li chemical shift is dominated by the Fermi contact (or paramagnetic) shift that arises from delocalization of unpaired electron spin density

from the transition metal *d* orbitals (here, Ni ions within about 5 Å from the central Li) onto the Li *s* orbitals via bridging oxygen *p* orbitals, and can reach up to 100s or even 1000s of ppm. The major resonance at 700 ppm has previously been attributed to Li in the interlayer space of LNO, while the 450 ppm signal has been tentatively assigned to Li in disordered, cubic rocksalt-type domains^{142,184,187} or Li in the Ni layer with Ni⁴⁺ neighbors^{185,186} (those assignments will be discussed in more detail in the next paragraph). The Li stoichiometry of the LNO phases can be determined from the Ni:Li ratio in the samples obtained from ICP (1:1.02 for LNO2, 1:1.00 for LNO2.5, and 1:1.00 for LNO3), and from the fraction of paramagnetic Li, as obtained from the paramagnetic to diamagnetic ⁷Li ssNMR signal intensity ratio. The Li stoichiometries of LNO2, LNO2.5, and LNO3 determined using this method – Li_{0.985}Ni_{1.015}O₂, Li_{0.980}Ni_{1.020}O₂, and Li_{0.975}Ni_{1.025}O₂, respectively –, agree well with those obtained from sXRD when the –90, 450, and 700 ppm signals are attributed to different types of Li local environments in the *R-3m* LNO phase observed by sXRD. Said differently, this analysis indicates that the –90 and 450 ppm signals correspond to defective Li environments in the LNO phase, rather than to (a) separate paramagnetic phase(s).

To facilitate the assignment of the experimental ssNMR spectra, hybrid density functional theory (DFT)/Hartree Fock (HF) calculations of ⁷Li ssNMR parameters were carried out on various Li-Ni-O structural models using the CRYSTAL17 all-electron *ab initio* linear combination of atomic orbitals software package.^{165,166} Computational parameters, and the methodology used to scale the ⁷Li Fermi contact shifts computed at 0 K to values comparable to the room temperature ssNMR experiments, are described in the Methods section and in **Supplementary Note 4.1**. As noted earlier, the Fermi contact shift of ⁷Li local environments in Li-Ni-O compounds arises from the delocalization of unpaired electron spin density from

the d orbitals on nearby open-shell Ni to the Li nucleus. More specifically, the contribution from each neighboring Ni ion to the overall ${}^7\text{Li}$ chemical shift is additive and depends on the Ni oxidation state (Ni^{2+} and Ni^{3+} have one and two unpaired d electrons, respectively, while Ni^{4+} is diamagnetic and does not contribute to the shift) and the Li-O-Ni interaction pathway geometry.⁸⁷ Due to the Jahn-Teller distortion of Ni^{3+} ions, there are four distinct Li-O-Ni interaction pathways in the ideal LiNiO_2 structure, depicted in **Figure 4.2c**: two $\approx 180^\circ$ Li-O- Ni^{3+} interactions involving either a short (δ_S) or a long (δ_L) Ni-O bond, a double $\approx 90^\circ$ Li-O- Ni^{3+} interaction featuring two short Ni-O bonds (δ_{SS}), and a double $\approx 90^\circ$ Li-O- Ni^{3+} interaction featuring one short and one long Ni-O bond (δ_{SL}). These interactions lead to four unique ${}^7\text{Li}$ shift contributions, with computed values listed in **Table S4.2**, that can then be used to reconstruct the shifts of a range of Li environments. For example, the unique Li environment in the ideal LiNiO_2 structure has four δ_S , two δ_L , two δ_{SS} , and four δ_{SL} interactions, and its predicted chemical shift ($\delta = 2 \times \delta_{SS} + 4 \times \delta_{SL} + 4 \times \delta_S + 2 \times \delta_L$) is in the range of 694 ppm (HYB20) to 543 ppm (HYB35) using the values in **Table S4.2**, confirming our assignment of the ca. 700 ppm resonance observed experimentally to Li in the interlayer of defect-free, stoichiometric domains in the LNO structure. We note that computed shifts are quoted as a range set by two calculations throughout this work, since shifts predicted with hybrid DFT/HF calculations are sensitive to the amount of HF exchange in the hybrid functional, with most experimental values falling within the range of values calculated with 20% (HYB20) and 35% (HYB35) HF exchange.^{87,88,93} The distribution of HYB20 ${}^7\text{Li}$ chemical shifts obtained on an ideal LiNiO_2 structure, and for a 2% Ni excess ($\text{Li}_{0.98}\text{Ni}_{1.02}\text{O}_2$) composition, are plotted as a histogram in **Figure 4.2d**. For each Ni_{Li} defect in $\text{Li}_{0.98}\text{Ni}_{1.02}\text{O}_2$, a Ni_M ion near the defect (along a 180° $\text{Ni}_{\text{Li}}\text{-O-Ni}_M$ interaction pathway) is reduced to 2+ to

maintain charge balance. This results in a broader distribution of Li environments in this material, and additional, overlapping ${}^7\text{Li}$ resonances near 700 ppm (black bars in **Figure 4.2d**), in line with the broadening of the 700 ppm resonance in the spectra collected on LNO2.5 and LNO3 (**Figure 4.2b**). In particular, some of the Li sites near $\text{Ni}^{2+}_M - \text{Ni}_{\text{Li}}$ defects are predicted to exhibit a chemical shift in the 780 – 790 ppm range, consistent with the increased ${}^7\text{Li}$ signal intensity on the left hand side (high frequency tail) of the 700 ppm resonance. The low intensity signal at –90 ppm in all of the spectra obtained on the as-synthesized cathodes (an enlarged view of this signal is provided in **Figure S4.5**) is most likely due to a small amount of Li in the Ni layers (Li_M defects) from Li/Ni antisite disorder in these compounds. This assignment, assisted by the Li-O- Ni^{3+} shift contributions computed on the ideal LiNiO_2 structure (**Table S4.2**), is further discussed in **Supplementary Note 4.2**.

While the CRYSTAL17 calculation results confirm the attribution of the broad 700 ppm resonance to Li in the interlayer space, with few nearby Ni_{Li} defects, and suggest that the weak signal at –90 ppm corresponds to a small amount of Li_M defects in the pristine LNO cathodes, the assignment of the 450 ppm environment remains unclear. As mentioned earlier, complementary insights from sXRD and ICP into the phase composition of the as-synthesized LNO2, LNO2.5, and LNO3 samples, and the Li stoichiometry of the $R-3m$ phase, strongly suggest that the 450 ppm signal corresponds to Li close to a structural defect in the $R-3m$ phase. For completeness, we also consider other Li-containing paramagnetic phases that have been proposed to form at the surface of LNO particles, such as a cubic (NiO-like) $\text{Li}_y\text{Ni}_{1-y}\text{O}$ phase¹⁸⁴ ($y < 0.3$), or a Ni-rich $\text{Li}_y\text{Ni}_{0.25}\text{NiO}_2$ or $\text{Li}_y\text{Ni}_{0.5}\text{NiO}_2$ ($y \leq 0.75$) layered phase¹³⁸. As discussed in more detail in **Supplementary Note 4.3**, we find that the ${}^7\text{Li}$ ssNMR signals from such phases do not agree with the observed 450 ppm resonance, allowing us to discard those options

and focus on identifying possible Li defective sites in the $R-3m$ phase. Since the presence of oxidized Ni species (diamagnetic Ni^{4+}) in LNO reduces the chemical shift of nearby ^7Li species relative to the baseline 700 ppm shift, it may be tempting to assign the 450 ppm signal to interlayer Li near oxidized Ni_M defects. However, such defects either require a commensurate amount of Li vacancies in the interlayer space, or Li_M defects, both of which are inconsistent with the following observations. First, the Li stoichiometry and lattice parameters obtained for the $R-3m$ phase from ICP, ssNMR, and sXRD on the three as-synthesized samples do not support the presence of Li vacancies in the interlayer space. Second, there are too few Li_M defects (based on the very weak -90 ppm resonance) to account for the relatively high fraction of Li in defective 450 ppm environments. Third, we would expect ^7Li nuclei nearby oxidized Ni_M defects to be less paramagnetic than ^7Li nuclei in defect-free, stoichiometric LiNiO_2 , and therefore to have a longer ^7Li ssNMR signal lifetime than the 700 ppm resonance, instead, we find that the 450 ppm and 700 ppm relax on very similar timescales. Interestingly, the intensity of the 450 ppm signal decreases with increasing Ni excess in the $R-3m$ phase (**Table S4.1**), accounting for 11%, 7%, and 5% of the total paramagnetic Li signal in the spectra collected on the LNO2, LNO2.5, and LNO3 samples, respectively, as shown in **Figure 4.2c**. That is, the propensity to form Li environments resonating at 450 ppm is inversely correlated to the presence of Ni_{Li} defects.

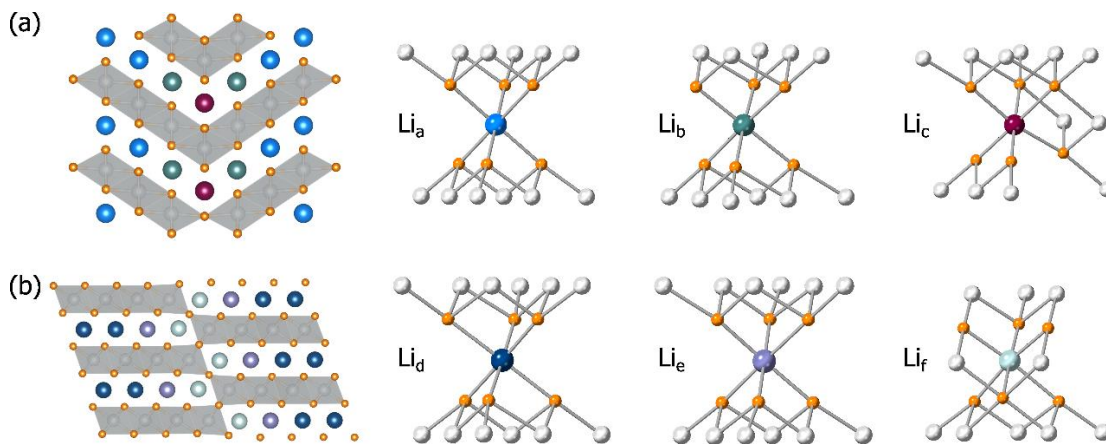


Figure 4.3. Schematic of planar defects in LNO and unique Li local environments for (a) a twin boundary, and for (b) an antiphase boundary, showing Li (various colors), Ni (grey) and O (orange) atoms. Li_a , Li_c , Li_d , and Li_e have similar bonding environments as Li in the ideal (defect-free and stoichiometric) LiNiO_2 structure, but local structure relaxation around the planar defects leads to varying Li-O-Ni coordination pathway geometries. Li_b and Li_f environments do not exist in ideal LNO and arise from the removal of select Li-O-Ni interactions due to the presence of planar defects. Schematics of the Li environments were prepared using the VESTA¹⁸⁸ and CRYSTAL maker software packages.

We next investigate the possibility of forming planar defects in the as-synthesized $R\text{-}3m$ phase. Planar defects, including twin boundaries and antiphase boundaries, have been observed in related Ni-rich NMCs and their density has been found to increase upon extended cycling,¹⁸⁹ eventually inducing a layered to rock salt phase transformation^{143,144} at the grain boundaries. Over the past few years, a growing number of studies have shown that ssNMR is a sensitive probe of planar defects in battery materials^{190–195}, including several layered oxide cathodes such as Li_2MnO_3 ^{190,193,195}, $\text{Li}[\text{Li}_{(1-2x)/3}\text{Ni}_x\text{Mn}_{2/3-x/3}]\text{O}_2$ ¹⁹⁴, NaMnO_2 ¹⁹². Indeed, ssNMR presents several advantages compared to more standard probes of planar defects, including transmission electron microscopy (TEM) and diffraction techniques. For example, unlike TEM, ssNMR is a low energy, non-invasive technique that probes all local environments impacted by the defects at once, irrespective of their position (bulk vs. surface regions of the particles) and orientation in single and poly-crystalline samples. Moreover, since planar defects generally introduce new coordination environments, entirely new ssNMR signals that are well separated from the resonant signals of the parent (ordered) compound typically arise and can

easily be quantified through signal integration. To identify possible ${}^7\text{Li}$ ssNMR signatures of planar defects in LNO, structural models of LiNiO_2 with a three dimensional periodic twin boundary or antiphase boundary were developed (see **Figure S4.9**). Given the computational cost of paramagnetic ssNMR calculations, the supercells were kept relatively small (160 atoms for the twin boundary model, and 48 atoms for the antiphase boundary model), with 3 and 4 Li sites on either side of the twin and antiphase boundary, respectively. Based on those models, a total of six different Li local environments were identified in the vicinity of the twin and antiphase boundaries (hereafter referred to as $\text{Li}_a - \text{Li}_f$), that are illustrated in **Figure 4.3**. While Li species that are at or two Li sites away from the twin boundary (Li_a and Li_c) have the same number of 90° and 180° Ni^{3+} -O-Li interactions as Li in ideal LiNiO_2 , slight changes in the Li-O-Ni bond lengths/angles due to the build up of strain near the planar defect are expected to affect the δ_s , δ_L , δ_{SS} , and δ_{SL} Fermi contact shift contributions. Li near (*i.e.*, one Li site away from) a twin boundary (Li_b) have one fewer 180° Li-O-Ni interaction as compared to the Li environment in the ideal LNO structure. The paramagnetic Ni^{3+} at 180° is replaced by a diamagnetic Li^+ , effectively switching off the corresponding Fermi contact shift contribution and reducing the chemical shift of Li_b . Li species that are one or two Li sites away from an antiphase boundary (Li_d and Li_e) have the same number of 90° and 180° Ni^{3+} -O-Li interactions as Li in ideal LiNiO_2 . A change in coordination is observed for Li at an antiphase boundary (Li_f), where three of the 180° Li-O-Ni interactions present for Li in ideal LiNiO_2 are switched off (replaced by Li-O-Li interactions). The predicted shifts for the six Li environments in the antiphase and twin boundary structures are summarized in **Table 4.1**. In the case of the antiphase boundary model, calculated shifts for Li_d and Li_f environments are in the range of 542 – 690 ppm and 484 – 590 ppm, respectively, close to the resonances observed

experimentally. Li_e , on the other hand, is predicted to have a chemical shift in the range of 794 – 954 ppm, and a signal intensity on par with that of Li_f since those two environments are present in a 1:1 ratio in the vicinity of the planar defects. Since no signal is observed in this region of the spectrum, we conclude that the concentration of antiphase boundaries in as-synthesized LNO2, LNO2.5, and LNO3 is below the ssNMR detection limit. In the case of the twin boundary model, calculated shifts for Li_a and Li_c are very similar and in the range 352 – 486 ppm and 342 – 477 ppm, respectively, in good agreement with the experimentally-observed 450 ppm signal. Notably, despite their similar coordination environments, Li_a and Li_c exhibit much lower chemical shifts than Li in ideal LiNiO_2 , likely due to the longer average Ni-O and Li-O bond lengths of 1.98 Å and 2.12 Å around Li_a and Li_c , as compared to bond lengths of 1.96 Å and 2.09 Å in defect-free LiNiO_2 , resulting in reduced orbital overlap and electron delocalization onto the Li *s* orbitals. The Li_b shift is predicted to lie in the 196 to 235 ppm range, and the intensity of this signal is expected to be significantly lower than that of the overlapping Li_a and Li_c resonances at ≈ 450 ppm. Consistent with this, a low intensity signal is observed in the baseline of the ^7Li ssNMR spectrum for LNO2, centered at ≈ 200 ppm (an enlarged view of this spectrum is shown in **Figure S4.10**). Overall, the ^7Li ssNMR spectra collected on the as-synthesized LNO cathodes, combined with *ab initio* predicted ^7Li chemical shifts on structures containing planar defects commonly observed in Ni-rich cathodes, provide strong evidence for the presence of twin boundaries in pristine LNO; conversely, no antiphase boundaries are detected.

Table 4.1. Predicted ^7Li ssNMR shifts for the six Li environments identified near planar defects in the two model structures containing periodic twin boundaries and antiphase boundaries.

		Total chemical shift (ppm)		
		Away from boundary	Near boundary	At boundary
Twin		Li_a : 352 to 486	Li_b : 196 to 235	Li_c : 342 to 477

Antiphase

Li_d: 542 to 690

Li_e: 794 to 954

Li_f: 484 to 590

To visualize twin boundaries in a representative LNO sample, a TEM lift out, approximately 100 nm in thickness, was extracted from the as-synthesized secondary particle of LNO₂ using a focused ion beam (FIB) and observed under a probe-corrected (scanning) transmission electron microscope ((S)TEM). Representative images of primary particles are shown in **Figure 4.4a**, and clearly indicate the presence of twin boundaries, evidenced as a change in contrast or resolution due to misalignment of a part of the grain and by selected area electron diffraction data (**Figure S4.11**). To assess the local structural distortions induced by the twin boundary, atomic-resolution STEM images were collected at the boundary, and a representative image is shown in **Figure 4.4b**, with its corresponding strain maps in **Figure 4.4c**. In **Figure 4b**, one twin is oriented along the [100] zone axis, and the other twin is slightly off-axis, leading to blurred atomic columns. A schematic of the orientation of the twin boundary and electron beam is shown in **Figure S4.12a**. Regions with intensity in the interlayer spacing are domains of rock salt NiO, which may have formed during sample preparation (air exposure for a few seconds) or analysis (potential beam damage). Focusing on the layered regions, intralayer Ni-Ni distances and interlayer spacings in the bulk and near the boundary were measured. The average interlayer spacing measured over the six layers closest to the twin boundary is 4.87 Å, which is larger than the average bulk d-spacing of 4.76 Å (the latter is consistent with the d-spacing determined from sXRD of 4.73 Å). We note that three of the six layers included in the measurement of the average interlayer spacing close to the twin boundary are part of the off-axis twin. To ensure that the misalignment of this twin does not affect the accuracy of the measurement, we measured the interlayer spacing in the bulk of the misaligned twin and found an average d-spacing of 4.78 Å. The similar bulk d-spacings for

both the aligned and off-axis twins suggests that the twin misalignment does not affect the d-spacing measurement significantly. The strain maps shown in **Figure 4.4c** indicate substantial strain variation within the twin boundary domains, extending up to 2.8 nm across the interface, which is equivalent to about 3 Li layers on either side of the twin plane. The structural distortion near the twin boundary (and over multiple layers) observed with STEM and strain mapping is consistent with the *ab initio* relaxed structure for the twin boundary model discussed earlier, and in particular with the longer Ni-O and Li-O bond lengths observed near the planar defect. Hence, STEM analysis confirms that none of the three Li environments identified near the twin boundary in the model structure used for the ssNMR calculations (including the ‘distant’ Li_a site in **Figure 4.3a**) are comparable to the Li environment in defect-free, stoichiometric LiNiO₂, and lend credence to the assignment of the 450 ppm signal to Li_a and Li_c local environments.

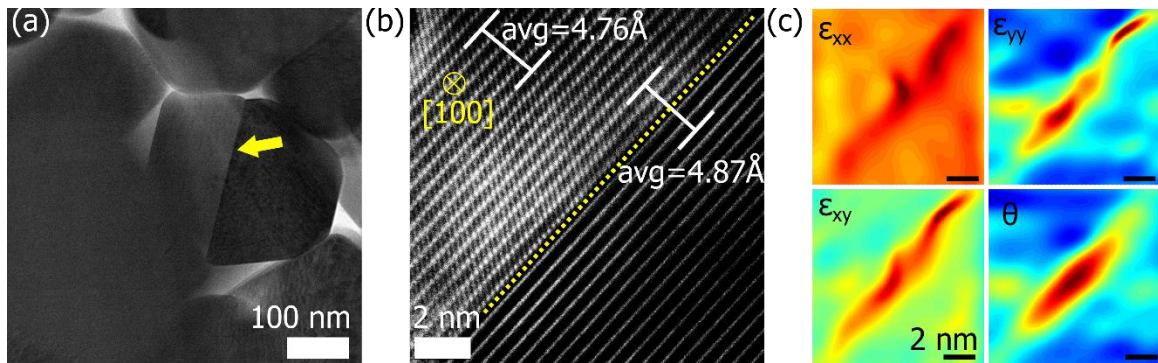


Figure 4.4. High resolution STEM images obtained on as-synthesized LNO₂. (a) Bright field STEM image of a twin boundary in a primary particle of LNO₂. The location of the twin boundary is indicated with a yellow arrow. (b) Atomic-resolution image of the twin boundary. The twin above the yellow line is oriented along the [100] zone axis and the twin below is misaligned, which leads to blurred atomic columns. d-spacings were averaged over six layers. (c) Strain maps, generated through post-processing of the atomic-resolution image in (b), encompass various strain components: compressive/tensile strains along the X (ϵ_{xx}) and Y (ϵ_{yy}) directions, shear strain (ϵ_{xy}), and lattice rotation (θ). To conduct the strain analysis, the averaged FFT is used as a 'reference lattice' to assess deviations in the diffraction spots. These maps illustrate substantial strain variation within the twin domain, extending up to 2.8 nm across the interface.

While twins were observed in a number of particles by TEM (additional images of other twins identified during data collection are included in **Figures S4.11** and **Figure S4.12**), the size and number of planar defects cannot be quantified with this technique, as this would require a different beam condition for each twin boundary in the sample. In contrast, if a ssNMR signature of the planar defects can be identified, and the number of local environments affected by the defect (size of the strained domains) can be determined, quantification of those planar defects becomes possible. For LNO, the 450 ppm ${}^7\text{Li}$ ssNMR signal corresponds to Li sites in the vicinity of a twin boundary and can be used as a signature of those defects. Given that this 450 ppm signal has been reported in prior work^{142,184,187}, twin boundaries are clearly a general phenomenon in pristine LNO cathodes. As we showed earlier, the twin boundary leads to the build up of strain across a domain extending out to 3 Li layers on either side of the twin plane; that is, for each Li_c atom along the plane, 4 Li_a environments are created, providing us with a scaling factor (of 5) to compute the concentration of twins from the fraction of Li resonating at 450 ppm. Using this method, we find that the more stoichiometric LNO2 compound is also the one with the largest concentration of twin boundaries ($\approx 2.2\%$), followed by LNO2.5 ($\approx 1.4\%$), followed by LNO3 ($\approx 1\%$). This trend can be rationalized by considering the structural distortions necessary to form twin boundaries: the larger the Ni off-stoichiometry in LNO, the more Ni_{Li} defects and Ni^{2+} ions in the Ni layers, making local distortions and twin boundaries less favorable (Ni^{2+} ions have a stronger preference for perfectly octahedral sites as compared to Jahn-Teller distorted Ni^{3+} ions). The formation energies of twin and antiphase boundaries were computed using the VASP software package on the same LNO supercells as those used earlier for the ssNMR calculations (depicted in **Figure S4.9**). We find that the formation energy of a twin boundary is about $7 \text{ meV}/\text{\AA}^2$, calculated with respect to the zig-zag

Jahn-Teller-distorted ground state. In practical terms, this energy is comparable to an O3-O1 stacking fault at low (< 25%) Li content, when the faulting probability is non-negligible.²⁷ In contrast, the formation energy of an antiphase boundary is significantly higher, about 29 meV/Å², which may explain why only twins are observed experimentally. Our twin boundary models were constructed from the highly symmetric, undistorted rhombohedral unit cell (see computational details), and during relaxation, Ni underwent the expected Jahn-Teller distortion, but settled in a collinear ordering probably due to the cell periodicity. Finding the optimal Jahn-Teller ordering around the planar defect is beyond the scope of this study, but it is possible that the calculated formation energy will decrease when Jahn-Teller distortions are allowed to comply with the strain field induced by the twin boundary,²⁷ further increasing its chances to form. Considering that our model is also relatively narrow and most likely suffers from artificial interactions between periodic images, the value of 7 meV/Å² is an upper limit for the formation energy. Our results are in line with a recent TEM study reporting twin boundaries in pristine LNO.¹⁹⁶ Importantly, our work provides the first bulk method (⁷Li ssNMR) to quantify the relative amount of twin boundaries in different LNO samples, and sheds light on the links between LNO composition and twin boundary formation. Besides low amounts of Ni_{Li} defects, it is expected that doping LNO with metals that can accommodate octahedral site distortions will facilitate the formation of twin boundaries in the as-prepared cathode. In fact, twin boundaries were first observed via TEM in as-synthesized LNO doped with Zr⁴⁺, Li⁺, and Mo⁶⁺.^{197,198} The concentration of both twin and antiphase boundaries in as-synthesized LNO-type cathodes is also likely related to the preparation method, as noted by Mu et al.¹⁹⁶ and Pokle et al.¹⁹⁹

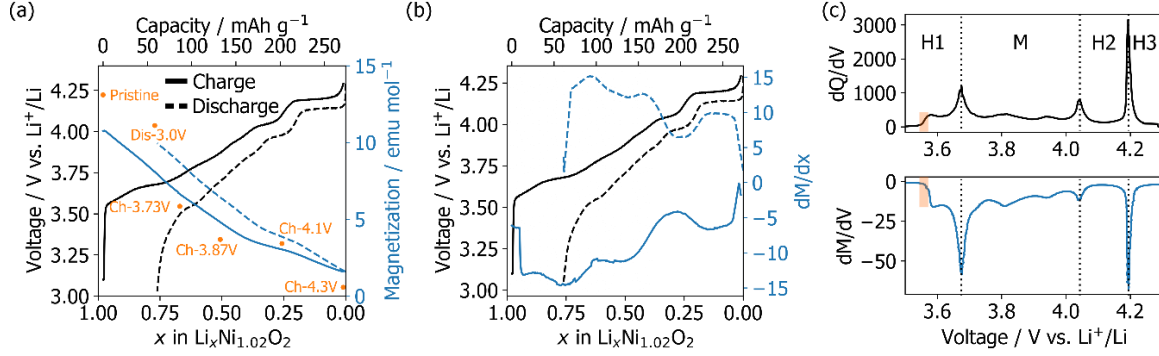


Figure 4.5. *Operando* magnetometry measurement on the first charge (–) and discharge (–) cycle for LNO₂ at 300 K, at a field of 0.5 T, and at a cycling rate of $\approx C/13$. (a) The voltage profile in black and corresponding magnetization (M) in blue after background subtraction. *Ex situ* magnetization at 300K for different states of charge (Ch) and discharge (Dis) are plotted in orange. (b) The rate of change of M as a function of Li content, dM/dx (emu mol⁻¹ Li⁻¹). (c) Differential capacity, dQ/dV (mAh g⁻¹ V⁻¹), and differential magnetization, dM/dV (emu mol⁻¹ V⁻¹) during the first charge process. The highlighted region corresponds to 3.5 V to 3.55 V, where there is a rise in dQ/dV without a corresponding rise in dM/dV . Profiles for dQ/dV , dM/dV , and dM/dx were smoothed with a moving average.

4.3.2. Impact of twin boundaries on the first cycle irreversible capacity of LiNiO₂.

Having established the composition, structure, and defect landscape in pristine Li_{1-y}Ni_{1+y}O₂ cathodes, we focus hereafter on the more stoichiometric composition (LNO₂) and investigate reaction mechanisms and irreversibilities during the first charge-discharge cycle. As mentioned earlier, the sensitivity of the magnetic interaction network to Ni_{Li} defects, to the Ni oxidation state, and to the local and long-range structure, makes electron spin characterization tools, such as magnetometry and EPR, ideal probes of the electrochemical processes in LNO.²⁰⁰ *Operando* EPR was attempted on LNO₂, but the combination of low signal intensity from the majority Ni³⁺ species in LNO, and sensitivity losses due to the presence of microwave-absorbing components in the *operando* electrochemical cell (e.g., high dielectric electrolyte) prevented us from detecting the cathode signal at room temperature (see **Figure S4.13**). Thus, we turned to *operando* magnetometry to track bulk redox and structural changes during the first cycle. Magnetization (M) values obtained on *ex situ* cathode samples stopped at various stages of charge and discharge (orange data points in **Figure 4.5a**) and from the

operando measurement (blue curve in **Figure 4.5a**) agree well, with slight discrepancies likely due to the imperfect background subtraction of signals arising from other components of the *operando* cell. A detailed analysis of the *operando* magnetometry results would require first principles calculations of the magnetic properties of LNO as a function of charge, which is beyond the scope of this study. Suffice is to say that the bulk magnetization (M) measured *operando* is an average property that depends on the magnetic couplings between neighboring Ni moments, which in turn depend on the oxidation state of the interacting Ni ions. Hence, qualitative insights into redox and structural processes can be drawn from an analysis of the dM/dx curves obtained on charge and discharge and plotted as a function of Li content in LNO2 in **Figure 4.5b**.

At room temperature, LNO is in the paramagnetic regime and M can be described by the Curie-Weiss equation (equation 1.1). M depends on the average Ni magnetic moment and is expected to decrease upon oxidation of Ni^{3+} ($S = 1/2$) to Ni^{4+} ($S = 0$) during charge, and to increase upon reduction of Ni^{4+} back to Ni^{3+} on discharge. We indeed find $\frac{dM}{dx}$ to be negative during the charge process, and positive during the discharge process. Interestingly, the abrupt downturn in $\frac{dM}{dx}$ at about $x = 0.25$ on charge coincides with the H2 to H3 transition and to the onset of the c lattice parameter collapse in LNO.^{156,201} The downturn indicates a more rapidly decreasing magnetization upon Li extraction at that point in charge, which is presumably related to a change in the $180^\circ \text{Ni}_{\text{Li}}\text{-O-Ni}_M$ superexchange interactions and to θ_{cw} as the interlayer distance collapses. Curie-Weiss fits of the magnetic susceptibility curves obtained for *ex situ* cathode samples within the H2 (4.1V cutoff) and H3 (4.3V cutoff) phase stability regions are shown in **Figure S4.14** and indicate an increase in θ_{cw} from 31(1) K to 47(3) K over the H2 to H3 transition region. Significant changes in the $180^\circ \text{Ni}_{\text{Li}}\text{-O-Ni}_M$ superexchange

interactions over this voltage range suggest that Ni species involved in the Ni_{Li}-O-Ni_M chains have not yet been oxidized to the 4+ oxidation state at x = 0.25, which may suggest that the strong 180° magnetic couplings stabilize lower Ni oxidation states. On subsequent discharge, M and $\frac{dM}{dx}$ evolve in a reverse manner as compared to the charge process, but the magnetization never reaches its initial value in the pristine state.

A comparison of the differential capacity (dQ/dV) and differential magnetization (dM/dV) from the *operando* dataset, plotted as a function of potential (V) for the first charge process in **Figure 4.5c**, highlights the interconnection between redox processes and magnetic properties in LNO, and more generally in cathode materials. Similar dQ/dV and dM/dV plots obtained during the first discharge process are provided in **Figure S4.15**. The maxima and minima in the dQ/dV and dM/dV curves are perfectly aligned, and reveal local charge ordering transitions (*e.g.*, Li/vacancy ordering transitions) within the bulk of the cathode that cannot be observed via high resolution sXRD. Those more subtle transitions result in the smaller dQ/dV and dM/dV features observed over the first hexagonal (H1) and monoclinic (M) phase stability domains of LNO. Yet, there is at least one important difference between the information provided by the capacity and magnetometry data. On the one hand, the capacity provides a convoluted picture of the redox processes at play during charge and discharge, in that it cannot distinguish between capacity obtained from redox processes occurring in the bulk of the cathode or at the electrode-electrolyte interface (side reactions). On the other hand, magnetization changes result from bulk redox reactions. This highlights the power of *operando* magnetometry to decouple the capacity originating from parasitic reactions or overpotentials, from that originating from bulk transition metal redox processes. For example, over the low potential region (3.50 V to 3.55 V) highlighted in orange in **Figure 4.5c**, the dQ/dV curve rises

before any change in the dM/dV curve ($dM/dV \approx 0 \text{ emu mol}^{-1} \text{ V}^{-1}$). This offset in voltage presumably corresponds to the overpotential needed before oxidation of LNO, in good agreement with the kinetic limitations reported over this potential range in prior studies.^{103,184} We use the magnetization data in **Figure 4.5a** to determine the extent of first cycle irreversible capacity attributable to irreversible bulk redox processes. Comparing the *operando* magnetization values obtained prior to cycling and at the end of the first discharge process, we find that 0.12 mol of Li (equivalent to 32 mAh g^{-1}) is not reinserted into the LNO structure at a cycling rate of 15 mA g^{-1} ($\approx C/13$). This contrasts with the first cycle irreversible capacity observed for the *operando* cell, equivalent to 0.21 mol of Li (equivalent to 56 mAh g^{-1}), which highlights the presence of side reactions/overpotentials over the voltage range of interest. We note that the total irreversible capacity recorded here is larger than that obtained when using more standard Swagelok or coin cells (see **Figure S4.16a** for the *operando* cell design and **Figure S4.16b** for a comparison of the first cycle voltage profiles obtained using different types of cells), which is presumably due to the low stack pressure and unusual geometry of the *operando* magnetometry cell. Nonetheless, the *operando* magnetometry results clearly show that a portion of the first cycle irreversibility in LNO is due to incomplete lithiation. To identify the source of this irreversibility, we investigate the structural changes induced upon electrochemical cycling in LNO using *ex situ* ssNMR, sXRD, and magnetometry.

Irreversible structural changes were probed in the discharged state after cycling up to either 4.1 V (D-4.1V) or 4.3 V (D-4.3V). Those two upper cutoff potentials were used to examine the effects of the *c* lattice parameter collapse at high states of charge. The first cycle irreversible capacity of LNO₂, after being charged up to 4.1 V and 4.3 V, is 31(1) mAh g^{-1} and 35(2) mAh g^{-1} (average of three cells), respectively, which is equivalent to 0.114(1) mol of Li

and 0.132(7) mol of Li (**Figure S4.17a**). Rietveld refinements of sXRD patterns (**Figure S4.18**) show that the H1 LNO structure is recovered on discharge to 3.0 V, regardless of the upper cutoff potential. Since Li occupancies cannot be determined with accuracy, due to the small x-ray scattering cross section of Li, we estimate the Li content in the two discharged samples from the H1 lattice parameters. Both samples have a c lattice parameter corresponding to approximately $x = 0.9$ in $\text{Li}_x\text{Ni}_{1-x}\text{O}_2$ based on previously reported *operando* sXRD values,^{156,201} which is consistent with the Li content computed from the magnetization of the discharged cathode obtained *operando* using a 4.3 V upper cutoff potential. Ni migration was also considered by refining the Ni_M and Ni_{Li} occupancies, resulting in a 1.7-1.8% Ni_{Li} occupation (a very small increase from the pristine value of 1.5%) and only a minor improvement in the fit ($R_{\text{wp}} = 10.09$ without Ni migration and $R_{\text{wp}} = 10.10$ with Ni migration for the sample with an upper voltage cutoff of 4.3 V). Hence, our sXRD results suggest that the long-range cathode structure does not change significantly, if at all, during the first cycle, and do not explain the irreversibilities observed in the capacity and magnetometry data, so we turn to ^7Li ssNMR to investigate more subtle changes in the local structure.

^7Li ssNMR spectra collected on D-4.1V and D-4.3V differ significantly from the pristine LNO2 spectrum, as shown in **Figure 4.6a**. The 700 ppm resonance associated with Li in fully lithiated LNO domains still dominates the spectra collected on discharge, but the 450 ppm signal attributed to Li near twin boundaries is no longer present, and a new resonance appears at 520 ppm. Further evidence for the presence of a new signal centered at 520 ppm, rather than mere (homogenous) broadening of the 700 ppm and 450 ppm resonances, is provided by fits of the ssNMR data in **Figure S4.19a**, as well as T2-filtered ^7Li ssNMR spectra in **Figure S4.19b**. The 520 ppm resonance is assigned to Li near a diamagnetic Ni^{4+} species in

the Ni layers, *i.e.*, in Li-poor domains of the cathode, resulting in a lower ^7Li chemical shift as explained earlier. This interpretation is consistent with the loss of >0.1 mol Li during the first cycle, and similar to that of Bae et al.²⁰², who based their assignment of a similar 520 ppm ^7Li signal off of Rietveld refinements of Li/Ni occupancies of their neutron diffraction data. The upper cutoff potential has no impact on the chemical shift of Li species in Li-poor domains, indicating that these domains have a similar Li content in the two samples, but the 520 ppm shoulder to the right hand side of the main ^7Li resonance at 700 ppm is more pronounced in the spectrum collected on the discharged cathode after charge to 4.3 V (**Figure 4.6a**), indicating greater irreversibility in this sample. Notably, both the new 520 ppm signal and the absence of the 450 ppm signal assigned to Li near twin boundaries in the spectra obtained on discharge to 3.0 V is consistent with incomplete relithiation of LNO domains near the twin boundary defects.

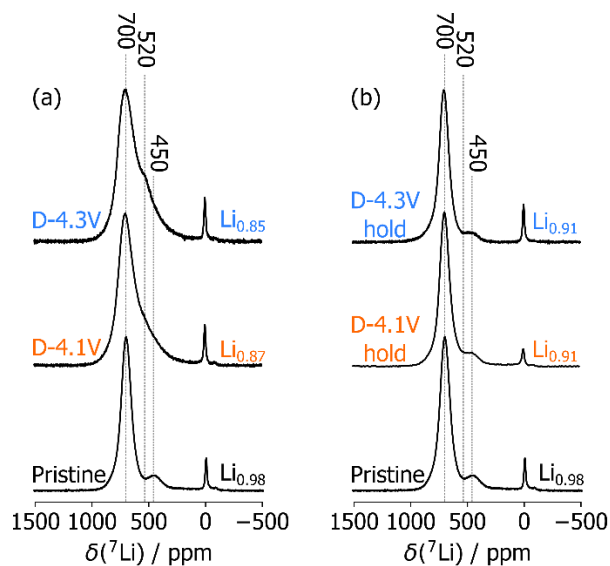


Figure 4.6. ${}^7\text{Li}$ ssNMR spectra collected on pristine and *ex situ* LNO₂ cathode samples ($B_0 = 2.35$ T and 60 kHz MAS). (a) Comparison of the spectra collected on the pristine cathode and on *ex situ* samples discharged to 3.0 V after charging to 4.1 (D-4.1V) and 4.3 V (D-4.3V). The 520 ppm signal present in the *ex situ* spectra is characteristic of Li species in Ni^{4+} -rich (i.e., Li-poor) LNO domains. (b) Comparison of the spectra collected on the pristine cathode and on *ex situ* samples discharged to 3.0 V after charging to 4.1 and 4.3 V, followed by a 10-hour voltage hold at 3.0 V. Li reintercalation near twin boundaries results in the reappearance of the 450 ppm signal observed in the pristine spectrum, and in reduction of nearby Ni^{4+} species to Ni^{3+} , as indicated by the loss of the 520 ppm signal.

We next quantify the impact of twin boundaries on the first cycle irreversibility of the LNO cathode, by carefully separating bulk from surface contributions to the irreversible capacity. When it comes to surface effects, Riewald *et al.* showed that the primary particle plays an important role in the first cycle irreversibility of LNO when the cathode is charged past its H2-H3 transition, resulting in particle cracking and exposure of the primary particles to the electrolyte.¹⁵⁸ In such a case, irreversible side-reactions between the electrode and the electrolyte at high voltage scale with the specific surface area of the particles. Surface effects can generally be mitigated by limiting the upper cutoff voltage to 4.1 V, thereby preventing particle cracking. Alternatively, the bulk magnetization of LNO is not affected by surface reactions and can be used to directly probe bulk processes and their irreversibilities, *e.g.*, the sluggish reinsertion of Li into sites near Ni_{Li} defects or near twin boundaries. In the case of

LNO₂, the irreversible Li content due to bulk effects, as determined from our *operando* magnetometry measurement using a 4.3 V upper cutoff voltage (0.12 mol of Li), and from the capacity measured on a Swagelok cell using a 4.1 V cutoff voltage (0.11 mol of Li, see **Figure S4.17a**), agrees well with the amount of Li near twin boundaries (≈ 0.11 mol of Li). Hence, for LNO₂, the bulk contribution to the first cycle irreversible capacity correlates well with the twin boundary defect concentration. For LNO₃, there are 5 mol of Li near twin boundaries, which is lower than the irreversible Li content due to bulk effects determined from capacity measurements using a 4.1 V cutoff voltage (0.11 mol of Li, see **Figure S4.17b**). We suspect that, as the Ni excess level increases from 2 to 3%, the first cycle irreversible capacity due to bulk effects comprises contributions from both twin boundaries and Ni_{Li} defects. Specifically, the irreversible capacity in excess of the twin boundary contribution is likely due to the difficult reinsertion of Li near Ni_{Li} defects, as has been reported by others.^{145,203}

Twin boundaries present in the bulk LNO cathode structure provide a potential explanation to the kinetic limitations related to Li reinsertion into the LNO cathode at low potentials. These kinetic limitations have previously been studied through the application of voltage holds or through high temperature cycling.^{103,156} We therefore applied a 10-hour voltage hold at 3.0 V on first discharge after cycling up to 4.1 V (D-4.1V-hold) and 4.3 V (D-4.3V-hold), and characterized the resulting *ex situ* cathode samples with ⁷Li ssNMR. Assuming that all of the capacity during the voltage hold comes from bulk lithiation of LNO, an additional 0.067(1) mol and 0.075(1) mol of Li is reinserted into D-4.1V-hold and D-4.3V-hold, respectively. The resulting ⁷Li ssNMR spectra, shown in **Figure 4.6b**, exhibit a signal at 450 ppm, while the 520 ppm signal is no longer present, indicating relithiation of the twin boundary regions and concurrent reduction of nearby Ni⁴⁺ species to Ni³⁺. Further, the intensity of the

450 ppm signal D-4.1V-hold and D-4.3V-hold accounts for about 0.08 mol and 0.07 mol of Li in *R-3m* phase, which agrees well with the amount of Li reinserted into the cathodes during the voltage hold. Yet, even with a 10-hour voltage hold, about 0.03 mol of Li is never reinserted during the first cycle (in a half cell configuration), which could be due to irreversible structural changes during cycling. For example, Li and transition metals have been found to more easily migrate (lower diffusion barriers) near planar defects in related oxide cathodes, leading to greater cation mixing around twin boundaries.¹⁴⁴ The impact of twin boundaries on Li reinsertion kinetics was studied over additional charge-discharge cycles, with cells subjected to 5 cycles with a 10-hour voltage hold at 3.0 V at the end of each discharge. Interestingly, the capacity recovered during the hold increases from 20(1) mAh g⁻¹ (0.075(1) mol of Li) up to 25(2) mAh g⁻¹ (0.092(9) mol of Li) over five cycles when cycled up to 4.3 V, but stays approximately constant for cells cycled up to 4.1 V (**Figure S4.20a**). One potential explanation for the gradual increase in the recovered capacity in D-4.3V-hold is the development of overpotentials during cycling due to the repeated H2-H3 transition at high voltage, resulting in particle cracking and electrolyte degradation at the freshly exposed surface. This overpotential inhibits relithiation and leads to a loss of Li content in the bulk. With increased overpotentials, the capacity observed before the voltage hold goes down with increasing cycle number (**Figure S4.20a**), and the 3.0 V hold recovers more of the capacity lost to overpotentials earlier on discharge.^{19,201} In the case of the 4.1 V cell, which does not experience impedance build up, Li sites near twin boundary defects are relithiated to the same extent after each cycle, indicating that the bulk structure is stable over first five cycles. To confirm the differences in bulk stability of D-4.1V-hold and D-4.3V-hold, ⁷Li ssNMR spectra were collected after 1 and 5 cycles (**Figure S4.20b,c**). While the 1st and 5th cycle spectra overlap perfectly for cells cycled up to

4.1 V, the spectral line shape evolves upon cycling (mostly in the 450-500 ppm region) for cells cycled up to 4.3 V. The integrated intensity for the twin boundary signal after the 5th cycle is equivalent to 0.07 mol of Li and 0.06 mol of Li for D-4.1V-hold and D-4.3V-hold, respectively, which is within error from the intensity of the twin boundary signal in the spectra collected during the 1st cycle.

Overall, if electrode-electrolyte interfacial reactivity is minimized, and for LNO compositions with minimal Ni excess ($y \leq 2\%$), the concentration of planar defects in LNO determines the achievable first cycle coulombic efficiency and limits the cyclable Li content on subsequent cycles. Hence, synthetic approaches are needed to minimize the concentration of planar defects in LNO to improve its cyclability. We find that the number of Li equivalents per mol of Ni used in the synthesis will influence both the concentration of Ni_{Li} defects and twin boundaries in LNO. Future work could investigate other synthetic parameters, such as the effect of calcination temperatures and cooling conditions (e.g. quenching), to minimize twin boundary concentrations. Additionally, given that defects in LNO have been found to be inherited from the hydroxide precursor,¹⁹⁹ ¹H ssNMR may be useful to screen for twin boundaries in Ni(OH)₂.

4.4. Conclusions

In this study, the impact of planar defects (twin boundaries) and off-stoichiometry on the Li intercalation properties of LiNiO₂ (LNO) was revealed using sXRD, ⁷Li ssNMR, TEM, and magnetometry. Notably, ⁷Li ssNMR was identified as a powerful diagnostic tool capable of quantifying the concentration of twin boundaries in Li_{1-y}Ni_{1+y}O₂ ($0 \leq y \leq 0.03$) cathodes prepared using different numbers of Li equivalents per mol of Ni. This method relies on the integration of a ~450 ppm ⁷Li ssNMR signal characteristic of Li near twin boundary defects,

the attribution of which was assisted by first principles calculations of paramagnetic ssNMR parameters. The concentration of twin boundaries was found to depend on the $\text{Li}_{1-y}\text{Ni}_{1+y}\text{O}_2$ composition, whereby greater Ni excess leads to fewer twin boundaries. Such planar defects directly impact Li reinsertion into the bulk LNO cathode. While *operando* magnetometry indicated that 0.11 mol of Li could not be reinserted into a nearly stoichiometric LNO cathode (with composition $\text{Li}_{0.98}\text{Ni}_{1.02}\text{O}_2$) after the initial-discharge process, *ex situ* ^7Li ssNMR revealed kinetic limitations associated with ~ 0.1 Li reinsertion into sites near the twin boundaries even at a relatively slow (C/10) cycling rate, irrespective of the upper cutoff voltage. Consistent with this, partial Li reinsertion into the twin boundary regions of $\text{Li}_{0.98}\text{Ni}_{1.02}\text{O}_2$ was achieved with a 3 V potential hold at the end of charge. With increasing Ni excess, Ni_{Li} defects were found to also contribute to the first cycle bulk structural irreversibility of $\text{Li}_{1-y}\text{Ni}_{1+y}\text{O}_2$ cathodes, in agreement with previous work. Overall, the results presented here suggest that twin boundaries in as-synthesized LNO-type cathodes contribute to their first cycle irreversible capacity at reasonable cycling rates. Consequently, synthetic approaches are needed to minimize the concentration of planar defects in this class of cathode materials and improve their cyclability.

4.5. Appendix for Twin Boundaries Contribute to the First Cycle Irreversibility of

LiNiO₂

Table S4.1. Rietveld refinement parameters for the data presented in this work.

Sample ID (space group)	Figure	R _{wp}	a (Å)	c (Å)	Ni-excess (y in Li _{1-y} Ni _{1+y} O ₂)
LNO2 (<i>R-3m</i>)	2a	8.5	2.8765(1)	14.1933(4)	0.0146(6)
LNO2.5 (<i>R-3m</i>)	S1a	5.3	2.8798(1)	14.2067(6)	0.0245(6)
LNO3 (<i>R-3m</i>)	S1b	8.8	2.8790(1)	14.2004(4)	0.0305(6)
Li _{0.05} Ni _{0.95} O (<i>Fm-3m</i>)	S4a	14.2	4.1629(2)	-	0.908(6)
Li _{0.75} Ni _{0.25} NiO ₂ (<i>R-3m</i>)	S4b	6.9	2.8995(1)	14.2420(4)	0.272(2)
LNO2-4.1V (<i>R-3m</i>)	S13a	8.8	2.8730(1)	14.2143(1)	0.015
LNO2-4.3V (<i>R-3m</i>)	S13b	10.1	2.8738(1)	14.2114(1)	0.015
LNO2-4.3V volt. Hold (<i>R-3m</i>)	S13c	12.4	2.8734(1)	14.1722(1)	0.015

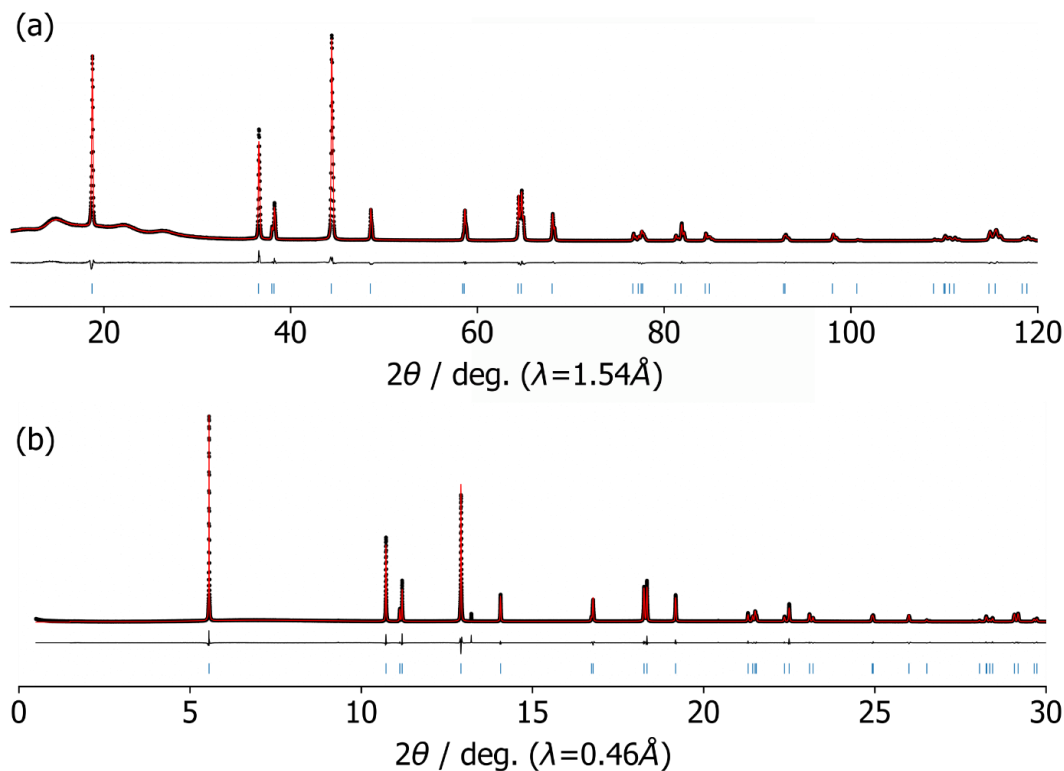


Figure S4.1. Additional XRD patterns for LNO compositions with varying Ni-excess. (a) XRD pattern was collected for LNO2.5 using an air-free holder on a laboratory-source Panalytical Empyrean diffractometer with Cu K α radiation in Bragg-Brentano geometry, and fit to a single $R-3m$ phase. The broad signal from 10° to 30° 2θ is due to a Kapton polyimide window and only partially corrected by subtracting the pattern of an empty sample holder. Low angle intensity corrections were applied with a surface roughness parameter. (b) sXRD pattern for LNO3 with a fit to an $R-3m$ phase with 3% Ni-excess.

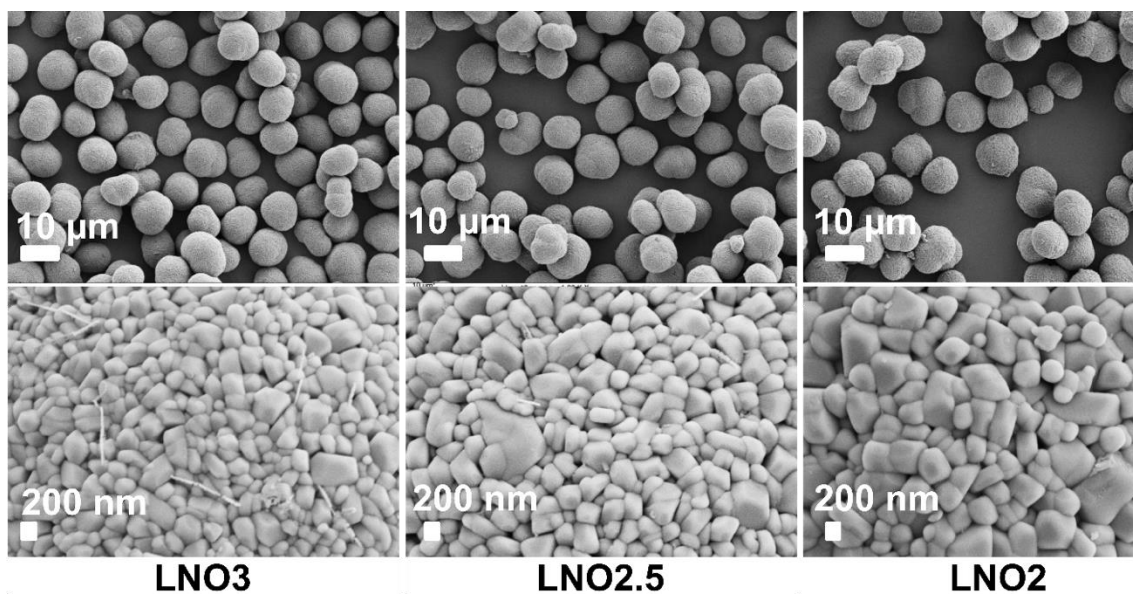


Figure S4.2. SEM images of secondary (top panel) and primary (bottom panels) particles for as-synthesized LNO2, LNO2.5, and LNO3 samples.

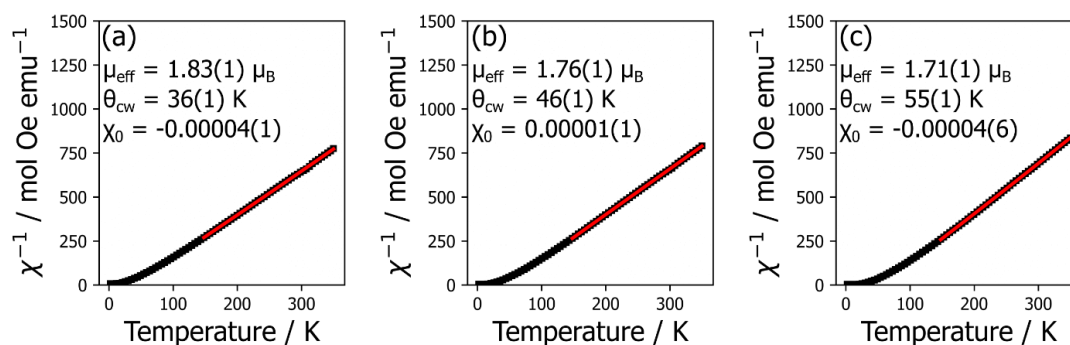


Figure S4.3. Inverse magnetic susceptibility curves for (a) LNO2, (b) LNO2.5, and (c) LNO3 measured at $H = 0.1$ T and with the temperature range of 2 K to 350 K. High temperature Curie Weiss fits within the temperature range of 150 K to 350 K are shown in red.

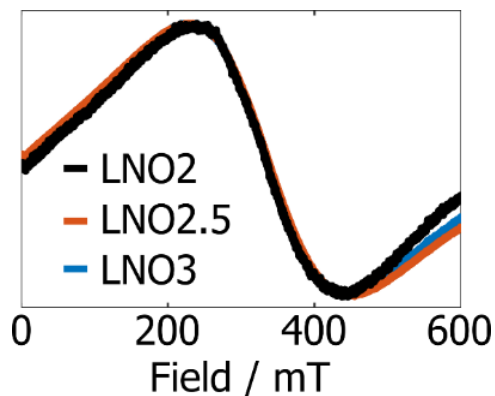


Figure S4.4. X-band EPR spectra acquired on LNO2, LNO2.5, and LNO3. Easyspin²⁹ was used to fit the broad signal and extract g-factors, which were approximately equal to 2.1 for all of the samples.

Supplementary Note 4.1. Parameters used in the CRYSTAL17 calculations and chemical shift scaling method.

The computed hyperfine (paramagnetic) ssNMR properties were obtained at 0 K for LiNiO₂, Li_{0.98}Ni_{1.02}O₂, twin boundary, and antiphase boundary structures. All computations were carried out on ferromagnetically-aligned cells. To compare CRYSTAL17 calculation results with experimental data acquired at room temperature, the computed shifts were subsequently scaled to a value consistent with the paramagnetic state of the system at the temperature of the ssNMR experiments, using a magnetic scaling factor Φ of the form:

$$\Phi(T_{exp}) = \frac{\langle M(T_{exp}) \rangle}{M_{sat}}, \quad (1)$$

where M_{sat} is the saturated (ferromagnetic) Ni³⁺ magnetic moment at 0 K, and $\langle M(T_{exp}) \rangle$ the bulk average magnetic moment measured at the sample experimental temperature, T_{exp} . Here, T_{exp} is set to 320 K to account for frictional heating caused by fast (60 kHz) sample rotation during ssNMR data acquisition.

The magnetic scaling factor in eq. (1) can be evaluated from the experimental magnetic properties of the material:

$$\Phi(T) = \frac{B_0 \mu_{eff}^2}{3k_B g_e \mu_B S(T-\Theta)}, \quad (2)$$

where B_0 is the external magnetic field, μ_{eff} is the effective magnetic moment per Ni site, k_B is Boltzmann's constant, g_e is the free electron g -value, μ_B is the Bohr magneton, S is the formal spin of Ni^{3+} ($S = 1/2$), and Θ is the Weiss constant. A derivation of eq. (2), starting from the Brillouin function in the low field, high temperature limit, can be found in a previous study by Kim et al.⁸⁸ Eq. (2) uses the “spin-only” expression for the magnetic moment and is only strictly valid when the orbital angular momentum is quenched.²⁰⁴ Yet, for systems where spin-orbit coupling effects are negligible, such as LiNiO_2 , the spin-only expression is a good approximation of the magnetic behavior of the system.

Table S4.2. Li-O-Ni³⁺ interaction pathways and their contributions to the ⁷Li Fermi contact shift in the ideal LiNiO_2 structure computed using the CRYSTAL17 software package and two hybrid DFT/HF exchange-correlation functionals with 20% (HYB20) and 35% (HYB35) of exact exchange. Those two calculations have been found to provide an upper and a lower bound to the experimental shift, respectively.

Li-O-Ni ³⁺ interaction pathway	Chemical shift contribution HYB20/HYB35 (ppm)
δ_S , 180° short	29/17
δ_{SS} , 90° short-short	8/18
δ_L , 180° long	319/251
δ_{SL} , 90° short-long	-19/-15

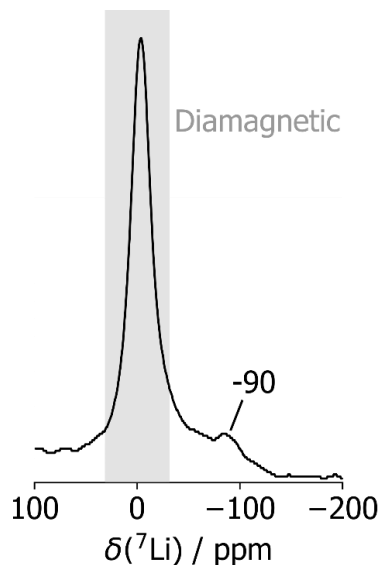


Figure S4.5. Enlarged view of the ^7Li ssNMR spectrum for pristine LNO₂. The typical ^7Li chemical shift range for diamagnetic compounds is highlighted in grey (30 ppm to -30 ppm).

Supplementary Note 4.2. Interpretation of the ^7Li ssNMR signal at -90 ppm in the as-synthesized LNO cathode spectra.

The weak signal at ca. -90 ppm in the spectra collected on as-synthesized LNO₂, shown in **Figure S4.5**, is outside of the diamagnetic frequency range and corresponds to Li species in the vicinity of paramagnetic Ni ions. Its negative chemical shift suggests that it arises from a very different Li environment than the interlayer Li in the LNO structure. Given the propensity for Li/Ni antisite disorder in LNO cathodes^{136,205}, we explore the possibility of a small amount of Li occupying Ni sites (Li_M defects) in these compounds, that would be difficult to detect with sXRD alone given the very weak Li scattering factor. A Li_M defect interacts with six Ni_M via 90° Li-O-Ni interaction pathways. Assuming that all six Ni_M surrounding the Li_M defect are in their 3+ oxidation state, two short-short and four short-long Ni^{3+} -O-Li interactions are expected, which leads to a predicted chemical shift in the range of -60 ppm to -25 ppm when using the 90° δ_{SS} and δ_{SL} shift contributions computed on the defect-free and stoichiometric LiNiO_2 structure (see **Table S4.2**). While the predicted Li_M shift range is in the negative ppm

range, in good agreement with the negative -90 ppm shift observed experimentally, its magnitude is not quite in line with the observed shift. Two reasons could explain the discrepancy. First, the computed δ_{SS} and δ_{SL} shift contributions are only rough estimates of the actual shift contributions for the Ni_M at $\sim 90^\circ$ from the Li_M defect, as the average Li_M -O- Ni_M bond angle (89.3°) deviates from the 89.8° Li_{Li} -O- Ni_M bond angles in the ideal $LiNiO_2$ structure, resulting in different orbital overlap and a different amount of unpaired electron spin density delocalized from the Ni d to the Li s orbital. Second, we have assumed that all six nearest-neighbor Ni_M are in their 3+ oxidation state, but it is in fact likely that one of the adjacent Ni_M is in the +4 oxidation state for local charge balance reasons (and to compensate for the presence of a complementary Ni^{2+} ion in the interlayer space, or Ni_{Li} defect).¹⁸⁶ Since Ni^{4+} is diamagnetic, it does not contribute to the observed 7Li chemical shift, which one can again roughly account for by either switching off a δ_{SL} or δ_{SS} contribution to the overall chemical shift, leading to a 15 to 18 ppm increase or a 7 to 17 ppm decrease in shift and extending the possible Li_M chemical shift range from -77 to -7 ppm. All in all, this analysis lends credence to the assignment of the -90 ppm resonance to Li_M defects in the as-synthesized LNO cathodes.

Supplementary Note 4.3. Assignment of the 450 ppm 7Li ssNMR signal: other Li-Ni-O phases considered.

To test whether the 450 ppm signal might originate from Li nuclei in surface phases, such as a cubic (NiO-like) $Li_yNi_{1-y}O$ phase^{184,202,206} ($y < 0.3$) or a Ni-rich $Li_yNi_{0.25}NiO_2$ or $Li_yNi_{0.5}NiO_2$ ($y \leq 0.75$) layered phase¹³⁸, we synthesized and characterized the $Li_{0.75}Ni_{0.25}NiO_2$ and $Li_{0.05}Ni_{0.95}O$ compositions (see **Figure S4.6** for XRD patterns and Rietveld refinements). As expected, at high Li concentrations ($Li_{0.75}Ni_{0.25}NiO_2$), Li and Ni occupy distinct layers, resulting in a single $R-3m$ phase best described as $[Li_{0.712(1)}Ni_{0.288(1)}]_{3b}[Li_{0.016(2)}Ni_{0.984(2)}]_{3a}O_2$.

At low Li concentrations ($\text{Li}_{0.05}\text{Ni}_{0.95}\text{O}$), a cubic $Fm-3m$ phase forms.¹²⁵ The ^7Li ssNMR spectrum collected on $\text{Li}_{0.75}\text{Ni}_{0.25}\text{NiO}_2$ features a single environment at 1050 ppm (see **Figure S4.7a**) while that obtained on $\text{Li}_{0.05}\text{Ni}_{0.95}\text{O}$ (see **Figure S4.7b**) features a very broad and low intensity resonance at 1100 ppm, even after significant signal averaging. *Clearly, neither of these signals resemble the 450 ppm signal observed in our as-synthesized LNO cathodes. Those discrepancies are further rationalized below.*

If we assume that the $\text{Li}_{0.75}\text{Ni}_{0.25}\text{NiO}_2$ compound synthesized here exhibits the same Ni-vacancy ordering as the one proposed by Xiao *et al.* for $\text{Ni}_{0.25}\text{NiO}_2$ ¹³⁸, and fill the vacant cation sites with Li, a single Li environment is expected in this structure (see **Figure S4.8**), in good agreement with the single ^7Li ssNMR resonance observed experimentally (the very small amount of Li in the Ni layers, as determined from the Rietveld refinement discussed above, is below the ssNMR detection limit). Li species in $\text{Li}_{0.75}\text{Ni}_{0.25}\text{O}_2$ interact with paramagnetic Ni species via six 180° interactions and eight 90° interactions, *i.e.*, two additional 90° Li-O-Ni interactions as compared to Li in the ideal LNO environment (700 ppm signal). Hence, the chemical shift of Li in $\text{Li}_{0.75}\text{Ni}_{0.25}\text{O}_2$ is expected to be greater than 700 ppm due to additional Fermi shift contributions and the presence of Ni^{2+} species in the Ni layers and the interlayer space (Ni^{2+} leads to larger paramagnetic shifts than Ni^{3+}), consistent with the observed 1050 ppm resonance (**Figure S4.7a**). In the case of $\text{Li}_{0.05}\text{Ni}_{0.95}\text{O}$, we expect Li to be well dispersed inside the NiO-like matrix, and we therefore expect a single Li environment (each Li is surrounded by mostly Ni^{2+} species, and one nearby Ni^{3+} for local charge balance) with a high paramagnetic shift. This is consistent with the single resonance observed at 1100 ppm in **Figure S4.7b**. This resonance is weak and extremely broad, which can again be accounted for by the high concentration of Ni^{2+} species in this compound, leading to extreme paramagnetic

broadening and a short-lived ^7Li ssNMR signal. Interestingly, despite the large difference in concentration of Ni^{2+} species in $\text{Li}_{0.05}\text{Ni}_{0.95}\text{O}$ and $\text{Li}_{0.75}\text{Ni}_{0.25}\text{O}_2$, their ^7Li chemical shift resonances are similar. A reduction in chemical shift for $\text{Li}_{0.05}\text{Ni}_{0.95}\text{O}$ may be due to strong AFM coupling between Ni-ions in this phase¹²⁵ as has been observed in related Mn-containing compounds²⁰⁷, which can result in similar chemical shifts between $\text{Li}_{0.05}\text{Ni}_{0.95}\text{O}$ and $\text{Li}_{0.75}\text{Ni}_{0.25}\text{O}_2$.

As a final note, while the results presented here indicate that the 450 ppm signal observed in the ssNMR spectra collected on the as-synthesized LNO2, LNO2.5, and LNO3 cathodes does not arise from a cubic (NiO-like) $\text{Li}_y\text{Ni}_{1-y}\text{O}$ phase, or a Ni-rich $\text{Li}_y\text{Ni}_{0.25}\text{NiO}_2$ or $\text{Li}_y\text{Ni}_{0.5}\text{NiO}_2$ ($y \leq 0.75$) layered phase, we cannot exclude the possible presence of, e.g., a Ni-rich phase at the surface of our LNO particles. Ample evidence for the presence of such surface phases has been provided for in the literature, and those are extremely difficult to detect with the bulk (sXRD, ssNMR) structural techniques used here.

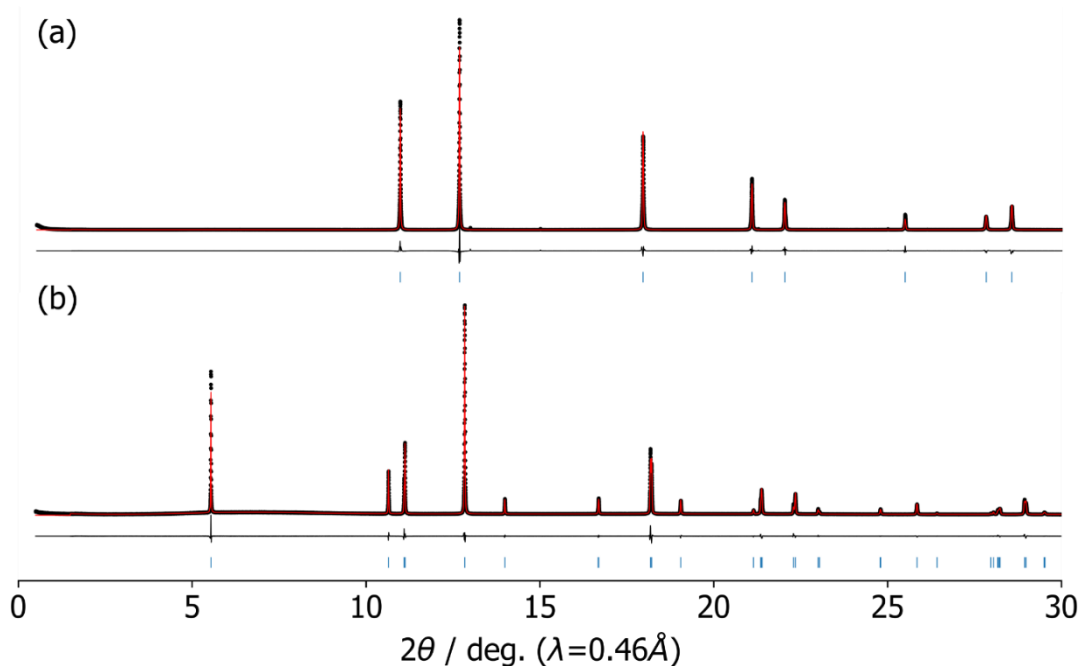


Figure S4.6. sXRD patterns for (a) $\text{Li}_{0.05}\text{Ni}_{0.95}\text{O}$ ($Fm-3m$) and (b) $\text{Li}_{0.75}\text{Ni}_{0.25}\text{NiO}_2$ ($R-3m$).

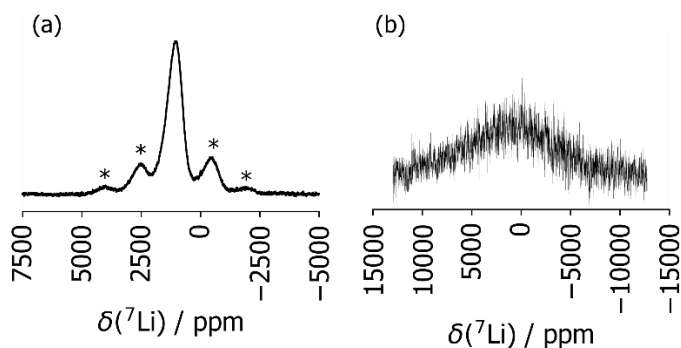


Figure S4.7. ^7Li ssNMR spectra for (a) $\text{Li}_{0.75}\text{Ni}_{0.25}\text{NiO}_2$ and (b) $\text{Li}_{0.05}\text{Ni}_{0.95}\text{O}$. Spinning sidebands are marked with an asterisk. The spectrum in (a) was acquired using the same number of scans (4k) as the spectra shown in **Figure 4.2c**, and the main resonance is centered at 1050 ppm. The spectrum in (b) was acquired through signal averaging over 304k scans, resulting in a low intensity broad resonance centered at 1100 ppm.

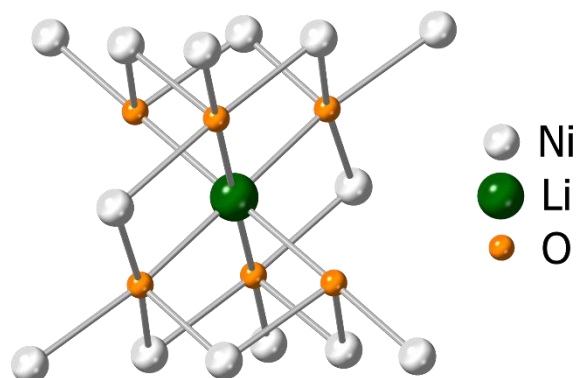


Figure S4.8. Li local environment in $\text{Li}_{0.75}\text{Ni}_{0.25}\text{NiO}_2$, based on Xiao *et al.*'s¹³⁸ structural model. Each Li has two extra Ni neighbors in the interlayer as compared to Li in ideal LiNiO_2 , resulting in a higher ^7Li chemical shift of 1050 ppm (as compared to the 700 ppm shift of LiNiO_2).

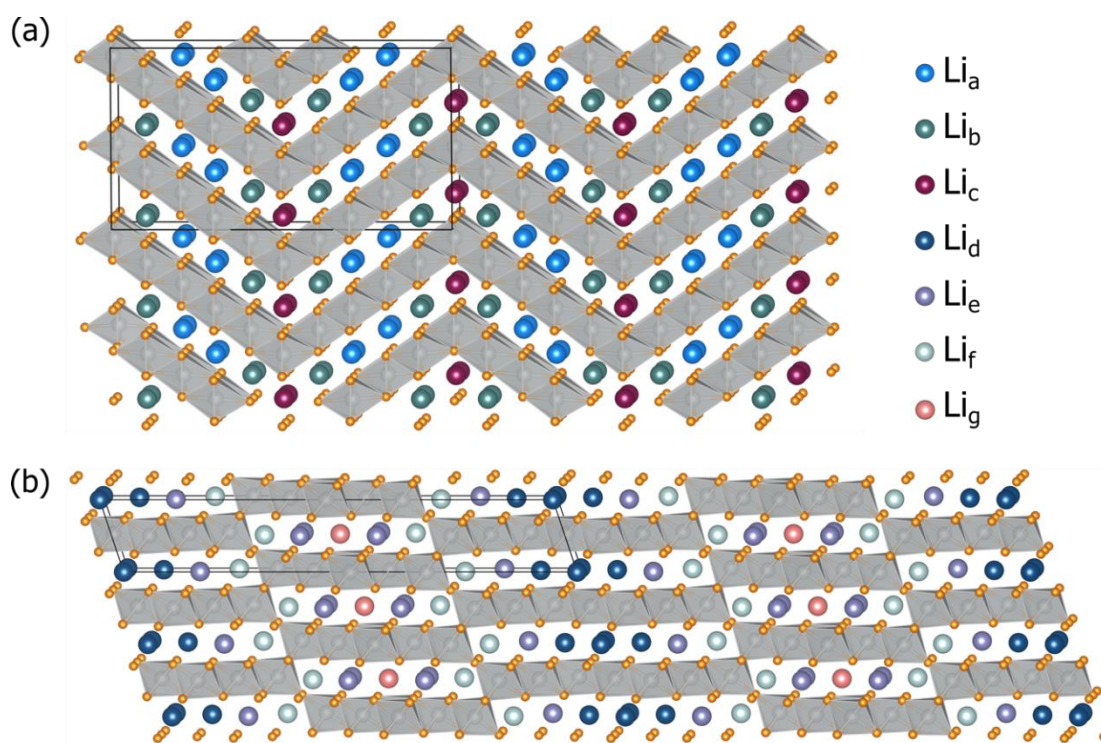


Figure S4.9. Supercells used for modeling (a) twin boundary and (b) antiphase boundary for paramagnetic ssNMR calculations, where the black box indicates a single unit cell. The color scheme for $\text{Li}_a - \text{Li}_f$ environments shown here is the same as in **Figure 4.3** in the main text. We note that in b), an additional, spurious Li environment (Li_g) is created by the use of a small supercell for the antiphase boundary model (and strain buildup in the structure relaxed from first principles) and is disregarded hereafter as it is likely not representative of the real structure.

Table S4.3. Relaxed unit cell parameters for the various Li-Ni-O structural models of interest to this work.

Structure	# atoms	a / Å	b / Å	c / Å	$\alpha / ^\circ$	$\beta / ^\circ$	$\gamma / ^\circ$	Volume / Å ³
LiNiO ₂	192	14.676	11.601	9.737	90.00	107.70	90.00	1579.3
Li _{0.98} Ni _{1.02} O ₂	240	9.800	14.488	14.626	90.06	107.81	90.03	1977.2
LiNiO ₂ antiphase boundary	48	4.897	2.872	29.133	90.01	108.07	90.04	389.5
LiNiO ₂ twin boundary	160	5.526	11.270	21.087	90.00	90.00	90.00	1313.3

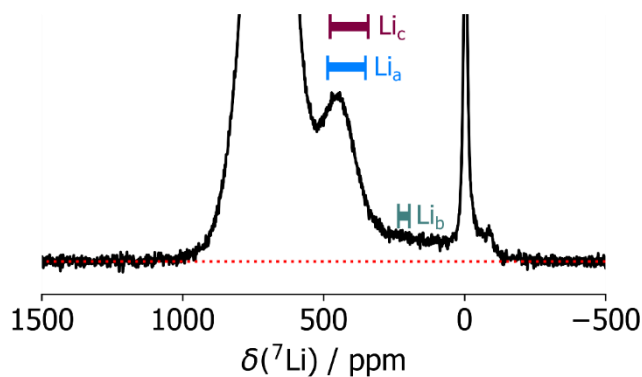


Figure S4.10. Enlarged view of the LNO2 ⁷Li ssNMR spectrum (Figure 4.2b in the main text). DFT predicted chemical shift ranges for Li_a, Li_b, and Li_c are shown. Red dotted line is a guide for the eye.

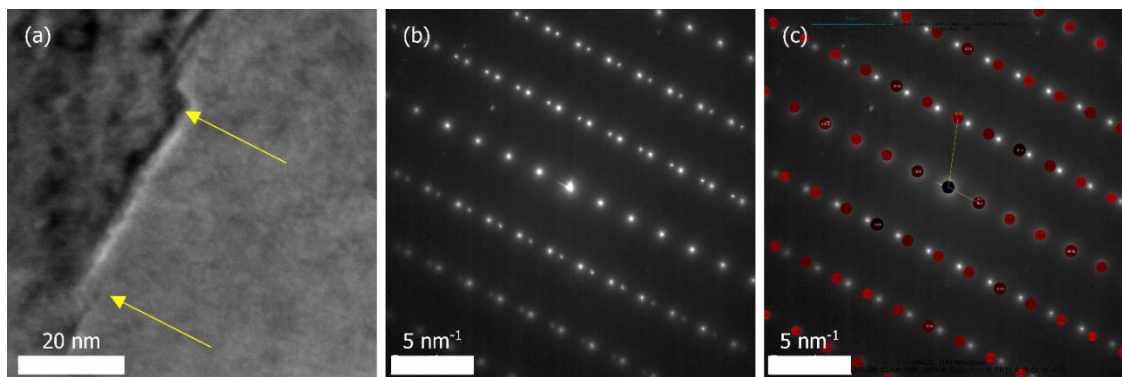


Figure S4.11. (a) HAADF image of a twin plane (highlighted with yellow arrows) in pristine LNO₂, as observed along the [001] zone axis, and (b) the corresponding SAED pattern. (c) The SAED pattern simulated along the [001] zone axis is overlaid with the experimental data shown in (b). Additional spots are caused by the twinned crystal.

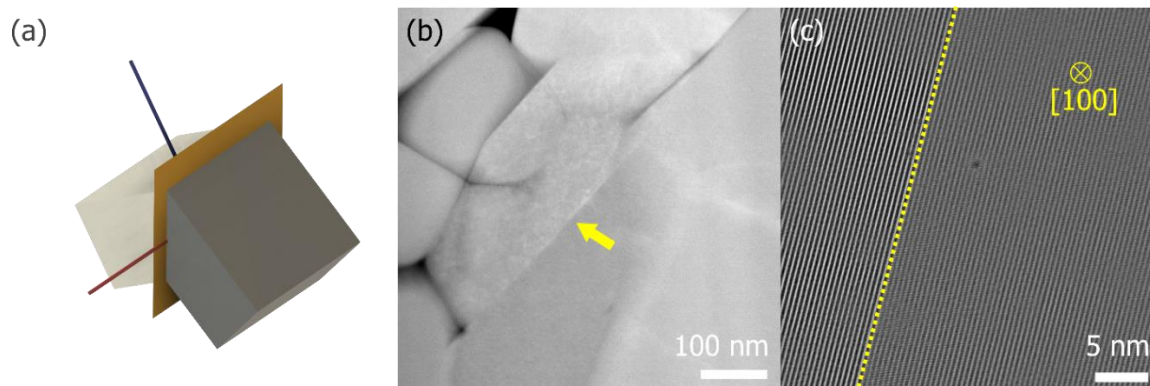


Figure S4.12. (a) Schematic of a twinned particle observed with different electron beam orientations. When the electron beam vector (red vector) is parallel to the twin boundary plane (orange), atomic columns of both twins can be observed. When the boundary is off axis to the electron beam (blue vector), only one twin can be tilted to observe atomic columns, as is the case for the TEM image in the main text. Additional twin boundaries identified in LNO₂ by STEM with (b) low magnification and (c) atomic resolution. The twin boundary is identified by the yellow arrow and line.

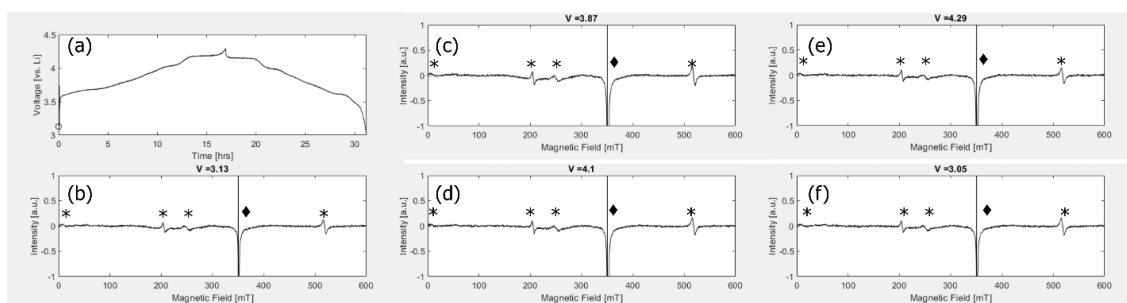


Figure S4.13. *Operando* EPR was conducted on LNO₂ using a Bruker EMXplus EPR spectrometer and a home-built cell at a cycling rate of 15 mA g⁻¹. The voltage profile is shown in (a) and spectra acquired at (b) OCV, (c) 3.87 V, (d) 4.1 V, (e) 4.3 V, and (f) discharged-3.0 V are shown. Asterisks mark signals from a ruby reference and the diamond marks overlapping signals from the Li metal anode and carbon additive.

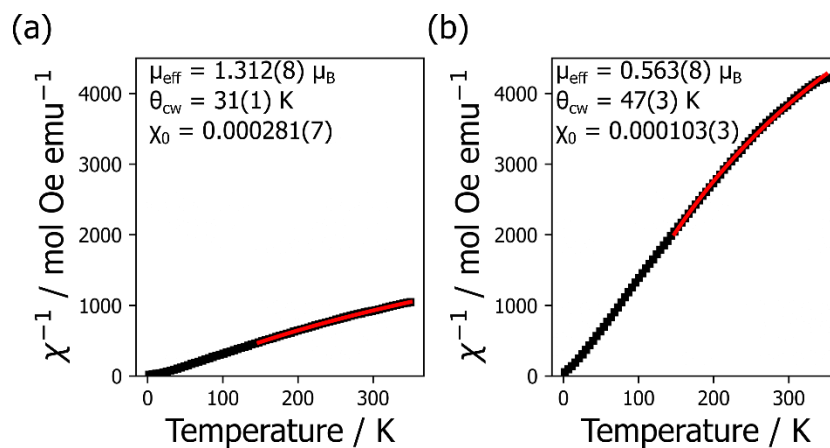


Figure S4.14. Inverse magnetic susceptibility curves for LNO₂ charged up to (a) 4.1 V and (b) 4.3 V. Curie-Weiss fits were done from 150 K to 350 K and are shown in red.

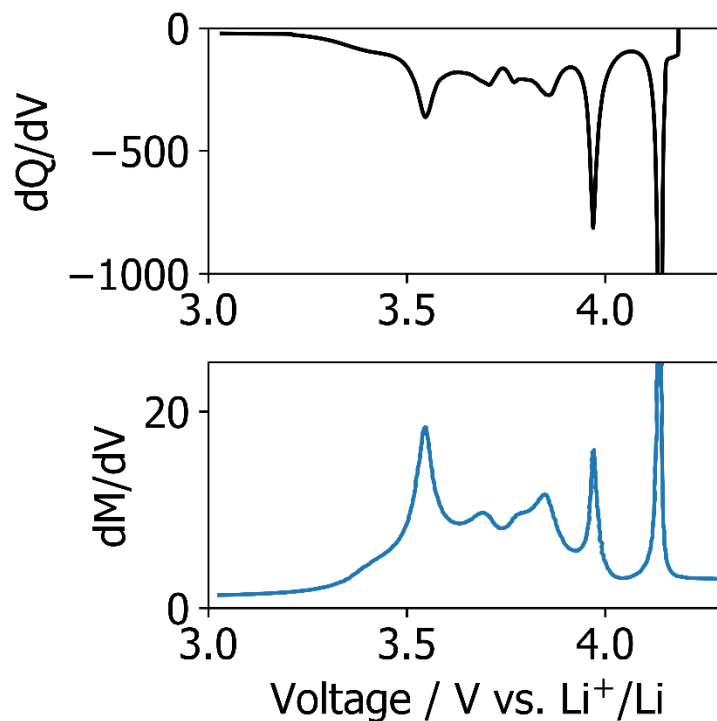


Figure S4.15. dQ/dV and dM/dV plots obtained during the first discharge of the *operando* magnetometry experiment on LNO₂, showing excellent alignment of the electrochemical and magnetic features as a function of a change in half cell potential.

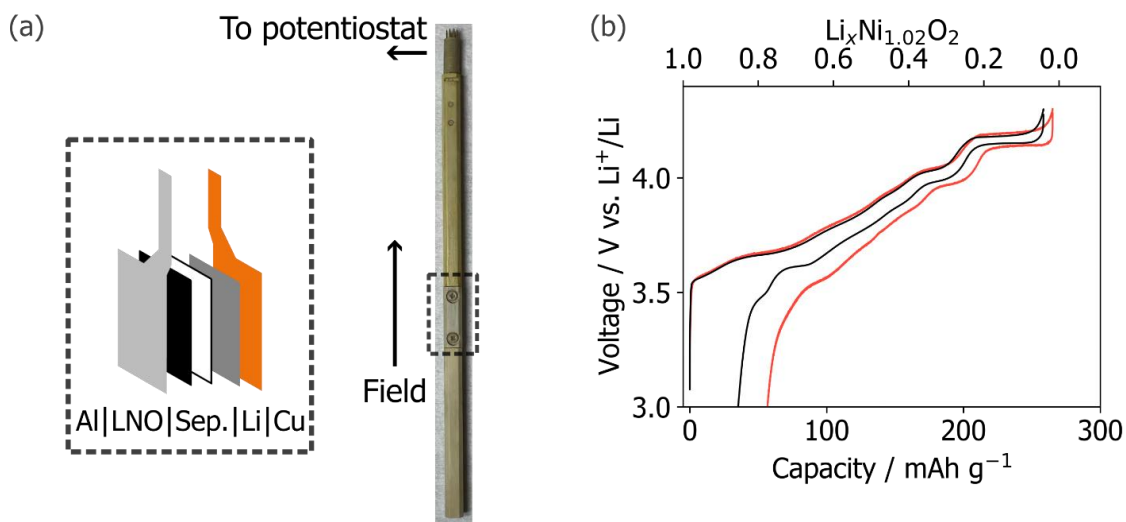


Figure S4.16. (a) Schematic of the *operando* magnetometry cell and (b) first cycle voltage profile comparisons of LNO₂ obtained using a Swagelok cell (black) and the *operando* magnetometry cell (red).

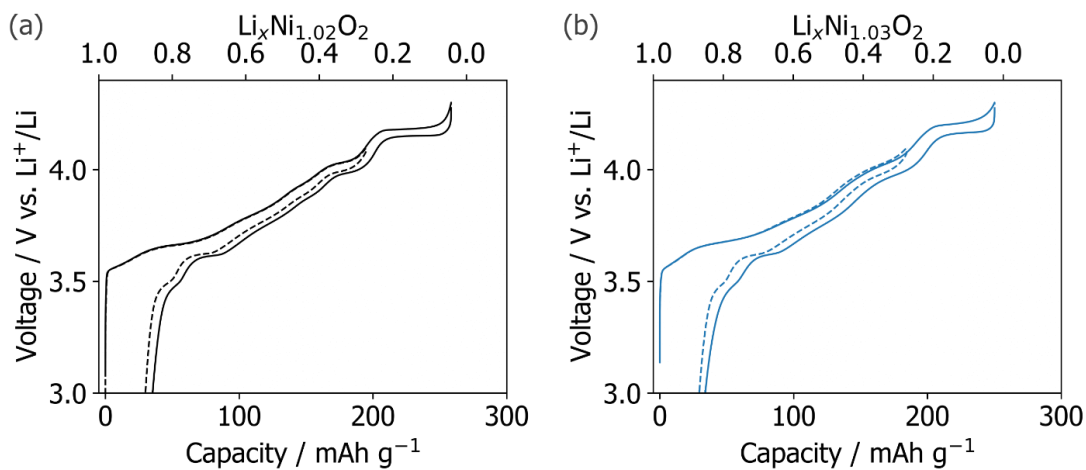


Figure S4.17. Voltage profile comparison for (a) LNO₂ (black) and (b) LNO₃ (blue) with an upper cutoff voltage of 4.3 V (solid) and 4.1 V (dashed), both using Swagelok cells.

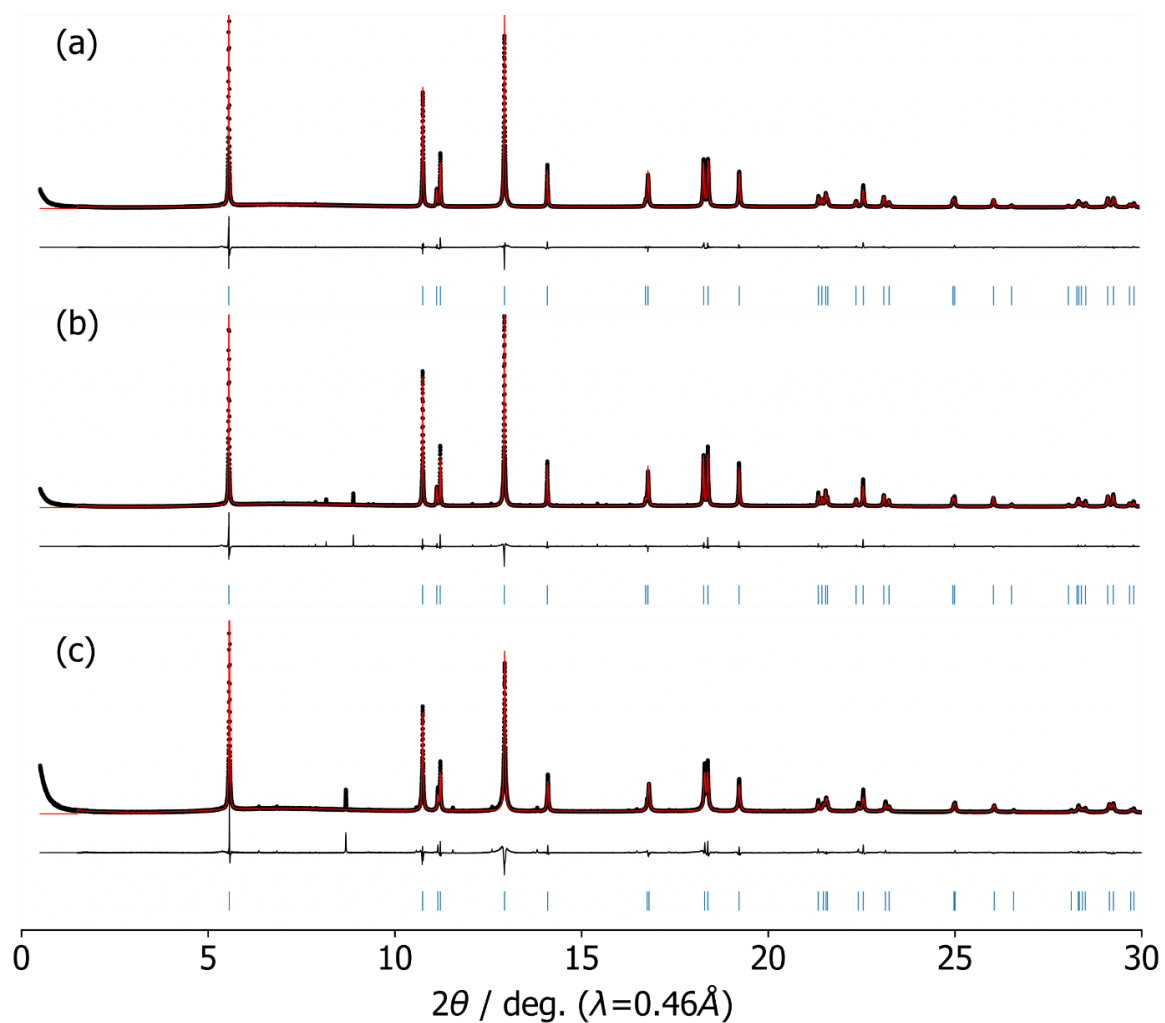


Figure S4.18. sXRD and Rietveld refinement of discharged cathodes after one cycle with an upper cutoff voltage of (a) 4.1 V, (b) 4.3 V, and (c) 4.3 V with a 10 hour voltage hold at 3.0 V. All samples were indexed to a $R\text{-}3m$ phase with minor impurity phases are present in (b) and (c). The patterns shown are enlarged and the 003 peak at $\sim 5.5^\circ 2\theta$ is truncated.

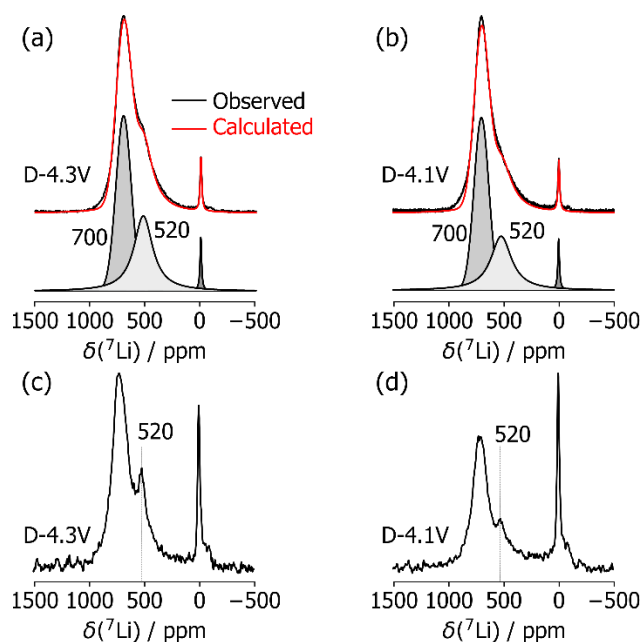


Figure S4.19. Fits of ^7Li ssNMR spectra collected on the two discharged cathode samples cycled up to (a) 4.3 V (D-4.3V) and (b) 4.1 V (D-4.1V), using two gaussians centered at 700 ppm and 520 ppm. Spectra obtained from T2-filtered experiments on the (c) D-4.3V and (d) D-4.1V samples. The spin echo delay was set to 32 rotor periods (~ 1 ms) to partially filter out faster decaying signals (here, the 700 ppm resonance that is short-lived due to the strong paramagnetic interactions with 12 nearest-neighbor Ni^{3+} species), and better observe slower relaxing signals (here, the 520 ppm that is longer lived due to the presence of one nearest-neighbor diamagnetic Ni^{4+}).

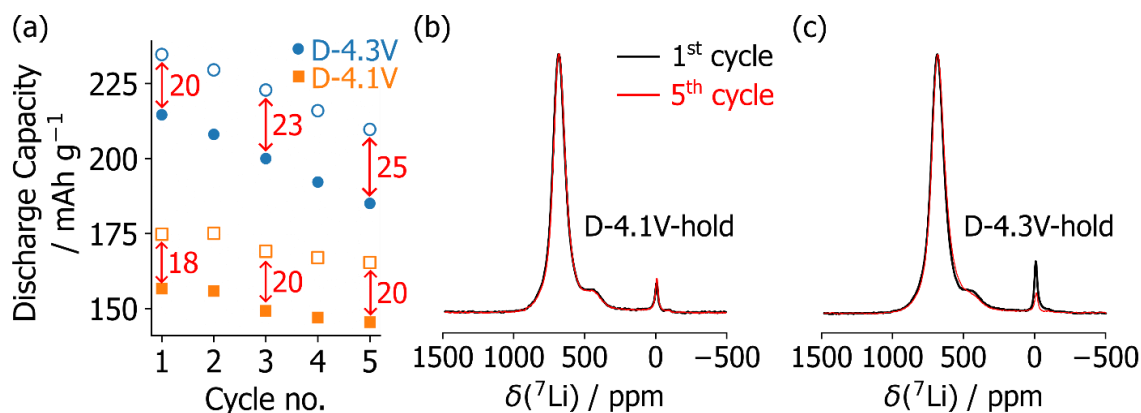


Figure S4.20. Stability of bulk structure over 5 cycles. (a) Reversible capacity over 5 cycles before (closed symbol) and after (open symbol) a 10-hour 3.0 V hold. For the 4.1 V cells, the capacity recovered during the voltage hold is stable over the first 5 cycles, while for the 4.3 V cells, a linear increase in recovered capacity is observed. ^7Li ssNMR spectra ($B_0 = 2.35$ T and 60 kHz MAS) of cathode samples collected after the 1st (solid black) and 5th (dashed red) cycle for (b) D-4.1V-hold and (c) D-4.3V-hold cells.

Chapter 5. New Insights into the Composition of Fatigued Phases Formed During Long-term Cycling of LiNiO_2 ⁴

Abstract. Bulk degradation modes in the LiNiO_2 cathode are examined using ex situ X-ray diffraction, magnetometry, and ssNMR. While a small amount of Ni migration is observed within the layered structure, the bulk structure evolves into a mosaic of domains with different electrochemical activities and Li stoichiometries, a phenomenon exacerbated upon high voltage cycling. This leads to the formation of so-called “fatigued” phases, which have limited capacity and impeded lithium extraction. Our combined XRD and ssNMR analysis can for the first time differentiate between fatigued phases in LiNiO_2 and determine their Li content.

⁴ The content of chapter 5 and its corresponding appendix section is currently being prepared for publication and is the result of a collaboration with BASF SE and Prof. Matteo Bianchini at the University of Bayreuth.

5.1. Introduction

The formation of a densified phase at the surface of Ni-rich NMCs (e.g., $\text{LiNi}_{0.8}\text{Mn}_{0.1}\text{Co}_{0.1}\text{O}_2$ or NMC811) during cycling has been proposed to limit the amount of Li that can be extracted from the core of the particles at high states of charge due to strain from the lattice mismatch between the densified surface phase and the bulk layered phase.²⁰⁸ The inability to fully delithiate the bulk phase is referred to as structural “fatigue”. For LNO, the formation of densified surface layers has been correlated with capacity loss,^{133,137,138,201} which implies the formation of fatigued phases or domains, although the exact nature of such phases/domains has not yet been determined. In fact, while XRD is widely used to track long-range structural changes in the electrode during electrochemical cycling, it is unable to provide information on the Li content and distribution within the crystal structure due to lithium’s very weak scattering factor. Conversely, ^7Li ssNMR is a powerful tool to investigate changes in the Li local environments. Here, we combine those two techniques to probe the long-range and short-range structure of LNO cathode samples collected at various stages of cycling to determine both the Li content and structure of the fatigued phases arising during long-term operation, and to better understand the nature of the defects in the as-synthesized material and after extended cycling.

5.2 Results and Discussion

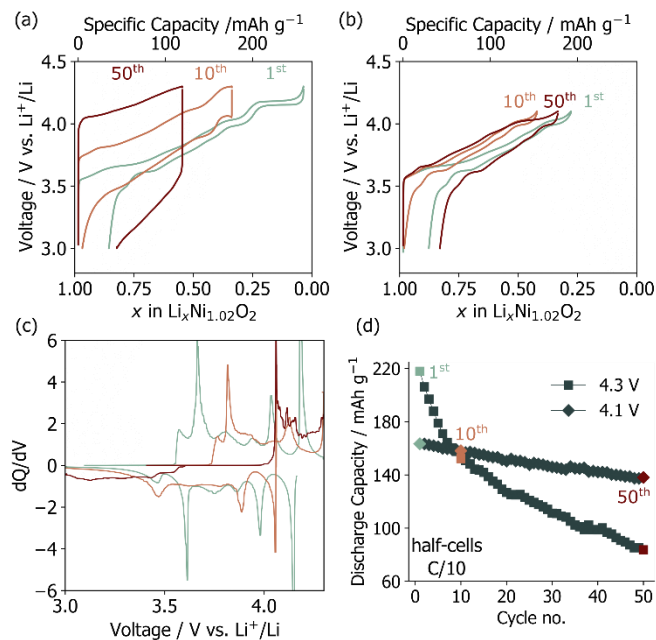


Fig. 5.1 Electrochemical data for LiNiO₂ half cells cycled at a rate of C/10. Voltage profiles for the 1st, 10th, and 50th cycle are shown for the (a) 4.3 V and (b) 4.1 V cells. (c) differential capacity, dQ/dV (mAh g⁻¹ V⁻¹), plot for a cell cycled up to 4.3 V. (d) The average discharge capacity of three cells cycled up to 4.3 V or 4.1 V over 50 cycles.

Polycrystalline Li_{1-y}Ni_{1+y}O₂ was synthesized through a co-calcination route outlined in previous reports^{122,209}, where the off-stoichiometry (y) was determined to be 0.015 (1.5%) based on Rietveld refinements of high resolution sXRD data previously reported on the same batch.²⁰⁹ Electrodes were fabricated and cycled in Li half cells. The main features in the voltage curves or differential capacity (dQ/dV) curve shown in **Fig. 5.1a-c** are related to the sequential phase transitions (H1 → M → H2 → H3 on charge, where H stands for hexagonal (*R-3m*) and M stands for monoclinic (*C2/m*)) occurring during electrochemical cycling^{7,201,210}, as detailed in **Fig. S5.1**. The discharge capacity averaged over three cells for each cycling condition is plotted in **Fig. 5.1d**. Cells cycled up to 4.3 V have a large initial discharge capacity of ~220 mAh g⁻¹, which rapidly decays to ~80 mAh g⁻¹ after 50 cycles. The loss of capacity is largely due to impedance

build up as seen in the large voltage hysteresis in the voltage profiles that develops from the 1st to the 50th cycle (**Fig. 5.1a**). When the H2-H3 transition is prevented by reducing the upper voltage cutoff to 4.1 V, the capacity retention is significantly improved (**Fig. 5.1b**), albeit at the cost of a reduced initial discharge capacity. Despite the improved stability when using a lower cutoff potential, a significant irreversible capacity is still observed in the 50th cycle. The capacity fade observed here is slightly more severe than in some prior reports,^{145,158,201} possibly due to the slower (C/10) (dis)charge rate used in the present work, which maximizes the extent of the H2-H3 phase transition and time spent at high potentials, or due to the use of relatively thick free standing electrode films ($\approx 11\text{-}15\text{ mg cm}^{-2}$). The evolution of the dQ/dV curve of LNO cycled up to 4.3 V is significant (**Fig. 5.1c**) and suggestive of major bulk structural rearrangements over the first 50 cycles, as discussed in more detail in **ESI Note 5.1**. In contrast, the electrochemical features of LNO are mostly unchanged upon long-term cycling to 4.1 V (**Fig. S5.2**).

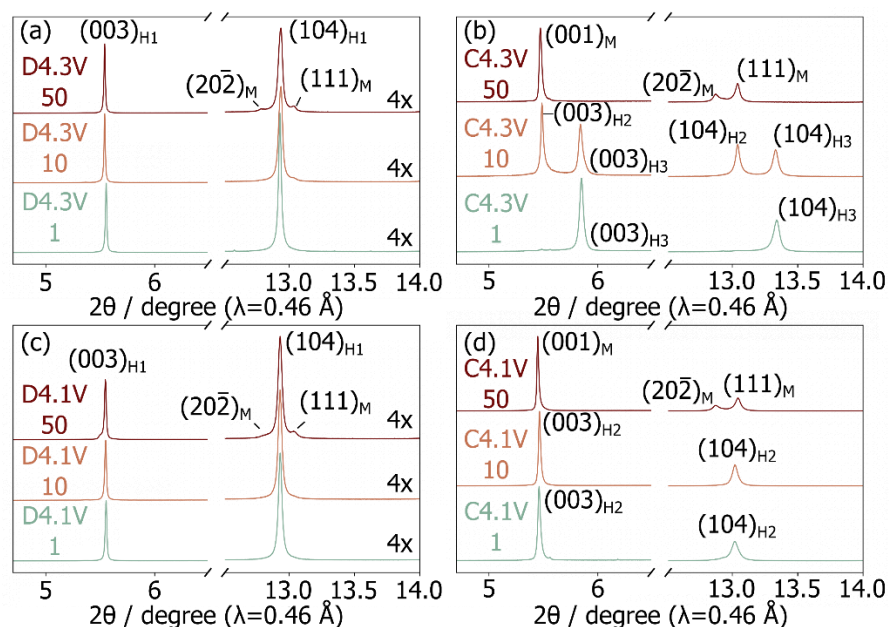


Fig. 5.2 Selected regions from sXRD patterns collected on *ex situ* samples in the (a,c) discharged and (b,d) charged states for cells cycled up to (a,b) 4.3 V and (c,d) 4.1 V. Crystallographic parameters derived from the refinements are tabulated in **Table S5.1** and full sXRD patterns are provided in **Fig. S5.3-6**.

To investigate structural degradation processes in LNO, *ex situ* cathode samples were extracted after 1, 10, and 50 cycles in the charged (4.3 V or 4.1 V) and discharged (3.0 V) state. Samples are labelled “C” or “D” when extracted on charge or discharge, respectively, with the upper cutoff voltage and cycle number indicated. A Le Bail fit of the sXRD data collected on the various *ex situ* samples of interest (**Fig. 5.2** and **Table S5.1**) was performed to identify the H1/M/H2/H3 crystalline phase(s). Relative changes in the Li content of these phases were inferred from the evolution of their refined lattice parameters, as discussed in more detail in **ESI Note 5.2**. Overall, we find that the discharged samples all contain a major H1 phase with a decreasing Li content upon cycling, while a secondary M phase grows with aging, especially for the D4.3V series. Both observations reveal a loss of Li inventory. More substantial differences are observed between charged samples. Li extraction becomes less effective after extended

cycling, consistent with previous work,^{133,158} and a gradual phase evolution from entirely H2 to entirely M is observed across the C4.1V sample series, while the C4.3V samples evolve from entirely H3, to H3 and H2, to entirely M.

Electrochemically-induced transition metal migration is a common degradation mode for layered oxide cathodes.^{208,211–215} In the case of NMC811, a small ($\sim 1\%$)^{208,215} or no²¹⁴ increase in Li-Ni mixing is observed upon extended cycling. While Ni migration has been reported after the first cycle of LiNiO₂¹³⁵, structural characterization of electrochemically cycled LNO samples has been limited to bulk phase identification without refinement of Ni_{Li} occupancies,^{133,216} save for one study that reports the presence of tetrahedral Ni in the Li layers after 20 cycles¹⁵⁴. Here, Rietveld refinements were performed on the *ex situ* sXRD patterns to obtain the Ni occupancy in the interlayer spacing. Due to overlap of M and H1 reflections, the Ni_{Li} fraction could not be determined with accuracy for D4.3V-10, D4.3V-50, and D4.1V-50. Refinements for charged samples were easier to perform and interpret since these samples are either single phase or comprised of two phases with no overlapping reflections. The Ni_{Li} occupancy does not evolve for samples C4.3V-1, C4.1V-1 and C4.1V-10 and remains at its pristine value of 1.5%. However, the Ni_{Li} occupancy slightly increases to 1.7% for both the H2 and H3 phases present in C4.3V-10, and for the single M phase in C-4.1V-50, and to 3.2% for the single M phase in C4.3V-50. Overall, these results indicate negligible Ni migration to the interlayer space upon cycling LNO up to 4.1 V, and a small amount of Ni migration (from 1.5% to 3.2%) with a 4.3 V upper cutoff voltage.

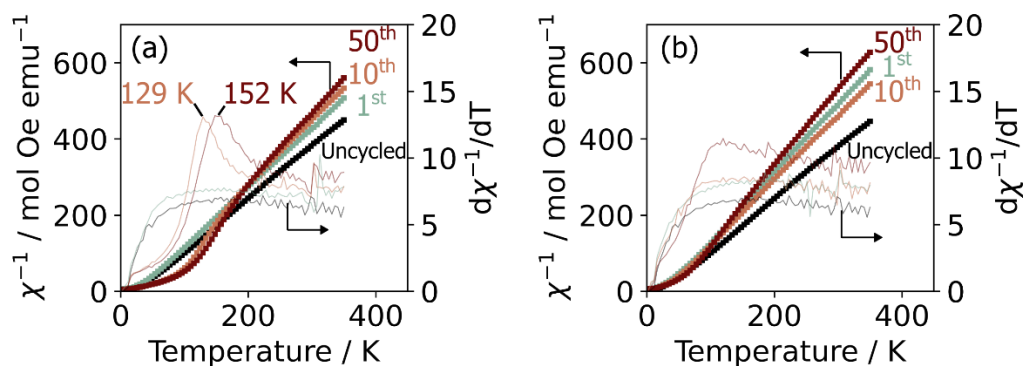


Fig. 5.3 Inverse magnetic susceptibility (χ^{-1}) vs. temperature (T) curves collected on *ex situ* samples in the discharged state after the 1st, 10th and 50th cycle up to (a) 4.3 V and (b) 4.1 V. Magnetic transition temperatures are identified by the differential magnetic susceptibility, $d\chi^{-1}/dT$ (mol Oe emu⁻¹ T⁻¹), shown in the secondary y-axis.

Next, we use SQUID magnetometry to assess Ni migration in the multi-phasic discharged samples that prove challenging to characterize with sXRD. While a paramagnet at room temperature, LNO ($\text{Li}_{1-y}\text{Ni}_{1+y}\text{O}_2$) is ferrimagnetic at temperatures below a certain transition temperature that increases with the Ni overstoichiometry (y) and fraction of Ni_{Li} defects.^{122,125,159} Here, $y = 0.015$ is fixed and the magnetic transition temperatures obtained from the inverse magnetic susceptibility (χ^{-1}) vs. temperature data curves (and derivative ($d\chi^{-1}/dT$) curves) in **Fig. 5.3a-b** for the D4.3V and D4.1V samples, respectively, can be used to track the evolution of Ni_{Li} defects with cycling. The effective magnetic moments (μ_{eff}) and Curie-Weiss constants (θ_{CW}) obtained from fits of the magnetic susceptibility data in the paramagnetic (Curie-Weiss) regime are listed in **Table S5.2** and discussed in **ESI Note 5.3**. As expected, χ^{-1} varies linearly with temperature in the paramagnetic regime, resulting in a constant ($d\chi^{-1}/dT$) curve at high temperatures for all samples. χ^{-1} is no longer linear with temperature in the magnetically coupled regime, leading to a sloped ($d\chi^{-1}/dT$) profile. For the D4.3V-10 and D4.3V-50 samples, a sharp magnetic transition manifests itself as a peak in the $d\chi^{-1}/dT$ profile at 129 K and 152 K, respectively, in contrast to the uncycled electrode, D4.3V-1, and all

of the D4.1V samples, for which no clear magnetic transition can be observed. Those results indicate a greater fraction of Ni_{Li} defects in LNO samples cycled over the larger voltage window, which increases with cycle number. Finally, the magnetic susceptibility data measured on the charged C-4.1V and C-4.3 V samples (χ^{-1} and $d\chi^{-1}/dT$ plotted in **Fig. S5.7**) show no clear magnetic transition temperature, which suggests that the magnetic clusters that lead to a magnetic transition in the D4.3V-10 and D4.3V-50 samples are at least partially oxidized on charge and are therefore a part of the redox-active LNO phase rather than a secondary magnetic phase.

Finally, the effects of electrochemical extended cycling on the local structure of LNO was investigated using ^7Li ssNMR. In LNO, the dominant spin interactions affecting the ^7Li ssNMR signal are the hyperfine (paramagnetic) interactions between unpaired electron spins arising from open-shell Ni^{2+} and Ni^{3+} species in the material (Ni^{4+} is low spin d^6 and therefore diamagnetic) and the ^7Li nuclear spins under consideration. Through-space dipolar couplings between the electron and nuclear spins result in severe broadening of the ssNMR resonances, while through-bond Fermi contact interactions result from delocalization of unpaired electron spin density from the $\text{Ni}^{2+/3+}$ d orbitals to the Li s orbitals via bridging O p orbitals and shift the ^7Li ssNMR resonant frequency by 10s up to > 1000 ppm such that the observed ^7Li chemical shift can be approximated by its Fermi contact contribution. All ^7Li spectra acquired on *ex situ* LNO samples exhibit a resonance at ~ 0 ppm assigned to diamagnetic Li impurities (e.g., Li_2CO_3 , Li_2O , LiPF_6 , LiF) present at the surface of the particles and resulting from surface reactivity or residual electrolyte salt. Spectra acquired on the D4.3V and D4.1V series are shown in **Fig. 5.4a** and **5.4c**, respectively, and are comprised of two resonances at ≈ 700 ppm

and 520 ppm. The ≈ 700 ppm and 520 ppm signals have been attributed to Li in a pristine LNO environment and near residual Ni^{4+} species,^{202,209} respectively, indicating the presence of both fully and partially lithiated domains in all of the discharged samples. In sample D4.3V-50, an additional resonance is observed at 1100 ppm, which is consistent with Li in Ni^{2+} -rich environments,²⁰⁹ e.g., near multiple Ni_{Li} defects. This assignment is consistent with the sXRD and SQUID magnetometry results discussed earlier.

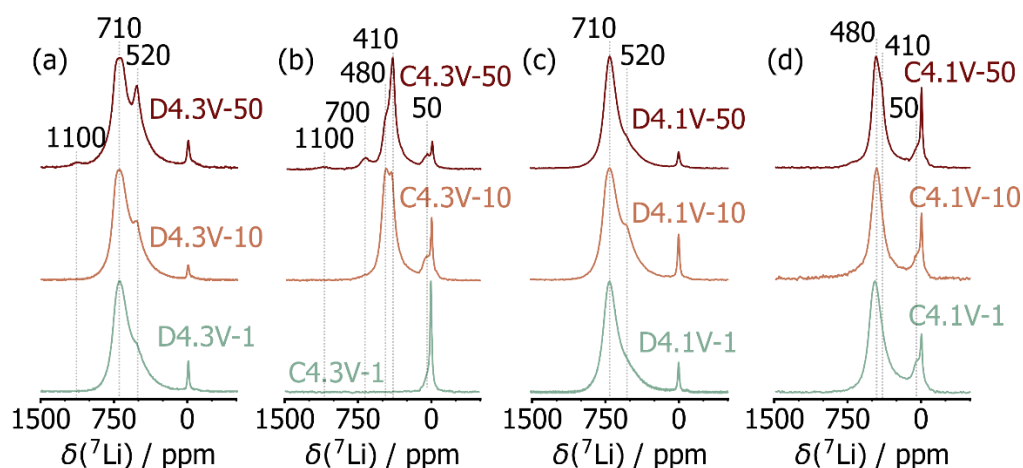


Fig. 4 ${}^7\text{Li}$ ssNMR spectra collected on *ex situ* samples in the (a,c) discharged and (b,d) charged states for cells cycled to (a,b) 4.3 V and (c,d) 4.1 V. All spectra were acquired at 2.35 T and 60 kHz MAS and are normalized to the most intense signal.

When it comes to *ex situ* samples extracted on charge, the ${}^7\text{Li}$ ssNMR spectrum evolves significantly across the C4.3V series (**Fig. 5.4b**), while minimal changes are observed for the C4.1V series (**Fig. 5.4d**), consistent with the improved structural stability of LNO when cycled over a smaller voltage window. Focusing on the 4.3V series, on initial charge (C4.3V-1), LNO is nearly completely delithiated, as indicated by the single, low intensity signal at 50 ppm present in the spectrum. This low intensity signal with a small paramagnetic shift is consistent with residual Li in the interlayer

space of LNO with mostly Ni^{4+} neighbors but (at least) one nearby Ni in a lower oxidation state. After 10 cycles (C4.3V-10), the spectrum exhibits two new signals at 410 ppm and 480 ppm, besides the low intensity signal at 50 ppm (see fitted spectrum in **Fig. S5.9**). The new, highly shifted resonances indicate the presence of Li and Ni^{3+} species in the charged cathode, in good agreement with the rapid loss of electrochemical activity and capacity upon cycling LNO up to 4.3 V. While the 410, 480, and 50 ppm signals are still present in the C4.3V-50 spectrum, two additional signals are observed at 700 ppm and 1100 ppm (see fitted spectrum in **Fig. S5.10**). The 700 ppm signal is attributed to Li species in fully lithiated and therefore electrochemically inactive LNO, presumably resulting from particle cracking and loss of contact with the composite electrode / current collector. The 1100 ppm resonance, previously attributed to Li near multiple Ni_{Li} defects in LNO, is present on both charge and discharge after 50 cycles, which suggests that these Li species are trapped in the interlayer space of LNO. Overall, similarly to NMC811²⁰⁸, the sXRD and ssNMR results presented here suggest the presence of both electrochemically active (close to fully delithiated) and fatigued (partially delithiated) particles or sub-particle domains at high states of charge at cycle 10 and 50. In NMC 811, phase separation occurs particle by particle, and whether a particle is only partially or fully electrochemically active is determined by the thickness of the densified surface layer.²⁰⁸

Overall, our results reveal that repeated electrochemical (de)lithiation induces significant changes to the long-range and the local structure of LNO, with degradation being accelerated upon cycling to 4.3 V. Irrespective of the upper cutoff voltage, the fraction of intermediate M phase grows at the expense of the H1 phase in the discharged

samples, indicating a net loss of Li inventory upon long-term cycling. The ability to extract Li from the LNO structure also becomes more limited with increasing cycle number, as evidenced by the incomplete conversion to the H3 phase upon charge to 4.3 V, or to the H2 phase upon charge to 4.1 V, and the increased Li signal intensity detected by ssNMR at the top of charge. In conjunction with the build-up of fatigued particles or sub-particle domains, a small amount of Ni migration (~1.5% of the Ni) is detected in samples cycled up to 4.3 V and leads to trapped Li in the interlayer space of LNO, as evidenced by the 1100 ppm signal in the ^7Li ssNMR spectra obtained after 50 cycles.

We find that sXRD and ssNMR can be used in tandem to determine the fraction and composition of the fatigued phases formed in LNO samples cycled up to 4.3 V. Our approach relies on a comparison of the ^7Li ssNMR spectra obtained on the C4.3V-10 and C4.3V-50 samples with those collected on *ex situ* samples obtained during the first charge process (**Fig. S5.8**), as described in more detail in **ESI Note 5.4**. While the C4.3V-1 sample contain a single H3 phase with Li content of 0.03 after correcting for Li loss to side reactions, the C4.3V-10 sample comprises an H2 and an H3 phase with a total Li content of 0.16, and the C4.3V-50 sample comprises a minor H1 phase (0.03% molar phase fraction assuming a Li content of 0.98) and two M phases with Li contents of 0.43 ($\text{M}_{0.43}$, 19.60% molar phase fraction) and 0.34 ($\text{M}_{0.34}$, 80.37% molar phase fraction), respectively, resulting in a total Li content of 0.35. The evolving Li content in the charged samples can be used to separate and quantify bulk contributions to the capacity decay. Specifically, the capacity loss due to the inability to extract Li from the bulk cathode amounts to 35.6 mAh g^{-1} from the 1st to the 10th cycle, and to 52.0 mAh g^{-1} from the 10th to 50th cycle. In comparison, the total capacity loss (quantified from

coulometry and encompassing both bulk and surface effects) amounts to 65.6 mAh g⁻¹ from the 1st to the 10th cycle, and to 68.7 mAh g⁻¹ from the 10th to the 50th cycle. The capacity loss due to bulk irreversibilities is lower than the total capacity decay at all stages of cycling, indicating additional surface contributions from, e.g., particle cracking or electrode/electrolyte reactivity. In fact, surface contributions become less severe after the 10th cycle due to deactivation of the H2-H3 phase transition.

5.3 Conclusions

In summary, this work furthers our understanding of the degradation processes and fatigued phases that form in LNO over extended cycling. The specific capacity of LNO is found to decay more rapidly over the first 10 cycles and to taper off after that, likely due deactivation of the H2-H3 transition that leads to additional bulk and surface degradation modes. We derive the Li content of the fatigued phases in samples charged to 4.3 V from combined sXRD and ssNMR analysis, which allows us to determine the contribution to the observed capacity decay due to limited bulk Li extraction. While this loss of capacity is related to the formation of a high impedance, densified layer at the surface of LNO particles^{19,138,217,218}, our sXRD, SQUID magnetometry, and ssNMR results all indicate that a small amount of Ni (~1.5% of the Ni) migrates into the interlayer space of LNO in the bulk upon cycling to 4.3 V and traps nearby Li species, in good agreement with prior work.^{145,154} Furthermore, prior work on related Ni-rich layered oxide cathodes has shown that the densified layer that builds up at the surface of the particles limits the amount of Li that can be extracted from the bulk cathode due to the required coherency between the surface layer and bulk layered rock salt phase, which prevents the large bulk volume changes that occur at high states of delithiation.²⁰⁸

Hence, the Li content of the fatigued phases determined herein, and their lattice parameters, may provide clues as to the exact nature of the densified layer formed at the surface of LNO.

5.4 Appendix for New Insights into the Composition of Fatigued Phases Formed

During Long-term Cycling of LiNiO₂

Experimental details

Material Synthesis: Li_{1-y}Ni_{1+y}O₂ active materials were synthesized using a solid-state synthesis route from coprecipitated Ni(OH)₂ precursors (Hunan Zoomwe Zhengyuan Advanced Material Trade Co., Ltd). LiOH·H₂O (Albemarle Corporation) was ground prior to the synthesis and mixed with Ni(OH)₂ in a laboratory blender (Kinematica AG). Li:Ni mol ratio of 1.04 was used. The mixture was placed in a ceramic crucible and fired in a laboratory box-type furnace (inn High Therm GmbH) under a flowing pure O₂ environment. The mixture was first heated to 400 °C and fixed at that temperature for 4 h and then the temperature was ramped up to 700 °C and held there for 6 h. A ramp rate of 3 °C was used for both heating steps.

Electrochemistry: Free-standing LNO: carbon black (Super C65; MTI Corporation): polytetrafluoroethylene (PTFE; Sigma Aldrich) films were fabricated in a mass ratio of 94:3:3. The electrode was cycled in Li half cells using Swagelok cells, 1 M LiPF₆ in ethylene carbonate, dimethylcarbonate, and diethylcarbonate (EC/DMC/DEC = 1/1/1 v/v/v) electrolyte, and Whatman GF/D glass microfiber separators. Cells were cycled from 3.0 V to an upper voltage cutoff of either 4.1 V or 4.3 V vs. Li/Li⁺ at a rate of C/10 (1 C = 200 mA g⁻¹). The loading density for the electrodes were ≈11-15 mg cm⁻². All cells were cycled on

an Arbin BT2000 or Bio-logic VMP-3e potentiostat. *Ex Situ* samples were prepared by cycling to the desired conditions and extracting the cathode inside an Ar filled glovebox. *Ex Situ* samples were washed in DMC (Sigma) and dried under vacuum before analysis.

X-ray Diffraction: *Ex Situ* samples were loaded into glass capillaries and measured at Beamline 11-BM at the Advanced Photon Source (APS). All patterns were collected in Debye–Scherrer geometry from 0.5° to 50° 2θ at room temperature with data points collected every 0.001° 2θ and a scan speed of $0.01^\circ/\text{s}$. Refinements were done using the TOPAS software suite¹¹⁵ and detailed in **ESI Note 5.2**.

Magnetometry: Samples were loaded into sealed quartz tubes (1 mm ID and 3 mm OD). SiO_2 powder (Advalue Tech) was used to center the cathode samples inside the quartz tubes. Measurements were done on a Quantum Design MPMS3 SQUID magnetometer. Zero field and field cooled M(T) measurements were carried out from 2 to 350 K with $H = 0.1$ T.

NMR: Solid state ^7Li ssNMR measurements were done on a wide bore Bruker BioSpin spectrometer with a DMX 500 MHz console and a home built 1.3 mm single X-broadband magic angle spinning (MAS) probe. All spectra were acquired at $B_0 = 2.35$ T (100 MHz for ^1H) with 60 kHz MAS using dry nitrogen and the probe was tuned to ^7Li (38.9 MHz). Samples were packed into 1.3 mm zirconia rotors inside an Ar glovebox and closed with Vespel caps. ^7Li chemical shifts were referenced to 0 ppm with 1M aqueous LiCl solutions. All acquisitions were done with a rotor synchronized spin-echo sequence with a 90° pulse of $0.45 \mu\text{s}$. A recycle delay of 50 ms was sufficient for paramagnetic signals to be fully relaxed. ssNMR data was processed using Bruker TopSpin 3.6.5 and spectral fits were done with DMfit.¹¹⁶

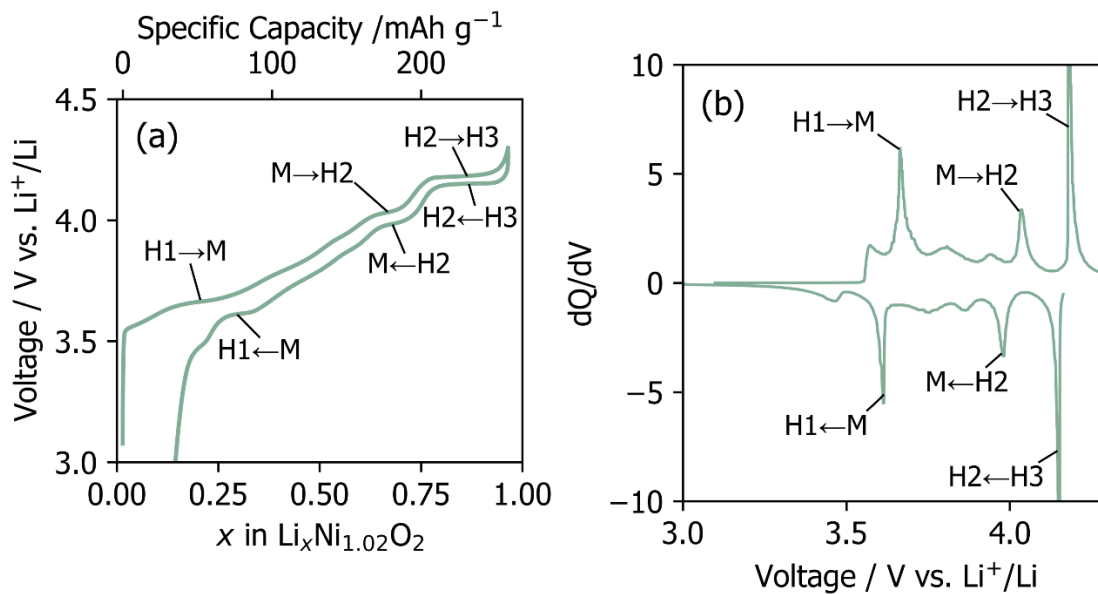


Fig. S5.1 (a) Voltage profile and (b) differential capacity, dQ/dV , ($\text{mAh g}^{-1} \text{V}^{-1}$), for the first charge-discharge cycle with phase transitions highlighted.

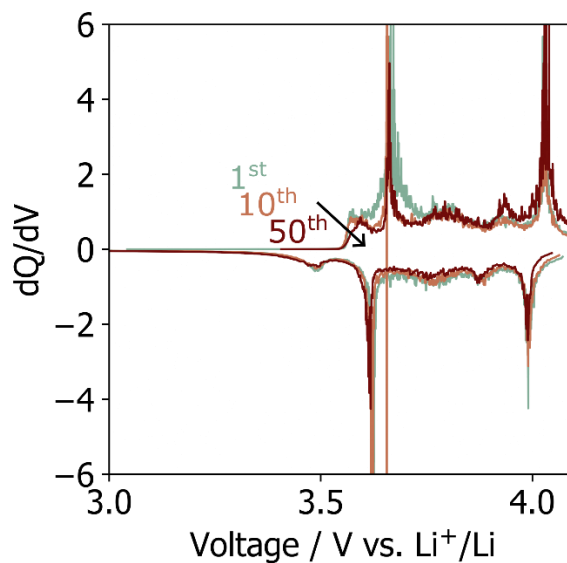


Fig. S5.2 Differential capacity, dQ/dV ($\text{mAh g}^{-1} \text{V}^{-1}$), plots obtained during the 1st, 10th, and 50th cycle with a 4.1V upper voltage cutoff.

ESI Note 5.1. Analysis of the differential capacity curves obtained for LNO half- cells cycled up to 4.1 or 4.3 V vs. Li/Li⁺

Differential capacity (dQ/dV) analysis was carried out to better understand the changes in the electrochemical processes taking place upon extended operation. Differential capacity plots for the 1st and 10th cycles for cells cycled up to 4.3 V (**Fig. 5.1c**) exhibit three prominent dQ/dV peaks that correspond to the two-phase reactions associated with the H1 to M, M to H2, and H3 to H3 phase transitions^{104,201}, while the 50th cycle differential capacity plot is relatively featureless. Local minima between H1 to M and M to H2 phase transitions in the differential capacity plot for the 1st cycle have been attributed to stable Li-vacancy orderings in the bulk at those compositions.^{104,219} Interestingly, the minimum immediately after the H1 → M transition is no longer present at the 10th cycle, which cannot simply be explained by an increase in impedance since this would lead to a shift of all of the peaks. The loss of the dQ/dV minimum suggests instead that the Li-vacancy orderings are disrupted by the structural changes taking place during cycling. In contrast, the dQ/dV features observed for cells cycled up to 4.1 V (**Fig. S5.2**) are relatively stable, with peak and local minima positions not changing significantly during extended cycling. The most notable change for the 4.1 V cells is the narrowing of the dQ/dV peak associated with the H1 to M phase transition on charge.

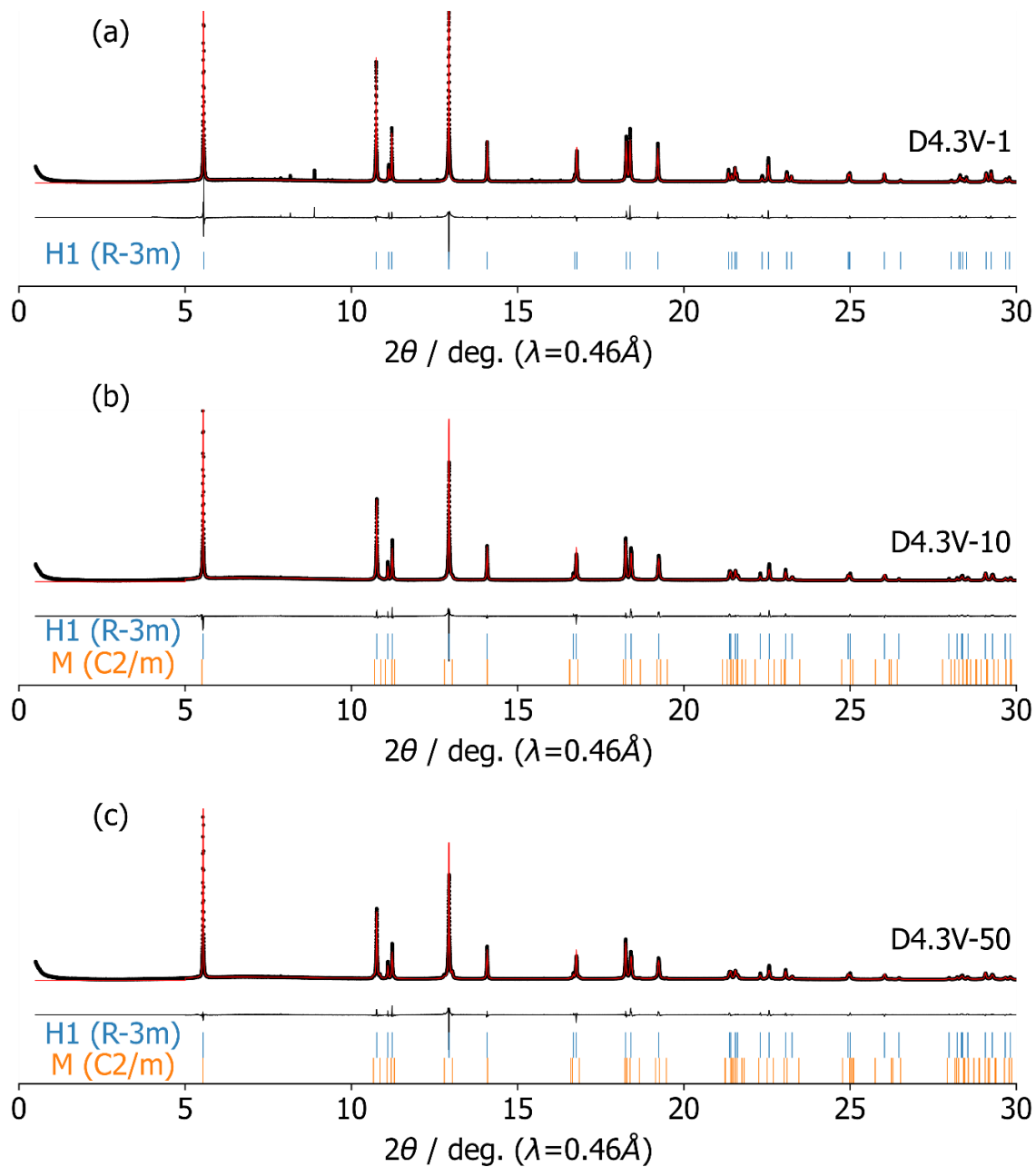


Fig. S5.3 Full synchrotron XRD patterns collected on the D4.3V sample series: (a) D4.3V-1 (b) D4.3V-10 (c) D4.3V-50.

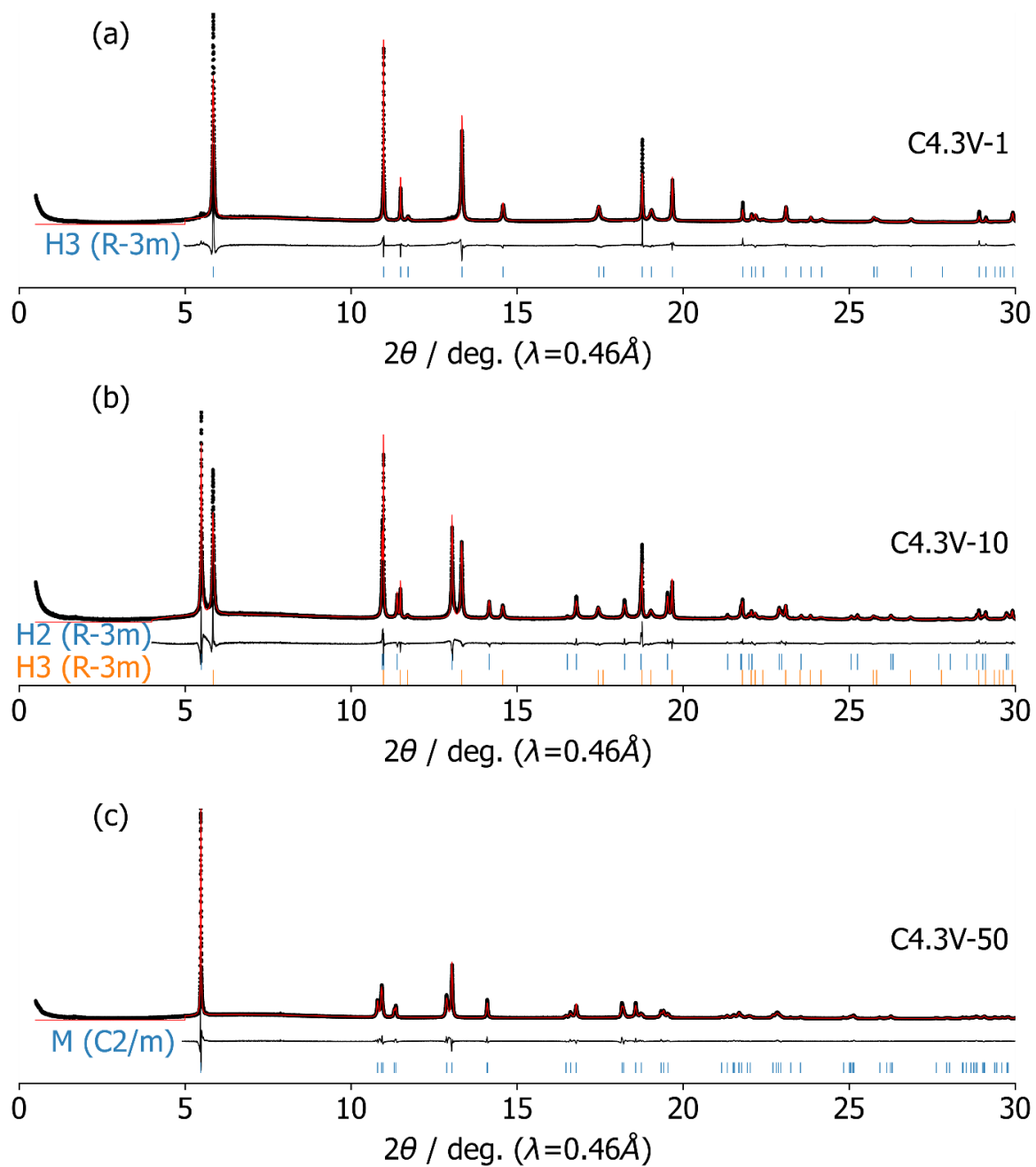
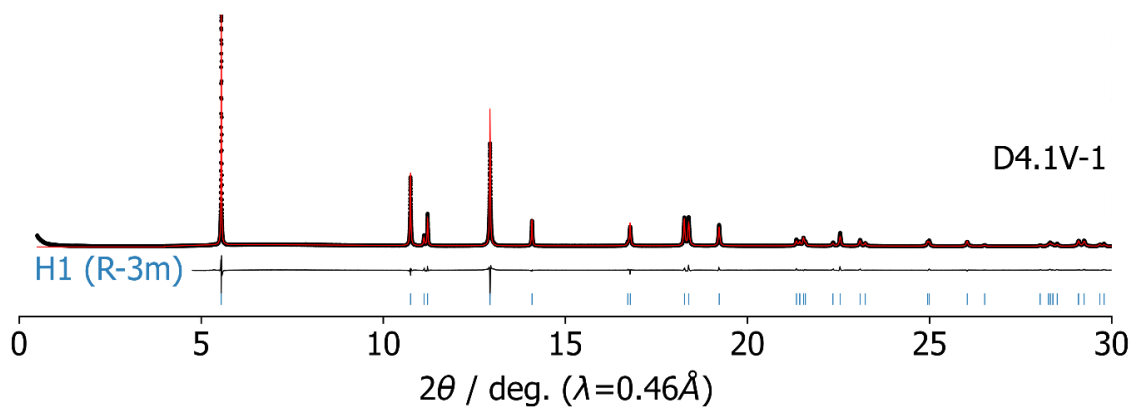
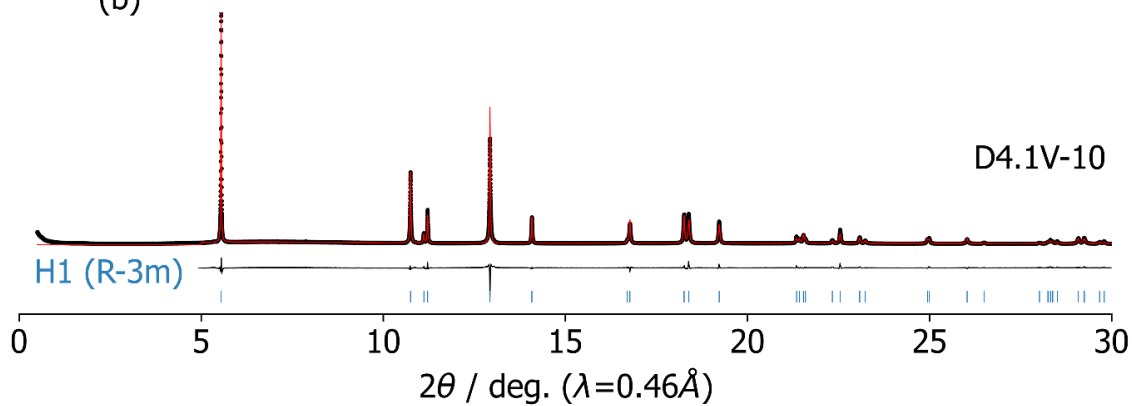


Fig. S5.4 Full synchrotron XRD patterns collected on the C4.3V sample series: (a) C4.3V-1 (b) C4.3V-10 (c) C4.3V-50.



(b)



(c)

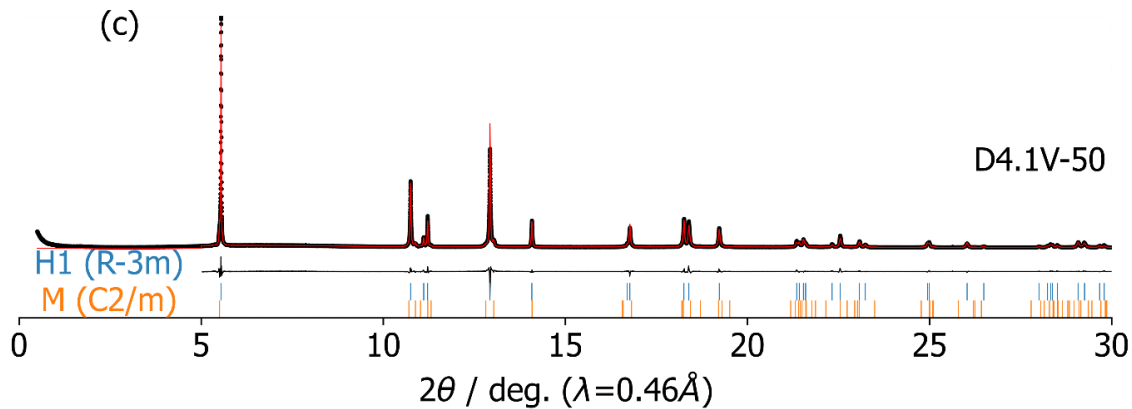


Fig. S5.5 Full synchrotron XRD patterns collected on the D4.1V sample series: (a) D4.1V-1 (b) D4.1V-10 (c) D4.1V-50.

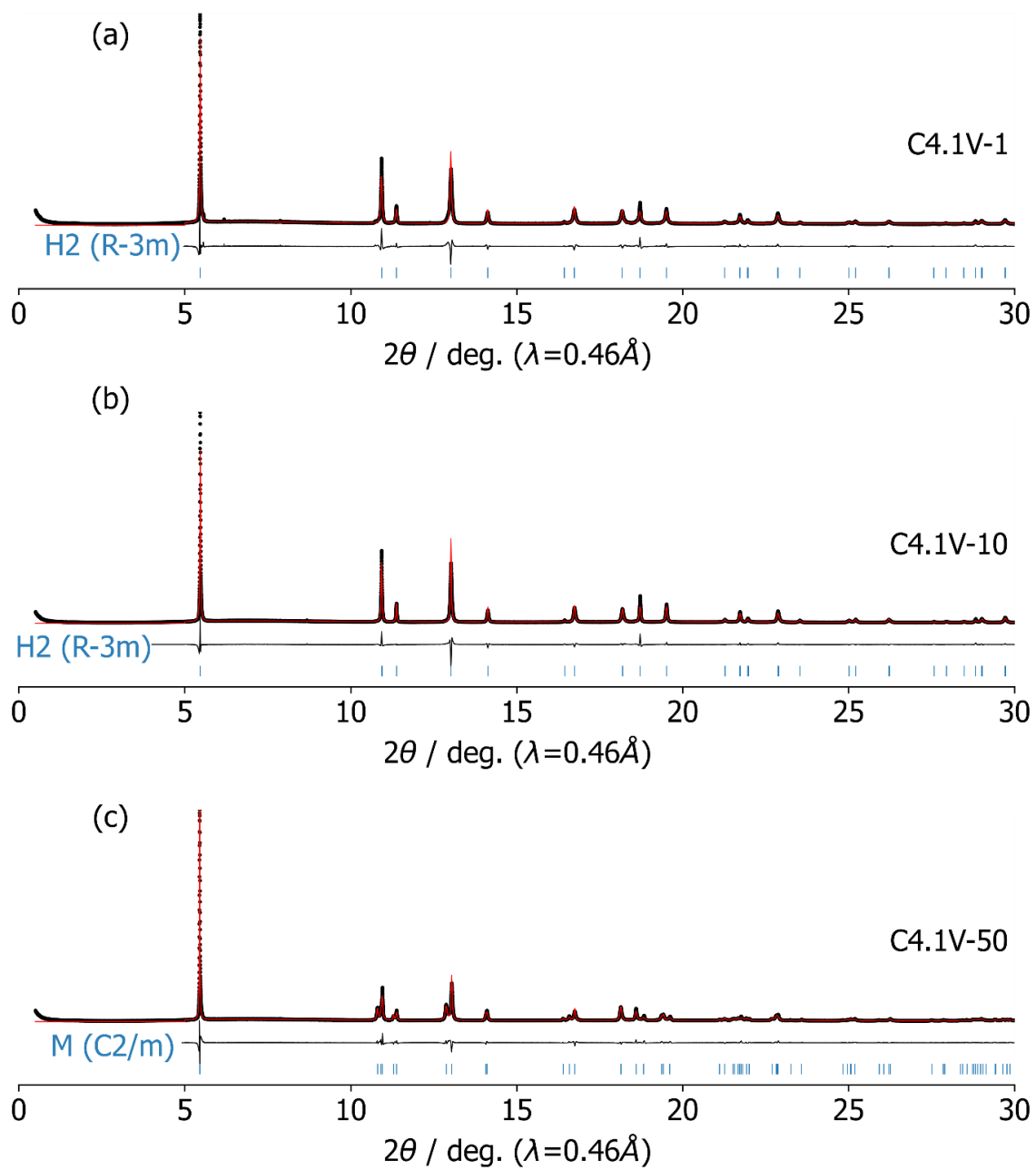


Fig. S5.6 Full sXRD patterns collected on the C4.1V sample series: (a) C4.1V-1 (b) C4.1V-10 (c) C4.1V-50.

Table S5.1. Structural refinement parameters for synchrotron XRD data presented in this work.

Sample	Rw p	Phase 1									Phase2								
		Space Group	a (Å)	B (Å)	c (Å)	be (°)	O_x	O_z	Ni_L i	Phase fraction	Space Group	a (Å)	B (Å)	c (Å)	be (°)	O_x	O_z	Ni_L i	Phase Fraction
C4.3V-1	12.2	R-3m	2.8152 (4)	-	13.4978 (2)	-	-	0.2638 (1)	0.0151 (7)	1									
C4.3V-10	10.3	R-3m	2.8165 (3)	-	13.5120 (2)	-	-	0.2649 (1)	0.0173 (8)	0.52	R-3m	2.8215 (4)	-	14.3855 (2)	-	-	0.264 (1)	0.0169 (8)	0.48
C4.3V-50	9.1	C2/m	4.9438 (6)	2.8195 (4)	5.0950 (8)	109.3484 (7)	0.2638 (3)	0.7868 (2)	0.0317 (7)	1									
D4.3V-1	10.0	R-3m	2.8741 (1)	-	14.2127 (6)	-	-	0.2593 (1)	0.0151 (4)	1									
D4.3V-10	9.4	R-3m	2.8693 (1)	-	14.2462 (7)	-	-	0.2597 (1)	0.0151 (4)	0.94	C2/m	4.9896 (8)	2.8279 (3)	5.0805 (5)	109.784 (1)	0.256 (4)	0.784 (3)	0.015 ^s	0.06
D4.3V-50	9.2	R-3m	2.8698 (1)	-	14.2456 (7)	-	-	0.2597 (1)	0.0150 (4)	0.9	C2/m	5.0040 (2)	2.8322 (1)	5.0597 (3)	109.905 (4)	0.278 (2)	0.796 (2)	0.015 ^s	0.1
C4.1V-1	10.6	R-3m	2.8235 (6)	-	14.4522 (3)	-	-	0.2650 (1)	0.0160 (7)	1									
C4.1V-10	11.6	R-3m	2.8231 (4)	-	14.4443 (2)	-	-	0.2651 (1)	0.0153 (6)	1									
C4.1V-50	10.6	C2/m	4.9403 (7)	2.8074 (5)	5.1112 (7)	109.1596 (7)	0.2648 (3)	0.7899 (2)	0.0173 (6)	1									
D4.1V-1	8.7	R-3m	2.8734 (1)	-	14.2153 (7)	-	-	0.2593 (4)	0.0156 (4)	1									
D4.1V-10	8.8	R-3m	2.8724 (1)	-	14.2228 (7)	-	-	0.2594 (5)	0.0175 (4)	1									
D4.1V-50	8.2	R-3m	2.872 (1)	-	14.2275 (7)	-	-	0.2602 (1)	0.0150 (4)	0.89	C2/m	4.9882 (3)	2.8240 (1)	5.0770 (2)	109.718 (4)	0.223 (1)	0.754 (1)	0.015 ^s	0.11

ESI Note 5.2. Relative in Li content in LNO phases based on their lattice parameters

Protocol for the analysis of the synchrotron XRD data: A Le Bail fit of the synchrotron XRD data collected on the various *ex situ* samples of interest was performed to identify the crystalline phase(s) present in each sample, and determine their space group and refined lattice parameters. The background was fit with a Chebyshev polynomial (10 terms) and additional refinement parameters included axial divergence, crystallite size, microstrain, zero shift, and absorption. These values were fixed in a following Rietveld refinement to obtain the occupancy of Li (3a) sites by Ni (Ni_{Li} occupancy). The total Ni content was fixed to 1.015 and the Ni occupancy factors of the 3a and 3b cation sites of the $R\text{-}3m$ structure were allowed to vary. Stephens peak shapes were used to model anisotropic broadening effects in samples obtained from cycled cells.¹⁶⁰ An attempt to refine for Ni migration into tetrahedral sites on charge led to an unrealistically large fraction of migrated Ni (~0.15) on first charge (C4.3V-1 sample), which remains stable after 10 cycles (C4.3V-10 sample). These results are inconsistent with the ssNMR and magnetometry results obtained on the same samples and are disregarded hereafter.

While a direct relationship has been established between LNO lattice parameters and the Li content in the cathode structure during the first charge-discharge cycle^{104,201}, differences in Ni off-stoichiometry between as-prepared $\text{Li}_{1-y}\text{Ni}_{1+y}\text{O}_2$ samples, and structural degradation during cycling complicate the analysis. Hence, we use a pragmatic approach and instead compare the lattice parameters of similar (e.g., M) phases across samples to infer changes in Li contents with cycling.

Analysis of discharged samples: All discharged samples are comprised of a major H1 phase (synchrotron XRD patterns for the D4.3V and D4.1V samples are shown in **Figures 5.2a** and **5.2c**, respectively), but additional reflections that belong to a monoclinic (M) phase are present in the patterns collected on the D4.3V-10, D4.3V-50, and D4.1V-50 samples. The $(003)_{\text{H1}}$ reflection shifts to lower angles from D4.3V-1 to D4.3V-10, corresponding to an increase in the c lattice parameter from 14.2127(6) Å to 14.2462(7) Å and to a decrease in the Li content within the H1 phase after 10 cycles. A similar $(003)_{\text{H1}}$ position and c lattice parameter is observed for the D4.3V-10 and D4.3V-50 samples, and hence very little change in Li content between these two phases. When it comes to the M phase, the $(001)_{\text{M}}$ reflection overlaps with the $(003)_{\text{H1}}$ peak and we therefore focus on the $(20\bar{2})_{\text{M}}$ and $(111)_{\text{M}}$ peak positions hereafter.

The positions of the $(20\bar{2})_M$ and the $(111)_M$ reflections for D4.3V-10 and D4.3V-50 are similar, which suggests that the M phases in these two samples have similar Li contents. Clearly, the aged cathode still partially converts from the intermediate M phase to the final H1 phase on discharge, albeit the extent of conversion gradually decreases upon cycling, as indicated by the smaller M phase fraction in D4.3V-10 (6 wt%) as compared to D4.3V-50 (10 wt%), consistent with a gradual loss of Li inventory.

The loss of Li inventory occurs at a slower rate when LNO is charged up to 4.1V, since the M phase can only be observed in the 50th cycle discharged sample (D4.1V-50). The $(003)_{H1}$ peak shifts to lower angles across the D4.1V sample series, corresponding to an increase in c lattice parameter from 14.2153(7) Å (D4.1V-1), to 14.2228(7) Å (D4.1V-10), to 14.2275(7) Å (D4.1V-50) and a decrease in Li content. While the c lattice parameters of the H1 phases present in the D4.1V and D4.3V samples are similar at cycle 1, the H1 phases present in the D4.1V-10 and D4.1V-50 samples contain more Li than those present in the D4.3V-10 and D4.3V-50 samples. The $(20\bar{2})_M$ and the $(111)_M$ peak for D4.1V-50 have the same positions as the D4.3V-10 and D4.3V-50 samples.

Analysis of charged samples: While the XRD patterns collected on cathode samples in the discharged state are overall quite similar, there are substantial differences between patterns obtained on samples stopped at 4.1 or 4.3 V on charge. In the absence of structural degradation, the C4.1V samples should be entirely H2, and the C4.3V samples should be entirely H3. A single H2 phase is indeed observed for C4.1V-1 and C4.1V-10, with a small difference in c lattice parameter between the two samples (14.45 Å and 14.44 Å, respectively). In the H2 phase region, a decrease in c lattice parameter is observed with decreasing Li content, which allows us to infer that the H2 phase in C4.1V-10 has a slightly lower Li content than that in C4.1V-1. In contrast, C4.1V-50 exhibits a single M phase, consistent with gradual structural degradation resulting in less effective Li extraction from the LNO cathode after 50 cycles. While the C4.3V-1 sample contains a single H3 phase with a very low Li content (0.01 based on charge passed), as expected, the C4.3V-10 sample contains a mixture of H2 and H3 phases, and the C4.3V-50 sample exhibits a single M phase, again suggesting a gradual loss of electrochemical activity that is more pronounced as the cathode is cycled above 4.1 V due to anisotropic lattice changes that lead to particle cracking and a rise in surface impedance. Overall, the *ex situ* synchrotron XRD analysis reveals that aging of LNO mostly hinders Li

extraction at high states of charge, with the M-H2 and H2-H3 phase transitions becoming inaccessible after 50 cycles, irrespective of the upper cutoff voltage, while Li-rich compositions (within the H1 compositional range) can be accessed in the discharged state. This loss of accessible capacity during the high voltage charge processes is similarly observed in Ni-rich NMCs.^{208,220–222}

Table S5.2. Magnetic moments and Curie-Weiss constants derived from Curie-Weiss fits of the magnetic susceptibility data.

Sample	μ_{eff} (μ_B)	θ_{cw} (K)	χ^0
As-synthesized $\text{Li}_{0.98}\text{Ni}_{1.02}\text{O}_2^*$	1.83(1)	36(1)	-
Pristine electrode	2.20(1)	41(1)	2.39E-04
D4.3V-1	2.07(6)	27(7)	5.07E-05
D4.3V-10	2.02(4)	47(4)	1.72E-04
D4.3V-50	1.90(4)	65(5)	2.04E-04
C4.3V-1	0.38(4)	91(17)	1.42E-04
C4.3V-10	0.99(2)	33(4)	2.48E-05
C4.3V-50	1.37(9)	52(13)	1.76E-04
D4.1V-1	2.05(5)	33(6)	7.77E-05
D4.1V-10	1.91(1)	53(2)	3.18E-04
D4.1V-50	1.67(5)	88(5)	4.93E-04
C4.1V-1	1.19(4)	35(8)	2.96E-04
C4.1V-10	1.00(3)	40(6)	3.18E-04
C4.1V-50	0.98(1)	35(3)	2.15E-04

* these results are reproduced from prior work.²⁰⁹

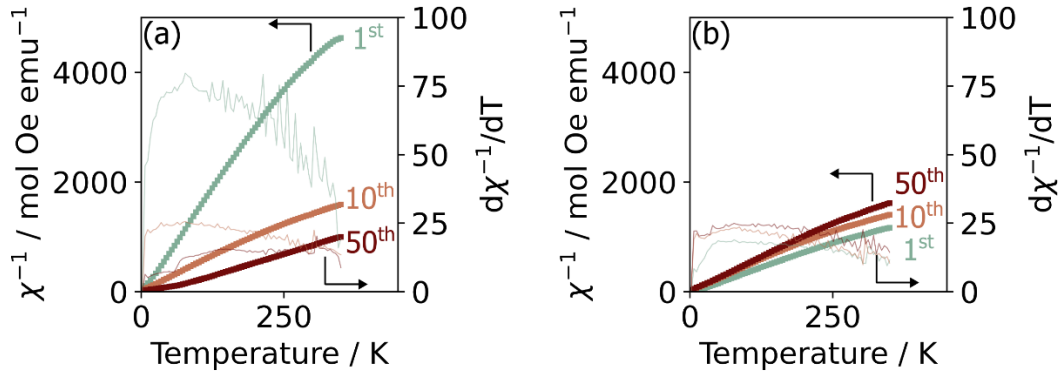


Fig. S5.7 Magnetic susceptibility plots for (a) C4.3V and (b) C4.1V sample series.

ESI Note 5.3. Evolution of the magnetic properties with cycling

The inverse magnetic susceptibility (χ^{-1}) vs. temperature data curves (and derivative ($d\chi^{-1}/dT$) curves) obtained for the discharged (D4.3V and D4.1V) sample series are shown in **Fig. 5.3**. The effective magnetic moments (μ_{eff}) and Curie-Weiss constants (θ_{cw}) obtained from fits of the magnetic susceptibility data in the paramagnetic (Curie-Weiss) regime are listed in **Table S5.2**. The effective magnetic moments of the D4.3V-1 and D4.1V-1 samples, of 2.07(6) μ_{B} and 2.05(5) μ_{B} , respectively, are higher than the spin-only (so) magnetic moment computed assuming a stoichiometric LiNiO₂ composition ($\mu_{\text{so}} = 1.73 \mu_{\text{B}}$). The larger magnetic moments obtained for the cycled cathode samples are likely due to magnetic contributions from the carbon additive and/or binder as observed in the larger μ_{eff} of the uncycled LNO electrode (2.20(1) μ_{B}) when compared to that of the as-synthesized material (1.83 μ_{B} , reported in our prior work²⁰⁹). Despite this additional magnetic contribution, the trends in μ_{eff} and θ_{cw} with cycle number provide insight into the degradation modes in LNO assuming that the contribution from non-LNO components does not change with aging. The effective magnetic moment obtained for *ex situ* samples in the discharged state shows a general decreasing trend from cycle 1 to 50, evolving from 2.07(6) μ_{B} to 1.90(4) μ_{B} for the D4.3V samples, and from 2.05(5) μ_{B} to 1.67(5) μ_{B} for the D4.1V samples. The main cause of the decreasing magnetic moment is likely the presence of residual Ni⁴⁺ on discharge, due to incomplete utilization of the Ni^{3+/4+} redox reservoir in aged cathodes, as discussed in the main text. Interestingly, the decrease in the effective magnetic moment with cycling is not as pronounced for the D4.3V samples as for the D4.1V samples, which could suggest at first glance that the structure of the cathode is more reversible when cycled over the larger voltage range, in contradiction with the synchrotron XRD results presented earlier. Another possibility is that the larger effective magnetic moments measured for the aged 4.3V samples result from a larger fraction of Ni²⁺, which would be consistent with Ni migration into the interlayer space.

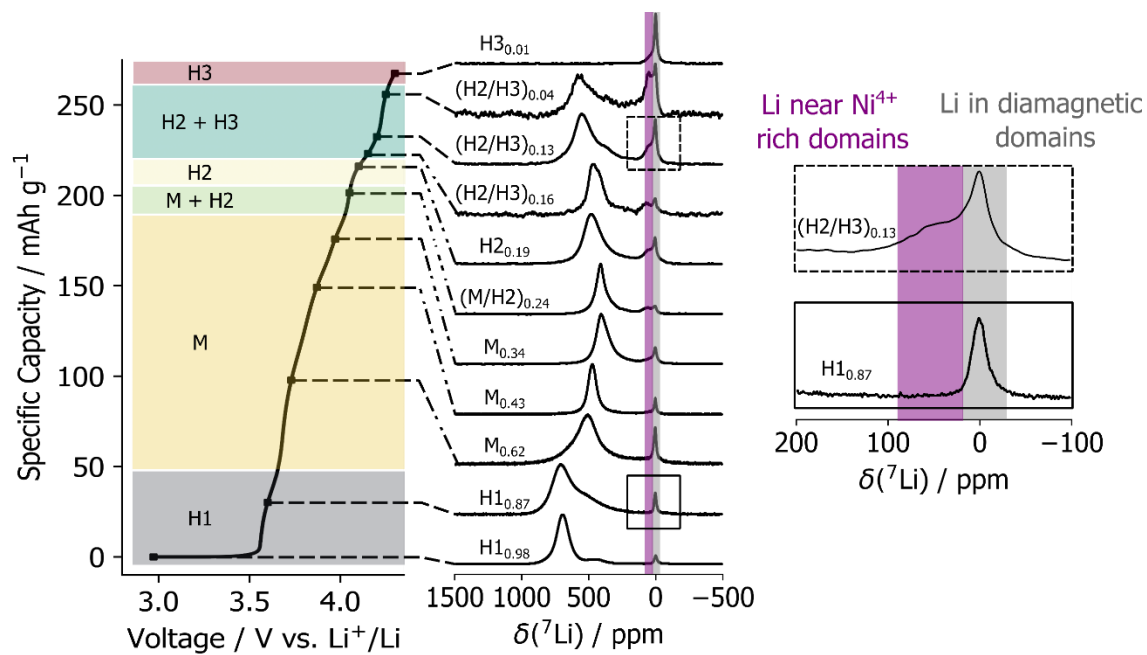


Fig. S5.8 ^7Li ssNMR spectra collected on *ex situ* cathode samples obtained at various stages during the first charge process. The sample labeling scheme adopted here comprises the symmetry label of the LNO phase(s) present in the sample at a given state of charge and the nominal Li content derived from the specific capacity.

Table S5.3. Summary of ^7Li ssNMR parameters obtained from fits of the ssNMR spectra obtained on *ex situ* LNO samples during the first charge process, along with other key descriptors of these samples.

V vs. Li/Li ⁺	x in Li _x Ni _{1-x} O ₂	sXRD phase(s)	Resonance 1				Resonance 2				Resonance 3				Resonance 4			
			δ / ppm	Intensity (a.u.) [*]	Line width (hz)	T2 (ms)	δ / ppm	Intensity (a.u.) [*]	Line width (hz)	T2 (ms)	δ / ppm	Intensity (a.u.) [*]	Line width (hz)	T2 (ms)	δ / ppm	Intensity (a.u.) [*]	Line width (hz)	T2 (ms)
OCV	0.98	H1	695	0.908	4262	2.390	448	0.092	5862	3.810								
3.60	0.87	H1	715	0.361	5480	0.505	579	0.639	13844	0.398								
3.73	0.62	M	514	0.967	7493	0.080	88	0.033	11589	1.124								
3.87	0.43	M	473	0.955	2875	0.178	56	0.045	4389	1.622								
3.97	0.34	M	408	0.501	3336	0.254	343	0.445	5495	0.105	44	0.054	3981	1.526				
4.05	0.24	M+H2	413	0.697	2764	0.372	336	0.220	4955	0.077	61	0.083	3054	2.226				
4.10	0.19	H2	479	0.440	4987	0.093	406	0.441	13923	0.174	35	0.119	4729	1.365				
4.15	0.16**	H2+H3	465	0.454	3690	0.138	406	0.448	5819	0.693	67	0.098	1157	2.923				
4.20	0.13**	H2+H3	546	0.677	6613	0.143	375	0.099	4778	0.624	232	0.096	9826	0.688	33	0.127	3804	1.865
4.25	0.04**	H2+H3	570	0.346	5785	0.241	389	0.400	14424	0.273	49	0.254	2594	1.892				
4.30	0.01**	H3	29	1.000	3843													

* Paramagnetic signal intensity (i.e. excludes intensity from diamagnetic Li signal at ~0 ppm) corrected by accounting for transverse relaxation (T2) effects.

** Nominal Li content based on the measured capacity. Given that parasitic electrochemical reactions tend to occur when cycling LNO above 4.1 V vs. Li/Li⁺, this nominal Li content underestimates the true Li content in the bulk cathode above this potential.

ESI Note 5.4. Composition of the fatigued LNO phases in C4.3V samples from combined ^7Li ssNMR and synchrotron XRD analysis

^7Li ssNMR can provide unique insights into the Li content in the fatigued phases in electrochemically cycled LNO samples. As mentioned in the main text, for LNO, the dominant contribution to the observed ^7Li shift is the paramagnetic shift, which depends sensitively on the amount of unpaired electron spin density at the Li nucleus, and hence on the number and type of Ni-O-Li bond pathways connecting nearby paramagnetic $\text{Ni}^{2+/3+}$ species to the Li nucleus. More specifically, each $\text{Ni}^{2+/3+}$ species in the first and second cation coordination shell around Li contributes a certain amount of paramagnetic shift that depends on the extent of Ni d - O p - Li s orbital overlap, hence on the Li-O and Ni-O bond lengths, and on the Li-O-Ni bond angle, as well as on the Ni oxidation state. The total (observed) ^7Li shift is then the sum over all Ni-O-Li bond pathway contributions, and as such provides information about the local distribution of Ni oxidation states and on the distribution of Li species within each phase in the *ex situ* LNO sample.

Evolution of the ^7Li ssNMR spectra collected on *ex situ* LNO samples obtained during the first charge process: The ^7Li spin echo spectra collected on *ex situ* samples stopped at different stages of the first charge process are shown in **Fig. S5.8**, and the ssNMR parameters derived from fits of those spectra are presented in **Table S5.3**. On initial charge, the nominal Li content in LNO can be derived from the capacity since the Li content in the cathode at the start of the charge process is known. The sample labeling scheme adopted hereafter and in **Fig. S5.8** comprises the symmetry label of the LNO phase(s) present in the sample at a given state of charge and the nominal Li content derived from the specific capacity. For example, the pristine cathode is labeled $\text{H1}_{0.98}$ as it is comprised of the initial $R\text{-}3m$ hexagonal phase (H1) and

contains 0.98 Li per formula unit. The main resonance in the pristine LNO (H1_{0.98}) spectrum appears at 700 ppm, with a minor signal (corresponding to approximately 11% of the Li intensity) at 450 ppm that has been assigned to Li near twin boundaries in our prior work.²⁰⁹ This secondary signal disappears at an early stage on charge and does not reappear on subsequent discharge due to sluggish Li reintercalation into the strained lattice sites near twin boundaries; it is therefore not considered in our analysis. The 700 ppm resonance corresponds to Li in defect-free, stoichiometric LiNiO₂, which interacts with 12 Ni³⁺ species via six 180° and six double 90° Ni-O-Li interactions.²⁰⁹

While one would expect the ⁷Li shift of the main LNO resonance to decrease during the charge process as Ni³⁺ is oxidized to diamagnetic Ni⁴⁺, the chemical shift instead evolves non monotonically (see **Fig. S5.8**), presumably due to the various structural changes occurring on charge, including phase transformations and changes in the interlayer spacing revealed by synchrotron XRD. The absence of a one-to-one correspondence between ⁷Li shift and Li content in LNO underscores the need to use synchrotron XRD and ssNMR results in tandem to identify the nature (structure and composition) of the fatigued phases. The shift of main ⁷Li resonance first decreases from 700 to 410 ppm as the Li content decreases from 0.98 (H1_{0.98} sample) down to 0.24 ((M/H2)_{0.24} sample). As the Li content in LNO further decreases from 0.24 to 0.04, an increase in the ⁷Li shift is observed from 410 to 570 ppm despite the average increase in the number of diamagnetic Ni⁴⁺ neighbors; this increase in the ⁷Li shift is attributed to the significant decrease in the *a* and *c* lattice parameters as the structure transforms from M to H2, and from H2 to H3.

Determination of the Li content of fatigued phases formed in the C4.3V sample series:

C4.3V-1: As mentioned earlier, for samples collected during the first charge process, the Li content can be computed from the specific capacity, assuming no electrochemical side-reactions. Given that electrolyte decomposition reactions are catalyzed at the surface of LNO particles above 4.1V^{19,141,158} and will also contribute to the specific capacity, the Li content computed from coulometry for C4.3V-1, which comes out as 0.01, is slightly underestimated. Our prior work²⁰⁹ has shown that the irreversible capacity (IRC) from surface effects can be deconvolved by taking the difference in IRC between a cell cycled up to 4.3 V (35(2) mAh g⁻¹), with contributions to IRC from both bulk and surface effects, and a cell cycled up to 4.1 V (31(1) mAh g⁻¹), with only contributions to IRC from the bulk. This difference in IRC corresponds to a Li content of approximately 0.02, *which gives an expected Li content of 0.03 for C4.3V-1.*

C4.3V-10: The Rietveld refinement of the synchrotron XRD pattern collected on C4.3V-10 (**Fig. S5.3b**) indicates a mixture of H2 and H3 phases in the sample, and a fit of the corresponding ⁷Li ssNMR spectrum reveals three Li environments at 480 ppm, 410 ppm, and 50 ppm, as shown in **Fig. S5.9a**. The phase composition and lineshape of the ⁷Li spectrum obtained for this sample match extremely well those obtained for the (H2/H3)_{0.16} sample on initial charge (see comparison of ⁷Li spectra in **Fig. S5.9b**). *From this, we deduce that the overall Li content for the C4.3V-10 sample is very close to 0.16.*

C4.3V-50: In the case of the C4.3V-50 sample, its synchrotron XRD pattern can be refined with a single M phase, but the six paramagnetic ⁷Li signals present in the corresponding ssNMR spectrum (see fitted spectrum in **Fig. S5.10a**) suggest the presence of multiple M phases with lattice parameters that are too similar to be resolved in the synchrotron XRD pattern. In fact, a linear combination of the spectra collected on the M_{0.43} and M_{0.34} samples

obtained during the first charge process is able to reproduce almost perfectly the lineshape of the C4.3V-50 spectrum, as shown in **Fig. S5.10b,c**, except from the signals at 700 and 1100 ppm that correspond to electrochemically-inactive domains. From this analysis, the phase fraction based on ^7Li ssNMR signal intensity with T2 correction in the C4.3V-50 spectrum associated with the $\text{H1}_{0.98}$, $\text{M}_{0.43}$ and $\text{M}_{0.34}$ phases comes out as 0.03%, 19.60%, and 80.37%, respectively. These phase fractions are then scaled by the respective Li content in each phase to obtain a Li contribution of 0.00029 (0.0003×0.98), 0.084 (0.1960×0.43) and 0.27 (0.8037×0.34), which sums to 0.35 for C4.3V-50.

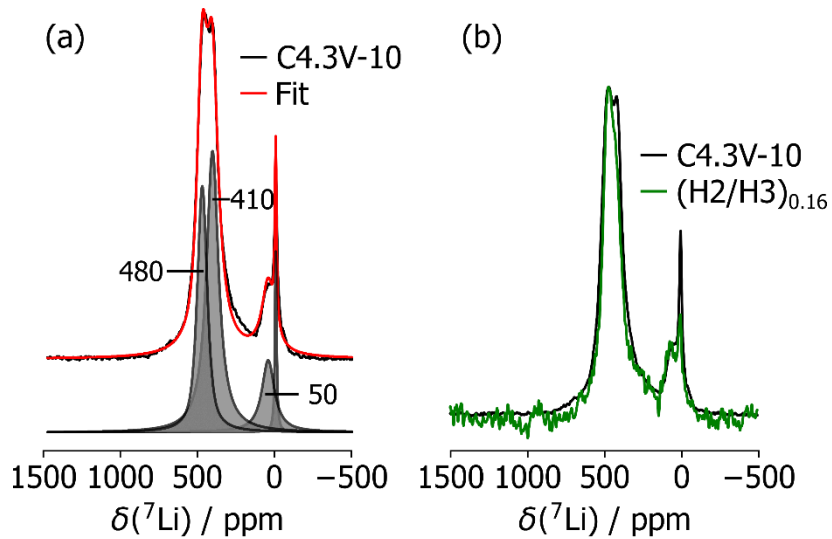


Fig. S5.9 (a) Fit of the ^7Li ssNMR spectrum obtained on C4.3V-10, revealing three Li resonances at 480 ppm, 410 ppm, and 50 ppm. (b) Comparison of the ^7Li ssNMR spectra collected on the C4.3V-10 sample and the $(\text{H2}/\text{H3})_{0.16}$ sample obtained during the first charge process.

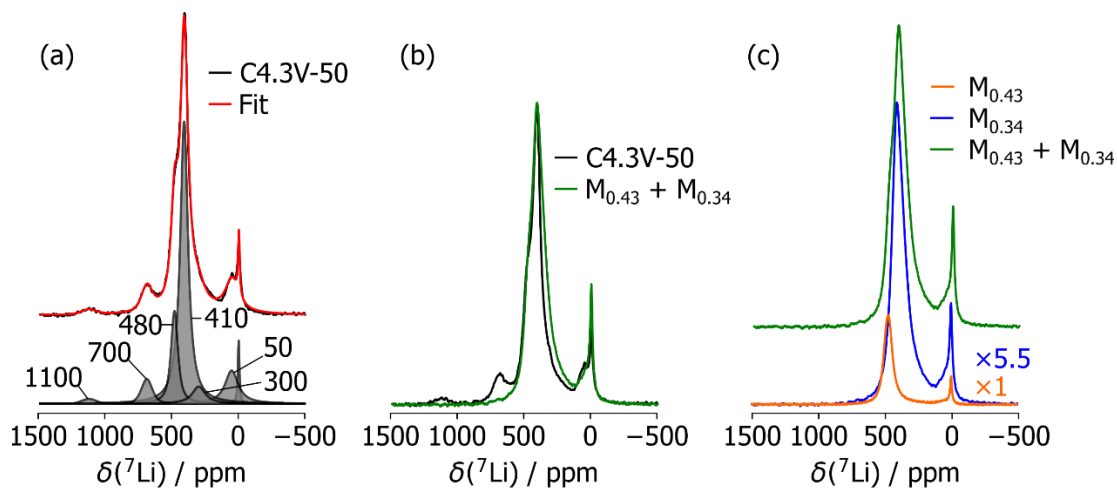


Fig. S5.10 (a) Fit of the ${}^7\text{Li}$ ssNMR spectrum obtained on C4.3V-50, revealing six Li resonances at 1100 ppm, 700 ppm, 480 ppm, 410 ppm, 50 ppm, and 0 ppm. (b) Comparison of the ${}^7\text{Li}$ ssNMR spectrum collected on the C4.3V-50 sample with the sum of spectra acquired on *ex situ* samples stopped to 3.87 V and 3.97 V during the initial charge process. The spectra collected on the M_{0.43} and M_{0.34} samples were scaled (M_{0.43}:M_{0.34} = 1:5.5) to match the lineshape of the C4.3V-50 spectrum. (c) Individual spectra acquired on the M_{0.43} and M_{0.34} samples obtained during the first charge process.

Chapter 6. Conclusions and Future

Work

Layered lithium transition metal oxides remain the highest performing cathode since their discovery. Attainable energy densities in this class of cathode are steadily reaching its theoretical limits with incremental improvements in performance enabled by extensive work in understanding the reaction mechanisms as well as defect-structure property relationships. Advancements in these regards are made in this dissertation through methodology development of *operando* electron spin probe techniques and investigation of the significant first cycle capacity loss as well as degradation modes in LiNiO_2 .

Two *operando* cells were developed that enable advanced in-house experiments to measure magnetization and EPR spectral changes induced by electrochemical cycling. These changes are correlated with the electronic structure changes in electrodes and provide insight into the reaction mechanisms occurring during operation. These connections can be confidently made when the electrochemistry of the *operando* cells is consistent with that from traditional cells such as Swagelok-type cells. The improved electrochemistry of the *operando* cells is enabled by application of sufficient pressures on the battery electrodes through a spring compression and clamping mechanism for the EPR and magnetometry cell, respectively. Additionally, low background cells are designed through careful selection of cell materials and components.

We demonstrated the tandem use of these cells on $\text{LiNi}_{0.5}\text{Mn}_{0.5}\text{O}_2$ (LNMO) and show that complementary insights are provided by both magnetometry and EPR. Three redox

processes are identified in the first charge process of LNMO when it is cycled up to 4.4 V. The length of the first charge processes is dictated by the Ni/Li antisite defect concentration in the material. The magnetization and EPR linewidth evolution is consistent with oxidation of Ni involved in 180° superexchange interactions with Ni defects in the Li layer, which leads to a fast rate of demagnetization and EPR linewidth broadening due to reduced exchange-narrowing effects. Afterwards, the remaining Ni^{2+} in the transition metal layer is oxidized to the $3+$ state and a corresponding reduced rate of demagnetization and EPR linewidth narrowing is observed. In a final step, Ni^{3+} is oxidized to Ni^{4+} and a non-linear decrease in magnetization and EPR linewidth broadening occurs due to the formation of diamagnetic Ni^{4+} , which does not participate in superexchange interactions that lead to exchange narrowing. *Operando* characterization of this mechanism allows us to pinpoint the exact voltages at which these reactions occur and determine that Ni oxidation occurs in a stepwise fashion rather than simultaneously.

The methodology and application of the *operando* electron spin probes can be improved in future work. EPR and magnetometry are bound to play an important role in the discovery of next-generation battery chemistries and in our understanding of their working principles and failure mechanisms. We focus here on future opportunities for the study of all-solid-state, Li-S, Li-O₂ and conversion batteries, which are particularly attractive due to their high theoretical energy densities.

The ability to quantify dendritic or mossy Li has important implications for the study of solid electrolyte systems, which have been proposed to prevent dendrite growth on account of their high bulk modulus and to enable the safe use of Li metal in all-solid-state devices. Since dendrite growth has been observed in ceramic electrolytes at high cycling rates, real-

time quantification of Li dendrites through *operando* EPR could shed light on the relative role of a high impedance interface, cycling rates and temperature on the formation of dendritic Li. EPR is also particularly well suited for the investigation of organic, Li-S and Li-O₂ batteries involving the formation/quenching of radical species on charge and discharge. Importantly, the very large theoretical capacities of Li-S and Li-O₂ systems are overshadowed by poorly reversible electrochemical processes that are not well understood. As of now, EPR has seldom been used to investigate the sources of irreversibility, leaving plenty of opportunities for future work. Finally, the application of advanced spectroscopic techniques is key to shed new light on electrochemical conversion mechanisms and to envisage new ways to improve the performance of conversion electrodes. EPR and magnetometry are uniquely suited for probing the growth of ferromagnetic particles in, *e.g.*, Fe-based conversion systems and for determining whether or not a conducting network is formed that enables reversible electron transfer processes during electrochemical cycling.^{77,85,86} Notably, conversion reactions result in the formation of metastable phases that relax to more stable states with time,⁷⁷ warranting the use of *operando* EPR and magnetometry to study the kinetics of relaxation processes.

Additional insights from these techniques can be enabled through variable temperature measurements, which enable Curie-Weiss fits to be performed *operando* and provide information on the Curie constant and Curie-Weiss temperature. This information can inform on the reaction mechanisms and local bonding environments of transition metals in battery electrodes. The limitation in *operando* Curie-Weiss analysis is the range of temperatures that cells can be cycled at, as well as the temporal resolution of the measurements. Furthermore, simulations can build upon this work and can assist in data interpretation of the evolving g-factor or super-exchange interactions. Simulations using *ab initio* Monte Carlo to determine

the evolution of magnetic properties in transition metal oxide cathodes with state of charge is ongoing work in our research group in collaboration with the Van der Ven group at the University of California, Santa Barbara. Additionally, the *operando* cells have only been used to study the first cycle of cathodes in this dissertation. The influence of structural degradation from aging on the redox reactions have not been studied *operando* here. Long term experiments are cost prohibitive, so we believe a good strategy to study these degradation modes would be to extract cycled cathodes from traditional cells after aging and cycle them in the *operando* cells.

Next, we investigated LiNiO₂ (LNO), a Ni-rich cathode composition which enables high energy density albeit at the cost of structural stability and capacity retention. A previously unassigned resonance in the ⁷Li ssNMR spectra for LNO is attributed to Li near twin boundary planar defects and is supported by first-principles calculation of ssNMR parameters and with atomic-resolution transmission electron microscopy imaging. This enables for the first time, quantification of twin boundary defects in layered cathodes and is used to study a series of LNO cathodes with different off-stoichiometry (y in Li_{1-y}Ni_{1+y}O₂). We find that the twin boundary defect concentration decreases with increasing y as a result of the larger resistance to bond length distortions for Ni as opposed to Li. *Ex situ* characterization of cycled cathodes shows that the Li twin boundary environments are not present after one charge-discharge cycle unless a voltage hold is applied at the end of the discharge step. This suggests that twin boundaries contribute to the first cycle irreversible capacity due to kinetic limitations of lithium reinsertion into the strained sites near the twin boundary.

Finally, we investigate structural changes in LNO that lead to poor capacity retention after prolonged electrochemical cycling. Structural degradation is found to be exacerbated by

high voltage cycling above 4.1 V at which the H2-H3 phase transition occurs and corresponding *c*-lattice collapse. Incomplete delithiation at high potentials results in the formation of “fatigued phases” with limited capacities. The Li content of these fatigued phases are derived through a combination of XRD and ^7Li ssNMR, which allows us to assign capacity fade to irreversibility in Li insertion into the bulk over other factors such as electrode/electrolyte interfacial reactions. This degradation mechanism is correlated with Ni-migration from the Ni layer into the Li layer as determined by Rietveld refinements of XRD data collected on cycled cathodes as well as the development of low temperature magnetic ordering in aged cathodes. After extensive cycling, multiple domains of fatigued phases are identified in the charged state with different Li compositions that are unresolved by XRD alone. At the intermediate stages of cycling (after 10 cycles) a mixture of H2 and H3 phases are present in the charged state with a total Li content of 0.16. After extended cycling over 50 cycles, two M phases or domains formed with a Li content of 0.43 and 0.34. Identification of these subdomains and their corresponding Li content provide new insights into the degradation modes of LNO, which will enable capacity decay mitigation strategies. One promising strategy to improve capacity retention in LNO is through the addition of dopants. Preliminary results on magnesium and aluminum doped LNO show improved capacity retention over undoped LNO due to improved structural stability as shown by a reduction in *c*-lattice parameter changes between the H2 and H3 phase and less defect formation. Additionally, introduction of small amounts of Mn dopants into LNO has been shown to improve its electrochemical performance.²²³ Mn has favorable EPR properties and is a highly magnetic ion, which will enable the application of the *operando* electron spin probes on this material. The

characterization tools used in this dissertation can provide unique insights into the mechanisms for performance improvement.

Bibliography

- (1) Mizushima, K.; Jones, P. C.; Wiseman, P. J.; Goodenough, J. B. Li_xCoO_2 : A New Cathode Material for Batteries of High Energy Density. **1980**, *15* (6), 783–789.
[https://doi.org/10.1016/0025-5408\(80\)90012-4](https://doi.org/10.1016/0025-5408(80)90012-4).
- (2) Lu, Z.; MacNeil, D. D.; Dahn, J. R. Layered $\text{Li}[\text{Ni}_x\text{Co}_{1-2x}\text{Mn}_x]\text{O}_2$ Cathode Materials for Lithium-Ion Batteries. *Electrochem. Solid-State Lett.* **2001**, *4* (12), 1–5.
<https://doi.org/10.1149/1.1413182>.
- (3) Chen, C. H.; Liu, J.; Stoll, M. E.; Henriksen, G.; Vissers, D. R.; Amine, K. Aluminum-Doped Lithium Nickel Cobalt Oxide Electrodes for High-Power Lithium-Ion Batteries. *J. Power Sources* **2004**, *128* (2), 278–285.
<https://doi.org/10.1016/j.jpowsour.2003.10.009>.
- (4) Li, H.; Cormier, M.; Zhang, N.; Inglis, J.; Li, J.; Dahn, J. R. Is Cobalt Needed in Ni-Rich Positive Electrode Materials for Lithium Ion Batteries? *J. Electrochem. Soc.* **2019**, *166* (4), A429–A439. <https://doi.org/10.1149/2.1381902jes>.
- (5) Majumder, S. B.; Nieto, S.; Katiyar, R. S. Synthesis and Electrochemical Properties of $\text{LiNi}_{0.80}(\text{Co}_{0.20-x}\text{Al}_x)\text{O}_2$ ($x = 0.0$ and 0.05) Cathodes for Li Ion Rechargeable Batteries. *J. Power Sources* **2006**, *154* (1), 262–267.
<https://doi.org/10.1016/j.jpowsour.2005.03.186>.
- (6) Chu, B.; Guo, Y. J.; Shi, J. L.; Yin, Y. X.; Huang, T.; Su, H.; Yu, A.; Guo, Y. G.; Li, Y. Cobalt in High-Energy-Density Layered Cathode Materials for Lithium Ion Batteries. *J. Power Sources* **2022**, *544* (August), 231873.

<https://doi.org/10.1016/j.jpowsour.2022.231873>.

- (7) Li, H.; Liu, A.; Zhang, N.; Wang, Y.; Yin, S.; Wu, H.; Dahn, J. R. An Unavoidable Challenge for Ni-Rich Positive Electrode Materials for Lithium-Ion Batteries. *Chem. Mater.* **2019**, *31* (18), 7574–7583. <https://doi.org/10.1021/acs.chemmater.9b02372>.
- (8) Kondrakov, A. O.; Geßwein, H.; Galdina, K.; De Biasi, L.; Meded, V.; Filatova, E. O.; Schumacher, G.; Wenzel, W.; Hartmann, P.; Brezesinski, T.; Janek, J. Charge-Transfer-Induced Lattice Collapse in Ni-Rich NCM Cathode Materials during Delithiation. *J. Phys. Chem. C* **2017**, *121* (39), 24381–24388. <https://doi.org/10.1021/acs.jpcc.7b06598>.
- (9) Malik, M.; Chan, K. H.; Azimi, G. Review on the Synthesis of $\text{LiNi}_x\text{Mn}_y\text{Co}_{1-x-y}\text{O}_2$ (NMC) Cathodes for Lithium-Ion Batteries. *Mater. Today Energy* **2022**, *28*, 101066. <https://doi.org/10.1016/j.mtener.2022.101066>.
- (10) Tang, L.; Cheng, X.; Wu, R.; Cao, T.; Lu, J.; Zhang, Y.; Zhang, Z. Monitoring the Morphology Evolution of $\text{LiNi}_{0.8}\text{Mn}_{0.1}\text{Co}_{0.1}\text{O}_2$ during High-Temperature Solid State Synthesis via in Situ SEM. *J. Energy Chem.* **2022**, *66*, 9–15. <https://doi.org/10.1016/j.jechem.2021.07.021>.
- (11) Deng, C.; Liu, L.; Zhou, W.; Sun, K.; Sun, D. Effect of Synthesis Condition on the Structure and Electrochemical Properties of $\text{Li}[\text{Ni}_{1/3}\text{Mn}_{1/3}\text{Co}_{1/3}]\text{O}_2$ Prepared by Hydroxide Co-Precipitation Method. *Electrochim. Acta* **2008**, *53* (5), 2441–2447. <https://doi.org/10.1016/j.electacta.2007.10.025>.
- (12) Liu, H.; Wu, Y. P.; Rahm, E.; Holze, R.; Wu, H. Q. Cathode Materials for Lithium Ion Batteries Prepared by Sol-Gel Methods. *J. Solid State Electrochem.* **2004**, *8* (7), 450–466. <https://doi.org/10.1007/s10008-004-0521-1>.

- (13) Dong, H.; Koenig, G. M. A Review on Synthesis and Engineering of Crystal Precursors Produced: Via Coprecipitation for Multicomponent Lithium-Ion Battery Cathode Materials. *CrystEngComm* **2020**, *22* (9), 1514–1530. <https://doi.org/10.1039/c9ce00679f>.
- (14) Wang, J.; Yu, Y.; Li, B.; Fu, T.; Xie, D.; Cai, J.; Zhao, J. Improving the Electrochemical Properties of $\text{LiNi}_{0.5}\text{Co}_{0.2}\text{Mn}_{0.3}\text{O}_2$ at 4.6 v Cutoff Potential by Surface Coating with Li_2TiO_3 for Lithium-Ion Batteries. *Phys. Chem. Chem. Phys.* **2015**, *17* (47), 32033–32043. <https://doi.org/10.1039/c5cp05319f>.
- (15) Gao, T.; Yang, G.; Yang, B.; Dai, Y. Effect of Particle Size and Crystallinity on the Charge and Discharge Property of Layered $\text{LiNi}_{0.5}\text{Mn}_{0.5}\text{O}_2$. *J. Alloys Compd.* **2016**, *680*, 694–700. <https://doi.org/10.1016/j.jallcom.2016.04.187>.
- (16) Kim, U. H.; Park, G. T.; Son, B. K.; Nam, G. W.; Liu, J.; Kuo, L. Y.; Kaghazchi, P.; Yoon, C. S.; Sun, Y. K. Heuristic Solution for Achieving Long-Term Cycle Stability for Ni-Rich Layered Cathodes at Full Depth of Discharge. *Nat. Energy* **2020**, *5* (11), 860–869. <https://doi.org/10.1038/s41560-020-00693-6>.
- (17) Garcia, J. C.; Bareño, J.; Yan, J.; Chen, G.; Hauser, A.; Croy, J. R.; Iddir, H. Surface Structure, Morphology, and Stability of $\text{Li}(\text{Ni}_{1/3}\text{Mn}_{1/3}\text{Co}_{1/3})\text{O}_2$ Cathode Material. *J. Phys. Chem. C* **2017**, *121* (15), 8290–8299. <https://doi.org/10.1021/acs.jpcc.7b00896>.
- (18) Abakumov, A. M.; Li, C.; Boev, A.; Aksyonov, D. A.; Savina, A. A.; Abakumova, T. A.; Tendeloo, G. Van; Bals, S. Grain Boundaries as a Diffusion-Limiting Factor in Lithium-Rich NMC Cathodes for High-Energy Lithium-Ion Batteries. *ACS Appl. Energy Mater.* **2021**, *4* (7), 6777–6786. <https://doi.org/10.1021/acsaem.1c00872>.
- (19) Yoon, C. S.; Jun, D. W.; Myung, S. T.; Sun, Y. K. Structural Stability of LiNiO_2

Cycled above 4.2 V. *ACS Energy Lett.* **2017**, *2* (5), 1150–1155.

<https://doi.org/10.1021/acsenergylett.7b00304>.

- (20) Liu, M.; Ren, Z.; Wang, D.; Zhang, H.; Bi, Y.; Shen, C.; Guo, B. Addressing Unfavorable Influence of Particle Cracking with a Strengthened Shell Layer in Ni-Rich Cathodes. *ACS Appl. Mater. Interfaces* **2021**, *13* (16), 18954–18960.
<https://doi.org/10.1021/acscami.1c05535>.
- (21) Whittingham, M. S.; Gamble, F. R. The Lithium Intercalates of the Transition Metal Dichalcogenides. *Mater. Res. Bull.* **1975**, *10* (5), 363–371.
[https://doi.org/10.1016/0025-5408\(75\)90006-9](https://doi.org/10.1016/0025-5408(75)90006-9).
- (22) Goodenough, J. B. Theory of the Role of Covalence in the Perovskite-Type Manganites [La,M(II)]MnO₃. *Phys. Rev.* **1955**, *100* (2), 564–573.
<https://doi.org/10.1103/PhysRev.100.564>.
- (23) Goodenough, J. B.; Loeb, A. L. Theory of Ionic Ordering, Crystal Distortion, and Magnetic Exchange Due to Covalent Forces in Spinel. *Phys. Rev.* **1955**, *98* (2), 391–408. <https://doi.org/10.1103/PhysRev.98.391>.
- (24) Goodenough, J. B. An Interpretation of the Magnetic Properties of the Perovskite-Type Mixed Crystals La_{1-x}Sr_xCoO_{3-λ}. *J. Phys. Chem. Solids* **1958**, *6* (2–3), 287–297. [https://doi.org/10.1016/0022-3697\(58\)90107-0](https://doi.org/10.1016/0022-3697(58)90107-0).
- (25) Goodenough, J. B. On the Influence of 3d⁴ Ions on the Magnetic and Crystallographic Properties of Magnetic Oxides. *J. Phys. le Radium* **1959**, *20* (2–3), 155–159.
<https://doi.org/10.1051/jphysrad:01959002002-3015500>.
- (26) Chernova, N. A.; Nolis, G. M.; Omenya, F. O.; Zhou, H.; Li, Z.; Whittingham, M. S. What Can We Learn about Battery Materials from Their Magnetic Properties? *J.*

- Mater. Chem.* **2011**, *21* (27), 9865–9875. <https://doi.org/10.1039/c1jm00024a>.
- (27) Liu, D.; Shadike, Z.; Lin, R.; Qian, K.; Li, H.; Li, K.; Wang, S.; Yu, Q.; Liu, M.; Ganapathy, S.; Qin, X.; Yang, Q. H.; Wagemaker, M.; Kang, F.; Yang, X. Q.; Li, B. Review of Recent Development of In Situ/Operando Characterization Techniques for Lithium Battery Research. *Adv. Mater.* **2019**, *31* (28), 1–57. <https://doi.org/10.1002/adma.201806620>.
- (28) Pecher, O.; Carretero-González, J.; Griffith, K. J.; Grey, C. P. Materials' Methods: NMR in Battery Research. *Chem. Mater.* **2016**, *29* (1), 213–242. <https://doi.org/10.1021/acs.chemmater.6b03183>.
- (29) Stoll, S.; Schweiger, A. EasySpin, a Comprehensive Software Package for Spectral Simulation and Analysis in EPR. *J. Magn. Reson.* **2006**, *178* (1), 42–55. <https://doi.org/10.1016/j.jmr.2005.08.013>.
- (30) Vleck van, J. H. The Dipolar Broadening of Magnetic Resonance Lines in Crystals. *Phys. Rev.* **1948**, *74* (9), 1168–1183. <https://doi.org/10.1103/PhysRev.74.1168>.
- (31) Moriya, T. Nuclear Magnetic Relaxation in Antiferromagnetics. *Progress of Theoretical Physics*. 1956, pp 23–44. <https://doi.org/10.1103/PhysRev.101.1435>.
- (32) Stoyanova, R.; Gorova, M.; Zhecheva, E. EPR Monitoring of Mn⁴⁺ Distribution in Li₄Mn₅O₁₂ Spinels. *J. Phys. Chem. Solids* **2000**, *61*, 615–620. <https://doi.org/10.3724/SP.J.1077.2010.00626>.
- (33) Anderson, P.W.; Weiss, P. R. Exchange Narrowing in Paramagnetic Resonance. *Rev. Mod. Phys.* **1953**, *25* (1), 269–276. <https://doi.org/10.1103/RevModPhys.25.269>.
- (34) Zheng, J.; Teng, G.; Xin, C.; Zhuo, Z.; Liu, J.; Li, Q.; Hu, Z.; Xu, M.; Yan, S.; Yang, W.; Pan, F. Role of Superexchange Interaction on Tuning of Ni/Li Disordering in

- Layered Li(NixMnyCoz)O₂. *J. Phys. Chem. Lett.* **2017**, 8 (22), 5537–5542.
<https://doi.org/10.1021/acs.jpcllett.7b02498>.
- (35) Chernova, N. A.; Ma, M.; Xiao, J.; Whittingham, M. S.; Breger, J.; Grey, C. P. Layered Li_xNi_yMn_zCo_{1-2y}O₂ Cathodes for Lithium Ion Batteries: Understanding Local Structure via Magnetic Properties. *Chem. Mater.* **2007**, 19 (19), 4682–4693.
<https://doi.org/10.1021/cm0708867>.
- (36) Feher, G.; Kip, A. F. Electron Spin Resonance Absorption in Metals. I. Experimental. *Phys. Rev.* **1955**, 98 (2), 337–348. <https://doi.org/10.1103/PhysRev.98.337>.
- (37) Dyson, F. J. Electron Spin Resonance Absorption in Metals. II. Theory of Electron Diffusion and the Skin Effect. *Phys. Rev.* **1955**, 98 (2), 349–359.
<https://doi.org/10.1103/PhysRev.98.349>.
- (38) Mladenov, M.; Stoyanova, R.; Zhecheva, E.; Vassilev, S. Effect of Mg Doping and MgO-Surface Modification on the Cycling Stability of LiCoO₂ Electrodes. *Electrochem. commun.* **2001**, 3 (8), 410–416. [https://doi.org/10.1016/S1388-2481\(01\)00192-8](https://doi.org/10.1016/S1388-2481(01)00192-8).
- (39) Mukai, K.; Aoki, Y.; Andreica, D.; Amato, A.; Watanabe, I.; Giblin, S. R.; Sugiyama, J. Thermally Activated Spin Fluctuations in Stoichiometric LiCoO₂ Clarified by Electron Paramagnetic Resonance and Muon-Spin Rotation and Relaxation Measurements. *Phys. Rev. B - Condens. Matter Mater. Phys.* **2014**, 89 (9).
<https://doi.org/10.1103/PhysRevB.89.094406>.
- (40) Zhecheva, E.; Stoyanova, R.; Shinova, E. EPR Analysis of the Local Structure of Ni³⁺ Ions in Ni-Based Electrode Materials Obtained under High-Pressure. *J. Mater. Sci.* **2007**, 42 (10), 3343–3348. <https://doi.org/10.1007/s10853-006-0744-x>.

- (41) Stoyanova, R.; Zhecheva, E.; Alcántara, R.; Tirado, J. L. Changes in Local Ni/Mn Environment in Layered $\text{LiMg}_x\text{Ni}_{0.5}\text{-XMn}_{0.5}\text{O}_2$ ($0 \leq x \leq 0.10$) after Electrochemical Extraction and Reinsertion of Lithium. *J. Mater. Chem.* **2006**, *16* (4), 359–369. <https://doi.org/10.1039/b513243f>.
- (42) Stoyanova, R.; Zhecheva, E.; Alcántara, R.; Lavela, P.; Tirado, J. L. EPR Studies of $\text{Li}_{1-x}(\text{Ni}_y\text{Co}_{1-y})_{1+x}\text{O}_2$ Solid Solutions. *Solid State Commun.* **1997**, *102* (6), 457–462. [https://doi.org/10.1016/S0038-1098\(97\)00008-2](https://doi.org/10.1016/S0038-1098(97)00008-2).
- (43) Stoyanova, R.; Zhecheva, E.; Vassilev, S. Mn^{4+} environment in Layered $\text{Li}[\text{Mg}_{0.5}\text{-XNi}_x\text{Mn}_{0.5}]\text{O}_2$ oxides Monitored by EPR Spectroscopy. *J. Solid State Chem.* **2006**, *179* (2), 378–388. <https://doi.org/10.1016/j.jssc.2005.10.038>.
- (44) Stoyanova, R.; Barra, A.-L.; Yoncheva, M.; Zhecheva, E.; Shinova, E.; Tzvetkova, P.; Simova, S. High-Frequency Electron Paramagnetic Resonance Analysis of the Oxidation State and Local Structure of Ni and Mn Ions in Ni,Mn-Codoped LiCoO_2 . *Inorg. Chem.* **2010**, *49* (4), 1932–1941. <https://doi.org/10.1021/ic902351u>.
- (45) Stoyanova, R. K.; Zhecheva, E. N.; Gorova, M. Y. EPR Evidence on Short-Range Co/Mn Order in LiCoMnO_4 Spinel. *J. Mater. Chem.* **2000**, *10* (6), 1377–1381. <https://doi.org/10.1039/a909066e>.
- (46) Zhecheva, E.; Stoyanova, R.; Alcántara, R.; Lavela, P.; Tirado, J. L. EPR Studies of Li Deintercalation from LiCoMnO_4 Spinel-Type Electrode Active Material. *J. Power Sources* **2006**, *159* (2), 1389–1394. <https://doi.org/10.1016/j.jpowsour.2005.11.088>.
- (47) Gourier, D.; Tranchant, A.; Baffier, N.; Messina, R. EPR Study of Electrochemical Lithium Intercalation in V_2O_5 Cathodes. *Electrochim. Acta* **1992**, *37* (15), 2755–2764. [https://doi.org/10.1016/0013-4686\(92\)85203-W](https://doi.org/10.1016/0013-4686(92)85203-W).

- (48) Li, C.; Shen, M.; Lou, X.; Hu, B. Unraveling the Redox Couples of VIII/VIV Mixed-Valent $\text{Na}_3\text{V}_2(\text{PO}_4)_2\text{O}_{1.6}\text{F}_{1.4}$ Cathode by Parallel-Mode EPR and in Situ/Ex Situ NMR. *J. Phys. Chem. C* **2018**, *122* (48), 27224–27232.
<https://doi.org/10.1021/acs.jpcc.8b09151>.
- (49) Geng, F.; Hu, B.; Li, C.; Zhao, C.; Lafon, O.; Trébosc, J.; Amoureux, J. P.; Shen, M.; Hu, B. Anionic Redox Reactions and Structural Degradation in a Cation-Disordered Rock-Salt $\text{Li}_{1.2}\text{Ti}_{0.4}\text{Mn}_{0.4}\text{O}_2$ cathode Material Revealed by Solid-State NMR and EPR. *J. Mater. Chem. A* **2020**, *8* (32), 16515–16526.
<https://doi.org/10.1039/d0ta03358h>.
- (50) Li, C.; Zhao, C.; Hu, B.; Tong, W.; Shen, M.; Hu, B. Unraveling the Critical Role of Ti Substitution in $\text{P}_2\text{-Na}_x\text{Li}_y\text{Mn}_{1-y}\text{O}_2$ Cathodes for Highly Reversible Oxygen Redox Chemistry. *Chem. Mater.* **2020**, *32* (3), 1054–1063.
<https://doi.org/10.1021/acs.chemmater.9b03765>.
- (51) Niemöller, A.; Jakes, P.; Eurich, S.; Paulus, A.; Kungl, H.; Eichel, R.-A.; Granwehr, J. Monitoring Local Redox Processes in $\text{LiNi}_{0.5}\text{Mn}_{1.5}\text{O}_4$ Battery Cathode Material by *in Operando* EPR Spectroscopy. *J. Chem. Phys.* **2018**, *148* (1), 014705.
<https://doi.org/10.1063/1.5008251>.
- (52) Goodenough, J. B. *Magnetism and the Chemical Bond*; Interscience- Wiley: New York, 1963.
- (53) Kanamori, J. Superexchange Interaction and Symmetry Properties of Electron Orbitals. *J. Phys. Chem. Solids* **1959**, *10* (2–3), 87–98. [https://doi.org/10.1016/0022-3697\(59\)90061-7](https://doi.org/10.1016/0022-3697(59)90061-7).
- (54) Niemöller, A.; Jakes, P.; Eichel, R. A.; Granwehr, J. In *Operando* EPR Investigation of

- Redox Mechanisms in LiCoO₂. *Chem. Phys. Lett.* **2019**, 716 (December 2018), 231–236. <https://doi.org/10.1016/j.cplett.2018.12.022>.
- (55) Hertz, J. T.; Huang, Q.; McQueen, T.; Klimczuk, T.; Bos, J. W. G.; Viciu, L.; Cava, R. J. Magnetism and Structure of Li_xCoO₂ and Comparison to Na_xCoO₂. *Phys. Rev. B* **2008**, 77 (7), 1–12. <https://doi.org/10.1103/PhysRevB.77.075119>.
- (56) Yoon, W.-S.; Lee, K.-K.; Kim, K.-B. Structural and Electrochemical Properties of LiAl_yCo_{1-y}O₂ Cathode for Li Rechargeable Batteries. *J. Electrochem. Soc.* **2000**, 147 (6), 2023. <https://doi.org/10.1149/1.1393479>.
- (57) Carretta, P.; Mariani, M.; Azzoni, C. B.; Mozzati, M. C.; Bradarić, I.; Savić, I.; Feher, A.; Šebek, J. Mesoscopic Phase Separation in Na_xCoO₂ (0.65 ≤ x ≤ 0.75). *Phys. Rev. B - Condens. Matter Mater. Phys.* **2004**, 70 (2), 1–9. <https://doi.org/10.1103/PhysRevB.70.024409>.
- (58) Ménétrier, M.; Saadoune, I.; Levasseur, S.; Delmas, C. The Insulator-Metal Transition upon Lithium Deintercalation from LiCoO₂: Electronic Properties and ⁷Li NMR Study. *J. Mater. Chem.* **1999**, 9 (5), 1135–1140. <https://doi.org/10.1039/a900016j>.
- (59) Schlenker, C.; Ahmed, S.; Buder, R.; Gourmala, M. Metal-Insulator Transitions and Phase Diagram of (Ti_{1-x}V_x)₄O₇: Electrical, Calorimetric, Magnetic and EPR Studies. *J. Phys. C Solid State Phys.* **1979**, 12 (17), 3503–3521. <https://doi.org/10.1088/0022-3719/12/17/021>.
- (60) Tang, M.; Dalzini, A.; Li, X.; Feng, X.; Chien, P. H.; Song, L.; Hu, Y. Y. Operando EPR for Simultaneous Monitoring of Anionic and Cationic Redox Processes in Li-Rich Metal Oxide Cathodes. *J. Phys. Chem. Lett.* **2017**, 8 (17), 4009–4016. <https://doi.org/10.1021/acs.jpcllett.7b01425>.

- (61) Eaton, G. R.; Eaton, S. S.; Barr, D. P.; Weber, R. T. *Quantitative EPR*; Springer-Verlag/Wien, 2010.
- (62) Radin, M. D.; Vinckeviciute, J.; Seshadri, R.; Ven, A. Van Der. Mn Oxidation as the Origin of the Anomalous Capacity of Mn - Containing Li - Excess Cathode Materials. *Nat. Energy* **2019**, *4* (August), 19–21. <https://doi.org/10.1038/s41560-019-0439-6>.
- (63) Koga, H.; Croguennec, L.; Ménétrier, M.; Mannesiez, P.; Weill, F.; Delmas, C. Different Oxygen Redox Participation for Bulk and Surface: A Possible Global Explanation for the Cycling Mechanism of $\text{Li}_{1.20}\text{Mn}_{0.54}\text{Co}_{0.13}\text{Ni}_{0.13}\text{O}_2$. *J. Power Sources* **2013**, *236*, 250–258. <https://doi.org/10.1016/j.jpowsour.2013.02.075>.
- (64) Wandt, J.; Marino, C.; Gasteiger, H. A.; Jakes, P.; Eichel, R. A.; Granwehr, J. Operando Electron Paramagnetic Resonance Spectroscopy-Formation of Mossy Lithium on Lithium Anodes during Charge-Discharge Cycling. *Energy Environ. Sci.* **2015**, *8* (4), 1358–1367. <https://doi.org/10.1039/c4ee02730b>.
- (65) Sathiya, M.; Leriche, J. B.; Salager, E.; Gourier, D.; Tarascon, J. M.; Vezin, H. Electron Paramagnetic Resonance Imaging for Real-Time Monitoring of Li-Ion Batteries. *Nat. Commun.* **2015**, *6*, 1–7. <https://doi.org/10.1038/ncomms7276>.
- (66) Niemöller, A.; Jakes, P.; Eichel, R. A.; Granwehr, J. EPR Imaging of Metallic Lithium and Its Application to Dendrite Localisation in Battery Separators. *Sci. Rep.* **2018**, *8* (1), 1–7. <https://doi.org/10.1038/s41598-018-32112-y>.
- (67) Vigreux, C.; Loiseau, P.; Binet, L.; Gourier, D. Anomalous Metallic Lithium Phases: Identification by ESR, ENDOR, and the Bistable Overhauser Effect. *Phys. Rev. B - Condens. Matter Mater. Phys.* **2000**, *61* (13), 8759–8770. <https://doi.org/10.1103/PhysRevB.61.8759>.

- (68) Hope, M. A.; Rinkel, B. L. D.; Gunnarsdóttir, A. B.; Märker, K.; Menkin, S.; Paul, S.; Sergeyev, I. V.; Grey, C. P. Selective NMR Observation of the SEI–Metal Interface by Dynamic Nuclear Polarisation from Lithium Metal. *Nat. Commun.* **2020**, *11* (1), 2224. <https://doi.org/10.1038/s41467-020-16114-x>.
- (69) Berliner, L. J.; Eaton, G. R.; Eaton, S. S. *Distance Measurements in Biological Systems by EPR*; 2002; Vol. 19. <https://doi.org/10.1007/b111467>.
- (70) Wang, Q.; Zheng, J.; Walter, E.; Pan, H.; Lv, D.; Zuo, P.; Chen, H.; Deng, Z. D.; Liaw, B. Y.; Yu, X.; Yang, X.; Zhang, J.-G.; Liu, J.; Xiao, J. Direct Observation of Sulfur Radicals as Reaction Media in Lithium Sulfur Batteries. *J. Electrochem. Soc.* **2015**, *162* (3), A474–A478. <https://doi.org/10.1149/2.0851503jes>.
- (71) Wujcik, K. H.; Wang, D. R.; Raghunathan, A.; Drake, M.; Pascal, T. A.; Prendergast, D.; Balsara, N. P. Lithium Polysulfide Radical Anions in Ether-Based Solvents. *J. Phys. Chem. C* **2016**, *120* (33), 18403–18410. <https://doi.org/10.1021/acs.jpcc.6b04264>.
- (72) Barchasz, C.; Molton, F.; Duboc, C.; Leprêtre, J. C.; Patoux, S.; Alloin, F. Lithium/Sulfur Cell Discharge Mechanism: An Original Approach for Intermediate Species Identification. *Anal. Chem.* **2012**, *84* (9), 3973–3980. <https://doi.org/10.1021/ac2032244>.
- (73) Nava, M. J.; Britt, D. R.; Nocera, D. G.; Cummins, C. C.; Lopez, N.; Wu, G.; Chow, G. K.; Zhang, S. On the Incompatibility of Lithium–O₂ Battery Technology with CO₂. *Chem. Sci.* **2017**, *8* (9), 6117–6122. <https://doi.org/10.1039/c7sc01230f>.
- (74) Cao, R.; Walter, E. D.; Xu, W.; Nasybulin, E. N.; Bhattacharya, P.; Bowden, M. E.; Engelhard, M. H.; Zhang, J. G. The Mechanisms of Oxygen Reduction and Evolution

- Reactions in Nonaqueous Lithium–Oxygen Batteries. *ChemSusChem* **2014**, 7 (9), 2436–2440. <https://doi.org/10.1002/cssc.201402315>.
- (75) Dahbi, M.; Wikberg, J. M.; Saadoune, I.; Gustafsson, T.; Svedlinh, P.; Edström, K. Electrochemical Behavior of $\text{LiNi}_{1-y}\text{ZCo}_y\text{Mn}_2\text{O}_2$ Probed through Structural and Magnetic Properties. *J. Appl. Phys.* **2012**, 111 (2). <https://doi.org/10.1063/1.3676434>.
- (76) Mohanty, D.; Gabrisch, H. Microstructural Investigation of $\text{Li}_x\text{Ni}_{1/3}\text{Mn}_{1/3}\text{Co}_{1/3}\text{O}_2$ ($x \leq 1$) and Its Aged Products via Magnetic and Diffraction Study. *J. Power Sources* **2012**, 220, 405–412. <https://doi.org/10.1016/j.jpowsour.2012.08.005>.
- (77) Gershinsky, G.; Bar, E.; Monconduit, L.; Zitoun, D. Operando Electron Magnetic Measurements of Li-Ion Batteries. *Energy Environ. Sci.* **2014**, 7 (6), 2012–2016. <https://doi.org/10.1039/c4ee00490f>.
- (78) Li, Q.; Li, H.; Xia, Q.; Hu, Z.; Zhu, Y.; Yan, S.; Ge, C.; Zhang, Q.; Wang, X.; Shang, X.; Fan, S.; Long, Y.; Gu, L.; Miao, G.; Yu, G.; Moodera, J. S. Extra Storage Capacity in Transition Metal Oxide Lithium-Ion Batteries Revealed by in Situ Magnetometry. *Nat. Mater.* <https://doi.org/10.1038/s41563-020-0756-y>.
- (79) Fehse, M.; Bessas, D.; Darwiche, A.; Mahmoud, A.; Rahamim, G.; La Fontaine, C.; Hermann, R. P.; Zitoun, D.; Monconduit, L.; Stievano, L.; Sougrati, M. T. The Electrochemical Sodiation of FeSb_2 : New Insights from Operando ^{57}Fe Synchrotron Mössbauer and X-Ray Absorption Spectroscopy. *Batter. Supercaps* **2019**, 2 (1), 66–73. <https://doi.org/10.1002/batt.201800075>.
- (80) Topolovec, S.; Kren, H.; Klinser, G.; Koller, S.; Krenn, H.; Würschum, R. Operando Magnetometry on Li_xCoO_2 during Charging/Discharging. *J. Solid State Electrochem.* **2016**, 20 (5), 1491–1496. <https://doi.org/10.1007/s10008-015-3110-6>.

- (81) Klinser, G.; Topolovec, S.; Kren, H.; Koller, S.; Goessler, W.; Krenn, H.; Würschum, R. Continuous Monitoring of the Bulk Oxidation States in $\text{Li}_x\text{Ni}_{1/3}\text{Mn}_{1/3}\text{Co}_{1/3}\text{O}_2$ during Charging and Discharging. *Appl. Phys. Lett.* **2016**, *109* (21), 0–4.
<https://doi.org/10.1063/1.4968547>.
- (82) Klinser, G.; Zettl, R.; Wilkening, M.; Krenn, H.; Hanzu, I.; Würschum, R. Redox Processes in Sodium Vanadium Phosphate Cathodes – Insights from Operando Magnetometry. *Phys. Chem. Chem. Phys.* **2019**, *21* (36), 20151–20155.
<https://doi.org/10.1039/c9cp04045e>.
- (83) Hu, Y.; Iwata, G. Z.; Mohammadi, M.; Silletta, E. V.; Wickenbrock, A.; Blanchard, J. W.; Budker, D.; Jerschow, A. Sensitive Magnetometry Reveals Inhomogeneities in Charge Storage and Weak Transient Internal Currents in Li-Ion Cells. *Proc. Natl. Acad. Sci. U. S. A.* **2020**, *117* (20), 10667–10672.
<https://doi.org/10.1073/pnas.1917172117>.
- (84) Wilamowski, Z.; Solnica, M.; Michaluk, E.; Havlicek, M.; Jantsch, W. EPR Line Shape and Magnetometry - Chances and Pitfalls. *Semicond. Sci. Technol.* **2011**, *26* (6).
<https://doi.org/10.1088/0268-1242/26/6/064009>.
- (85) Nwokeke, U. G.; Alcántara, R.; Tirado, J. L.; Stoyanova, R.; Yoncheva, M.; Zhecheva, E. Electron Paramagnetic Resonance, X-Ray Diffraction, Mössbauer Spectroscopy, and Electrochemical Studies on Nanocrystalline FeSn_2 Obtained by Reduction of Salts in Tetraethylene Glycol. *Chem. Mater.* **2010**, *22* (7), 2268–2275.
<https://doi.org/10.1021/cm902898k>.
- (86) Dong, Z.; Wang, Q.; Zhang, R.; Chernova, N. A.; Omenya, F.; Ji, D.; Whittingham, M. S. Reaction Mechanism of the Sn_2Fe Anode in Lithium-Ion Batteries. *ACS Omega*

- 2019**, *4* (27), 22345–22355. <https://doi.org/10.1021/acsomega.9b02417>.
- (87) Middlemiss, D. S.; Ilott, A. J.; Clément, R. J.; Strobridge, F. C.; Grey, C. P. Density Functional Theory-Based Bond Pathway Decompositions of Hyperfine Shifts: Equipping Solid-State NMR to Characterize Atomic Environments in Paramagnetic Materials. *Chem. Mater.* **2013**, *25* (9), 1723–1734. <https://doi.org/10.1021/cm400201t>.
- (88) Kim, J.; Middlemiss, D. S.; Chernova, N. A.; Zhu, B. Y. X.; Masquelier, C.; Grey, C. P. Linking Local Environments and Hyperfine Shifts: A Combined Experimental and Theoretical ³¹P and ⁷Li Solid-State NMR Study of Paramagnetic Fe(III) Phosphates. *J. Am. Chem. Soc.* **2010**, *132* (47), 16825–16840. <https://doi.org/10.1021/ja102678r>.
- (89) Carlier, D.; Ménétrier, M.; Grey, C. P.; Delmas, C.; Ceder, G. Understanding the NMR Shifts in Paramagnetic Transition Metal Oxides Using Density Functional Theory Calculations. *Phys. Rev. B - Condens. Matter Mater. Phys.* **2003**, *67* (17), 1–14. <https://doi.org/10.1103/PhysRevB.67.174103>.
- (90) Chen, H.; Freeman, C. L.; Harding, J. H. Charge Disproportionation and Jahn-Teller Distortion in LiNiO₂ and NaNiO₂: A Density Functional Theory Study. *Phys. Rev. B - Condens. Matter Mater. Phys.* **2011**, *84* (8), 1–7. <https://doi.org/10.1103/PhysRevB.84.085108>.
- (91) Sicolo, S.; Mock, M.; Bianchini, M.; Albe, K. And Yet It Moves: LiNiO₂, a Dynamic Jahn-Teller System. *Chem. Mater.* **2020**, *32* (23), 10096–10103. <https://doi.org/10.1021/acs.chemmater.0c03442>.
- (92) Rougier, A.; Delmas, C.; Chadwick, A. V. Non-Cooperative Jahn-Teller Effect in LiNiO₂: An EXAFS Study. *Solid State Commun.* **1995**, *94* (2), 123–127. [https://doi.org/10.1016/0038-1098\(95\)00020-8](https://doi.org/10.1016/0038-1098(95)00020-8).

- (93) Trease, N. M.; Seymour, I. D.; Radin, M. D.; Liu, H.; Liu, H.; Hy, S.; Chernova, N.; Parikh, P.; Devaraj, A.; Wiaderek, K. M.; Chupas, P. J.; Chapman, K. W.; Whittingham, M. S.; Meng, Y. S.; Van Der Van, A.; Grey, C. P. Identifying the Distribution of Al³⁺ in LiNi_{0.8}Co_{0.15}Al_{0.05}O₂. *Chem. Mater.* **2016**, *28* (22), 8170–8180. <https://doi.org/10.1021/acs.chemmater.6b02797>.
- (94) Waldmann, T.; Iturrondobeitia, A.; Kasper, M.; Ghanbari, N.; Aguesse, F.; Bekaert, E.; Daniel, L.; Genies, S.; Gordon, I. J.; Löble, M. W.; De Vito, E.; Wohlfahrt-Mehrens, M. Review—Post-Mortem Analysis of Aged Lithium-Ion Batteries: Disassembly Methodology and Physico-Chemical Analysis Techniques. *J. Electrochem. Soc.* **2016**, *163* (10), A2149–A2164. <https://doi.org/10.1149/2.1211609jes>.
- (95) Koga, H.; Croguennec, L.; Ménétrier, M.; Mannesiez, P.; Weill, F.; Delmas, C.; Belin, S. Operando X-Ray Absorption Study of the Redox Processes Involved upon Cycling of the Li-Rich Layered Oxide Li_{1.20}Mn_{0.54}Co_{0.13}Ni_{0.13}O₂ in Li Ion Batteries. *J. Phys. Chem. C* **2014**, *118* (11), 5700–5709. <https://doi.org/10.1021/jp412197z>.
- (96) Allen, J. P.; O’Keefe, C. A.; Grey, C. P. Quantifying Dissolved Transition Metals in Battery Electrolyte Solutions with NMR Paramagnetic Relaxation Enhancement. *J. Phys. Chem. C* **2023**, *127* (20), 9509–9521. <https://doi.org/10.1021/acs.jpcc.3c01396>.
- (97) Merryweather, A. J.; Schnedermann, C.; Jacquet, Q.; Grey, C. P.; Rao, A. Operando Optical Tracking of Single-Particle Ion Dynamics in Batteries. *Nature* **2021**, *594* (7864), 522–528. <https://doi.org/10.1038/s41586-021-03584-2>.
- (98) Wu, Y.; Liu, N. Visualizing Battery Reactions and Processes by Using In Situ and In

Operando Microscopies. *Chem* **2018**, *4* (3), 438–465.

<https://doi.org/10.1016/j.chempr.2017.12.022>.

- (99) Gong, C.; Pu, S. D.; Gao, X.; Yang, S.; Liu, J.; Ning, Z.; Rees, G. J.; Capone, I.; Pi, L.; Liu, B.; Hartley, G. O.; Fawdon, J.; Luo, J.; Pasta, M.; Grovenor, C. R. M.; Bruce, P. G.; Robertson, A. W. Revealing the Role of Fluoride-Rich Battery Electrode Interphases by Operando. *Adv. Energy Mater.* **2021**, *11*, 2003118. <https://doi.org/10.1002/aenm.202003118>.
- (100) Mehdi, B. L.; Qian, J.; Nasybulin, E.; Park, C.; Welch, D. A.; Faller, R.; Mehta, H.; Henderson, W. A.; Xu, W.; Wang, C. M.; Evans, J. E.; Liu, J.; Zhang, J. G.; Mueller, K. T.; Browning, N. D. Observation and Quantification of Nanoscale Processes in Lithium Batteries by Operando Electrochemical (S)TEM. *Nano Lett.* **2015**, *15* (3), 2168–2173. <https://doi.org/10.1021/acs.nanolett.5b00175>.
- (101) Märker, K.; Reeves, P. J.; Xu, C.; Griffith, K. J.; Grey, C. P. Evolution of Structure and Lithium Dynamics in LiNi_{0.8}Mn_{0.1}Co_{0.1}O₂ (NMC811) Cathodes during Electrochemical Cycling. *Chem. Mater.* **2019**, *31* (7), 2545–2554. <https://doi.org/10.1021/acs.chemmater.9b00140>.
- (102) Talaie, E.; Bonnick, P.; Sun, X.; Pang, Q.; Liang, X.; Nazar, L. F. Methods and Protocols for Electrochemical Energy Storage Materials Research. *Chem. Mater.* **2017**, *29* (1), 90–105. <https://doi.org/10.1021/acs.chemmater.6b02726>.
- (103) Grenier, A.; Reeves, P. J.; Liu, H.; Seymour, I. D.; Märker, K.; Wiaderek, K. M.; Chupas, P. J.; Grey, C. P.; Chapman, K. W. Intrinsic Kinetic Limitations in Substituted Lithium-Layered Transition-Metal Oxide Electrodes. *J. Am. Chem. Soc.* **2020**, *142* (15), 7001–7011. <https://doi.org/10.1021/jacs.9b13551>.

- (104) Mock, M.; Bianchini, M.; Fauth, F.; Albe, K.; Sicolo, S. Atomistic Understanding of the LiNiO₂-NiO₂ Phase Diagram from Experimentally Guided Lattice Models. *J. Mater. Chem. A* **2021**, *9* (26), 14928–14940. <https://doi.org/10.1039/d1ta00563d>.
- (105) Schweidler, S.; Bianchini, M.; Hartmann, P.; Brezesinski, T.; Janek, J. The Sound of Batteries: An Operando Acoustic Emission Study of the LiNiO₂ Cathode in Li-Ion Cells. *Batter. Supercaps* **2020**, *3* (10), 1021–1027. <https://doi.org/10.1002/batt.202000099>.
- (106) Lanz, P.; Sommer, H.; Schulz-Dobrick, M.; Novák, P. Oxygen Release from High-Energy XLi₂MnO₃·(1 - X)LiMO₂ (M = Mn, Ni, Co): Electrochemical, Differential Electrochemical Mass Spectrometric, in Situ Pressure, and in Situ Temperature Characterization. *Electrochim. Acta* **2013**, *93*, 114–119. <https://doi.org/10.1016/j.electacta.2013.01.105>.
- (107) Armstrong, R.; Holzapfel, M.; Novák, P.; Johnson, C. S.; Kang, S. H.; Thackeray, M. M.; Bruce, P. G. Demonstrating Oxygen Loss and Associated Structural Reorganization in the Lithium Battery Cathode Li[Ni_{0.2}Li_{0.2}Mn_{0.6}]O₂. *J. Am. Chem. Soc.* **2006**, *128* (26), 8694–8698. <https://doi.org/10.1021/ja062027+>.
- (108) Swallow, J. E. N.; Fraser, M. W.; Kneusels, N. J. H.; Charlton, J. F.; Sole, C. G.; Phelan, C. M. E.; Björklund, E.; Bencok, P.; Escudero, C.; Pérez-Dieste, V.; Grey, C. P.; Nicholls, R. J.; Weatherup, R. S. Revealing Solid Electrolyte Interphase Formation through Interface-Sensitive Operando X-Ray Absorption Spectroscopy. *Nat. Commun.* **2022**, *13* (1). <https://doi.org/10.1038/s41467-022-33691-1>.
- (109) Gittleston, F. S.; Ryu, W. H.; Taylor, A. D. Operando Observation of the Gold-Electrolyte Interface in Li-O₂ Batteries. *ACS Appl. Mater. Interfaces* **2014**, *6* (21),

- 19017–19025. <https://doi.org/10.1021/am504900k>.
- (110) Chen, D.; Mahmoud, M. A.; Wang, J. H.; Waller, G. H.; Zhao, B.; Qu, C.; El-Sayed, M. A.; Liu, M. Operando Investigation into Dynamic Evolution of Cathode-Electrolyte Interfaces in a Li-Ion Battery. *Nano Lett.* **2019**, *19* (3), 2037–2043. <https://doi.org/10.1021/acs.nanolett.9b00179>.
- (111) Leriche, J. B.; Hamelet, S.; Shu, J.; Morcrette, M.; Masquelier, C.; Ouvrard, G.; Zerrouki, M.; Soudan, P.; Belin, S.; Elkaïm, E.; Baudalet, F. An Electrochemical Cell for Operando Study of Lithium Batteries Using Synchrotron Radiation. *J. Electrochem. Soc.* **2010**, *157* (5), A606. <https://doi.org/10.1149/1.3355977>.
- (112) Klinser, G.; Stückler, M.; Kren, H.; Koller, S.; Goessler, W.; Krenn, H.; Würschum, R. Charging Processes in the Cathode $\text{LiNi}_{0.6}\text{Mn}_{0.2}\text{Co}_{0.2}\text{O}_2$ as Revealed by Operando Magnetometry. *J. Power Sources* **2018**, *396* (April), 791–795. <https://doi.org/10.1016/j.jpowsour.2018.06.090>.
- (113) Xia, Q.; Li, X.; Wang, K.; Li, Z.; Liu, H.; Wang, X.; Ye, W.; Li, H.; Teng, X.; Pang, J.; Zhang, Q.; Ge, C.; Gu, L.; Miao, G. X.; Yan, S.; Hu, H.; Li, Q. Unraveling the Evolution of Transition Metals during Li Alloying-Dealloying by In-Operando Magnetometry. *Chem. Mater.* **2022**, *34* (13), 5852–5859. <https://doi.org/10.1021/acs.chemmater.2c00618>.
- (114) Lei, C. H.; Bareño, J.; Wen, J. G.; Petrov, I.; Kang, S. H.; Abraham, D. P. Local Structure and Composition Studies of $\text{Li}_{1.2}\text{Ni}_{0.2}\text{Mn}_{0.6}\text{O}_2$ by Analytical Electron Microscopy. *J. Power Sources* **2008**, *178* (1), 422–433. <https://doi.org/10.1016/j.jpowsour.2007.11.077>.
- (115) Coelho, A. A. TOPAS and TOPAS-Academic: An Optimization Program Integrating

- Computer Algebra and Crystallographic Objects Written in C++. *J. Appl. Crystallogr.* **2018**, *51*, 210–218. <https://doi.org/10.1107/S1600576718000183>.
- (116) Massiot, D.; Fayon, F.; Capron, M.; King, I.; Le Calve, S.; Alonso, B.; Durand, J.-O.; Bujoli, B.; Gan, Z.; Hoatson, G. Modelling One- and Two-dimensional Solid-state NMR Spectra. *Magn. Reson. Chem.* **2002**, *40*, 70–76. <https://doi.org/10.1002/mrc.984>.
- (117) Bree, G.; Horstman, D.; Low, C. T. J. Light-Weighting of Battery Casing for Lithium-Ion Device Energy Density Improvement. *J. Energy Storage* **2023**, *68* (October 2022), 107852. <https://doi.org/10.1016/j.est.2023.107852>.
- (118) Bruker. An EPR Primer. In *Xerox User's Guide*; 2000; pp 1–24.
- (119) Hall, D. S.; Self, J.; Dahn, J. R. Dielectric Constants for Quantum Chemistry and Li-Ion Batteries: Solvent Blends of Ethylene Carbonate and Ethyl Methyl Carbonate. *J. Phys. Chem. C* **2015**, *119* (39), 22322–22330. <https://doi.org/10.1021/acs.jpcc.5b06022>.
- (120) Yoon, W. S.; Grey, C. P.; Balasubramanian, M.; Yang, X. Q.; McBreen, J. In Situ X-Ray Absorption Spectroscopic Study on LiNi_{0.5}Mn_{0.5}O₂ Cathode Material during Electrochemical Cycling. *Chem. Mater.* **2003**, *15* (16), 3161–3169. <https://doi.org/10.1021/cm030220m>.
- (121) Esquinazi, P.; Hergert, W.; Spemann, D.; Setzer, A.; Ernst, A. Defect-Induced Magnetism in Solids. *IEEE Trans. Magn.* **2013**, *49* (8), 4668–4674. <https://doi.org/10.1109/TMAG.2013.2255867>.
- (122) Kurzhals, P.; Riewald, F.; Bianchini, M.; Sommer, H.; Gasteiger, H. A.; Janek, J. The LiNiO₂ Cathode Active Material: A Comprehensive Study of Calcination Conditions and Their Correlation with Physicochemical Properties. Part I. Structural Chemistry. *J.*

- Electrochem. Soc.* **2021**, *168* (11), 110518. <https://doi.org/10.1149/1945-7111/ac33e5>.
- (123) Goonetilleke, D.; Schwarz, B.; Li, H.; Fauth, F.; Suard, E.; Mangold, S.; Indris, S.; Brezesinski, T.; Bianchini, M.; Weber, D. Stoichiometry Matters: Correlation between Antisite Defects, Microstructure and Magnetic Behavior in the Cathode Material $\text{Li}_{1-z}\text{Ni}_{1+z}\text{O}_2$. *J. Mater. Chem. A* **2023**, *11* (25), 13468–13482. <https://doi.org/10.1039/d3ta01621h>.
- (124) Bréger, J.; Meng, Y. S.; Hinuma, Y.; Kumar, S.; Kang, K.; Shao-Horn, Y.; Ceder, G.; Grey, C. P. Effect of High Voltage on the Structure and Electrochemistry of $\text{LiNi}_{0.5}\text{Mn}_{0.5}\text{O}_2$: A Joint Experimental and Theoretical Study. *Chem. Mater.* **2006**, *18* (20), 4768–4781. <https://doi.org/10.1021/cm060886r>.
- (125) Barton, P. T.; Premchand, Y. D.; Chater, P. A.; Seshadri, R.; Rosseinsky, M. J. Chemical Inhomogeneity, Short-Range Order, and Magnetism in the LiNiO_2 - NiO Solid Solution. *Chem. - A Eur. J.* **2013**, *19* (43), 14521–14531. <https://doi.org/10.1002/chem.201301451>.
- (126) Arachi, Y.; Kobayashi, H.; Emura, S.; Nakata, Y.; Tanaka, M.; Asai, T.; Sakaebe, H.; Tatsumi, K.; Kageyama, H. Li De-Intercalation Mechanism in $\text{LiNi}_{0.5}\text{Mn}_{0.5}\text{O}_2$ Cathode Material for Li-Ion Batteries. *Solid State Ionics* **2005**, *176* (9–10), 895–903. <https://doi.org/10.1016/j.ssi.2004.10.024>.
- (127) Johnson, C. S.; Kim, J.-S.; Kropf, J. A.; Kahaian, A. J.; Vaughey, J. T.; Fransson, L. M. L.; Edström, K.; Thackeray, M. M. Structural Characterization of Layered $\text{Li}_x\text{Ni}_{0.5}\text{Mn}_{0.5}\text{O}_2$ ($0 < x < 2$) Oxide Electrodes for Li Batteries. *Chem. Mater.* **2003**, *15*, 2313–2322. <https://doi.org/10.1021/cm0204728>.
- (128) Popovych, V.; Bester, M.; Stefaniuk, I.; Kuzma, M. Dyson Line and Modified Dyson

- Line in the EPR Measurements. *Nukleonika* **2015**, *60* (3), 385–388.
<https://doi.org/10.1515/nuka-2015-0068>.
- (129) Shinova, E.; Stoyanova, R.; Zhecheva, E.; Ortiz, G. F.; Lavela, P.; Tirado, J. L. Cationic Distribution and Electrochemical Performance of LiCo_{1/3}Ni_{1/3}Mn_{1/3}O₂ Electrodes for Lithium-Ion Batteries. *Solid State Ionics* **2008**, *179* (38), 2198–2208.
<https://doi.org/10.1016/j.ssi.2008.07.026>.
- (130) Anderson, P.W.; Weiss, P. R. Exchange Narrowing in Paramagnetic Resonance. *Exch. Organ. Behav. Teach. J.* **1953**, *679* (1948).
- (131) Ryu, H. H.; Sun, H. H.; Myung, S. T.; Yoon, C. S.; Sun, Y. K. Reducing Cobalt from Lithium-Ion Batteries for the Electric Vehicle Era. *Energy Environ. Sci.* **2021**, *14* (2), 844–852. <https://doi.org/10.1039/d0ee03581e>.
- (132) Li, J.; Fleetwood, J.; Hawley, W. B.; Kays, W. From Materials to Cell: State-of-the-Art and Prospective Technologies for Lithium-Ion Battery Electrode Processing. *Chem. Rev.* **2022**, *122* (1), 903–956. <https://doi.org/10.1021/acs.chemrev.1c00565>.
- (133) Xu, J.; Hu, E.; Nordlund, D.; Mehta, A.; Ehrlich, S. N.; Yang, X. Q.; Tong, W. Understanding the Degradation Mechanism of Lithium Nickel Oxide Cathodes for Li-Ion Batteries. *ACS Appl. Mater. Interfaces* **2016**, *8* (46), 31677–31683.
<https://doi.org/10.1021/acsami.6b11111>.
- (134) Wang, C.; Zhang, R.; Kisslinger, K.; Xin, H. L. Atomic-Scale Observation of O₁ Faulted Phase-Induced Deactivation of LiNiO₂ at High Voltage. *Nano Lett.* **2021**, *21* (8), 3657–3663. <https://doi.org/10.1021/acs.nanolett.1c00862>.
- (135) Park, K.-Y.; Zhu, Y.; Torres-Castanedo, C. G.; Jung, H. J.; Luu, N. S.; Kahvecioglu, O.; Yoo, Y.; Seo, J.-W. T.; Downing, J. R.; Lim, H.-D.; Bedzyk, M. J.; Wolverton, C.;

- Hersam, M. C. Elucidating and Mitigating High-Voltage Degradation Cascades in Cobalt-Free LiNiO₂ Lithium-Ion Battery Cathodes. *Adv. Mater.* **2021**, *34*, 2106402. <https://doi.org/10.1002/adma.202106402>.
- (136) Chen, J.; Yang, Y.; Tang, Y.; Wang, Y.; Li, H.; Xiao, X.; Wang, S.; Darma, M. S. D.; Etter, M.; Missyul, A.; Tayal, A.; Knapp, M.; Ehrenberg, H.; Indris, S.; Hua, W. Constructing a Thin Disordered Self-Protective Layer on the LiNiO₂ Primary Particles Against Oxygen Release. *Adv. Funct. Mater.* **2022**, *2211515*, 1–11. <https://doi.org/10.1002/adfm.202211515>.
- (137) Li, X.; Wang, Q.; Guo, H.; Artrith, N.; Urban, A. Understanding the Onset of Surface Degradation in LiNiO₂ Cathodes. *ACS Appl. Energy Mater.* **2022**, *5*, 5730–5741. <https://doi.org/10.1021/acsaem.2c00012>.
- (138) Xiao, P.; Shi, T.; Huang, W.; Ceder, G. Understanding Surface Densified Phases in Ni-Rich Layered Compounds. *ACS Energy Lett.* **2019**, *4* (4), 811–818. <https://doi.org/10.1021/acsenerylett.9b00122>.
- (139) Bianchini, M.; Roca-Ayats, M.; Hartmann, P.; Brezesinski, T.; Janek, J. There and Back Again—The Journey of LiNiO₂ as a Cathode Active Material. *Angew. Chemie - Int. Ed.* **2019**, *58* (31), 10434–10458. <https://doi.org/10.1002/anie.201812472>.
- (140) Liu, H. S.; Zhang, Z. R.; Gong, Z. L.; Yang, Y. Origin of Deterioration for LiNiO₂ Cathode Material during Storage in Air. *Electrochem. Solid-State Lett.* **2004**, *7* (7). <https://doi.org/10.1149/1.1738471>.
- (141) Pan, R.; Jo, E.; Cui, Z.; Manthiram, A. Degradation Pathways of Cobalt-Free LiNiO₂ Cathode in Lithium Batteries. *Adv. Funct. Mater.* **2022**, 2211461. <https://doi.org/10.1002/adfm.202211461>.

- (142) Li, H.; Hua, W.; Etter, M.; Mangold, S.; Melinte, G.; Pietro, N.; Casati, M.; Ehrenberg, H.; Indris, S. Investigation of Structural and Electronic Changes Induced by Postsynthesis Thermal Treatment of LiNiO₂. **2022**.
<https://doi.org/10.1021/acs.chemmater.2c00995>.
- (143) Zou, L.; Zhao, W.; Jia, H.; Zheng, J.; Li, L.; Abraham, D. P.; Chen, G.; Croy, J. R.; Zhang, J. G.; Wang, C. The Role of Secondary Particle Structures in Surface Phase Transitions of Ni-Rich Cathodes. *Chem. Mater.* **2020**, *32* (7), 2884–2892.
<https://doi.org/10.1021/acs.chemmater.9b04938>.
- (144) Li, S.; Yao, Z.; Zheng, J.; Fu, M.; Cen, J.; Hwang, S.; Jin, H.; Orlov, A.; Gu, L.; Wang, S.; Chen, Z.; Su, D. Direct Observation of Defect-Aided Structural Evolution in a Nickel-Rich Layered Cathode. *Angew. Chemie* **2020**, *132* (49), 22276–22283.
<https://doi.org/10.1002/ange.202008144>.
- (145) Phattharasupakun, N.; Cormier, M. M. E.; Lyle, E.; Zsoldos, E.; Liu, A.; Geng, C.; Liu, Y.; Li, H.; Sawangphruk, M.; Dahn, J. R. Correlating Cation Mixing with Li Kinetics: Electrochemical and Li Diffusion Measurements on Li-Deficient LiNiO₂ and Li-Excess LiNi_{0.5}Mn_{0.5}O₂. *J. Electrochem. Soc.* **2021**, *168* (9), 090535.
<https://doi.org/10.1149/1945-7111/ac24ba>.
- (146) Kobayashi, Y.; Tabuchi, M.; Miyashiro, H.; Kuriyama, N. A New Design of Highly Reversible LiNiO₂: Defect Formation in Transition Metal Site. *J. Power Sources* **2017**, *364*, 156–162. <https://doi.org/10.1016/j.jpowsour.2017.08.027>.
- (147) Ong, P. V.; Yang, Z.; Sushko, P. V.; Du, Y. Formation, Structural Variety, and Impact of Antiphase Boundaries on Li Diffusion in LiCoO₂ Thin-Film Cathodes. *J. Phys. Chem. Lett.* **2018**, *9* (18), 5515–5520. <https://doi.org/10.1021/acs.jpcclett.8b02185>.

- (148) Mesnier, A.; Manthiram, A. Synthesis of LiNiO₂ at Moderate Oxygen Pressure and Long-Term Cyclability in Lithium-Ion Full Cells. *ACS Appl. Mater. Interfaces* **2020**, *12* (47), 52826–52835. <https://doi.org/10.1021/acsami.0c16648>.
- (149) Delmas, C.; Fouassier, C.; Hagenmuller, P. Structural Classification and Properties of the Layered Oxides. *Phys. B+C* **1980**, *99* (1–4), 81–85. [https://doi.org/10.1016/0378-4363\(80\)90214-4](https://doi.org/10.1016/0378-4363(80)90214-4).
- (150) Chen, Z.; Lu, Z.; Dahn, J. R. Staging Phase Transitions in Li_xCoO₂. *J. Electrochem. Soc.* **2002**, *149* (12), A1604. <https://doi.org/10.1149/1.1519850>.
- (151) Motohashi, T.; Katsumata, Y.; Ono, T.; Kanno, R.; Karppinen, M.; Yamauchi, H. Synthesis and Properties of CoO₂, the x = 0 End Member of the Li_xCoO₂ and Na_xCoO₂ Systems. *Chem. Mater.* **2007**, *19* (21), 5202–5202. <https://doi.org/10.1021/cm702533v>.
- (152) Robert, R.; Villevieille, C.; Novák, P. Enhancement of the High Potential Specific Charge in Layered Electrode Materials for Lithium-Ion Batteries. *J. Mater. Chem. A* **2014**, *2* (23), 8589–8598. <https://doi.org/10.1039/c3ta12643a>.
- (153) Amatucci, G. G.; Tarascon, J. M.; Klein, L. C. CoO₂, The End Member of the Li_xCoO₂ Solid Solution. *J. Electrochem. Soc.* **1996**, *143* (3), 1114–1123. <https://doi.org/10.1149/1.1836594>.
- (154) Ikeda, N.; Konuma, I.; Rajendra, H. B.; Aida, T.; Yabuuchi, N. Why Is the O₃ to O₁ Phase Transition Hindered in LiNiO₂ on Full Delithiation? *J. Mater. Chem. A* **2021**, *9* (29), 15963–15967. <https://doi.org/10.1039/d1ta03066c>.
- (155) Sadowski, M.; Koch, L.; Albe, K.; Siculo, S. Planar Gliding and Vacancy Condensation: The Role of Dislocations in the Chemomechanical Degradation of

Layered Transition-Metal Oxides. *Chem. Mater.* **2022**.

<https://doi.org/10.1021/acs.chemmater.2c03069>.

- (156) Mock, M.; Bianchini, M.; Fauth, F.; Albe, K.; Sicolo, S. Atomistic Understanding of the LiNiO₂-NiO₂ phase Diagram from Experimentally Guided Lattice Models. *J. Mater. Chem. A* **2021**, *9* (26), 14928–14940. <https://doi.org/10.1039/d1ta00563d>.
- (157) Li, X.; Gao, A.; Tang, Z.; Meng, F.; Shang, T.; Guo, S.; Ding, J.; Luo, Y.; Xiao, D.; Wang, X.; Su, D.; Zhang, Q.; Gu, L. Robust Surface Reconstruction Induced by Subsurface Ni Li Antisites in Ni-Rich Cathodes. *Adv. Funct. Mater.* **2021**, *31*, 2010291. <https://doi.org/10.1002/adfm.202010291>.
- (158) Riewald, F.; Kurzhals, P.; Bianchini, M.; Sommer, H.; Janek, J.; Gasteiger, H. A. The LiNiO₂ Cathode Active Material: A Comprehensive Study of Calcination Conditions and Their Correlation with Physicochemical Properties Part II. Morphology. *J. Electrochem. Soc.* **2022**, *169* (2), 020529. <https://doi.org/10.1149/1945-7111/ac4bf3>.
- (159) Goodenough, J. B.; Vvickham Aud, D. G.; Croft, W. J. Some Magnetic and Crystallographic Properties of the System Li_xNi_{1-2x}O. *J. Phys. Chem. Solids Pergamon Press* **1958**, *5*, 107–116. [https://doi.org/10.1016/0022-3697\(58\)90136-7](https://doi.org/10.1016/0022-3697(58)90136-7).
- (160) Stephens, P. W. Phenomenological Model of Anisotropic Peak Broadening in Powder Diffraction. *J. Appl. Crystallogr.* **1999**, *32* (2), 281–289. <https://doi.org/10.1107/S0021889898006001>.
- (161) Kresse, G.; Hafner, J. Ab Initio Molecular-Dynamics Simulation of the Liquid-Metalamorphous- Semiconductor Transition in Germanium. *Phys. Rev. B* **1994**, *49* (20), 14251–14269. <https://doi.org/10.1103/PhysRevB.49.14251>.
- (162) Kresse, G.; Hafner, J. Ab Initio Molecular Dynamics for Liquid Metals. *Phys. Rev. B*

- 1993**, 47 (1), 558–561. <https://doi.org/10.1103/PhysRevB.47.558>.
- (163) Kresse, G.; Furthmüller, J. Efficient Iterative Schemes for Ab Initio Total-Energy Calculations Using a Plane-Wave Basis Set G. *Phys. Rev. B* **1996**, 54 (16), 11169. <https://doi.org/10.1021/acs.jpca.0c01375>.
- (164) Peng, H.; Yang, Z.; Perdew, J. P.; Sun, J. Versatile van Der Waals Density Functional Based on a Meta-Generalized Gradient Approximation. *Phys. Rev. X* **2016**, 6, 041005–1. <https://doi.org/10.1103/PhysRevX.6.041005>.
- (165) Dovesi, R.; Erba, A.; Orlando, R.; Zicovich-Wilson, C. M.; Civalleri, B.; Maschio, L.; Rérat, M.; Casassa, S.; Baima, J.; Salustro, S.; Kirtman, B. Quantum-mechanical Condensed Matter Simulations with CRYSTAL. *Wiley Interdiscip. Rev. Comput. Mol. Sci.* **2018**, 8 (4), e1360. <https://doi.org/10.1002/wcms.1360> SOFTWARE.
- (166) Dovesi, R.; Saunders, V. R.; Roetti, C.; Orlando, R.; Zicovich-Wilson, C. M.; Pascale, F.; Civalleri, B.; Doll, K.; Harrison, N. M.; Bush, I. J.; D’Arco, P.; Llunel, M.; Causà, M.; Noël, Y.; Maschio, L.; Erba, A.; Rérat, M.; Casassa, S. CRYSTAL17 User’s Manual. **2018**, 211.
- (167) Becke, A. D. A New Mixing of Hartree-Fock and Local Density-Functional Theories. *J. Chem. Phys.* **1993**, 98 (2), 1372–1377. <https://doi.org/10.1063/1.464304>.
- (168) Lee, C.; Yang, W.; Parr, R. G. Development of the Colle-Salvetti Correlation-Energy Formula into a Functional of the Electron Density. *Phys. Rev. B* **1988**, 37 (2), 785. <https://doi.org/10.1103/PhysRevB.37.785>.
- (169) Vosko, S. H.; Wilk, L.; Nusair, M. Accurate Spin-Dependent Electron Liquid Correlation Energies for Local Spin Density Calculations: A Critical Analysis. *Can. J. Phys.* **1980**, 58 (8), 1200–1211. <https://doi.org/10.1139/p80-159>.

- (170) Stephens, P. J.; Devlin, F. J.; Chabalowski, C. F.; Frisch, M. J. Ab Initio Calculation of Vibrational Absorption. *J. Phys. Chem.* **1994**, *98* (45), 11623–11627.
<https://doi.org/10.1021/j100096a001>.
- (171) Muscat, J.; Wander, A.; Harrison, N. M. On the Prediction of Band Gaps from Hybrid Functional Theory. *Chem. Phys. Lett.* **2001**, *342* (3–4), 397–401.
[https://doi.org/10.1016/S0009-2614\(01\)00616-9](https://doi.org/10.1016/S0009-2614(01)00616-9).
- (172) Corá, F.; Alfredsson, M.; Mallia, G.; Middlemiss, D. S.; Mackrodt, W. C.; Dovesi, R.; Orlando, R. The Performance of Hybrid Density Functionals in Solid State Chemistry. In *Structure and Bonding*; 2004; pp 171–232. <https://doi.org/10.1007/b97944>.
- (173) Feng, X.; Harrison, N. M. Magnetic Coupling Constants from a Hybrid Density Functional with 35% Hartree-Fock Exchange. *Phys. Rev. B - Condens. Matter Mater. Phys.* **2004**, *70* (9), 2–5. <https://doi.org/10.1103/PhysRevB.70.092402>.
- (174) Middlemiss, D. S.; Lawton, L. M.; Wilson, C. C. A Solid-State Hybrid Density Functional Theory Study of Prussian Blue Analogues and Related Chlorides at Pressure. *J. Phys. Condens. Matter* **2008**, *20* (33), 335231.
<https://doi.org/10.1088/0953-8984/20/33/335231>.
- (175) de P. R. Moreira, I.; Illas, F.; Martin, R. L. Effect of Fock Exchange on the Electronic Structure and Magnetic Coupling in NiO. *Phys. Rev. B - Condens. Matter Mater. Phys.* **2002**, *65* (15), 1551021–15510214.
<https://doi.org/10.1103/PhysRevB.65.155102>.
- (176) Schäfer, A.; Horn, H.; Ahlrichs, R. Fully Optimized Contracted Gaussian Basis Sets for Atoms Li to Kr. *J. Chem. Phys.* **1992**, *97* (4), 2571–2577.
<https://doi.org/10.1063/1.463096>.

- (177) Monkhorst, H. J.; Pack, J. D. Special Points for Brillouin-Zone Integrations. *Phys. Rev. B* **1976**, *13* (12), 5188. <https://doi.org/10.1039/c8ta11250a>.
- (178) Hÿtch, M. J.; Snoeck, E.; Kilaas, R. Quantitative Measurement of Displacement and Strain Fields from HREM Micrographs. *Ultramicroscopy* **1998**, *74* (3), 131–146. [https://doi.org/10.1016/S0304-3991\(98\)00035-7](https://doi.org/10.1016/S0304-3991(98)00035-7).
- (179) Hÿtch, M. J.; Potez, L. Geometric Phase Analysis of High-Resolution Electron Microscopy Images of Antiphase Domains: Example Cu₃Au. *Philos. Mag. A Phys. Condens. Matter, Struct. Defects Mech. Prop.* **1997**, *76* (6), 1119–1138. <https://doi.org/10.1080/01418619708214218>.
- (180) Johnson, C. L.; Hÿtch, M. J.; Buseck, P. R. Nanoscale Waviness of Low-Angle Grain Boundaries. *Proc. Natl. Acad. Sci. U. S. A.* **2004**, *101* (52), 17936–17939. <https://doi.org/10.1073/pnas.0408348102>.
- (181) Rougier, A.; Delmas, C.; Chouteau, G. Magnetism of Li_{1-z}Ni_{1+z}O₂: A Powerful Tool for Structure Determination. *J. Phys. Chem. Solids* **1996**, *57* (6–8), 1101–1103. [https://doi.org/10.1016/0022-3697\(95\)00403-3](https://doi.org/10.1016/0022-3697(95)00403-3).
- (182) Bianchi, V.; Caurant, D.; Baffier, N.; Belhomme, C.; Chappel, E.; Chouteau, G.; Bach, S.; Pereira-Ramos, J. P.; Sulpice, A.; Wilmann, P. Synthesis, Structural Characterization and Magnetic Properties of Quasistoichiometric LiNiO₂. *Solid State Ionics* **2001**, *140* (1–2), 1–17. [https://doi.org/10.1016/S0167-2738\(01\)00706-8](https://doi.org/10.1016/S0167-2738(01)00706-8).
- (183) Stoyanova, R.; Zhecheva, E.; Friebel, C. Magnetic Interactions in Layered LiNiO₂ Revealed by EPR of Ni³⁺. *J. Phys. Chem. Solids* **1993**, *54* (1), 9–13. [https://doi.org/10.1016/0022-3697\(93\)90107-3](https://doi.org/10.1016/0022-3697(93)90107-3).
- (184) Li, H.; Hua, W.; Liu-Théato, X.; Fu, Q.; Desmau, M.; Missyul, A.; Knapp, M.;

- Ehrenberg, H.; Indris, S. New Insights into Lithium Hopping and Ordering in LiNiO₂ Cathodes during Li (De)Intercalation. *Chem. Mater.* **2021**, *33* (24), 9546–9559.
<https://doi.org/10.1021/acs.chemmater.1c02680>.
- (185) Karger, L.; Weber, D.; Goonetilleke, D.; Mazilkin, A.; Li, H.; Zhang, R.; Ma, Y.; Indris, S.; Kondrakov, A.; Janek, J.; Brezesinski, T. Low-Temperature Ion Exchange Synthesis of Layered LiNiO₂ Single Crystals with High Ordering. *Chem. Mater.* **2023**, *35*, 648–657. <https://doi.org/10.1021/acs.chemmater.2c03203>.
- (186) Bianchini, M.; Schiele, A.; Schweidler, S.; Sicolo, S.; Fauth, F.; Suard, E.; Indris, S.; Mazilkin, A.; Nagel, P.; Schuppler, S.; Merz, M.; Hartmann, P.; Brezesinski, T.; Janek, J. From LiNiO₂ to Li₂NiO₃: Synthesis, Structures and Electrochemical Mechanisms in Li-Rich Nickel Oxides. *Chem. Mater.* **2020**, *32* (21), 9211–9227.
<https://doi.org/10.1021/acs.chemmater.0c02880>.
- (187) Kim, U.-H.; Jun, D.-W.; Park, K.-J.; Zhang, Q.; Kaghazchi, P.; Aurbach, D.; Major, D. T.; Goobes, G.; Dixit, M.; Leifer, N.; Wang, C. M.; Yan, P.; Ahn, D.; Kim, K.-H.; Yoon, C. S.; Sun, Y.-K. Pushing the Limit of Layered Transition Metal Oxide Cathodes for High-Energy Density Rechargeable Li Ion Batteries. *Energy Environ. Sci.* **2018**, *11*, 1271–1279. <https://doi.org/10.1039/c8ee00227d>.
- (188) Momma, K.; Izumi, F. VESTA 3 for Three-dimensional Visualization of Crystal, Volumetric and Morphology Data. *J. Appl. Crystallogr.* **2011**, *44*, 1272–1276.
<https://doi.org/10.1107/S0021889811038970>.
- (189) Ahmed, S.; Pokle, A.; Bianchini, M.; Schweidler, S.; Beyer, A.; Brezesinski, T.; Janek, J.; Volz, K. Understanding the Formation of Antiphase Boundaries in Layered Oxide Cathode Materials and Their Evolution upon Electrochemical Cycling. *Matter*

- 2021**, 4 (12), 3953–3966. <https://doi.org/10.1016/j.matt.2021.10.001>.
- (190) Serrano-Sevillano, J.; Carlier, D.; Saracibar, A.; Lopez Del Amo, J. M.; Casas-Cabanas, M. DFT-Assisted Solid-State NMR Characterization of Defects in Li₂MnO₃. *Inorg. Chem.* **2019**, 58 (13), 8347–8356. <https://doi.org/10.1021/acs.inorgchem.9b00394>.
- (191) Sebti, E.; Evans, H. A.; Chen, H.; Richardson, P. M.; White, K. M.; Giovine, R.; Koirala, K. P.; Xu, Y.; Gonzalez-Correa, E.; Wang, C.; Brown, C. M.; Cheetham, A. K.; Canepa, P.; Clément, R. J. Stacking Faults Assist Lithium-Ion Conduction in a Halide-Based Superionic Conductor. *J. Am. Chem. Soc.* **2022**, 144 (13), 5795–5811. <https://doi.org/10.1021/jacs.1c11335>.
- (192) Clément, R. J.; Middlemiss, D. S.; Seymour, I. D.; Ilott, A. J.; Grey, C. P. Insights into the Nature and Evolution upon Electrochemical Cycling of Planar Defects in the β-NaMnO₂ Na-Ion Battery Cathode: An NMR and First-Principles Density Functional Theory Approach. *Chem. Mater.* **2016**, 28 (22), 8228–8239. <https://doi.org/10.1021/acs.chemmater.6b03074>.
- (193) Seymour, I. D.; Middlemiss, D. S.; Halat, D. M.; Trease, N. M.; Pell, A. J.; Grey, C. P. Characterizing Oxygen Local Environments in Paramagnetic Battery Materials via ¹⁷O NMR and DFT Calculations. *J. Am. Chem. Soc.* **2016**, 138 (30), 9405–9408. <https://doi.org/10.1021/jacs.6b05747>.
- (194) Bréger, J.; Jiang, M.; Dupré, N.; Meng, Y. S.; Shao-Horn, Y.; Ceder, G.; Grey, C. P. High-Resolution X-Ray Diffraction, DIFFaX, NMR and First Principles Study of Disorder in the Li₂MnO₃-Li[Ni_{1/2}Mn_{1/2}]O₂ Solid Solution. *J. Solid State Chem.* **2005**, 178 (9), 2575–2585. <https://doi.org/10.1016/j.jssc.2005.05.027>.

- (195) Li, X.; Li, X.; Monluc, L.; Chen, B.; Tang, M.; Chien, P. H.; Feng, X.; Hung, I.; Gan, Z.; Urban, A.; Hu, Y. Y. Stacking-Fault Enhanced Oxygen Redox in Li₂MnO₃. *Adv. Energy Mater.* **2022**, *12* (18), 1–10. <https://doi.org/10.1002/aenm.202200427>.
- (196) Mu, X.; Hui, X.; Wang, M.; Wang, K.; Li, Y.; Zhang, Y.; Sui, M.; Yan, P. Mitigating Twin Boundary-Induced Cracking for Enhanced Cycling Stability of Layered Cathodes. **2023**. <https://doi.org/10.1021/acsaem.3c00602>.
- (197) Yoon, C. S.; Choi, M.; Jun, D.; Zhang, Q.; Kaghazchi, P.; Kim, K.; Sun, Y. Cation Ordering of Zr-Doped LiNiO₂ Cathode for Lithium-Ion Batteries. *Chem. Mater.* **2018**, *30*, 1808–1814. <https://doi.org/10.1021/acs.chemmater.8b00619>.
- (198) Li, B.; Rouse, G.; Zhang, L.; Avdeev, M.; Deschamps, M.; Abakumov, A. M.; Tarascon, J.-M. Constructing “Li-Rich Ni-Rich” Oxide Cathodes for High-Energy Density Li-Ion Batteries. *Energy Env.* **2023**, *16*, 1210–1222. <https://doi.org/10.1039/d2ee03969a>.
- (199) Pokle, A.; Weber, D.; Bianchini, M.; Janek, J.; Volz, K. Probing the Ni(OH)₂ Precursor for LiNiO₂ at the Atomic Scale: Insights into the Origin of Structural Defect in a Layered Cathode Active Material. *Small* **2022**, *2205508*, 1–9. <https://doi.org/10.1002/sml.202205508>.
- (200) Nguyen, H.; Clément, R. J. Rechargeable Batteries from the Perspective of the Electron Spin. *ACS Energy Lett.* **2020**, *5*, 3848–3859. <https://doi.org/10.1021/acsenerylett.0c02074>.
- (201) de Biasi, L.; Schiele, A.; Roca-Ayats, M.; Garcia, G.; Brezesinski, T.; Hartmann, P.; Janek, J. Phase Transformation Behavior and Stability of LiNiO₂ Cathode Material for Li-Ion Batteries Obtained from In Situ Gas Analysis and Operando X-Ray Diffraction.

- ChemSusChem* **2019**, *12* (10), 2240–2250. <https://doi.org/10.1002/cssc.201900032>.
- (202) Bae, C.; Dupre, N.; Kang, B. Further Improving Coulombic Efficiency and Discharge Capacity in LiNiO₂ Material by Activating Sluggish ~3.5 v Discharge Reaction. *ACS Appl. Mater. Interfaces* **2021**, *13* (20), 23760–23770. <https://doi.org/10.1021/acsami.1c04359>.
- (203) Delmas, C.; Pérès, J. P.; Rougier, A.; Demourgues, A.; Weill, F.; Chadwick, A.; Broussely, M.; Perton, F.; Biensan, P.; Willmann, P. On the Behavior of the Li_xNiO₂ System: An Electrochemical and Structural Overview. *J. Power Sources* **1997**, *68* (1), 120–125. [https://doi.org/10.1016/S0378-7753\(97\)02664-5](https://doi.org/10.1016/S0378-7753(97)02664-5).
- (204) Delmas, C.; Carlier, D.; Ceder, G.; Ménétrier, M.; Grey, C. P. Understanding the NMR Shifts in Paramagnetic Transition Metal Oxides Using Density Functional Theory Calculations. *Phys. Rev. B* **2003**, *67* (17), 174103. <https://doi.org/10.1103/PhysRevB.67.174103>.
- (205) Zheng, J.; Ye, Y.; Liu, T.; Xiao, Y.; Wang, C.; Wang, F.; Pan, F. Ni/Li Disordering in Layered Transition Metal Oxide: Electrochemical Impact, Origin, and Control. *Acc. Chem. Res.* **2019**, *52* (8), 2201–2209. <https://doi.org/10.1021/acs.accounts.9b00033>.
- (206) Lin, F.; Markus, I. M.; Nordlund, D.; Weng, T. C.; Asta, M. D.; Xin, H. L.; Doeff, M. M. Surface Reconstruction and Chemical Evolution of Stoichiometric Layered Cathode Materials for Lithium-Ion Batteries. *Nat. Commun.* **2014**, *5*, 3529. <https://doi.org/10.1038/ncomms4529>.
- (207) Joo Lee, Y.; Grey, C. P. ⁶Li Magic-Angle Spinning (MAS) NMR Study of Electron Correlations, Magnetic Ordering, and Stability of Lithium Manganese(III) Oxides. *Chem. Mater.* **2000**, *12* (12), 3871–3878. <https://doi.org/10.1021/cm000469t>.

- (208) Xu, C.; Märker, K.; Lee, J.; Mahadevegowda, A.; Reeves, P. J.; Day, S. J.; Groh, M. F.; Emge, S. P.; Ducati, C.; Layla Mehdi, B.; Tang, C. C.; Grey, C. P. Bulk Fatigue Induced by Surface Reconstruction in Layered Ni-Rich Cathodes for Li-Ion Batteries. *Nat. Mater.* **2021**, *20* (1), 84–92. <https://doi.org/10.1038/s41563-020-0767-8>.
- (209) Nguyen, H.; Silverstein, R.; Zaveri, A.; Cui, W.; Kurzhals, P.; Sicolo, S.; Bianchini, M.; Seidel, K.; Clément, R. J. Twin Boundaries Contribute to The First Cycle Irreversibility of LiNiO₂. *Adv. Funct. Mater.* **2023**, 2306168. <https://doi.org/10.1002/adfm.202306168>.
- (210) Delmas, C.; Ménétrier, M.; Croguennec, L.; Levasseur, S.; Pérès, J. P.; Poullier, C.; Prado, G.; Fournès, L.; Weill, F. Lithium Batteries: A New Tool in Solid State Chemistry. *Int. J. Inorg. Mater.* **1999**, *1* (1), 11–19. [https://doi.org/10.1016/S1463-0176\(99\)00003-4](https://doi.org/10.1016/S1463-0176(99)00003-4).
- (211) Li, W.; Liu, X.; Celio, H.; Smith, P.; Dolocan, A.; Chi, M.; Manthiram, A. Mn versus Al in Layered Oxide Cathodes in Lithium-Ion Batteries: A Comprehensive Evaluation on Long-Term Cyclability. *Adv. Energy Mater.* **2018**, *8*, 1703154. <https://doi.org/10.1002/aenm.201703154>.
- (212) Sharma, A.; Rajkamal, A.; Kobi, S.; Kumar, B. S.; Paidi, A. K.; Chatterjee, A.; Mukhopadhyay, A. Addressing the High-Voltage Structural and Electrochemical Instability of Ni-Containing Layered Transition Metal (TM) Oxide Cathodes by “Blocking” the “TM-Migration” Pathway in the Lattice. *ACS Appl. Mater. Interfaces* **2021**, *13* (22), 25836–25849. <https://doi.org/10.1021/acsami.1c01347>.
- (213) Kim, N. Y.; Yim, T.; Song, J. H.; Yu, J. S.; Lee, Z. Microstructural Study on Degradation Mechanism of Layered LiNi_{0.6}Co_{0.2}Mn_{0.2}O₂ Cathode Materials by

- Analytical Transmission Electron Microscopy. *J. Power Sources* **2016**, *307*, 641–648.
<https://doi.org/10.1016/j.jpowsour.2016.01.023>.
- (214) Friedrich, F.; Strehle, B.; Freiberg, A. T. S.; Kleiner, K.; Day, S. J.; Erk, C.; Piana, M.; Gasteiger, H. A. Capacity Fading Mechanisms of NCM-811 Cathodes in Lithium-Ion Batteries Studied by X-Ray Diffraction and Other Diagnostics. *J. Electrochem. Soc.* **2019**, *166* (15), A3760–A3774. <https://doi.org/10.1149/2.0821915jes>.
- (215) Strehle, B.; Friedrich, F.; Gasteiger, H. A. A Comparative Study of Structural Changes during Long-Term Cycling of NCM-811 at Ambient and Elevated Temperatures. *J. Electrochem. Soc.* **2021**, *168* (5), 050512. <https://doi.org/10.1149/1945-7111/abf780>.
- (216) Kong, F.; Liang, C.; Wang, L.; Zheng, Y.; Peranathan, S.; Longo, R. C.; Ferraris, J. P.; Kim, M.; Cho, K. Kinetic Stability of Bulk LiNiO₂ and Surface Degradation by Oxygen Evolution in LiNiO₂-Based Cathode Materials. *Adv. Energy Mater.* **2019**, *9*, 1802586. <https://doi.org/10.1002/aenm.201802586>.
- (217) Pan, R.; Jo, E.; Cui, Z.; Manthiram, A. Degradation Pathways of Cobalt-Free LiNiO₂ Cathode in Lithium Batteries. *Adv. Funct. Mater.* **2023**, *33*, 2211461.
<https://doi.org/10.1002/adfm.202211461>.
- (218) Mukherjee, P.; Lu, P.; Faenza, N.; Pereira, N.; Amatucci, G.; Ceder, G.; Cosandey, F. Atomic Structure of Surface-Densified Phases in Ni-Rich Layered Compounds. *ACS Appl. Mater. Interfaces* **2021**, *13* (15), 17478–17486.
<https://doi.org/10.1021/acsami.1c00143>.
- (219) Arroyo y de Dompablo, M. E.; Van der Ven, A.; Ceder, G. First-Principles Calculations of Lithium Ordering and Phase Stability on Li_xNiO₂. *Phys. Rev. B - Condens. Matter Mater. Phys.* **2002**, *66* (6), 1–9.

<https://doi.org/10.1103/PhysRevB.66.064112>.

- (220) Schweidler, S.; De Biasi, L.; Garcia, G.; Mazilkin, A.; Hartmann, P.; Brezesinski, T.; Janek, J. Investigation into Mechanical Degradation and Fatigue of High-Ni NCM Cathode Material: A Long-Term Cycling Study of Full Cells. *ACS Appl. Energy Mater.* **2019**, *2* (10), 7375–7384. <https://doi.org/10.1021/acsaem.9b01354>.
- (221) Aishova, A.; Park, G. T.; Yoon, C. S.; Sun, Y. K. Cobalt-Free High-Capacity Ni-Rich Layered Li[Ni_{0.9}Mn_{0.1}]O₂ Cathode. *Adv. Energy Mater.* **2020**, *10* (4). <https://doi.org/10.1002/aenm.201903179>.
- (222) Jamil, S.; Li, C.; Fasehullah, M.; Liu, P.; Xiao, F.; Wang, H.; Bao, S.; Xu, M. Ni/Li Antisite Induced Disordered Passivation Layer for High-Ni Layered Oxide Cathode Material. *Energy Storage Mater.* **2022**, *45* (November 2021), 720–729. <https://doi.org/10.1016/j.ensm.2021.12.025>.
- (223) Xu, T.; Du, F.; Wu, L.; Fan, Z.; Shen, L.; Zheng, J. Boosting the Electrochemical Performance of LiNiO₂ by Extra Low Content of Mn-Doping and Its Mechanism. *Electrochim. Acta* **2022**, *417* (March), 140345. <https://doi.org/10.1016/j.electacta.2022.140345>.